

December 2021

**IEA Wind TCP Task 29**

**Detailed Aerodynamics  
of Wind Turbines**

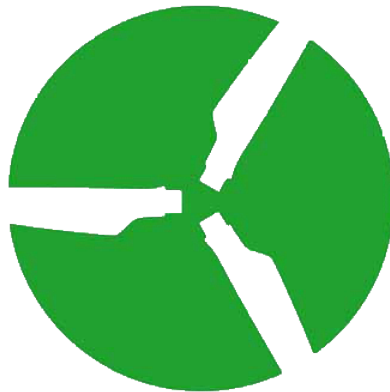


**iea wind**

# IEA Wind TCP Task 29, Phase IV: Detailed Aerodynamics of Wind Turbines

J.G. Schepers, K. Boorsma, H.Aa. Madsen, G.R. Pirrung,  
Ö. S. Özcakmak, G. Bangga, G. Guma, T. Lutz, T. Potentier,  
C. Braud, E. Guilmineau, A. Croce, S. Cacciola,  
A. P. Schaffarczyk, B. A. Lobo, S. Ivanell, H. Asmuth, F. Bertagnolio,  
N.N. Sørensen, W. Z. Shen, C. Grinderslev, A. M. Forsting,  
F. Blondel, P. Bozonnet, R. Boisard,  
K. Yassin, L. Höning, B. Stoevesandt, M. Imiela,  
L. Greco, C. Testa, F. Magionesi,  
G. Vijayakumar, S. Ananthan, M. A. Sprague, E. Branlard, J. Jonkman,  
M. Carrion, S. Parkinson, E. Cicirello

December 24, 2021



**iea wind**

# Contents

<b>1</b>	<b>Introduction: Background and goal</b>	<b>9</b>
1.1	Introduction . . . . .	9
1.2	History and background of IEA Task29 Phase IV . . . . .	11
1.3	Goal . . . . .	11
1.4	Dissemination . . . . .	12
<b>2</b>	<b>Work plan, deliverables, meetings</b>	<b>13</b>
2.1	Workplan . . . . .	13
2.2	Deliverables and reports . . . . .	14
2.3	Meetings . . . . .	14
<b>3</b>	<b>WP1: The database</b>	<b>17</b>
3.1	Introduction . . . . .	17
3.2	The DanAero data base and IEA Task 29, phase IV . . . . .	17
3.3	Establishing the DanAero data base within IEA Task 29, phase IV . . . . .	18
3.4	The DanAero data base - turbine model . . . . .	18
3.4.1	Aerodynamic-aeroelastic modelling . . . . .	18
3.4.2	HAWC2-aeroelastic-model-setup . . . . .	19
3.4.3	CFD modelling . . . . .	19
3.5	The DanAero data base - experimental data . . . . .	19
3.5.1	Field measurements Tjaereborg . . . . .	19
3.5.2	The calibrated data . . . . .	20
3.5.3	The raw data . . . . .	24
3.5.4	Wind tunnel measurements at LM . . . . .	24
3.5.5	Measurement campaigns and operational modes of the turbine . . . . .	24
3.5.6	The selection of files for the benchmark cases . . . . .	24
3.6	Data file for first round of benchmark - axial flow, case IV.1 . . . . .	25
3.7	Data file for second round of benchmark - sheared flow, case IV.2.1 . . . . .	31
3.8	Data file for second round of benchmark - yawed flow, case IV.2.2 . . . . .	32
3.9	Measurement checks and strain gauge calibration using an aeroelastic model . . . . .	33
3.9.1	Motivation for calibration . . . . .	33
3.9.2	Calibration procedure . . . . .	33
3.9.3	Results in uniform inflow case . . . . .	37
3.9.4	Conclusions on the calibration . . . . .	38
<b>4</b>	<b>WP2: Comparison between calculations and measurements</b>	<b>39</b>
4.1	Introduction . . . . .	39
4.2	First round: Axial flow, Case IV.1 . . . . .	40
4.2.1	Lifting line codes . . . . .	40
4.2.2	CFD and panel codes . . . . .	42
4.2.3	CFD sensitivity study . . . . .	42
4.2.4	Model types comparison . . . . .	45
4.3	Second round: Shear (Case IV.2.1) and yawed flow (Case IV.2.2) . . . . .	48

4.3.1	Lifting line codes . . . . .	48
4.3.2	CFD and panel codes . . . . .	49
4.3.3	CFD synthesized airfoil data . . . . .	49
4.3.4	Model types . . . . .	51
<b>5</b>	<b>Task 3.1: Effects of Inflow Turbulence</b>	<b>56</b>
5.1	Introduction . . . . .	56
5.1.1	Motivation and Goals . . . . .	56
5.1.2	Participants . . . . .	57
5.2	Test Matrix . . . . .	57
5.2.1	Empty Box . . . . .	57
5.2.2	Rotor Simulations . . . . .	58
5.2.3	General Flow Conditions . . . . .	61
5.3	Results and Discussion . . . . .	62
5.3.1	Empty Box Case . . . . .	62
5.3.2	Rotor Case . . . . .	62
5.4	Concluding Remarks on Task 3.1: Effects of Inflow Turbulence . . . . .	69
<b>6</b>	<b>Task 3.2: Yawed inflow</b>	<b>71</b>
<b>7</b>	<b>Task 3.3: Wake effects</b>	<b>73</b>
7.1	Introduction . . . . .	73
7.1.1	Motivation and Goals . . . . .	73
7.2	Participants and Models . . . . .	73
7.3	Case description . . . . .	74
7.4	Numerical Set-up . . . . .	75
7.5	Results . . . . .	76
7.5.1	Case A - Partial wake . . . . .	76
7.5.2	Case B - Full wake . . . . .	78
7.6	Concluding remarks on Task 3.3: Wake effects . . . . .	79
<b>8</b>	<b>Task 3.4: 2D-3D airfoil characterization</b>	<b>83</b>
8.1	Introduction . . . . .	83
8.2	iBEM solver . . . . .	83
8.2.1	Description . . . . .	83
8.2.2	Other information . . . . .	84
8.3	Results and perspectives . . . . .	84
<b>9</b>	<b>Task 3.5: Aeroelastic analyses</b>	<b>90</b>
9.1	Aeroelastic simulations and modal analyses . . . . .	90
9.2	Results . . . . .	91
9.2.1	Modes of isolated blade . . . . .	91
9.2.2	Modes of turbine at standstill . . . . .	94
9.2.3	Campbell diagram of the entire turbine <i>in vacuo</i> and in air . . . . .	96
9.2.4	Nominal Wind Profile (NWP) simulations . . . . .	100
9.3	Conclusions and comments on Task 3.5: Aeroelastic analyses . . . . .	105
<b>10</b>	<b>Task 3.6: Boundary Layer Transition</b>	<b>106</b>
10.1	Introduction . . . . .	106
10.2	Discussion of Results from DAN-AERO and Aerodynamic Glove on MM92 Experiments . . . . .	106
10.2.1	DAN-AERO . . . . .	106
10.2.2	Aerodynamic Glove . . . . .	111
10.3	Targeted search for a possible low-pass cutoff . . . . .	111
10.3.1	Background . . . . .	111
10.3.2	LES investigations . . . . .	111

10.4	CFD runs . . . . .	115
10.5	Summary and Conclusions of Task 3.6: Boundary Layer Transition . . . . .	115
10.6	Outlook to future experiments on boundary layer transition . . . . .	117
<b>11</b>	<b>Task 3.7: Acoustics</b>	<b>118</b>
11.1	Test cases definition . . . . .	118
11.2	Comparison of different wind turbine noise codes . . . . .	119
11.3	Main results from the comparison benchmark . . . . .	119
11.4	Conclusions on Task 3.7: Acoustics and outlooks . . . . .	119
<b>12</b>	<b>WP4: New aerodynamic experiments</b>	<b>123</b>
<b>13</b>	<b>WP5: Integration and communication to other IEA Tasks and former phases</b>	<b>125</b>
<b>14</b>	<b>Conclusions and recommendations</b>	<b>127</b>
<b>A</b>	<b>Comparison Round Data Format and Test Cases</b>	<b>144</b>
A.1	First round: Uniform inflow . . . . .	145
A.2	Second round: Shear and Yawed flow . . . . .	152
<b>B</b>	<b>Lifting line code description</b>	<b>160</b>
B.1	DNV GL - Bladed - Code description . . . . .	161
B.2	DTU - EllipSys3D/Actuator Line/FLEX5 - Code description . . . . .	162
B.3	Description of DTU - HAWC2 codes . . . . .	164
B.3.1	Introduction . . . . .	164
B.3.2	The HAWC2 code . . . . .	164
B.3.3	The structural part of HAWC2 . . . . .	164
B.3.4	EllipSys3D-AL . . . . .	165
B.4	IFPEN DeepLines Wind <sup>TM</sup> solver . . . . .	166
B.4.1	DeepLines Wind <sup>TM</sup> aero-elastic model . . . . .	166
B.4.2	<i>AeroDeeP</i> : Blade Element Momentum (BEM) model . . . . .	166
B.4.3	<i>CASTOR</i> : Free-wake lifting-line vortex filaments flow solver . . . . .	168
B.4.4	DanAero simulations setup . . . . .	168
B.5	NREL OpenFAST - Code description and simulation setup . . . . .	170
B.5.1	BEM . . . . .	170
B.5.2	Lifting line vortex methods . . . . .	170
B.5.3	Structural modeling . . . . .	171
B.5.4	Other information . . . . .	172
B.6	ONERA - PUMA - Actuator Line/Free Wake - Code description . . . . .	174
B.7	TNO Aero Module . . . . .	175
B.7.1	Model . . . . .	175
B.7.2	Settings . . . . .	175
B.8	POLIMI Codes Description . . . . .	176
B.8.1	The Cp-Lambda code . . . . .	176
B.8.2	Periodic stability analysis through system identification . . . . .	177
<b>C</b>	<b>CFD and panel codes descriptions</b>	<b>179</b>
C.1	Description of the simulations for the comparison rounds IV1.1 (axial inflow), IV2.1 (shear) and IV2.2 (yaw) with the DLR TAU code . . . . .	179
C.1.1	Flow Solver TAU . . . . .	179
C.1.2	General Set-up . . . . .	179
C.1.3	Axial Flow (Case IV.1.1) . . . . .	180
C.1.4	Sheared and Yawed Flow (Case IV.2.1, Case IV.2.2) . . . . .	181
C.1.5	Acknowledgement . . . . .	183
C.2	DTU - EllipSys3D - Code description and simulation setup . . . . .	184

C.2.1	Flow solver . . . . .	184
C.2.2	Computational grids . . . . .	184
C.2.3	Simulation setups . . . . .	186
C.3	NREL - Exawind - Code description and simulation setup . . . . .	187
C.3.1	Flow solver . . . . .	187
C.3.2	Computational grids for steady inflow (Case IV.1.1, Case IV.2.1 and Case IV.2.2) . . . . .	187
C.3.3	Simulation setup for steady inflow (Case IV.1.1, Case IV.2.1 and Case IV.2.2) . . . . .	188
C.4	ForWind-IWES-HSEmden/Leer - Description of OpenFOAM simulations . . . . .	189
C.4.1	General Description . . . . .	189
C.4.2	Simulation tasks' description . . . . .	190
C.5	CNR-INM, FUNAERO: code description and simulation setup for for rounds IV1.1 (axial inflow), IV2.1 (shear) and IV2.2 (yaw) . . . . .	193
C.5.1	General model description . . . . .	193
C.5.2	Simulation setup . . . . .	193
C.5.3	Rotor and tower structural modelling . . . . .	194
C.6	ONERA - ELSA - Code description . . . . .	195
C.7	Code description ANSYS FLUENT, used by Kiel UAS . . . . .	196
C.7.1	Code description . . . . .	196
C.7.2	Solution Methods . . . . .	196
C.7.3	Mesh . . . . .	196
C.7.4	Discussion . . . . .	198
C.7.5	Resources . . . . .	198
C.7.6	Acknowledgement . . . . .	198
C.8	USTUTT Code description and setup . . . . .	199
C.8.1	FLOWer Code . . . . .	199
C.8.2	B-GO . . . . .	199
C.8.3	SIMPACK Software . . . . .	199
C.8.4	AeroDyn . . . . .	200
C.8.5	Setup for Task 1: Uniform Inflow . . . . .	200
C.8.6	Setup for Tasks 2.1 and 2.2: Shear & Yaw . . . . .	202
C.8.7	Setup for Task 3.1: Effects of Inflow Turbulence . . . . .	204
C.8.8	Setup for Task 3.5: Aeroelastic Effects . . . . .	204
C.9	UU Code descriptions . . . . .	206
C.9.1	elbe - LBM-LES . . . . .	206
C.9.2	OpenFOAM - RANS and LES . . . . .	206
C.10	NREL wt_perf - Code description . . . . .	207
C.10.1	Code description . . . . .	207
<b>D</b>	<b>WP2 Comparison plots: Axial flow</b> . . . . .	<b>208</b>
D.1	Lifting line codes . . . . .	208
D.1.1	Lifting line variables . . . . .	210
D.1.2	Loads and deformations . . . . .	214
D.2	CFD and panel codes . . . . .	218
D.2.1	Pressure distributions . . . . .	219
D.2.2	Loads and performance . . . . .	222
<b>E</b>	<b>WP2 Comparison plots: Shear and yawed flow</b> . . . . .	<b>223</b>
E.1	Lifting line codes . . . . .	223
E.1.1	Lifting line variables . . . . .	224
E.1.2	Loads and performance . . . . .	237
E.2	CFD and panel codes . . . . .	241
E.2.1	Pressure distributions . . . . .	242
E.2.2	Loads and performance . . . . .	251

<b>F</b>	<b>WP1: The database - Figures for shear and yaw cases</b>	<b>255</b>
F.1	File and graphs for second round of benchmark - sheared flow IV.2.1 . . . . .	255
F.2	File and graphs for second round of benchmark - yawed flow IV.2.2 . . . . .	260

# Acknowledgement

The authors would like to thank IEA TCP Wind for facilitating the IEA Task29 Phase IV project in their framework. The contributions of the participants to IEA Task29 Phase IV have been funded in various national programmes:

- The contributions from TNO, Suzlon, CWI and DNV-GL were partly funded by the Top sector Energy Subsidy from the Dutch Ministry of Economic Affairs and Climate within the framework of the WindTrue project.
- The Swedish activities were financed by The Swedish Energy Agency. The Swedish computer resources were granted by the Swedish National Infrastructure for Computing (SNIC).
- The computational resources for the University of Stuttgart were provided by the High Performance Computing Center Stuttgart (HLRS) and the Leibniz Supercomputing Center (LRZ).
- The work was supported by the North-German Supercomputing Alliance (HLRN), which was used by Kiel University of Applied Sciences
- The simulations from ForWind/Fraunhofer IWES were performed using the HPC Cluster EDDY in the University of Oldenburg, a part of WIMS-Cluster project
- The US work was coauthored by the National Renewable Energy Laboratory, operated by Alliance for Sustainable Energy, LLC, for the U.S. Department of Energy (DOE) under Contract No. DE-AC36-08GO28308. Funding provided by the U.S. Department of Energy Office of Energy Efficiency and Renewable Energy Wind Energy Technologies Office. The views expressed in the article do not necessarily represent the views of the DOE or the U.S. Government. The U.S. Government retains and the publisher, by accepting the article for publication, acknowledges that the U.S. Government retains a nonexclusive, paid-up, irrevocable, worldwide license to publish or reproduce the published form of this work, or allow others to do so, for U.S. Government purposes. A portion of this research was performed using computational resources sponsored by the Department of Energy's Office of Energy Efficiency and Renewable Energy and located at the National Renewable Energy Laboratory.
- The Danish participation and contributions have been carried out based on funding from EUDP 2018-I, contract J.nr. 64018-0084. However, this funding covers mainly participation in IEA Task 29 IV project meetings and preparations for this as well as the final reporting. Other contributions have come from DTU through e.g. funding of PhD students, that have participated in the IEA task 29 IV.



# Abstract

This report describes the final results of the fourth phase of IEA TCP Wind Task 29. The project period of this fourth phase was from January 1<sup>st</sup> 2018 until December 31<sup>st</sup> 2020. It was the follow-up of three former IEA Task 29 phases (often denoted as Mexnext-I to Mexnext-III). In all phases wind turbine aerodynamic models were validated and improved with detailed aerodynamic measurements. In these detailed aerodynamic experiments pressure distributions at different locations along the rotor blades are measured anyhow where measurements of e.g. inflow velocities and boundary layer transition are very nice to know. The first three phases were mainly built around wind tunnel measurements on a small scale wind turbine with rotor diameter of 4.5 meter from the (New) Mexico project but the present phase was built around field measurements from the DanAero experiment. This DanAero experiment was carried out at atmospheric field conditions on a 2MW turbine by Danish Technical University DTU and 4 industrial partners (LM Glassfiber, Siemens WindPower, Vestas and Dong Energy) in 2 periods from 2007 until 2010 and from 2010 until 2013. Amongst others surface pressures and inflow velocities were measured at four sections along a blade and a row of surface flush mounted microphones was installed at the outer part of the blade.

In IEA Task29 Phase IV the DanAero data were made available to the IEA Task 29 participants which enabled a detailed analysis in a collaborative action. Amongst others a critical scrutinising of data took place with subsequent further improvement of measurement quality. Moreover the measurements were used as validation material for the many design models which are available in the consortium. A wide variety of models could be considered ranging from high fidelity (but time consuming) CFD to lower fidelity but efficient engineering models. Intermediate methods (e.g. free wake methods) were applied as well.

Several calculational rounds were carried out where calculations were compared with measurements. Amongst others a case was defined at simple steady and axi-symmetric conditions close to a measurement case with little shear and little yaw but also measurement cases at high yaw and high shear were simulated.

Moreover the level of detail from the DanAero experiment allowed an in-depth analysis of several wind turbine aerodynamic aspects, e.g.

- Aerodynamic response to turbulent inflow;
- Sheared inflow;
- 2D/3D aerodynamics;
- Aeroelastic effects
- Transition characteristics in realistic flow conditions;
- Acoustics.

The project was carried out by a consortium which consisted of research groups and industries from 9 different countries

- China: Chinese Wind Energy Association, CWEA
- Denmark: Technical University of Denmark, DTU, Siemens-Gamesa Renewable Energy
- France: IFPEN, LHEEA lab - Centrale Nantes/CNRS , ONERA, EDF

- Germany: ForWind/Fraunhofer IWES, Kiel University of Applied Sciences, University of Stuttgart, WindNovation, Enercon Deutsches Zentrum für Luft- und Raumfahrt e.V., DLR University of Applied Sciences Emden
- Italy: PoliMi, RSE , CNR - INM
- Netherlands: TNO Energy Transition (formerly ECN, Operating Agent), Delft University of Technology, TUDelft, DNV-GL Suzlon Blade Technology, SBT, CWI, LM and University of Twente, UTwente
- Sweden: Uppsala University, Campus Gotland,
- Switzerland: UAS Rapperswil
- USA: National Renewable Energy Laboratory, NREL

# Chapter 1

## Introduction: Background and goal

### 1.1 Introduction

This report describes the results of the fourth phase of IEA Task 29 on wind turbine aerodynamics. This fourth phase, like the first 3 phases (denoted as Mexnext-I to Mexnext-III ) is carried out as an IEA Wind Task, i.e. a collaborative international project organised under the auspices of the Technology Collaboration Program (TCP) Wind from the International Energy Agency (IEA).

In IEA Task29 Phase IV the following countries and parties participated (between brackets the contact persons are listed):

- China: Chinese Wind Energy Association, CWEA (Cai Fengbo, He Dexin, Zhenyu Zhang)
- Denmark: Technical University of Denmark, DTU (H. Madsen, N. Sørensen, G. Pirrung, W. Z. Shen, C. Grinderslev, A. Meyer Forsting, F. Bertagnolio, Ö. S. Özçakmak, S. G. Horcas) Siemens-Gamesa Renewable Energy (Alejandro Gonzales, Alex Loeven)
- France: IFPE (F. Blondel, P. Bozonnet), LHEEA lab - Centrale Nantes/CNRS (C. Braud, T. Potentier, E. Guilmineau, A. Ducoin, Z. Jing), ONERA (C. Lienard, R. Boisard), EDF (Benoit de Laage de Meux)
- Germany: ForWind/Fraunhofer IWES (B. Stoevesandt, K. Yassin, L. Hoening), Kiel University of Applied Sciences (A. P. Schaffarczyk, B. A. Lobo), University of Stuttgart (T. Lutz, G. Guma, G. Bangga ), WindNovation (D. Schulze), Enercon (T. Kuehn, P. Weihing), Deutsches Zentrum für Luft- und Raumfahrt e.V., DLR (M. Imiela), University of Applied Sciences Emden (I. Herraetz)
- Italy: PoliMi (A. Croce, S. Cacciola), RSE (L. Serri), CNR - INM (L. Greco)
- Netherlands: TNO Energy Transition (formerly ECN, G. Schepers, K. Boorsma. M. Caboni), Delft University of Technology, TUDelft (C. Ferreira, Wei Yu, A. Vire), DNV-GL (M. Carrion), Suzlon Blade Technology, SBT (C. Rodriguez), CWI (B. Sanderse), LM (M. Kloosterman) and University of Twente, UTwente (A. van Garrel)
- Sweden: Uppsala University, Campus Gotland, (S. Ivanell, H. Asmuth, G. P. Navarro Diaz, K. Nilsson)
- Switzerland: UAS Rapperswil (S. Barber)
- USA: National Renewable Energy Laboratory, NREL (J. Jonkman, E. Branlard, G. Vijayakumar, S. Ananthan, M.A.Sprague)

The focus of IEA Task29 Phase IV was on the validation, improvement and understanding of aerodynamic models as implemented in wind turbine design codes by analysing detailed aerodynamic measurements from the DanAero experiment. In order to understand the importance of this subject it first has to be realised that wind turbine design codes are essential for industry to assess the lifetime and the energy production

before the investment is made to build a turbine prototype. The aerodynamic model is then the most challenging component of these codes because every aerodynamic process, in its basis, is described by means of the so-called Navier Stokes equations which cannot be solved in an analytical way where also a numerical solution of the Navier Stokes equations is out of reach due to extreme calculational demands. The difficulty of accurate aerodynamic modelling is perhaps most convincingly illustrated by the fact that solving the Navier Stokes equations (as a matter of fact 'only' proving that a smooth solution exists) is one of the seven Millenium Prize Problems as formulated by the Clay Mathematics institute in 2000. As such every aerodynamic model inherently suffers from simplifications. For wind turbine aerodynamics an additional difficulty arises from the fact that the computational effort for design calculations is more extreme than it is for most other applications (e.g. fixed wing aerospace), see [1]. This necessitates the use of engineering models which are very efficient, but also very simplified aerodynamic models based on the Blade Element Momentum (BEM) method. Obviously more advanced methods like Computational Fluid Dynamic (CFD) codes are applied too, but their use is, due to the calculational demands, restricted to specific studies and load cases. From a practical point of view the simplifications in engineering methods inevitably go together with a large uncertainty band, which is even larger for modern MW scale wind turbines. The larger uncertainties with increased size are partly a result of unknown (high) Reynolds effects where moreover the stronger flexibilities will lead to larger deflections and more pronounced non-linear aero-elastic behavior with unknown aerodynamic implications. Other uncertainties result from the thick(er) airfoils which are applied on large rotors and which are very difficult to model accurately in an aerodynamic sense. Last but not least the changed relation between the scales in atmospheric inflow to the scales of the turbine (blades) lead to larger uncertainties for increased rotor size. In order to reduce the uncertainty band of aerodynamic models and to make them reliable enough for the design of cost-effective turbines, they need to be improved and validated with good measurements. It is then explained in [2] that conventional wind turbine measurements of e.g. power and blade root bending moment lack sufficient detail for that purpose by which very special rotor aerodynamic experiments are needed (often denoted as detailed aerodynamic experiments). In these detailed aerodynamic experiments pressure distributions at different locations along the rotor blades should be measured anyhow where measurements of e.g. inflow velocities and boundary layer transition are very nice to know. However, detailed aerodynamic measurements on MW-scale wind turbines have never been published at least not until DanAero experimental data were released in the present project. This DanAero experiment was carried out at atmospheric field conditions on a 2MW turbine in a Danish project by Danish Technical University DTU and 4 industrial partners (LM Glassfiber, Siemens WindPower, Vestas and Dong Energy) in 2 periods from 2007 until 2010 and from 2010 until 2013. The level of detail from the instrumentation lies far above the level at conventional wind turbine measurements. Amongst others surface pressures and inflow velocities were measured at four sections along a blade and a row of surface flush mounted microphones was installed at the outer part of the blade enabling the study of transition and the surface pressure spectrum which is the source of trailing edge noise. The unique data from the DanAero experiment, including a description of the turbine, were made available to the participants of IEA Task29 Phase IV so that it could form a basis for a thorough analysis. Doing this analysis in a cooperation under auspices of IEA TCP Wind has led to many mutual benefits for the participants. The large size of the consortium brought ample manpower for the analysis where the learning process by combining several complementary experiences and modelling techniques gave valuable insights which could not be found when the analysis was carried out individually.

This report first describes the background and goal of IEA Task29 Phase IV in the sections 1.2 and 1.3. Dissemination of results has taken place in very different forms, as explained in section 1.4. Then the working procedure and the work plan of IEA Task29 Phase IV is described in chapter 2. The uniqueness of the DanAero experiment and the database are described in chapter 3. Several calculational rounds were defined in which results from a large variety of aerodynamic models were compared with DanAero measurements. The measurements have also been used to improve physical understanding of many aerodynamic phenomena on MW scale wind turbines. Thereto several subjects have been defined which could be studied with the DanAero measurements

The comparison of DanAero data with results from different aerodynamic models and the subsequent analysis of DanAero measurements is described in chapter 4 and the chapters 5 to 11. These chapters are generally written on a high aerodynamic level and they are meant to be reference material for the aerodynamic specialist.

In chapter 12 it is explained that the analyses on the DanAero data did not only enhance the aerodynamic modelling knowledge but it also led to experimental insights with which future large scale aerodynamic experiments can be designed in an even better way. Such aerodynamic experiments are now being initiated at several countries of IEA TCP Wind.

In order to gain maximum benefit of the enhanced knowledge from IEA Task29 Phase IV for wind turbine design it should be integrated with the knowledge on other relevant disciplines. For this reason a number of cooperations with other IEA Tasks which have connections to aerodynamics are established. These are described in chapter 13. This chapter also explains how the knowledge from IEA Task29 Phase IV is integrated with the knowledge from the previous phases of Task 29 (Mexnext-I to Mexnext-III ). In these previous phases wind tunnel measurements were analysed where the present phase uses field measurements. Finally conclusions and recommendations are given in chapter 14.

## 1.2 History and background of IEA Task29 Phase IV

The background of IEA Task29 Phase IV is related to the striking observation that only very limited detailed aerodynamic experiments have been performed in public domain even though, as explained in section 1.1, such experiments are essential for validation and improvement of aerodynamic models.

The few examples of detailed aerodynamic measurements have almost all been brought in IEA Tasks. This started with IEA Task 14 and 18 in the 1990's, see [3] and [4]. In IEA Tasks 14 and 18 field measurements were collected on 5 facilities with which first insights on rotor aerodynamics were generated. Amongst others the pressure distributions and loads were measured at different locations along the blade.

In IEA Task 20 measurements from the NREL Phase IV experiment were analysed. These measurements were taken by NREL in the year 2000 on a 10 meter turbine in the NASA-Ames wind tunnel [5] and [6].

Task 20 was followed by IEA Task 29 where the first three phases (Mexnext-I to Mexnext-III ) were built around measurements taken on a wind turbine model with a diameter of 4.5 m, which was placed in the largest European wind tunnel, the German Dutch Wind Tunnel, DNW. In these experiments pressures and loads were measured, like it was done in IEA Task 14/18 and 20 but in addition the underlying flow field data was mapped with Particle Image Velocimetry (PIV). The measurements were taken in December 2006 within the EU project Mexico [7] and in July 2014 within the New Mexico experiment [8]. The analysis from the first three phases were very successful, see [9], [10] and [11] where the fact that flow field measurements were taken in addition to pressure and load measurements gave unique insights on so-called induction aerodynamics, which turned out to be an important source of uncertainties in wind turbine design codes. Still the wind tunnel environment made that there are still other significant uncertainties in wind turbine aerodynamics which could not be evaluated or only to a smaller extent. In this respect one could think of the aerodynamic/aero-elastic response (including boundary layer transition) to turbulent inflow with shear since the flow in the wind tunnel is non-turbulent and non-sheared where the small scale of a wind tunnel model makes aero-elastic effects very limited opposite to the situation for a representative full scale wind turbine. These subjects could be investigated in the Danish DanAero experiment which was carried out in the period around 2010 but the results of this experiment were initially restricted to the DanAero consortium only. At a later stage they were made available to the Task 29 consortium, see chapter 3. They were then analysed in the fourth phase of Task 29, i.e. the phase which is described in the present report.

The fact that the DanAero experiment is done under atmospheric conditions and full scale gives it added value to the wind tunnel measurements from Task 20 and the first three phases of Task 29. The DanAero experiment also has added value compared to the before mentioned field measurements from IEA Tasks 14 and 18 because it applies more advanced measurement techniques (e.g. microphones) and because of the much larger scale (the largest rotor diameter in IEA Tasks 14/18 was 27 meter where the diameter of the DanAero turbine is 80 meter)

## 1.3 Goal

The main goal of IEA Task29 Phase IV is to enhance the wind turbine aerodynamic knowledge level and to validate, improve and develop aerodynamic models for wind turbine design codes in a multinational

cooperative activity. The analysis is largely (though not exclusively) based on DanAero measurements. More specifically models are validated and improved for the following aspects:

- Aerodynamic response to turbulent inflow;
- Sheared inflow;
- 2D/3D aerodynamics;
- Aeroelastic effects
- Transition characteristics in realistic flow conditions;
- Acoustics.

Different categories of models are considered (CFD methods, panel methods, free wake methods, engineering methods etc.).

The thorough analysis of the DanAero measurements goes together with a critical scrutinising of data and a subsequent further improvement of measurement quality.

## 1.4 Dissemination

IEA Task 29 has resulted in a huge amount of publications, presentations and other dissemination activities, see the bibliography section of this report. Amongst others the Wind Energy Aerodynamics Handbook [12] can be mentioned as recent example with high impact. This handbook is now under preparation at Springer Publishers and it intends to become a main reference work for all questions on the field of wind turbine aerodynamics. Approximately 10 chapters of this Handbook rely partly or completely on results from IEA Task 29. Apart from the ‘conventional’ dissemination by means of workshops, conference presentations, journal articles etc, IEA Task 29 is characterised by the large amount of MSc and PhD students who actively participate in the project. All these students mention their participation to be a great learning experience. Not only content wise (Task 29 works on the forefront of wind turbine aerodynamics) but their attendance to meetings, including the network building with other task participants trains their personal skills. After their graduation these students often find positions in the wind energy society where they spread the Task 29 knowledge. In this way Task 29 contributes to the Human Capital Agenda. It is this outflow of knowledgeable students which is considered to be a very important dissemination form. An inventory was made of the students which have been active in Task 29 and their further career. It turned out difficult to retrace all students, partly because Task 29 has run for a long period where some of the original participants are not active anymore. As a result it is only possible to give approximate numbers. The approximation is based on an inventory at the institutes which participated since the beginning of Task 29 (Kiel UAS, DTU, USTUTT, TNO, TUDelft, Forwind/Fraunhofer and University of Uppsala). These 7 institutes employed a total of 46 students already, 13 of them found a position in wind industry after their graduation. Generally the number of participating institutes per IEA Task 29 phase was in the order of 20 which makes it likely that the total amount of students which participated in Task 29 has been far above 100. At least 18 PhD students are counted. It is also remarkable that several students (at least 6) found positions at other Task 29 participants. Outflow of graduated students to other IEA Task 29 participants is seen as the ultimate form of cooperation in IEA Task 29!

# Chapter 2

## Work plan, deliverables, meetings

### 2.1 Workplan

The workplan of IEA Task29 Phase IV has been approved at the 80<sup>th</sup> Executive Committee Meeting in November 2017 in Huatulco, Mexico. IEA Task29 Phase IV started on January 1<sup>st</sup> 2018 and ended on December 31<sup>st</sup> 2020.

IEA Task29 Phase IV consisted of 3 main technical work packages (WP's):

- WP1: Processing and presentation of data. In this Work Package the measurement data from the DanAero experiment have been processed, documented and stored into a database. The Work Package also included an assessment of the measurement quality.
- WP2: Comparison of calculated results from different types of codes with DanAero measurement data. In this Work Package, the calculated results from several codes were compared to a selection of measurements from WP1. It served as a thorough validation of different codes from which insights were gained into phenomena which need further investigation (see WP3). The calculations were carried out in two rounds. The first round was a comparison with measurements at more or less axi-symmetric conditions (i.e. a small yaw angle, low shear and a low turbulence level) where the second round was a comparison with measurements at large yaw and large shear. Every round consisted of the following phases:
  - Definition of the calculational round;
  - Performance of calculations;
  - Processing of data and comparing with measurements;
  - Evaluation and interpretation of results

Both rounds required several iterations in which the insights from the former iterations were taken into account. These insights could be misunderstandings on sign conventions, the need for additional output properties in order to understand the results better but also more fundamental model improvements.

- WP3: Deeper investigation into phenomena. In this Work Package a deeper investigation of various aerodynamic and aero-elastic phenomena took place. The phenomena were investigated with isolated submodels, simple analytical tools or by physical rules. Every phenomenon was studied in a separate task for which leaders were appointed. The phenomena/tasks which were defined are (between brackets the leaders and the participants of each task are mentioned)
  - Task 3.1 Turbulent inflow (USTUTT)
  - Task 3.2 Yawed flow (This activity was eventually put on hold because yaw formed part of the calculational rounds from WP2 already)
  - Task 3.3 Wake inflow (University of Uppsala)

- Task 3.4 2D/3D airfoil characteristics (ECN-Nantes)
- Task 3.5 Aero-elastic effects (PoliMi)
- Task 3.6 Transition (Kiel UAS)
- Task 3.7 Acoustics (DTU)

The Work Packages 1 to 3 are described in chapters 3 to 11.

In addition there was a fourth Work Package WP4 which addressed new aerodynamic experiments, see chapter 12 and WP5 ensured communication with other IEA Tasks, see chapter 13. WP5 also integrated the insights from the previous IEA Task 29 phases (i.e. the phases which were built around wind tunnel measurements) to the present phase which is built around field measurements.

Finally WP0 concerned the management of the Task.

## 2.2 Deliverables and reports

Almost all deliverables from IEA Task29 Phase IV were of reporting type and they are included in the present document. This holds for the WP2 deliverables which are denoted as DIV.3 to DIV.7 and which give the model descriptions, the descriptions of 2 calculational rounds and the comparison between 2 rounds of calculations and measurements. These are reported in chapter 4 and the appendices. The deliverable DIV.8 which was planned in WP4 culminated in the work plan for a new IEA Task 47 "Innovative aerodynamic experiments and simulations on wind turbines in turbulent inflow" as explained in chapter 12.

In addition there are the following deliverables:

- WP1: DIV.1 and DIV.2 (Preliminary and Final database). In August 2018, the DanAero measurements were released to the IEA Task29 Phase IV participants. The data are stored on a DTU website. The database was accompanied by a detailed documentation of its content. Moreover Matlab scripts are added with which overview graphs of operational conditions can be made to facilitate the analysis of data. After the release of the database several participants dived into the DanAero data. The observations and experiences from the participants on the measurements with lessons learned are shared within the consortium and it led to measurement corrections and instructions on how to interpret the data. These experiences and lessons learned are compiled in a separate working document [13]. In this way other participants could easily understand the data and they did not have to invent the wheel again.

The resulting improvement in measurement quality is seen as a major benefit from the cooperation within IEA Task 29. It also gives important learning experiences for the new dedicated aerodynamic experiments which will form part of IEA Task 47.

- WP0: DIV.9 to DIV.16: These are management deliverables (i.e. progress reports for every IEA ExCo meeting, minutes of plenary meetings and the present final report). Moreover a sharepoint has been created on a DTU server where documents and data have been uploaded. The progress reports have, in line with IEA procedures, been delivered to the IEA ExCo at least two weeks before their bi-annual meetings. Written reports and a presentation were delivered at the second meeting of the year where a presentation was delivered at the first meeting of the year. The minutes of the plenary meetings, see section 2.3 are given in [14], [15], [16]. Several web meetings have been organised which are reported in minutes as well [17].

The minutes have been distributed between the IEA Task29 Phase IV partners and they are together with the presentations, uploaded to the sharepoint.

## 2.3 Meetings

Within IEA Task29 Phase IV a total of 3 plenary meetings were held.



- The first meeting was held on June 19<sup>th</sup> 2018, [14]. This meeting was held prior to the Science of Making Torque Conference at PoliMi in Milano Italy where most Task 29 participants were present anyhow. The kick-off meeting of IEA Task29 Phase IV was attended by 26 participants. It must be noted that the meeting was held in Italy which became a new participant from July 1<sup>st</sup> 2018 onward i.e. very shortly after this meeting. At the meeting the work plan was discussed and all participants presented their plans and they informed the consortium about the chances of participation. Also the database of DanAero measurements was presented by DTU. This database would be released shortly after the meeting.
- The second meeting was held at NREL Boulder (USA) in March 2019, [15]. The meeting was organised together with the IEA Task 31 consortium. The IEA Task 29 meeting was supposed to be held over a period of 2 days but it had to be compressed in 1 day because a weather alarm led to a closure of the meeting location. The meeting was attended by 25 participants in person. A web meeting facility was added with which 6 participants joined the meeting remotely. At the moment of the second meeting the consortium was established and the database of DanAero measurements was released. Most of the discussion took place on the first comparisons between calculations and DanAero experimental results where some striking differences were found. These differences were larger than expected from the first three phases of Task 29 where comparisons were made between calculations and wind tunnel measurements. Part of these differences were caused by post processing issues and misunderstandings on conventions. As a result the definition of cases was refined with several additional clarifications. Also a limited number of activities from WP3 were discussed but the fact that the meeting had to be shortened made that these activities could not be discussed in depth.
- Due to the fact that the second meeting has to be shortened an additional intermediate meeting was organised in June 2019 at the Wind Energy Science conference in Cork Ireland [18] where many IEA Task29 Phase IV participants were present anyhow. The meeting was attended by 17 participants in person where approximately 10 participants joined by web meeting. At the meeting a further discussion took place on the comparison between the first round of calculations and measurements as a follow-up of the discussions at the second meeting. Despite the simplicity of the cases and the refinement and clarifications which were added to the definition of the case after the second meeting, several non-understood differences between calculations and measurements remained. At the meeting some first results from lifting line codes for the second round at large shear and/or yaw were also supplied. This comparison showed large differences too.
- The third meeting was held on February 4 and 5 2020 at CNR-INM in Rome [16]. It was again a hybrid meeting where 22 participants attended in person and approximately 7 participants joined the meeting remotely. At this meeting a further discussion took place on the bottlenecks in understanding the large differences between calculations and measurements. These large differences were mainly found in the results from the lifting line codes. On the other hand very encouraging results were obtained from CFD codes which showed a very good agreement with the measurements of the second round. Still some differences between CFD results and measurements remained even for the relatively simple first round.

At the third meeting all WP3 activities were in full progress and they were discussed as well. An evaluation on the results of IEA Task29 Phase IV was also done at the third meeting.

- Shortly after the third meeting the outbreak of Covid 19 led to a drastic change in the communication within the group of IEA Task29 Phase IV . Until then the communication had always relied heavily on close personal contacts but after the meeting at CNR-INM no further personal meetings could be organised. For this reason regular progress web meetings were organised on a 2 monthly basis [17]. As a matter of fact these web meetings were already organised since October 2019 but they formed an addition the personal meetings. After the outbreak of Corona these web meetings became the most important way of communication. The web meetings are generally attended by some 25 participants.

Several meetings were ‘enlighthened’ with ‘edutainment’ e.g. presentations on the lifes of famous scientists like Enrico Forlanini, Corradino D’Ascanio, Christmas puzzles on aerodynamic problems and other price

awards for the solution of non-understood scientific problems which initially hampered the progress of Task 29.

# Chapter 3

## WP1: The database

H.Aa. Madsen and G.R. Pirrung

### 3.1 Introduction

The experimental data are from detailed measurements on a full-scale turbine carried out in 2009 in Denmark within the DanAero MW project [19] and [20]. In the DanAero project, which is a short name for the EFP2007 project "Experimental Rotor and Airfoil Aerodynamics on MW Wind Turbines", a number of innovative and coordinated measurements on two modern full scale MW turbines as well as wind tunnel measurements on various airfoil sections were conducted. One of the full scale measurements comprised inflow measurements with a five hole pitot tube on a Siemens 3.6MW turbine at the DTU test field Høvsøre in Denmark. In the other major experiment pressure measurements were conducted at four radial sections on one of the blades of a 2MW NM80 turbine (with rotor diameter of 80 meter and hub height of 59.89 meter) in combination with inflow measurements with five hole pitot tubes. Several other measurements on the turbine and in a nearby meteorological tower were carried out.

The project was carried out in the period from March 2007 to December 2009 in a cooperation between Risø DTU and the companies LM Wind Power, Vestas Wind Systems, Siemens Wind Power and DONG Energy. Funding was provided by the Danish research funding agency EFP (now EUDP) in combination with eigen funding from the project partners. The outcome of the DanAero project was a comprehensive and unique experimental data-set, which contains data that the wind energy research community and the industry can benefit from.

As a follow up on the project the EUDP funded the DanAero MW II project (short DanAero II) [21] which was initiated in 2010 with the participants Risø DTU (now DTU Wind Energy), LM Wind Power, Vestas Wind Systems A/S and Siemens Wind Power. The overall objective of DanAero II was to organize, calibrate and document the data obtained in DanAero I and to explore in details the influence of atmospheric and wake turbulence on MW turbine performance, loading and stability.

### 3.2 The DanAero data base and IEA Task 29, phase IV

During the time of the DanAero projects from 2007 to 2013 and a few years after the experimental data were only accessible for the project partners. However, at the initiation of the IEA Task29 Phase IV in 2018 the DanAero partners agreed that the data as well as the data for aerodynamic and aeroelastic modelling of the NM80 2MW turbine could be shared with the partners participating in the IEA Task29 Phase IV on the condition of not distributing the data outside this forum. Also measurements from the wind tunnel tests are made available while the inflow measurements on the Siemens 3.6MW turbine are not shared.

### 3.3 Establishing the DanAero data base within IEA Task 29, phase IV

The data base has been build up on a DTU share point site only accessible for researchers from countries within IEA Task 29, phase IV, see opening page of the data base in Figure 3.1.

On the left part of the opening page there are several folders. First there is the folder "The DanAero project" containing information about the two DanAero projects mentioned above. In these projects the experimental results for the data base were measured and processed.

Another folder "References and publications" further down should also be mentioned at this stage. It contains several articles, conference papers and reports worked out and published during the DanAero projects execution and the years after.

**However, other reports and notes in other folders are not public and in particular reports describing in detail the measurement set-up as well as the aerodynamic and aeroelastic description of the NM80 turbine are strictly confidential. This is released through a short NDA that all users of the data base have to sign before getting access to the data base.** There has been expressed an interest from several participants in IEA Task29 Phase IV on having an example of an aeroelastic model set-up for the NM80 turbine. Therefore a zip file with such model input for the HAWC2 aeroelastic code [22] has been provided. See further information in the note "HAWC2-model-set-up-NM80-turbine.pdf" in the same folder.

130

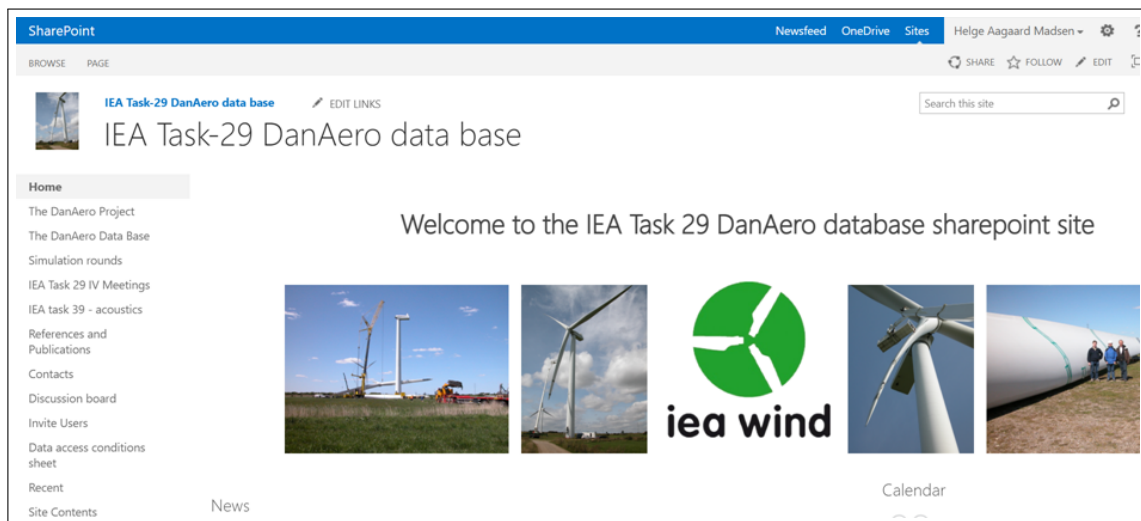


Figure 3.1: Opening page of the DanAero data base established at a sharepoint at DTU.

The second folder in the list to the left on the opening page is named "The DanAero data base". This can be characterized as the key folder of the data base with several sub folders which will be described below.

### 3.4 The DanAero data base - turbine model

#### 3.4.1 Aerodynamic-aeroelastic modelling

Here the data for the aerodynamic and and aeroelastic modelling of the turbine are contained in the excel sheet "IEA-Task-29-IV-NM80-turbine definition\_hama\_January\_02\_2020.xlsx" together with two reports describing the aerodynamic and aeroelastic modelling input.

### 3.4.2 HAWC2-aeroelastic-model-setup

There has been expressed an interest from several participants in the IEA Task29 Phase IV work on having an example of an aeroelastic model set-up for the NM80 turbine. Therefore a zip file with such model input for the HAWC2 aeroelastic code [22] has been provided. See further information in the note "HAWC2-model-set-up-NM80-turbine.pdf" in the same folder.

### 3.4.3 CFD modelling

The "v1.zip" file contains an IGES file of the blade surface. Besides the IGES representation of the rotor geometry an EllipSys style multi-block surface (nm80-v1.x2d) and volume mesh is provided for the zero pitch situations (nm80-v1.x3dunf). See further details in the small note "read-me-text\_turbine-modelling\_v1.pdf" in the same folder.

## 3.5 The DanAero data base - experimental data

The experimental data comprise two major parts:

1. Field measurements Tjaereborg
2. Wind tunnel measurements at LM

### 3.5.1 Field measurements Tjaereborg

The data in this folder comprises the data from the blade surface pressure and inflow measurements on the NM80 turbine. Two important reports can be found in this folder.

The instrumentation report "DanAero\_Instrumentation.pdf" describes the experimental set-up in details, the calibration of the different sensors and finally the calibrated data base including the description of the contents of the different file types and how to read them.

The other report "DANAERO\_MeasurementCampaigns\_v1.pdf" presents an overview of the measurement files from each measurement campaign in the form of 10 min. statistics of some selected sensors. Also the mode of operation (e.g. fixed or variable speed) of the turbine is shown.

Here we will only give a short summary of measurement set-up and the data files.

An overview of the instrumentation of one of the blades on the NM80 turbine is presented in Figure 3.2. About 60 pressure taps were installed at four radial positions on the blade and close to each of the sections a five hole pitot tube was mounted to measure the local inflow. Additionally 60 flush mounted surface microphones were mounted at a radial position 3m from the tip. As the two outboard sections are not accessible from inside the blade a new blade was manufactured for the experiment and the instrumentation was inserted during the manufacturing process of the blade.

Three different data acquisition systems were used to sample all the sensors. One system was sampling all the sensors on the turbine, except the blade surface pressures, and the nearby meteorological tower with a frequency of 35Hz, see Figure 3.3. Another data acquisition system sampled the surface pressures at a frequency of 100Hz. Finally a third system was dedicated to sample the surface microphones at frequency of 50kHz, however only over a period of 10sec with an interval of 1 minute in order to reduced the amount of measurement data. It should be mentioned that data from all three measurement systems are synchronized with a common sync signal.

An overview of the sensors on the blade is shown in 3.4. Strain gauges for measuring strain, both flapwise, edgewise and torsion, were installed at 10 radial positions. Additionally 3-component accelerometers + temperature sensors at 4 radial positions and finally the blade instrumentation with pressure taps, five hole pitot tubes and microphones as mentioned above.

The sensors on the tower, nacelle and drive train are listed in Figure 3.5. It comprises strain gauges at the bottom and top of the tower and on the shaft. Additionally sensors measuring the turbine operational characteristics as well as the nacelle wind speed.

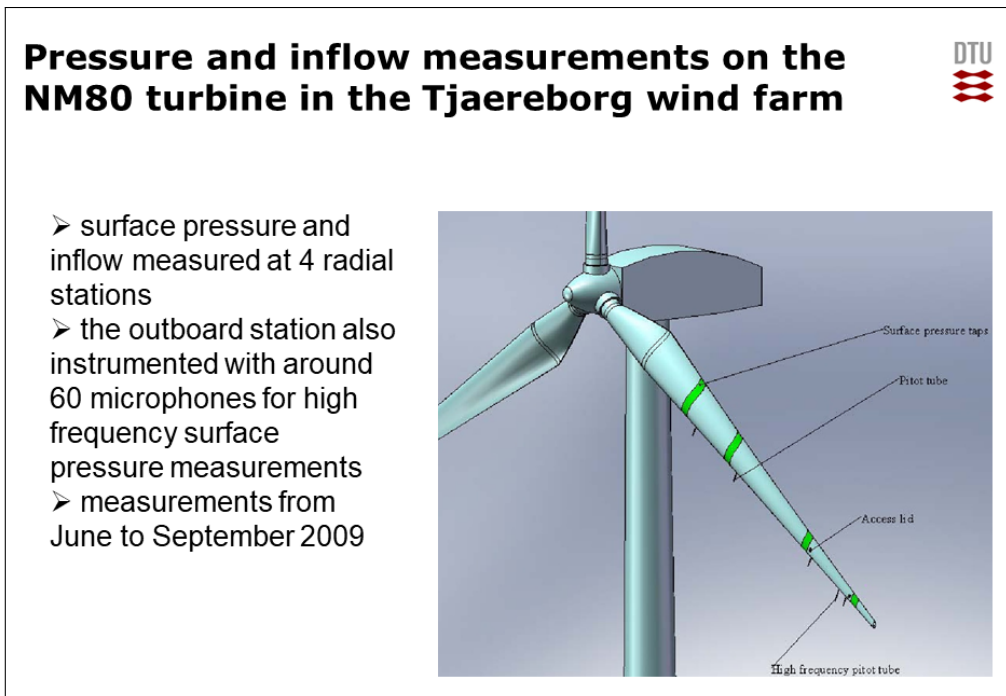



Figure 3.2: Overview of the instrumentation of one of the blades of the NM80 2MW turbine in Tjaereborg.

Finally, the instrumentation on the meteorological tower is shown in Figure 3.6. It comprises anemometers at six different heights from maximum to minimum blade tip height and three sonics with wind vanes temperature sensors at the same heights. Finally, measurement of barometric pressure and precipitation.

### 3.5.2 The calibrated data

In the sub folder "Calibrated data" the calibrated data sets from the three measurements systems mentioned above are stored together with Matlab scripts to load the data. The complete original DanAero data base is not uploaded but about 78 10 min. time series from different measurement days from 16-7-2009 to 1-9-2009 are uploaded. As mentioned above an overview of the files in the original data base can be found in the report "DANAERO\_MeasurementCampaigns\_v1.pdf" which should be used to achieve information about the operational conditions for the individual uploaded files.

However, it is important to mention that the data files originally sampled data files for measurements on the turbine and meteorological mast at a frequency of 35Hz have been extended with derived channels from the two other measurement systems. The aerodynamic forces  $f_x$ ,  $f_y$  integrated from the pressure distributions



## Type of data files


### Three data acquisition systems

- Turbine and met. data – 35 Hz
- Surface pressure data at 100 Hz
- Microphone data – 50 kHz over 10 sec. each minute

### Wind tunnel pressure measurements on the four airfoil sections

- most outboard section also with microphones

Figure 3.3: Three different data acquisition systems were used on the NM80 turbine storing the data in three different file types with different scan frequencies. The measurements on 2D blade sections in the LM wind tunnel comprised pressure measurements and high frequency microphone measurements.



## Measured quantities on the turbine and met. mast - 1 of 3

Instrument	Sensor	Position [m]	Sampling rate [Hz]
Strain gauges	Flapwise and edgewise moments	{3.0, 8.0, 13.0, 16.0, 19.0, 22.0, 26.0, 30.0, 34.0, 37.0}	35
Five-hole Pitot tubes	Relative velocity and flow angles	{14.5, 20.3, 31.0, 36.0}	35
Pressure taps	Surface pressure	{13.0, 19.0, 30.0, 37.0}	100
Accelerometers	Acceleration	{13.0, 19.0, 30.0, 37.0}	35
Thermometer	Blade temperature	{13.0, 19.0, 30.0, 37.0}	35
Microphones	Surface pressure	37.0	50000

*Table 3.1. Instrumentation on the LM38.8 blade*

Figure 3.4: Overview of the sensors on the blade of the NM80 2MW turbine.

## Measured quantities on the turbine and met. mast - 2 of 3



Instrument	Sensor	Position	Sampling rate [Hz]
Strain gauges	Tower moments	Tower top/bottom	35
Strain gauges	Shaft moments	Shaft	35
-	Electrical power	nacelle	35
-	Rotor azimuth angle	nacelle	35
-	Rotational speed	nacelle	35
-	Yaw angle	nacelle	35
-	Pitch angle	nacelle	35
Cup anemometer	Wind speed at nacelle	nacelle	35

*Table 3.2. Instrumentation of tower, nacelle and drive train*

Figure 3.5: Overview of the sensors on the tower, nacelle and drive train.



## Measured quantities on the turbine and met. mast - 3 of 3



Instrument	Sensor	Height [m]	Sampling rate [Hz]
Cup anemometers	Wind speed	{17.0, 28.5, 41.0, 57.0, 19.0, 77.0, 93.0}	35
Sonic anemometers	Velocity, wind direction and temperature	{17.0, 57.0, 93.0}	35
Wind vanes	Wind direction	{17.0, 57.0, 93.0}	35
Thermometer	Temperature	{5.7, 57.0, 93.0}	35
Barometer	Pressure	5.7	35
-	Precipitation	5.7	35

Table 3.3. Instrumentation of the nearby met mast

Figure 3.6: Overview of the sensors on the tower, nacelle and drive train.

## Files with combined and derived channels - 35 Hz - 174 channels



- Combines calibrated data from all three data acquisition systems
  - turbine data
  - met. data
  - $f_y$ ,  $f_x$  at the four sections from integration of the pressure distributions
  - a few pressure taps
  - transition position

Figure 3.7: Overview of the channels in the calibrated and combined 35Hz files containing derived channels from the two other measurement systems. The aerodynamic forces  $f_x$ ,  $f_y$  integrated from the measured pressure distributions (100Hz) and the transition position derived from the 50kHz microphone measurements. However, all channels downsampled to 35Hz

at the four radial sections and derived transition position from the microphones data, see the overview of channels in Figure 3.7. So in total the 10 min. files now contain 174 channels at a frequency of 35Hz with the time as the first column. The files can e.g. be read with the post processing tools Windap and Pdap that can be downloaded from the HAWC2 homepage "<https://www.hawc2.dk/download/post-processing-tools>"

### 3.5.3 The raw data

Besides the calibrated data sets a few raw data files have been uploaded in the "raw data" folder. This is mainly relevant for the 35Hz data sets with measurements on the turbine and meteorological mast. In particular it allows to re-calibrate the strain gauge channels as shown below in section 3.9.

### 3.5.4 Wind tunnel measurements at LM

Besides the uploaded data from field measurements on the NM80 turbine there are 2D sectional data which are measured in the wind tunnel from LM in the folder "Wind tunnel measurements at LM". These wind tunnel measurements are done on sections based on blade geometry scans so that deviations from the design geometry are included. These measurement support one of the main objectives of the DanAero experiments which was to provide experimental data that can be used to study the different behaviour of a blade section on a rotor in turbulent inflow and a similar blade section in 2D steady wind tunnel flow.

### 3.5.5 Measurement campaigns and operational modes of the turbine

Measurements in the DanAero project were carried out over 11 measurement days from the end of June to mid-September in 2009. During that period the turbine was only operated during the measurement campaigns so the expenses for the power production losses from the turbine were considerable which meant that the total measurement period should be as short as possible. On the other hand the measurement days were also costly and sparse due to several reasons: 1) two technicians from Vestas had to be on the site to operate the turbine; 2) a 60m lift had to be rented and available on the measurement days in order to access the instrumentation on the blades; 3) weather should be absolutely dry and 4) DTU technicians should be available.

It was planned to conduct measurements for the turbine in different operational modes as shown in Table 3.1. Three major modes, 1-3 relating to the turbine control were used: 1) turbine in normal operation; 2) turbine operating at constant speed at a pitch angle of -1 deg and 3) turbine operating at constant speed with a pitch angle of -4.5 deg. The negative pitch settings were used in order to achieve measurements with angles of attack approaching the stall region which is known to cause complex flow on the blades. However, only a minor part of all the different modes could be covered during the conducted campaigns. One reason is that the turbine often was operating in the wake of another turbine as the turbine is situated in a small wind farm of 8 turbines. Another is that often there were minor problems with parts of the measurement or data acquisition system requiring stop of the turbine.

A major problem occurred on the 7th of August as a pressure line controlling the valves to the two outboard scanni valve pressure scanners broke. As it was in the part of the blade that could not be accessed the pressure measurements from these two stations do not have the same quality in the last part of the campaigns after 7th of August as compared to the quality of the first measurements.

### 3.5.6 The selection of files for the benchmark cases

In IEA Task29 Phase IV the DanAero data are being used as comparison material for benchmark cases see chapter 4. These benchmark cases are simulated with different fidelity aerodynamic models. The focus of these models is on representing the aerodynamics (and aero-elastics) of a wind turbine and not on the control. For this reason the cases from chapter 4 are defined with fixed rotational speed and fixed pitch. Therefore one of the criteria in selecting the experimental cases have been to find time slots where the turbine rotational speed has been almost constant if the test case is selected from a file where the turbine has been operated in the variable speed mode. The same considerations apply for the inflow where periods with constant conditions have been searched for. This obviously limits the available data so that the selected time series for the benchmark cases are much shorter than 10 minutes.

ID number	Configuration
1	Normal operation, yaw=0
2	Pitch=-1, constant RPM, yaw=0
3	Pitch=-4.5, constant RPM, yaw=0
4	Normal operation, yaw=+/-10
5	Pitch=-1, constant RPM, yaw=+/-10
6	Pitch=-4.5, constant RPM, yaw=+/-10
7	Normal operation, yaw=+/-20
8	Pitch=-1, constant RPM, yaw=+/-20
9	Pitch=-4.5, constant RPM, yaw=+/-20
10	Normal operation, yaw=+/-30
11	Pitch=-1, constant RPM, yaw=+/-30
12	Pitch=-4.5, constant RPM, yaw=+/-30
13	Normal operation, yaw=+/-40
14	Pitch=-1, constant RPM, yaw=+/-40
15	Pitch=-4.5, constant RPM, yaw=+/-40
16	Normal operation, yaw=+/-50
17	Pitch=-1, constant RPM, yaw=+/-50
18	Pitch=-4.5, constant RPM, yaw=+/-50
19	Stand still
20	Pitch step

Table 3.1: The intended configurations of the NM80 wind turbine to be operated during the measurement campaigns.

### 3.6 Data file for first round of benchmark - axial flow, case IV.1

For this case IV.1 a 120s interval from the data file Tjaereborg.20090716.1250.000035 from 240 to 360s has been selected. The statistics derived from the 35Hz time series for the meteorological data, the turbine operation and the aerodynamic sectional forces are shown in Table 3.2.

The interval between the red vertical lines in Figure 3.8 which shows power and rotational speed, indicate the selected time series. It is clear that these two parameters are reasonably constant for the selected 120s whereas this would not be the case for if wider interval had been chosen.

The wind speed and wind direction are presented in Figure 3.9 and 3.10. In the latter figure the yaw position is also shown and is seen to be close to the wind direction resulting in almost zero yaw.

Pressure distributions are shown in Figures 3.11, 3.12, 3.13 and 3.14 at four radial positions. The distributions were derived by binning pressure on azimuth with  $\pm 5$ deg intervals around 0, 90, 180 and 270deg azimuth. Finally, the aerodynamic sectional forces at the four radial positions, integrated from the pressure distributions, are shown in the Figures 3.15 and 3.16.

	Unit	Mean	Stddev	Min	Max
Wind speed at 17m	[m/s]	5.83	0.55	4.26	6.98
Wind speed at 28.5m	[m/s]	6.04	0.39	4.90	7.46
Wind speed at 41m	[m/s]	5.94	0.40	4.90	7.06
Wind speed at 57m	[m/s]	6.08	0.41	5.20	7.16
Wind speed at 77m	[m/s]	5.99	0.50	4.74	7.25
Wind speed at 93m	[m/s]	6.20	0.41	5.09	7.14
Wind dir at 17m	[deg]	233.70	5.82	213.30	251.05
Wind dir at 57m	[deg]	229.59	4.81	211.74	240.75
Wind dir at 93m	[deg]	231.40	4.61	213.75	245.95
Yaw position	[deg]	228.97	0.00	228.96	228.97
Yaw error	[deg]	-0.61	4.81	-11.77	17.23
Fx03	[N/m]	40	14	2	90
Fx05	[N/m]	78	19	20	147
Fx08	[N/m]	120	23	56	191
Fx10	[N/m]	112	19	60	174
Fy03	[N/m]	476	67	245	739
Fy05	[N/m]	821	92	504	1142
Fy08	[N/m]	1248	124	802	1598
Fy10	[N/m]	1286	111	814	1621
Power	[kW]	247.7	14.2	193.0	269.0
Rotation speed	[rpm]	12.3	0.1	12.0	12.6
Pitch	[deg]	0.15	0.00	0.15	0.15
Density	[kg/m <sup>3</sup> ]	1.23	0.00	1.22	1.23

Table 3.2: Statistics of selected data channels for Case 1b - uniform inflow

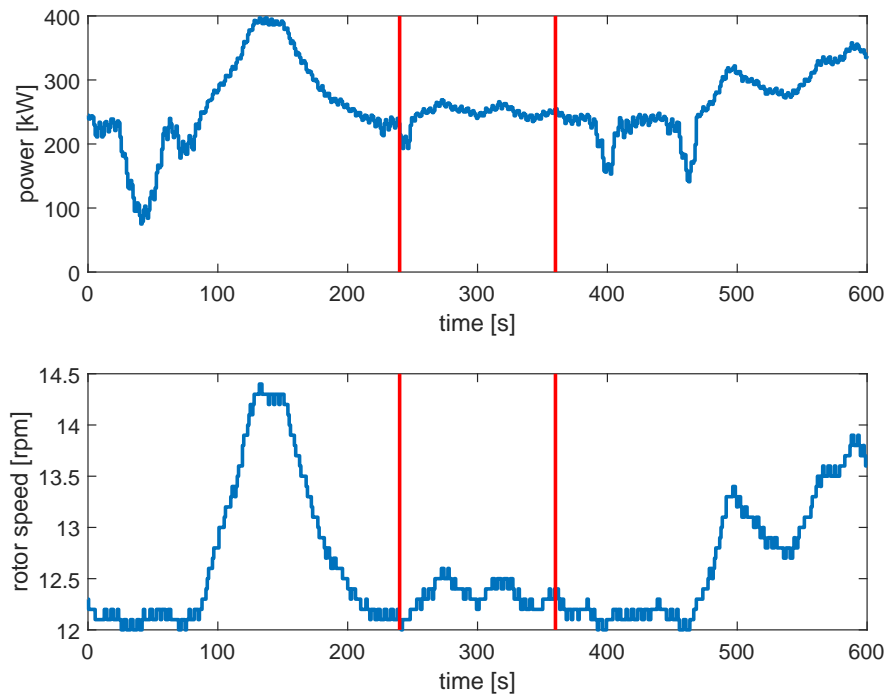


Figure 3.8: Rotor power and rotor speed for the whole 10min. data file.

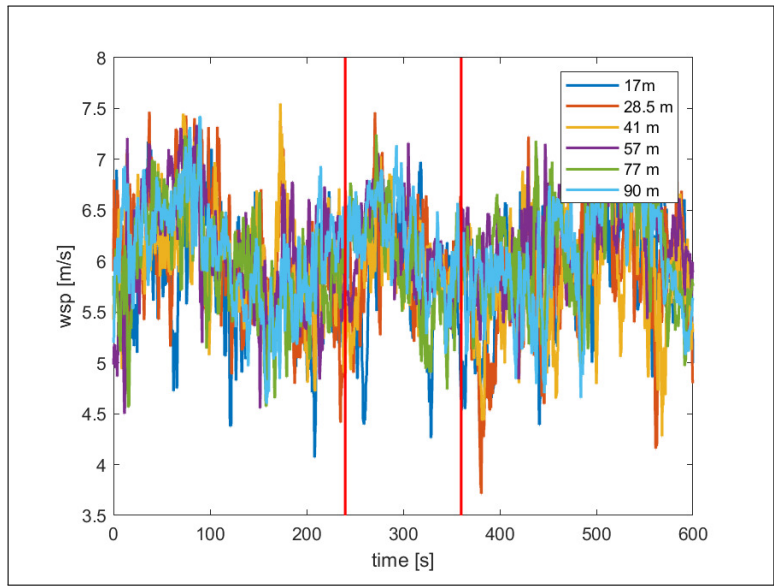


Figure 3.9: Wind speed at the meteorological mast at the different heights.

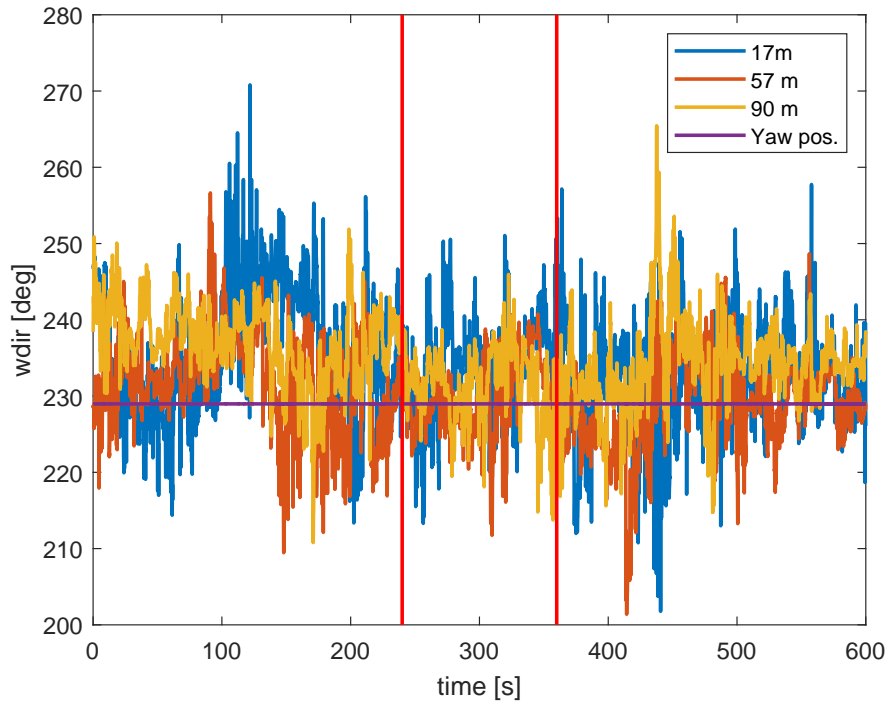


Figure 3.10: Rotor power and rotor speed for the whole 10min. data file.

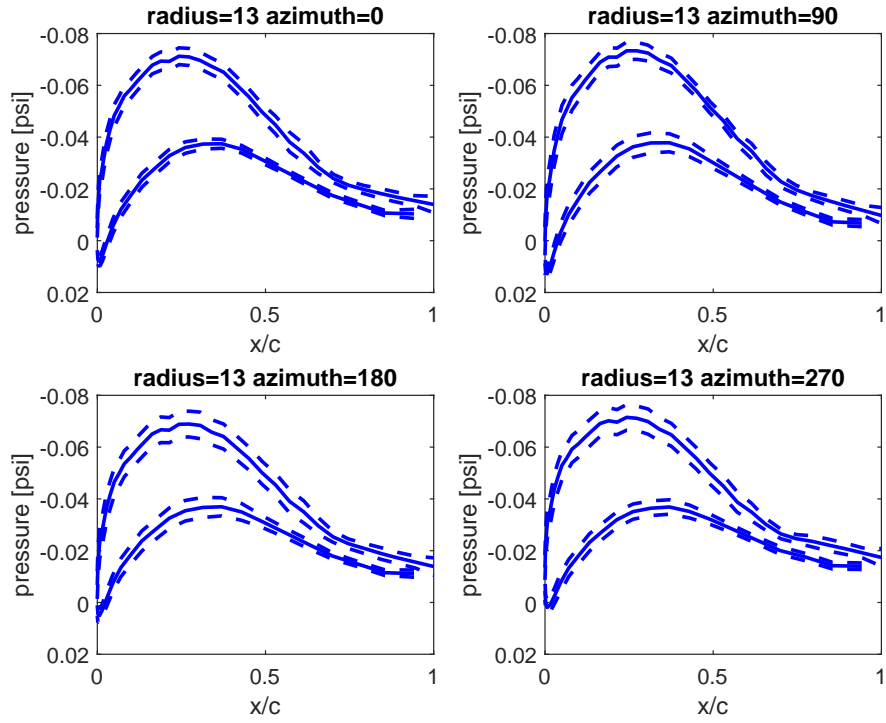


Figure 3.11: Pressure distributions at radius 13m at four azimuth positions. Dashed lines show mean  $p$  plus/minus one standard deviation, respectively.

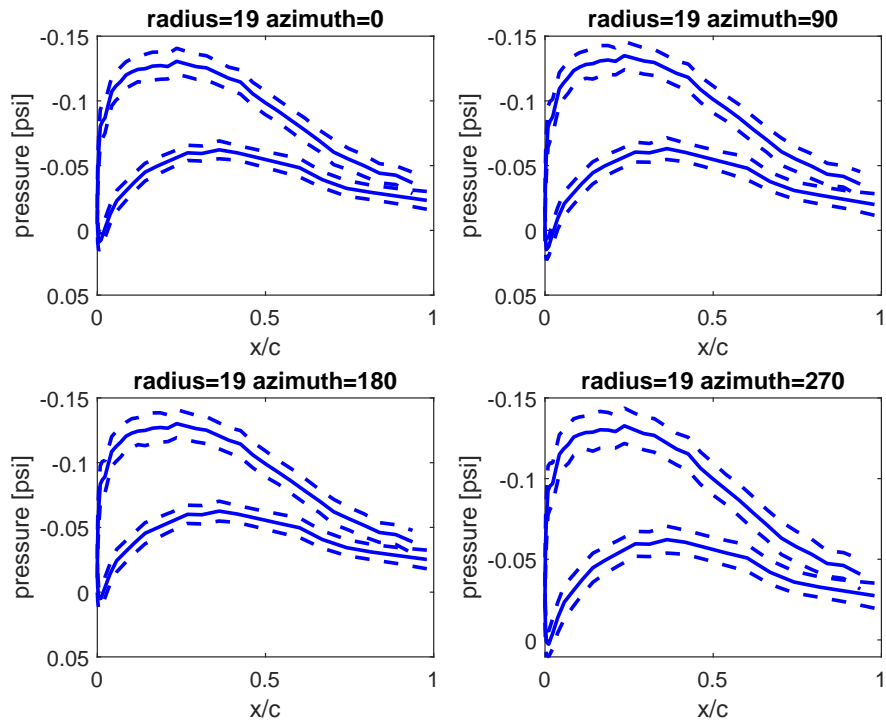


Figure 3.12: Pressure distributions at radius 19m at four azimuth positions. Dashed lines show mean  $p$  plus/minus one standard deviation, respectively.

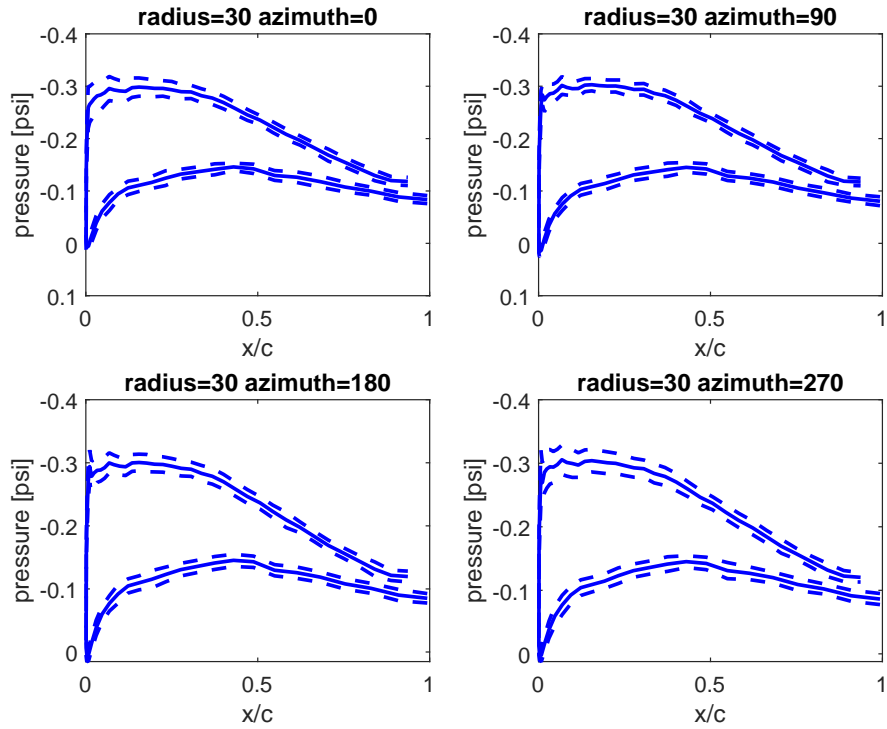


Figure 3.13: Pressure distributions at radius 30m at four azimuth positions. Dashed lines show mean  $p$  plus/minus one standard deviation, respectively.

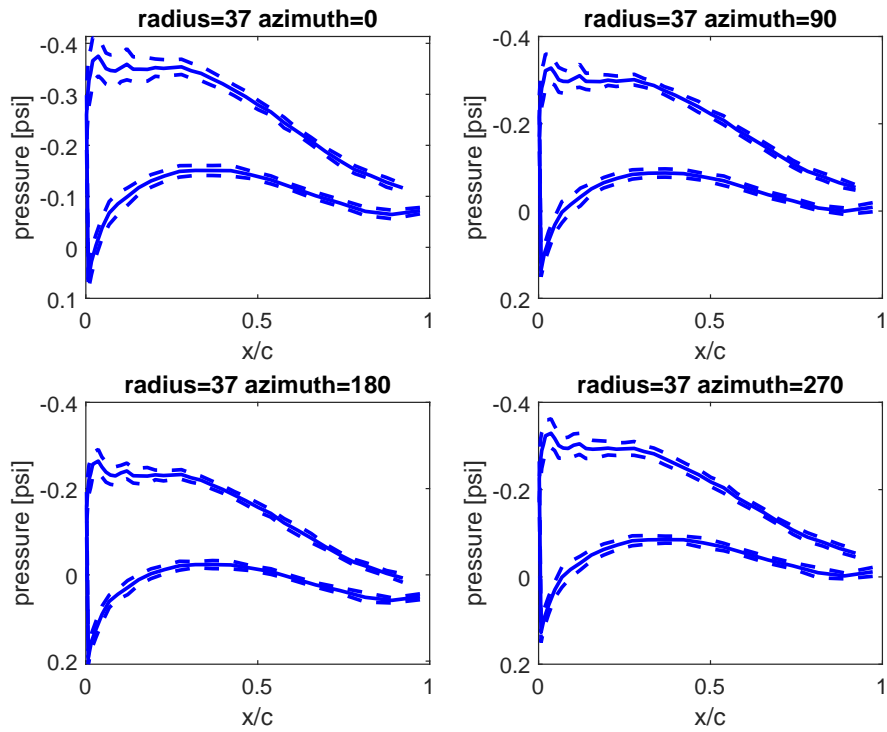


Figure 3.14: Pressure distributions at radius 37m at four azimuth positions. Dashed lines show mean  $p$  plus/minus one standard deviation, respectively.

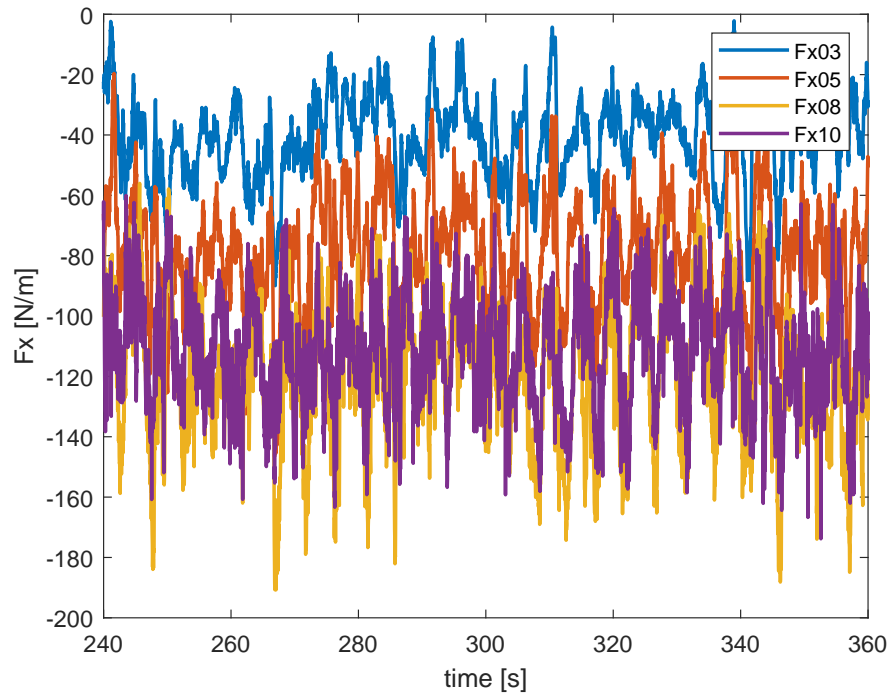


Figure 3.15: Time traces of tangential force at four radial positions.

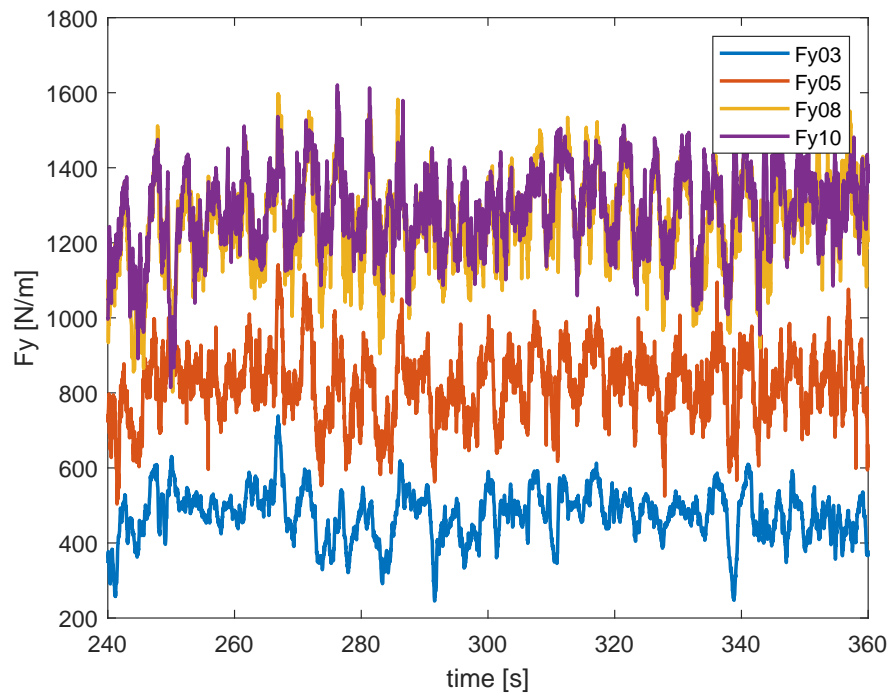


Figure 3.16: Time traces of normal force four radial positions..



### 3.7 Data file for second round of benchmark - sheared flow, case IV.2.1

For this case IV.2.1 a 142s interval from the data file Tjaereborg\_20090901\_1250\_000035 from 429 to 572s has been selected. The statistics derived from the 35Hz time series for the meteorological data, the turbine operation and the aerodynamic sectional forces are shown in Table 3.3. The shear in the flow is further illustrated in the Figure below 3.4 and it can be seen that is is a quite smooth shear of an exponential type.

Further figures characterizing the shear case can be found in the Appendix F.1.

	Unit	Mean	Stddev	Min	Max
Wind speed at 17m	[m/s]	7.18	0.69	5.43	8.77
Wind speed at 28.5m	[m/s]	8.29	0.45	6.61	9.39
Wind speed at 41m	[m/s]	9.02	0.37	8.02	10.30
Wind speed at 57m	[m/s]	9.83	0.36	8.79	10.88
Wind speed at 77m	[m/s]	10.54	0.51	9.40	11.91
Wind speed at 93m	[m/s]	11.03	0.63	9.68	12.97
Wind dir at 17m	[deg]	161.56	4.94	142.18	188.81
Wind dir at 57m	[deg]	161.64	1.99	151.52	167.98
Wind dir at 93m	[deg]	164.88	2.16	158.36	171.79
Yaw position	[deg]	155.61	0.00	155.60	155.61
Yaw error	[deg]	-6.02	1.99	-12.37	4.09
Fx03	[N/m]	203	47	59	351
Fx05	[N/m]	344	72	115	548
Fx08	[N/m]	458	107	168	746
Fx10	[N/m]	438	85	178	667
Fy03	[N/m]	1280	155	772	1642
Fy05	[N/m]	2280	201	1545	2782
Fy08	[N/m]	3824	375	2589	4807
Fy10	[N/m]	3510	285	2504	4134
Power	[kW]	990.6	97.4	828.0	1255.0
Rotation speed	[rpm]	16.2	0.1	16.0	16.4
Pitch	[deg]	-4.75	0.00	-4.75	-4.75
Density	[kg/m <sup>3</sup> ]	1.22	0.00	1.22	1.22

Table 3.3: Statistics of selected data channels for Case IV.2.1 - sheared flow

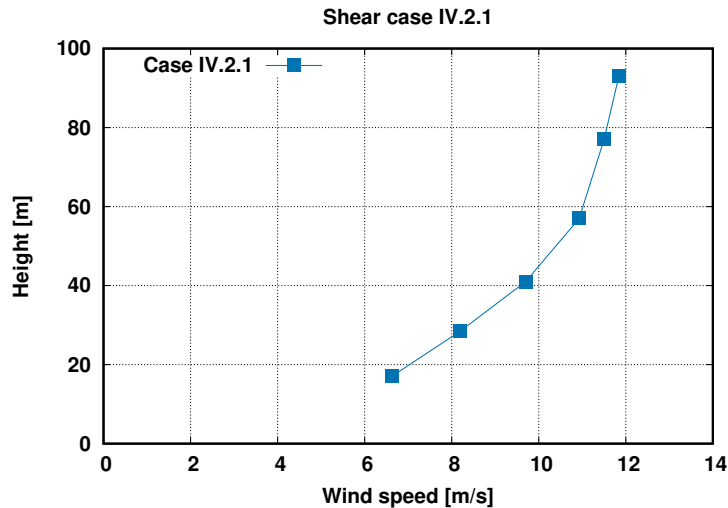


Table 3.4: Wind shear at meteorological mast for Case IV.2.1 - sheared flow

### 3.8 Data file for second round of benchmark - yawed flow, case IV.2.2

For this case IV.2.2 a 360s interval from the data file Tjaereborg\_20090819\_1510\_000035 from 0-360s has been selected. The statistics derived from the 35Hz time series for the meteorological data, the turbine operation and the aerodynamic sectional forces are shown in Table 3.5. The shear in the flow is further illustrated in the Figure below 3.6. Contrary to the shear in case IV.2.1. above the shear is here more irregular, mainly existing from hub height and below.

Further figures characterizing the yaw case can be found in the Appendix F.2.

	Unit	Mean	Stddev	Min	Max
Wind speed at 17m	[m/s]	5.81	0.83	3.98	8.12
Wind speed at 28.5m	[m/s]	6.80	0.80	4.67	9.14
Wind speed at 41m	[m/s]	7.90	0.60	5.44	9.29
Wind speed at 57m	[m/s]	8.81	0.44	7.70	9.81
Wind speed at 77m	[m/s]	8.97	0.46	7.81	10.07
Wind speed at 93m	[m/s]	9.03	0.45	7.84	9.98
Wind dir at 17m	[deg]	168.78	6.91	142.66	193.79
Wind dir at 57m	[deg]	166.54	2.38	161.01	173.67
Wind dir at 93m	[deg]	166.89	2.35	161.51	172.72
Yaw position	[deg]	128.11	0.01	128.10	128.12
Yaw error	[deg]	-38.43	2.38	-45.56	-32.90
Fx03	[N/m]	102	32	3	189
Fx05	[N/m]	197	49	45	306
Fx08	[N/m]	269	86	56	468
Fx10	[N/m]	313	94	104	528
Fy03	[N/m]	954	89	605	1222
Fy05	[N/m]	1861	138	1436	2257
Fy08	[N/m]	3184	257	2380	4020
Fy10	[N/m]	3056	283	2356	3830
Power	[kW]	514.8	51.2	429.0	678.0
Rotation speed	[rpm]	16.2	0.1	16.1	16.4
Pitch	[deg]	-4.75	0.00	-4.75	-4.75
Density	[kg/m <sup>3</sup> ]	1.22	0.00	1.22	1.22

Table 3.5: Statistics of selected data channels for Case IV.2.2 - yawed flow

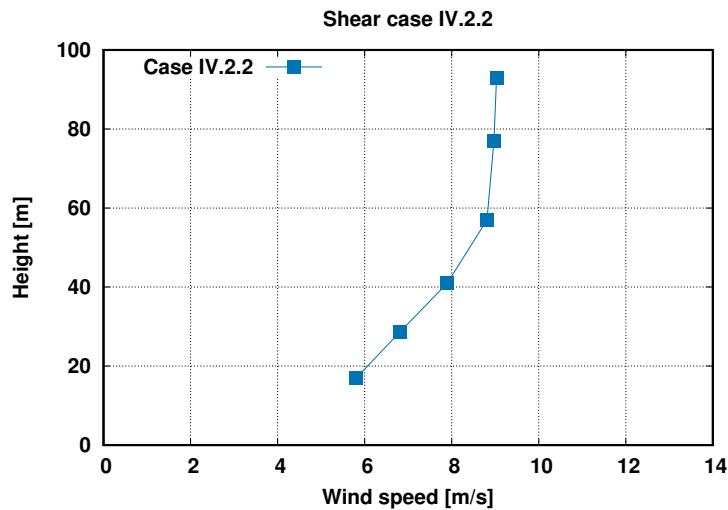


Table 3.6: Wind shear at meteorological mast for Case IV.2.2 - yawed flow

## 3.9 Measurement checks and strain gauge calibration using an aeroelastic model

The cooperation within IEA Task29 Phase IV led to a thorough analysis of DanAero data by a large consortium with ample manpower. This enabled a critical scrutinization of the measurements and corrections which are reported in [13]. Moreover, in the DanAero measurement campaign, strain gauges were placed at 10 sections of the instrumented blade. These sensors were originally calibrated in static tests, but most sections were recalibrated in the field. Unfortunately these new calibration values are not available any more. To mitigate this, all the strain gauge signals in the calibrated data files are based on the strain gauges closest to the blade root where the calibration was known. All other strain gauges signals are actually just the scaled blade root signal to give a reasonable load distribution [23].

To obtain additional information on the load distribution in a given measured time series, a recalibration of the strain gauge signals is necessary.

### 3.9.1 Motivation for calibration

The comparison in uniform inflow showed large discrepancies between all computations and the measured forces from the sections with pressure taps. An example comparison with HAWC2 computations is shown in Figure 3.17. The measured forces are lower than the computed forces at all locations. Because this overprediction was very consistent in the numerical results, the use of the distributed strain gauges as a second opinion from the measurement seems to be beneficial.

If the moment distributions from the strain gauges are consistent with the force distributions, then the differences between measurements and simulations must be due to errors in the simulation input, either in the operation conditions or the aeroelastic turbine data.

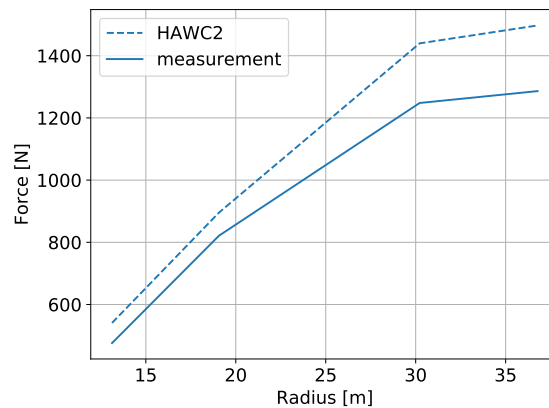


Figure 3.17: Poor agreement between measured and computed normal forces in the axial inflow case.

### 3.9.2 Calibration procedure

The recalibration is performed using measurements during idling, for the following reasons:

1. The aerodynamic forces in idling are low.
2. The moment is dominated by the gravitational moment. The blade mass distribution is one of the aspects of the model that is known very accurately.
3. The idling cases include large pitch angles such that the mass moment is in flapwise direction for a large part of the time.

To mitigate influences of drift in the sensors, the calibration is performed using an idling case (time series starting July 16th, 2009 at 13:10) that is very close to the benchmark case used as basis for the uniform inflow comparison (July 16th, 2009 at 12:50).

A corresponding HAWC2 simulation for the idling case is set up. This simulation includes as input the wind field with custom shear and veer to match the met mast data, time series of azimuth positions, time series of pitch angle, see Figure 3.18.

The azimuth angle from the calibrated data file needed some additional work: The azimuth sensor doesn't know in which direction the rotor is moving when it is idling. It only knows how many angle increments have been passed. As a result of the sometimes wrong rotation direction; the rotor was originally assumed to always rotate clockwise; there was an unphysical discontinuity in the original azimuth signal. This discontinuity was removed. Comparing the measured acceleration at blade 1 to the product of 9.81 times the sine of the azimuth angle allows to modify the azimuth signal to be sure that the rotor is rotating in the right direction, see Figure 3.19. As expected the measured acceleration in the idling case is dominated by the gravity acceleration, but an offset is present. This offset does not influence the procedure because to determine the direction of rotation only the changes in acceleration are relevant, not the absolute value. The original and fixed azimuth signals are shown in Figure 3.20.

A HAWC2 simulation with these given inputs (wind field with custom shear and veer, corrected time series of azimuth positions, time series of pitch angle) is performed to compare the predicted moments with the measured moments at the strain gauge positions. The first 320 seconds of the idling time series at 13:10 on the 16th of July, 2009, were used to calibrate both flapwise and edgewise moments. Calibration of the edgewise moments is possible because the pitch angle is reduced from roughly 275 seconds onwards, see Figure 3.18. The strain gauges are mounted with an angle offset of  $\theta_0 = -10.8$  deg, [23], such that:

$$M_{flap,meas} = M_{f,meas} \cos \theta_0 - M_{e,meas} \sin \theta_0 \quad (3.1)$$

$$M_{edge,meas} = M_{f,meas} \sin \theta_0 + M_{e,meas} \cos \theta_0 \quad (3.2)$$

The calibration used 4 coefficients for each radial position, 2 gains and 2 offsets, such that:

$$M_{f,meas} = x_0 M_{f,raw} - x_1 \quad (3.3)$$

$$M_{e,meas} = x_2 M_{e,raw} - x_3 \quad (3.4)$$

The coefficients were optimized for the minimum root mean square error between calibrated measurements and computations in the first 320 seconds of the time series. The resulting coefficients are shown in table 3.7. For comparison, the coefficients  $x_0$  and  $x_1$  for the section at 3 meters radius that were originally determined from the pull tests in the lab were -0.19 and -6080. So for this section, where the coefficients were not changed in the field after the initial calibration, the deviation of the recalibrated coefficients is roughly 5% for the gain and 9% for the offset. This gives some confidence in the recalibration procedure.

Some examples comparing the simulated moments with measured moments using the old and new calibration are shown in Figures 3.21 to 3.26. It can be seen that the agreement for the flapwise moment is generally better than for the edgewise moment. The changes due to the new calibration get generally more pronounced towards the outboard part of the blade, and the flapwise moment measurements at section 34.04 meters behaved qualitatively different than expected. No satisfactory calibration was possible and this section was discarded in the following comparison.

Radial pos. [m]	$x_0$ [-]	$x_1$ [-]	$x_2$ [-]	$x_3$ [-]
3.04	-2.0118e-01	-6.5922e+03	8.0328e-02	2.5843e+03
8.04	-1.0145e-01	-3.2122e+03	-1.2268e-01	-4.1583e+03
13.04	-1.0181e-01	-3.2582e+03	-9.7955e-02	-3.2734e+03
16.04	-7.5618e-02	-2.4426e+03	-5.5249e-02	-1.8248e+03
19.04	-5.6112e-02	-1.8110e+03	-2.9080e-02	-8.2170e+02
22.04	-3.9840e-02	-1.2950e+03	-6.6421e-03	-1.8695e+02
26.04	-2.7031e-02	-8.8447e+02	-6.6791e-03	-1.7729e+02
30.04	-9.5315e-03	-3.1996e+02	-3.0193e-03	-1.0019e+02
(34.04)	-9.7086e-03	-3.1997e+02	-3.1172e-03	-1.0016e+02
37.04	-6.0389e-04	-2.1859e+01	-1.7889e-03	-5.8657e+01

Table 3.7: Calibration coefficients obtained for the first 320 seconds of the time series at 13:10 on the 16th of July, 2009. The calibrated moments at 34.04 m did not agree qualitatively with the simulated moments so this section is discarded.

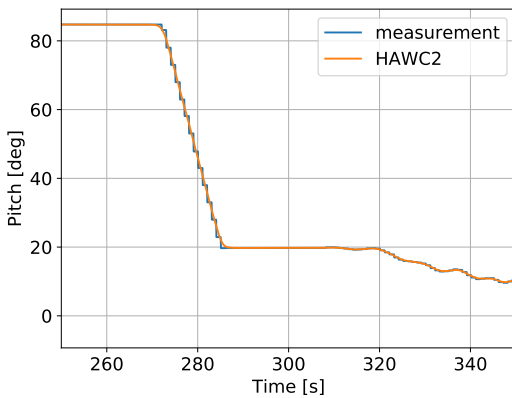


Figure 3.18: Measured pitch signal compared to the pitch signal tracked by the HAWC2 simulation. The pitch is at a constant 84.75 degrees for the first part of the time series.

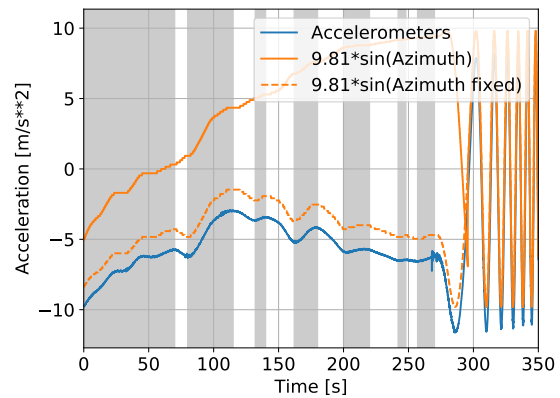


Figure 3.19: Comparison of accelerometer measurements with the gravity contribution expected from the azimuth position. Reversing the rotor rotation in the grey marked parts of the time series leads to qualitative agreement.

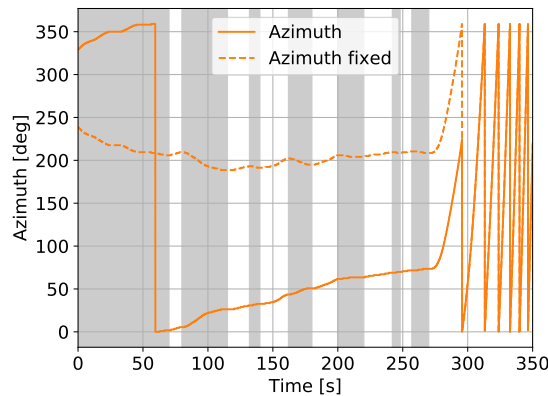


Figure 3.20: Measured azimuth signal and fixed azimuth signal. The jump in value just before 300 seconds is unphysical and has been removed in the fixed signal. (Rotation direction was reversed in the marked areas)

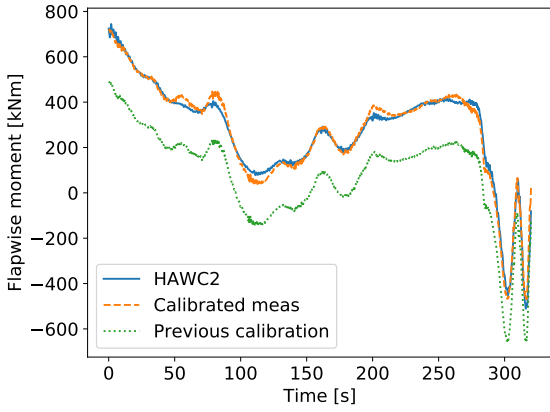


Figure 3.21: Flapwise moment at 3.04 m radius. The original calibration was made for this location.

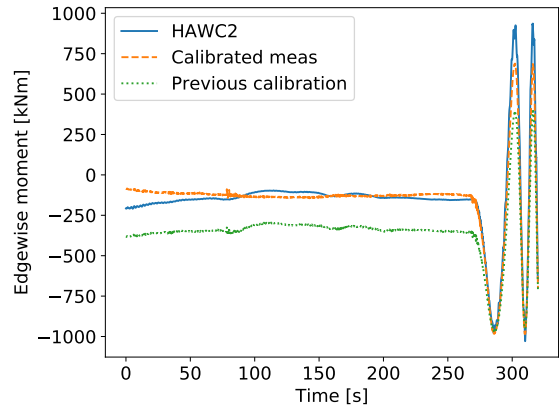


Figure 3.22: Edgewise moment at 3.04 m radius.

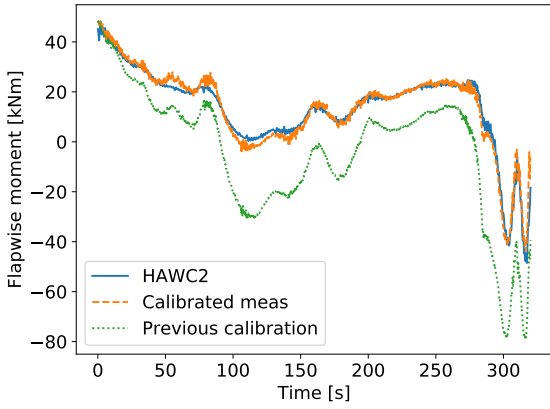


Figure 3.23: Flapwise moment at 26.04 m radius.

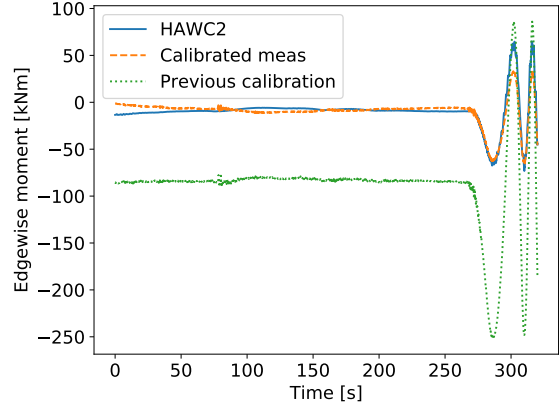


Figure 3.24: Edgewise moment at 26.04 m radius.

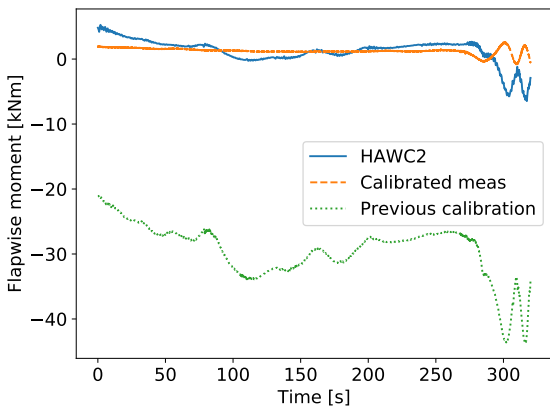


Figure 3.25: Flapwise moment at 34.04 m radius. The measured moment at this station does not show the expected trends and is discarded.

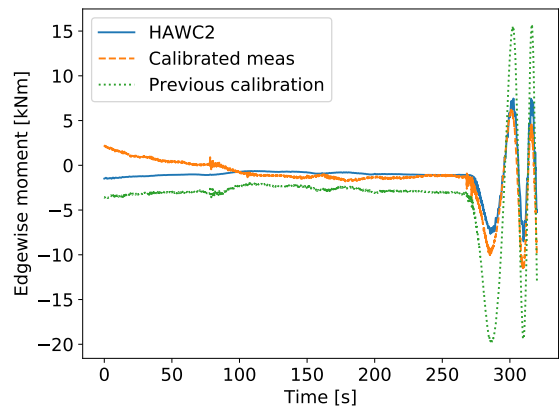


Figure 3.26: Edgewise moment at 34.04 m radius.

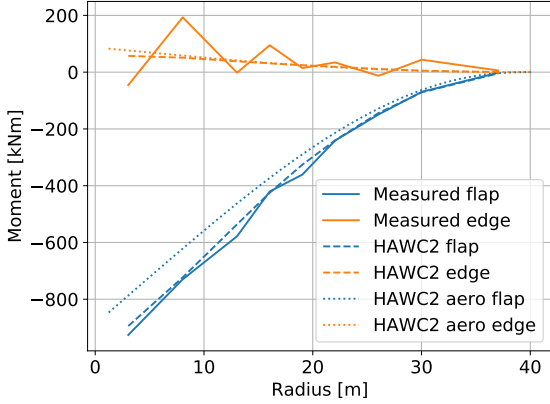


Figure 3.27: Comparison of measured (by strain gauges) and computed moments. There is good agreement for the measured and computed flapwise moment. The 'HAWC2 aero' denoted moment is without structural contributions, for example due to centrifugal forces.

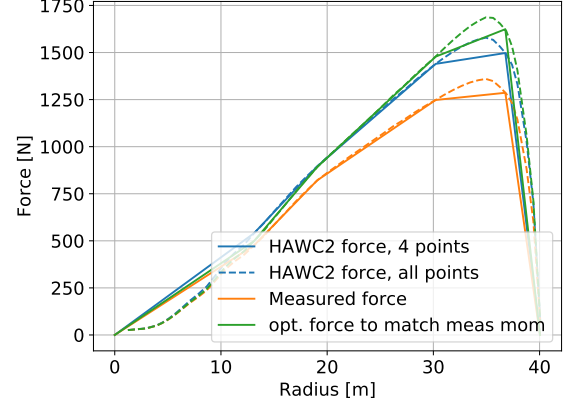


Figure 3.28: To obtain more accurate aerodynamic moment, the high resolution force distribution computed by HAWC2 was scaled to pass through the measured forces at the four instrumented section. An optimized force distribution was found that matches the 'measured aerodynamic moment' (defined as the measured moment - difference between structural and aerodynamic moments in HAWC2)

### 3.9.3 Results in uniform inflow case

The new calibration coefficients shown in Table 3.7 were applied to the uniform inflow case according to Equations (3.1)-(3.4). The recalibrated moments are compared with a HAWC2 simulation for uniform inflow. The HAWC2 simulation is identical to the uniform inflow case used in WP2 but including tilt and gravity for a more direct comparison. A comparison of the moments is shown in Figure 3.27. The mean measured edgewise moment is showing a similar trend as the computed moments, but the large 1P variations due to gravity clearly make the small mean value less reliable. The measured and computed flapwise moment distribution are in very good agreement. The figure also includes an aerodynamic moment that is obtained from integrating the aerodynamic force distribution. The difference between the structural and aerodynamic moment in HAWC2 includes moments due to gravity (prebend/deflection and tilt cause the gravity loading in flap to have a non-zero mean) and centrifugal forces.

The measured aerodynamic forces are only available at four stations, and due to this low resolution a significant error would be made towards the root and tip if they would directly be used to obtain a moment distribution. To approximate a force distribution at higher resolution, the predicted force distribution from HAWC2 is scaled to pass through the measured forces at the pressure tap locations. This scaling is done with a function that has the values 1 at the root and tip,  $f_{meas}/f_{HAWC2}$  at the measurement points and is piecewise linear in between. The resulting force distribution is shown in Figure 3.28, along with a third pair of force distributions, that are the result of an optimization. The optimization varied the forces at the four pressure tap locations with the objective to match the measured moment distribution. The effects due to gravity and centrifugal forces estimated by HAWC2 were added to the aerodynamic moment in the optimization and the total moment was then compared to the moment distribution measured by the strain gauges. The resulting moment is shown in Figure 3.29 and a good match between the moment expected from the optimal force distribution (green line in Figure 3.28) and the measured moment can be seen.

This indicates that the measured force distribution is not consistent with the measured moment distribution. A considerably larger force distribution would be necessary to cause the measured moments, and this force distribution is much closer to the distributions predicted by the different codes in the WP2 code comparison.

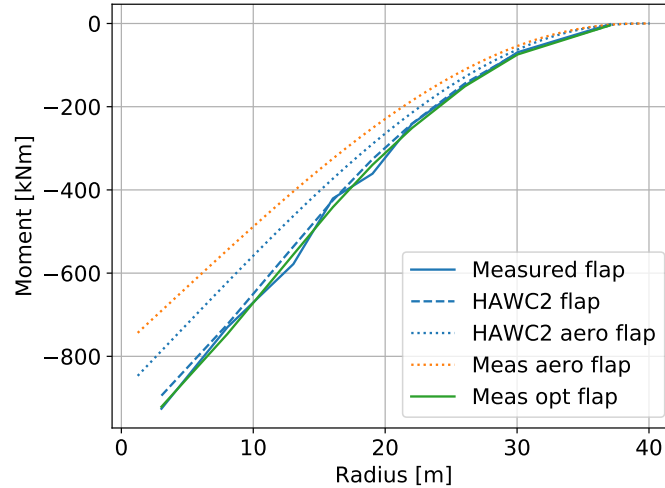


Figure 3.29: The moment indicated by the green line was obtained by adding the difference between structural and aerodynamic moments from HAWC2 to the moment caused by the optimized force distribution shown in Figure 3.28. It matches the moment measured by the recalibrated strain gauges well.

### 3.9.4 Conclusions on the calibration

After correcting the direction of rotation in the azimuth sensor, a recalibration of the strain gauges was possible using an idling case. An exception to this is the section at 34.04 m where no qualitative agreement with the expected gravity moments was found. The recalibrated moments match moments predicted by HAWC2 well also outside of the idling sequence at most radial sections.

The new calibration coefficients were applied to the uniform inflow case investigated in WP2. The resulting moment distribution indicates a slightly larger aerodynamic forcing than predicted by HAWC2 and a much larger aerodynamic forcing than measured at the pressure tap locations. This inconsistency between the force and moment measurements needs further investigation and it needs to be borne in mind when evaluating differences between calculations and measurements in WP2 as discussed in the next chapter.



# Chapter 4

## WP2: Comparison between calculations and measurements

### 4.1 Introduction

Several participants of IEA Task29 Phase IV performed turbine simulations on the DanAero experiment with a variety of aerodynamic models. In its basis a distinction can be made between CFD and panel methods on one hand which model the blade surface directly and lifting line methods which, as the name already suggests, model the blade as a lifting line. A further distinction can be made between lifting line Blade Element Momentum (BEM) methods and lifting line Free Vortex Wake (FVW) methods. The results from the calculations were compared mutually and with the experimental values.

The comparison has been performed for the measurement cases described in section 3.5.6 where it is explained that measurement series have been selected at more or less axial flow (case IV.1) and at significant shear (case IV.2.1) and at significant yaw (case IV.2.2). Appendix A gives detailed information on how these measurements have been translated into a consistent definition of a Benchmark case. In this respect it is important to realise that for all WP2 cases the wind speed, wind shear and yaw angle were defined to be constant. Cases with turbulent inflow, i.e. variations of wind speed in time are considered in Task 3.1 see chapter 5.

Appendix B and C can be consulted for all model descriptions corresponding to the displayed calculations. Section 4.2 is dedicated to the first round comparison results in axial flow. Section 4.3 describes the second round comparison results in shear and yawed flow. The latter two sections describe the main results of the comparison, an overview of all comparison results in terms of figure plots is presented in appendix D and E.

## 4.2 First round: Axial flow, Case IV.1

The first case IV.1 is summarized in Table 4.1, based on the measurement data point with relatively steady and uniform inflow and constant operational conditions (see chapter 3). The case is subdivided in case IV.1.1 where the turbine, i.e. tower, rotor etc should be modeled rigid, and case IV.1.2 where flexibilities are included. A more detailed description of the conditions and the data format and variable definition can be found in appendix A. All variables are displayed as supplied. An exception lies in the non-dimensionalized values of normal and tangential force. These are non-dimensionalized using undisturbed local dynamic pressure (determined from wind and local rotational speed) to allow for a solid comparison of airfoil coefficients between experiment and simulations along the span without the complications of uncertainty in rotor induced velocities. The definition for the normal force, which is equivalent to the tangential force can be given as

$$F_{nc\_qc} = \frac{F_n}{0.5\rho(U_\infty^2 + (\omega r)^2)c}, \quad \text{with} \quad (4.1)$$

$F_{nc\_qc}$	[-]	Non-dimensionalized chordnormal force
$F_n$	[N/m]	Chordnormal force
$\omega$	[rad/s]	Rotor speed
$\rho$	[kg/m <sup>3</sup> ]	Air density
$U_\infty$	[m/s]	Wind speed
$r$	[m]	Local radius
$c$	[m]	Local chord.

Another exception lies in the axial force and torque which are post-processed to thrust and power coefficients  $C_{d_{ax}}$  and  $C_p$  using

$$C_{d_{ax}} = \frac{F_{ax}}{0.5\rho U_\infty^2 \pi R^2}, \quad \text{and} \quad C_p = \frac{\text{Torque } \omega}{0.5\rho U_\infty^3 \pi R^2}, \quad \text{with} \quad (4.2)$$

$C_{d_{ax}}$	[-]	Axial force coefficient
$C_p$	[-]	Power coefficient
$F_{ax}$	[N]	Rotor axial force
Torque	[Nm]	Rotor torque
$R$	[m]	Rotor radius.

The flatwise moment  $M_{flat}$  is another deduced variable which has been added to this comparison round. The displayed measured value has been obtained from the post-processed strain gauge signals. For the simulation results a script was used to linearly integrate the given force distribution perpendicular and tangential to the rotor plane along the blade span resulting in the flap- and leadwise moments, which are rotated using the pitch angle to obtain the flatwise moment. The legend of each graph refers to the parties and their codes that were used to perform the simulations. The model description corresponding to the legend entries can be found in appendix B and C.

As mentioned above appendix D displays all underlying plots. Separate sections are dedicated to plots with lifting line code results (i.e. codes that make use of airfoil polars in table format) and CFD (plus panel code) results.

### 4.2.1 Lifting line codes

The *lifting line variables* comparison plots for case IV.1 are given in section D.1. These variables are calculated from both lifting line BEM methods and lifting line Free Vortex Wake methods.

The effective velocity  $U_{eff}$  (Figure D.1) is in good agreement between the codes, indicating that the inputted operational conditions are consistent between the codes. Small differences can be observed in the inboard region, where induction starts to play a role over the elsewhere dominant rotational velocity. The angle of attack AOA shows larger variations, caused by the differences in axial and tangential induced velocities  $U_i$  and  $V_i$  as shown in Figure D.2. A closer look at the axial induced velocity  $U_i$  shows that,

Table 4.1: DanAero comparison cases (axial flow)

Case nr	Model	Wind speed $U_\infty$ [m/s]	Pitch angle [°]	Rot. speed $\omega$ [rpm]	Tip speed ratio $\lambda$ [-]	Angle of attack $\alpha^\dagger@80\%R$ [°]	Axial induction factor $a^\dagger@80\%R$ [-]
IV.1.1	Rigid	6.1	0.15	12.3	8.4	4.0	0.38
IV.1.2	Flexible	6.1	0.15	12.3	8.4	4.0	0.38

† estimate

especially apparent for the participants that delivered both BEM and free vortex wake results, the free vortex wake codes feature a roughly 10% lower induced velocity. A similar observation was made in the final report of Mexnext-III [11] for the New Mexico case in the turbulent wake state, which featured a high axial induction factor similar to the case under investigation here.

The bottom two plots of these Figures show the difference (delta) between Case IV.1.1 and IV.1.2, of which the only difference is the introduction of flexibility for Case IV.1.2. As the blades are suspended from the root, the effects of flexibility are mostly noticeable in the outboard region of the blades. Because of the flapwise prebend, which is 'flattened' for the flexible case, the wind faces the blades more head-on resulting in slightly larger loads (and larger effective velocity, induced velocities and angle of attack) towards the tip. Generally speaking the trends between the codes are similar although level differences around 5 to 10% remain despite the prescribed airfoil data for this round.

The resulting *loads* in terms of sectional normal and tangential force  $F_n$  and  $F_t$  are given in Figure D.4. Consistent with the induced velocities and angles of attack, the agreement in  $F_n$  is fair between the computational results with a spread around 5%. Dividing the loads by the local undisturbed dynamic pressure in Figure D.5 allows to better zoom in on the differences along the span. A closer look at the levels in Figure D.5c shows again a difference between vortex wake codes and BEM codes, where the latter generally feature a lower loading than vortex code results. This is also reflected in the integral loads from Figure D.7 (blade root flatwise moment, axial force and power). Acknowledging the earlier observed variations in axial induced velocities, this discrepancy is in contradiction with momentum theory where a higher loading is accompanied with more induction. Grouping the results by code type, as will be shown in section 4.2.4 allows to better observe the loading differences.

The comparison with measured values (obtained from integration of the measured pressure distributions) shows the normal force to be consistently overpredicted by approximately 10% for all radial positions. Despite the limitation of four radial stations it could be expected that this overprediction is reflected in the measured flatwise moments from Figure D.7c as well. However the observed differences for this moment are around  $\pm 2\%$ , where it should be noted that the measured flatwise moments are obtained from the strain gauge rather than the pressure measurements. Contrary to the normal force, the tangential force (Figures D.4d and D.5d) reveals an under instead of over prediction. Here it must be noted that the measured values only contain the contribution of pressure, whereas the simulations are based on airfoil coefficients which also contain the friction forces. For the tangential direction this contribution is significant (as will be shown in section 4.2.3) and taking this into account will result in a better agreement between measurements and simulations. In addition to that it is known that obtaining tangential force from integration of a finite number of pressures is very sensitive to the distribution of the taps especially around leading and trailing edge. Summarizing, tangential forces obtained from pressure distributions should be interpreted with care.

Figure D.6 then displays the predicted *deformations* between the aero-elastic codes. Here it is shown that besides some outliers most codes agree within 1% for the flapwise deformation ( $dx$ ), whereas there is a bit more scatter in the edgewise deformation ( $dy$ ). However in absolute sense we are comparing differences less than a centimeter. As some of the participants did not provide results for the flexible case (IV.1.2), several colors are visible on the zero line.

## 4.2.2 CFD and panel codes

The CFD and panel code results for case IV.1 are given in section D.2. It is noted that although a comparison is made with the measurements (for which the blades are obviously flexible), the CFD simulations were mostly performed for a rigid blade. The lifting line simulations as described in the previous section give an indication of the effect of flexibility on the average levels. Starting with a comparison of the *sectional geometries* used by the codes, Figure D.8 shows the shapes of the four sections. Theoretically these shapes should be identical, but some offsets appear and in some cases even local twist differences are apparent. The question remains whether these deviations are due to different ways of post-processing (e.g. a different orientation or location of the section) or if the geometries are not identical. As the blade geometry was prescribed by an IGES file the latter should not be the case.

The *pressure distribution* comparison plots in Figure D.9 show the models tend to agree well for all radial positions, although the inviscid panel code is unable to predict separated flow in the most inboard station in Figure D.9a. But at this station also the CFD codes struggle to match the measured pressure distribution on the suction side just before the trailing edge. For the other three radial positions the suction levels are 5 to 10% higher in comparison to the experiment. At  $r=30.20$  m (Figure D.9c) the linear shape of the measured pressure distribution on the pressure side just before the chordwise position of maximum thickness differs from the rounded shape as predicted by all simulations. A separate sectional study was performed by DTU to compare the performance between design and measured geometries, of which the first was used for this comparison round. This however revealed very small differences in comparison to the differences shown here. Besides these small deviations one can conclude that generally speaking the pressure distributions are in good agreement between simulations and between simulations and experiment.

The resulting *loads and performance* are then compared in Figure D.10. Although the differences in the pressure distribution appear minor, these differences stand out more in the integrated force values. Both for the chord normal and tangential force a similar conclusion can be drawn as for the lifting line codes with respect to the discrepancy with the measurements. However contrary to the lifting line results, for some of the CFD results the contribution of friction has been removed from the integrated force values. The differences between the simulations themselves triggered a sensitivity study which is described in the next section.

## 4.2.3 CFD sensitivity study

DLR, DTU, Kiel UAS and IAG University of Stuttgart carried out a study to post-process their CFD data using a common tool at IAG to improve the consistency of the solutions. Additional simulations were ran using a finer mesh resolution to asses the impact of the grid resolution. The properties of the coarse and fine mesh are summarized in Table 4.2. Here it is noted that DTU used a fine mesh with full rotor topology, while the others used a periodic boundary condition. Although for the periodic fine mesh the chordwise

Table 4.2: Coarse and fine mesh properties

Name	Topology	Total nr of cells [M]	First cell normal size [m]	Chordwise nr of cells [-]	Spanwise nr of cells [-]	Domain size [D]
Coarse	full rotor (360°)	14	$1.0 \times 10^{-6}$	256	128	10
Fine	full rotor (360°)	113	$0.5 \times 10^{-6}$	512	256	10
Fine	blade periodic (120°)	26	$2.0 \times 10^{-6}$	256	200	10

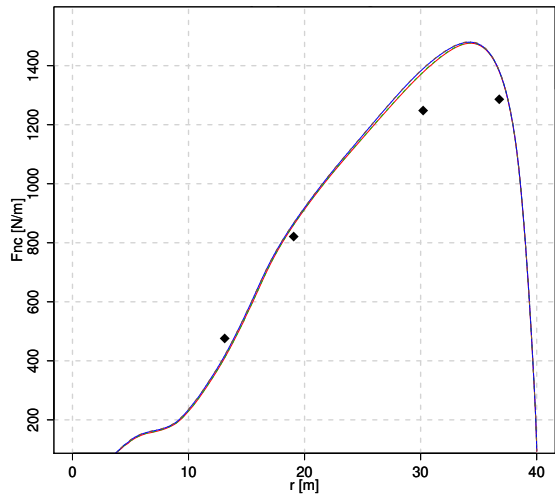
resolution is the same as the coarse mesh and the first cell normal size is even larger, the total number of cells for a full rotor equivalent of this mesh would roughly differ by a factor of 6 ( $26 \times 3 / 14$ ). Apparently the majority of the extra cells for this fine mesh are placed in the wake and the background mesh.

In addition to the grid sensitivity study, the results of the coarse and fine mesh were post-processed to observe the contribution of friction to the integrated forces. The following results can then be visualized:

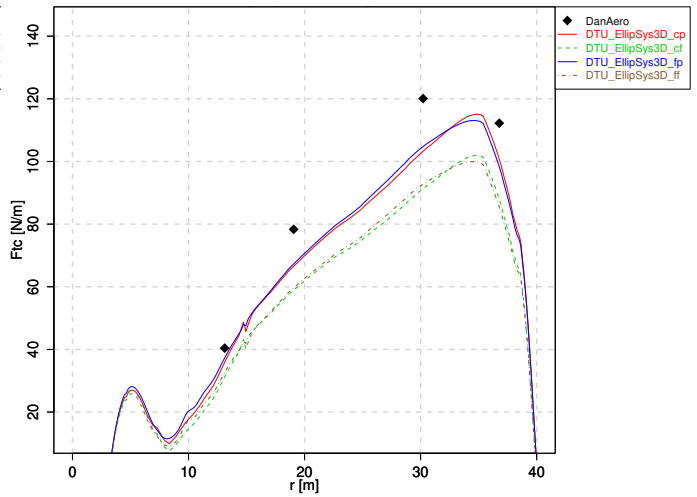
- cf coarse mesh, friction included
- cp coarse mesh, pressure only
- ff fine mesh, friction included
- fp fine mesh, pressure only

The resulting comparison plots are shown in Figure 4.1. For the DTU result in Figures 4.1a and 4.1b it becomes clear that the mesh refinement hardly has an influence on the results and the coarse mesh suffices. For the IAG University of Stuttgart results in Figures 4.1c and 4.1d this conclusion does not hold and level differences up to 10% can be observed. The same holds for the DLR results (which are not shown here for the sake of brevity). The latter two codes are compressible solvers for which the grid requirements are more strict than for incompressible solvers such as the DTU EllipSys3D code. Although the underlying pressure distributions are not shown here, these compressible codes reveal a different suction level causing the integral loads to improve for the fine mesh. Figures 4.1e and 4.1f demonstrate that refining the mesh improves the consistency between the codes significantly. Apart from the blade root region inboard of 10m span the results are close to identical.

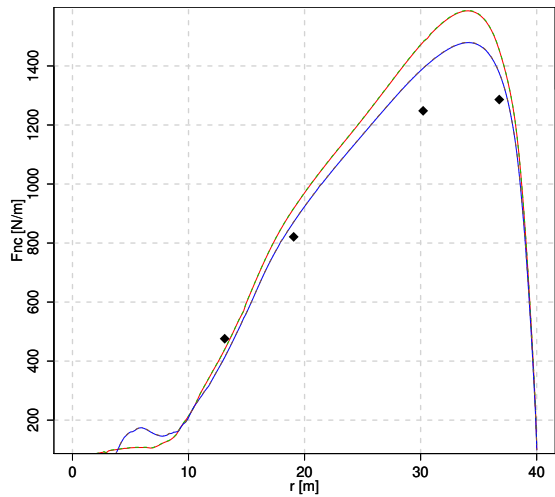
As expected the effect of friction is hardly present in the normal force, which can be deduced from Figures 4.1a and 4.1c. For the tangential force this is different, especially for the three most outboard stations which feature moderate angles of attack with attached flow. The friction reduces the tangential force by approximately 15%, consistent between the two code results displayed here.



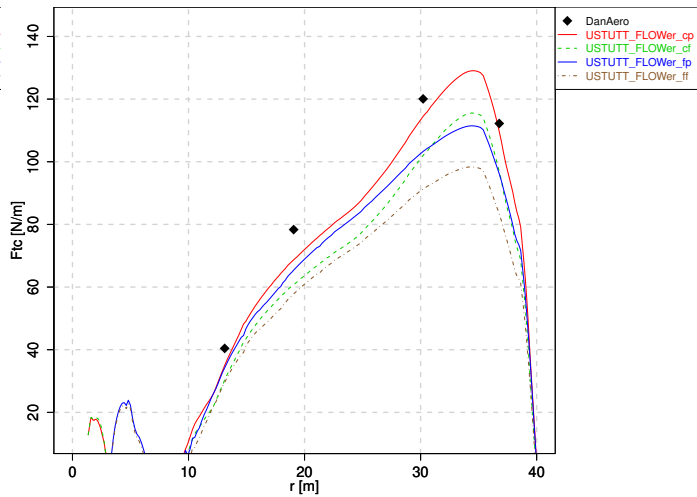
(a) Fnc, Case IV.1.1, DTU



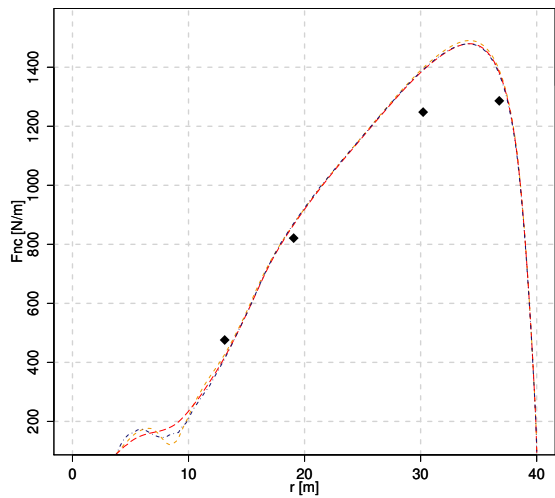
(b) Ftc, Case IV.1.1, DTU



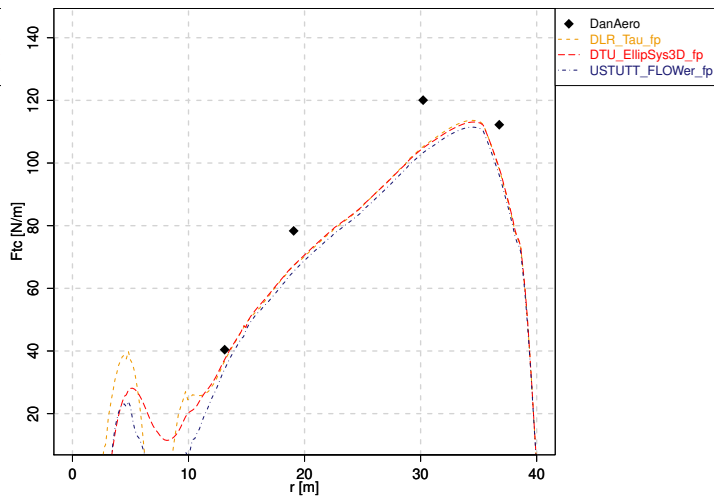
(c) Fnc, Case 1.1, IAG



(d) Ftc, Case 1.1, IAG



(e) Fnc, Case 1.1, fp



(f) Ftc, Case 1.1, fp

Figure 4.1: Effect of sensitivity studies on predicted loads

## 4.2.4 Model types comparison

In addition to displaying the loading results from the various codes as described in the section above, the supplied data also gives the opportunity to calculate an average result for each code type. Here the following code types are distinguished:

- BEM  
Blade Element Momentum methods using the airfoil data as prescribed in appendix A.
- FVW  
Lifting line free vortex wake methods, also using the prescribed airfoil data.
- CFD  
Computational fluid dynamics codes, which model the rotor blade geometry and the 3D space around it. In most cases the blade boundary layer is modeled as fully turbulent.

In addition to the code types listed above there are also a panel code and actuator line codes that joined the comparison round, but they were excluded from the averaging as the number of codes for these types are too few (<3) to perform statistics on. A summary of the codes used to determine the average is given in Table 4.3.

Table 4.3: Summary of codes used for code type averaging (axial flow)

Code type	Code names
BEM	Bladed4.8_BEM, DTU_HAWC2, IFPEN_BEM, NREL_ED, PhatAero-BEM PoliMi_Cp-Lambda
FVW	IFPEN_VL, NREL_VC, PhatAero-AWSM
CFD	DLR_TAU, DTU_EllipSys3D, FW_IWES_Emden, NREL_CFD, Onera_ElsA Kiel UAS_TAU, USTUTT_FLOWer

To obtain the loading averages, first the normal and tangential force are determined at the same spanwise four positions as the instrumented sections using linear interpolation from the supplied radial distributions. A simple average  $\bar{x}$  is determined using

$$\bar{x} = \frac{1}{n} \sum_{i=1}^n (x_i) \quad .$$

In addition to that, to give an indication of the variability between the results, a partly transparent band is plotted around the average of each code type illustrating the standard error  $x_{err}$  between the supplied results of a code type

$$x_{err} = \sqrt{\frac{\sum_{i=1}^n (x_i - \bar{x})^2}{n(n-1)}}.$$

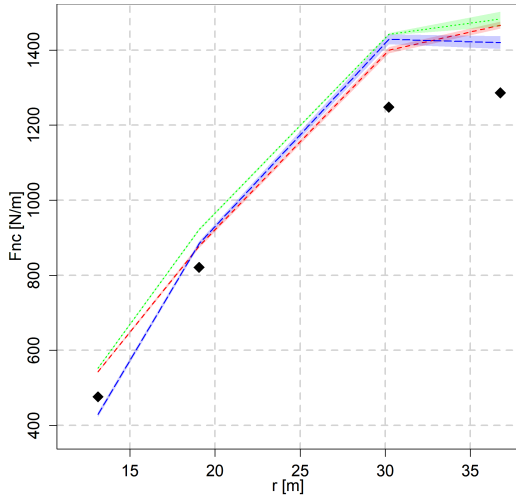
The same procedure is applied to the flatwise moments, axial force and torque (average levels only). This process is only performed for the rigid results because the CFD results are mostly rigid.

The results are illustrated in Figure 4.2. One can conclude that the level of the normal force generally agrees within 5% between the different code types. However the tip region shows more of a fall-off for CFD and the root region features a sudden drop in level for the CFD results. The higher loading for free vortex wake models as discussed in section 4.2.1 is also apparent from the plots. For the tangential force the differences between the code types are larger but in absolute sense these are rather small. The reason for the good trend overlay between CFD and FVW opposed to BEM is not fully understood and could as

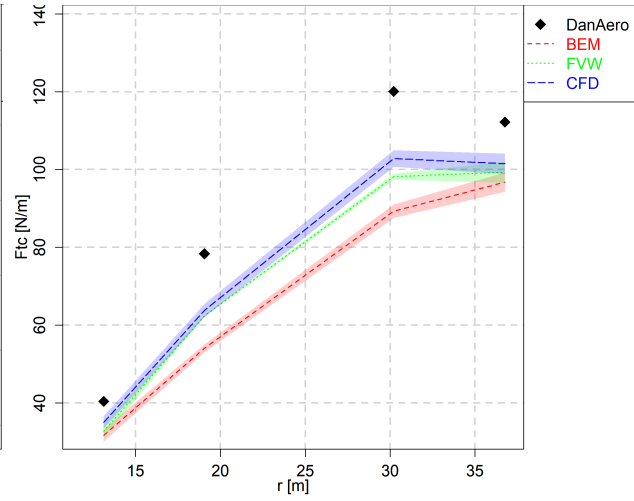
well be attributed to coincidence. The bands showing the variability between results from each code type are similar between the different types and amount to  $\pm 1\%$  for the normal force and  $\pm 5\%$  for the tangential force. In the previous phases of IEA Task 29 the 'human factor' would result in a larger spread between CFD results. The dedicated efforts to minimize this spread as described in section 4.2.3 seem to have paid off.

Comparing against the measurements, the normal force is overpredicted by approximately 10% for almost all sections while the flatwise moment agrees within  $\pm 2\%$  as was observed in the dedicated section discussing lifting line code and CFD results. For the discussion on the tangential force discrepancy the reader is referred to the lifting line code discussion in section 4.2.1. Summarizing one can conclude that the differences between the various simulations is on the decrease, which is good news. Compared to wind tunnel experiments like New Mexico featuring controlled conditions, it remains a challenge to achieve good agreement of absolute levels between measurements and simulations in the field.

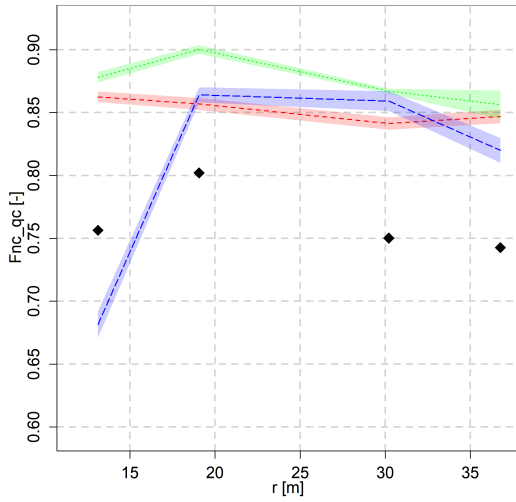




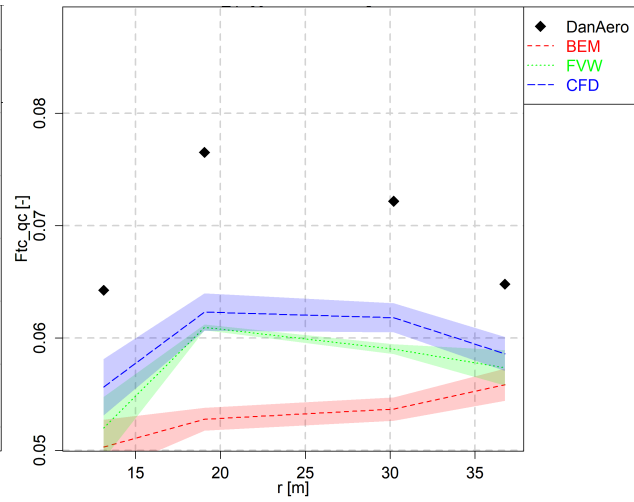
(a) Fnc, Case 1.1



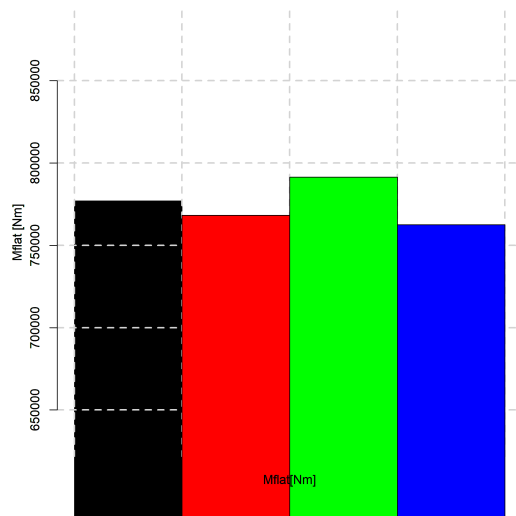
(b) Ftc, Case 1.1



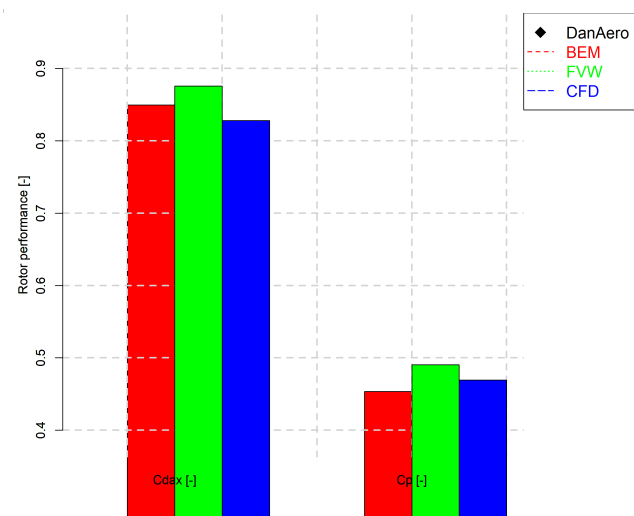
(c) Fnc\_qc, Case 1.1



(d) Ftc\_qc, Case 1.1



(e) Mflat, Case 1.1



(f) Performance, Case 1.1

Figure 4.2: Loads comparison by model types for round 1

### 4.3 Second round: Shear (Case IV.2.1) and yawed flow (Case IV.2.2)

Two cases are defined featuring a significant vertical wind shear and yaw misalignment (also including vertical shear) as summarized in Table 4.4, carefully selected from the available measured time series (see chapter 3). As we are studying the load variation due to shear and yaw, the results are presented as a function of rotor azimuth angle. A more detailed description of the conditions and the data format and variable definition can be found in appendix A. To better compare the loads trends as a function of azimuth angle, the mean over the rotor revolution has been subtracted from these results now showing a 'delta'. The surface pressures have been normalized with undisturbed dynamic pressure following

$$C_p = \frac{P}{0.5\rho(U_\infty^2 + (\omega r)^2)}, \quad \text{with} \quad (4.3)$$

$C_p$	[-]	Non-dimensionalized pressure
$p$	[Pa]	Static pressure relative to atmosphere
$\omega$	[rad/s]	Rotor speed
$\rho$	[kg/m <sup>3</sup> ]	Air density
$U_\infty$	[m/s]	Wind speed
$r$	[m]	Local radius.

The maximum pressure at the stagnation point was then forced to 1 by applying an offset. For the measurements, since results of multiple revolutions is available, the standard deviation between these measured values gives an indication of the repeatability. The standard deviation is indicated in the graphs by a grey band around the mean value, as described in the experimental data reduction chapter (chapter 3).

Table 4.4: DanAero comparison cases (shear and yawed flow)

Case nr	Shear exponent	Wind speed $U_\infty$ [m/s]	Yaw angle [°]	Pitch angle [°]	Rot. speed [rpm]	Tip speed ratio $\lambda$ [-]	Angle of attack $\alpha^\dagger@80\%R$ [°]	Axial induction factor $a^\dagger@80\%R$ [-]
IV.2.1	0.249	9.792	-6.02	-4.75	16.2	6.9	10.0	0.41
IV.2.2	0.262	8.429	-38.34	-4.75	16.2	8.1	7.0	0.42

<sup>†</sup> Estimate of azimuth averaged value

#### 4.3.1 Lifting line codes

The *lifting line variables* comparison plots are given in section E.1. The effective velocity  $U_{eff}$  variation (Figures E.1 and E.7) shows a good agreement between most of the codes, indicating consistency between the inputted operational conditions. Discrepancies here can also be caused by faulty post-processing, for example by a discrepancy in the radial position used to extract the data. Where in Case IV.2.2 (featuring a large yaw angle) the effective velocity variation with azimuth angle is dominated by the advancing and retreating effect, the sheared Case IV.2.1 is expected to be dominated by the wind velocity variation due to the vertical shear. However it appears that instead this case shows a peak in the effective velocity for the blade approaching the downward pointing position (180° azimuth). It is noted that this case includes a 6° yaw angle and the 5° tilt is modeled as well, which apparently are dominating the shear effect.

The axial induced velocity variation  $U_i$  in Figures E.2 and E.8 anyhow reveal large variations and opposite trends between the underlying models. This can be expected for the BEM codes in the yawed case due to

the different skewed wake models used, but for the sheared Case IV.2.1 this is unexpected. A closer look at the induced velocity variation in Figure E.2 reveals most codes to predict a counter-intuitive axial induction increase for the blade approaching the downward pointing position, acknowledging the relatively low wind speed experienced in this position due to the vertical wind shear. The reason for this will be discussed in section 4.3.3. For the tangential induced velocity (Figures E.3 and E.9) the differences between the codes are even larger showing large amplitude variations for the free vortex wake and actuator models in comparison to BEM. The effect on angle of attack AOA (Figures E.4 and E.10) remains limited, relatively reducing the scatter.

The *loads* comparison can be found in Figures E.13 and E.15 for the normal force  $F_n$  (plus flapwise moment) and Figures E.14 and E.16 for the tangential force  $F_t$ . For the sheared Case IV.2.1 it becomes apparent that none of the lifting line codes are able to convincingly predict the normal force variation due to shear, illustrated by amplitude differences and especially by the reversed trend at 48%R in Figure E.13b. Acknowledging the relatively high operating angles of attack in stall for this case, this discrepancy could be airfoil data related. Although the angle of attack variation in Figure E.4b shows a dip for a downward pointing blade ( $180^\circ$  azimuth), the lifting line normal forces show a peak apart from the dip induced by the tower passage. The trend agreement between measured and predicted tangential forces is much better. For the yawed case the normal force variation in Figure E.15 shows a large spread between the predictions, although most of the vortex and actuator line codes are able to accurately predict the trend. Similar to Case IV.2.1, the predicted tangential force trend is generally in good agreement between codes themselves and experiment.

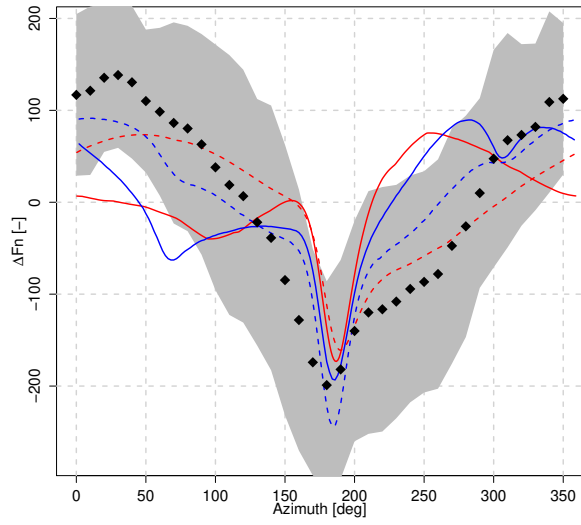
### 4.3.2 CFD and panel codes

Section E.2 shows the CFD and panel code related plots in yaw. The *pressure distributions* are given for all four radial stations at  $0^\circ, 90^\circ, 180^\circ$  and  $270^\circ$  azimuth in Figures E.17 to E.24. Generally speaking the trend with azimuth is well captured, but the separated flow conditions for Case IV.2.1 (especially inboard) are a challenge for the panel code and some of the CFD codes. For both cases the measured pressure distributions at 92%R (Figures E.20 and E.24) feature a dip at the suction side around 20% chord, which seem rather fierce to be introduced by transition. It is noted that the CFD simulations feature a turbulent boundary layer on the blades.

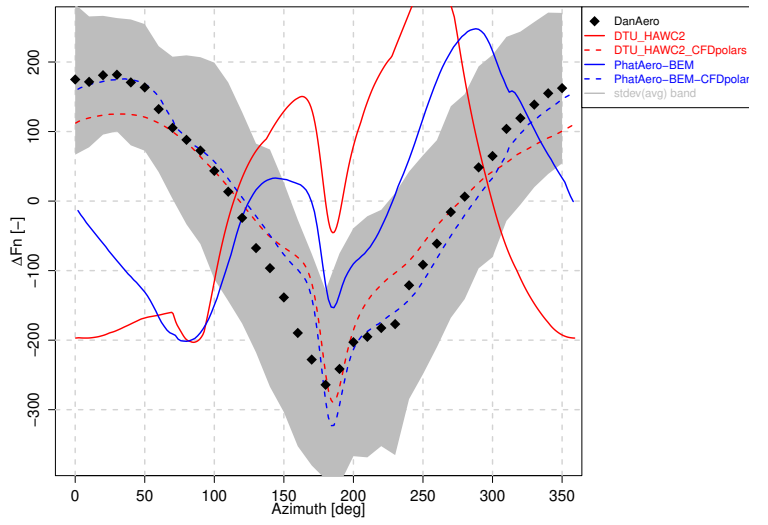
The corresponding *loads* comparison can be found in Figures E.25 to E.28. As expected the results are in agreement with the pressure distributions and generally speaking the codes are able to predict the azimuthal variation of the loads much better than the lifting line codes. This especially holds for the sheared case, where most predictions are within the experimental uncertainty band. For the yawed case there is more variability between the codes, especially for the normal force.

### 4.3.3 CFD synthesized airfoil data

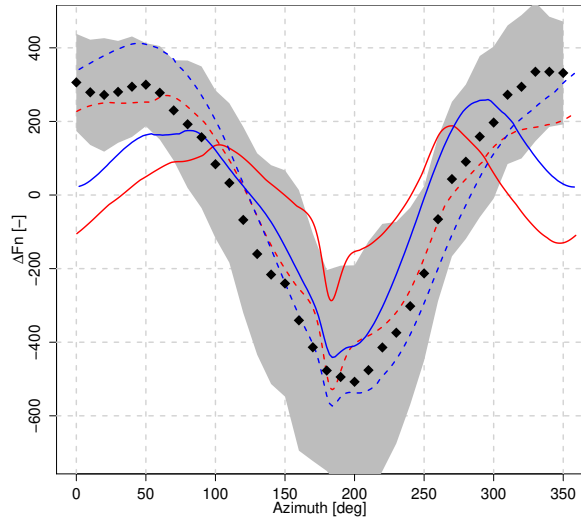
The poor agreement of lifting line codes with measurements for the shear case together with the encouraging CFD results instigated further investigations. IAG University of Stuttgart provided an airfoil data set synthesized from 3D rotational CFD computations employing the azimuthal averaging method [24] as described in section 5.2.2. Two participants then re-simulated case IV.2.2 with their BEM codes. The resulting normal force trends are given in Figure 4.3.



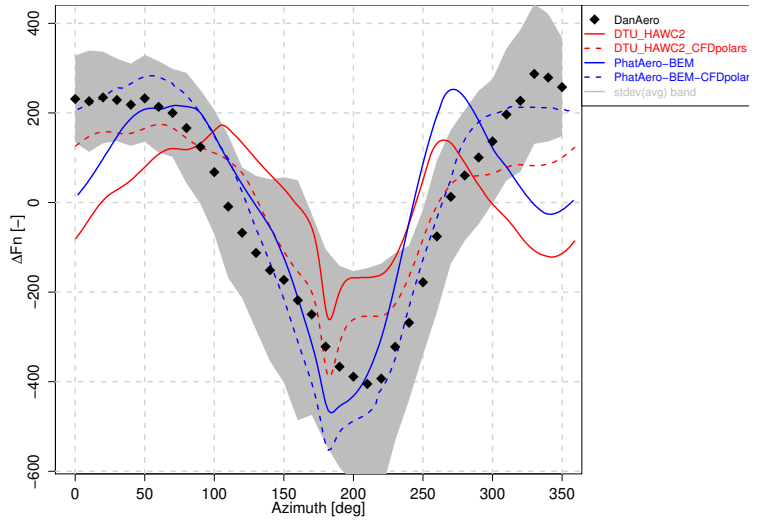
(a)  $F_n$ ,  $r/R=33\%$



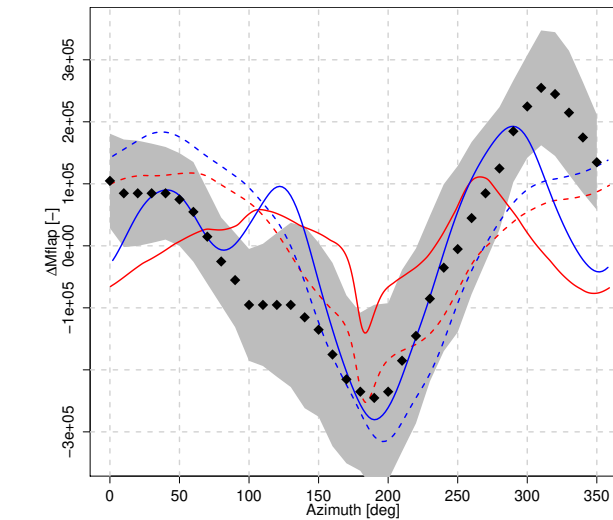
(b)  $F_n$ ,  $r/R=48\%$



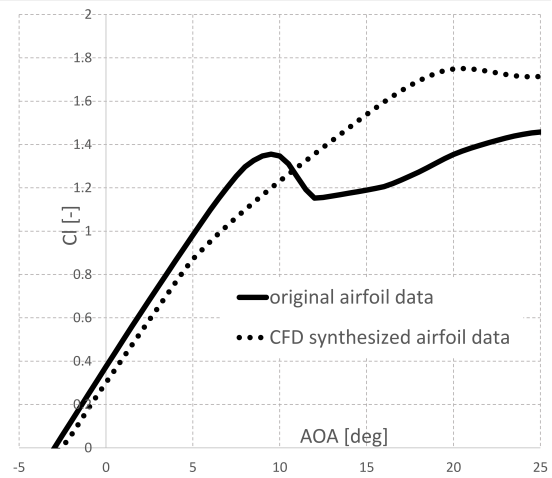
(c)  $F_n$ ,  $r/R=76\%$



(d)  $F_n$ ,  $r/R=92\%$



(e) Mflap



(f) Lift curves at  $r/R=48\%$

Figure 4.3: Normal force  $F_n$  variation and airfoil data using CFD synthesized airfoil data, Case IV.2.1

It is clear that for Case IV.2.1 the results featuring the CFD synthesized polars outperform the results with the original polars. This indicates the earlier found discrepancies to be airfoil data related. Revisiting the lifting line codes discussion from section 4.3.1 it was noted that the airfoils are operating in the stall region and apparently the stall delay due to the 3D rotational effects is not correctly taken into account by the original airfoil data. Comparing the underlying polars at  $r = 48\%R$  in Figure 4.3f clearly shows the stall delay as predicted by CFD. This explains the loading and induction increase rather than decrease for a downward pointing blade when using the original airfoil data as the lift will increase rather than decrease for an angle of attack decrease when coming back from stall around  $12^\circ$ . For case IV.2.2, which is dominated by induction aerodynamics and featuring angles of attack further away from stall, it can be shown that the CFD synthesized polars hardly impact the trend variation.

### 4.3.4 Model types

Similar to the axial flow analysis as described in section 4.2.4, results between code types have been averaged to give a better overview of the differences between them. The same code types are distinguished, a summary of the codes used to determine the average is given in Table 4.5. In addition to the code types listed above there are also a panel code and actuator line codes that joined the comparison round, but they were excluded from the averaging as the number of codes for these types are too few ( $<3$ ) to perform statistics with. To

Table 4.5: Summary of codes used for code type averaging (shear and yawed flow)

Code type	Code names
BEM	Bladed4.8_BEM, DTU_HAWC2, IFPEN_BEM, NREL_ED, PhatAero-BEM PoliMi_Cp-Lambda
FVW	IFPEN_VL, NREL_VC, Onera_PUMA, PhatAero-AWSM
CFD	DLR_TAU, DTU_EllipSys3D, NREL_CFD, USTUTT_FLOWer

obtain the loading averages and standard error, the same data reduction procedure is adopted as for axial flow. Since we are interested in the load variation as a function of azimuth, all supplied code results are linearly mapped onto an azimuth angle distribution with a step of  $5^\circ$ , prior to calculating the average and standard error for each code type.

The results are illustrated in Figure 4.4 to 4.7. The normal force trends in Figure 4.4 clearly illustrate the merit of CFD simulations versus lifting line codes. However the previous section also demonstrated that using CFD synthesized airfoil data can improve the performance of these codes, thereby illustrating the discrepancies to be airfoil data related. The variability within each code type (as illustrated by the colored band around the mean results) is of the same order for all code types for this case, although there seems to be a significant variability in the amplitude of the dip around  $180^\circ$  azimuth as predicted by CFD codes. The stall delay mainly affects lift, which is why the agreement in the tangential force variation in Figure 4.5 is much better for all code types.

For the yawed case a different image appears, as oblique inflow is dominated by induction rather than airfoil aerodynamics. This is illustrated by the normal force in Figure 4.6 which shows the maximum normal force at the outer part of the blade near an azimuth angle of  $270^\circ$  where the maximum normal force at the inner part is near an azimuth angle of  $90^\circ$ . This is explained by induction effects from the skewed wake, see [1]: At the inner part of the blade the azimuthal load variation at yawed conditions is mainly determined by the induction from the skewed root vortex where the load variation at the outer part of the blade is mainly determined by the induction from the skewed tip vortex which gives a  $180^\circ$  different phase shift to the induction (and resulting load) variation. This skewed wake effect is inherently modelled by CFD and vortex methods by which they almost completely fall within the experimental uncertainty band, especially for the outboard sections. BEM codes rely on uncertain engineering methods to model these

skewed wake effects by which the variability between BEM codes is more than two times larger than vortex and CFD codes. Similar to Case IV.2.1, the tangential force variation (Figure 4.7) is subject to smaller variability and better agreement with the measurements than the normal force variation.

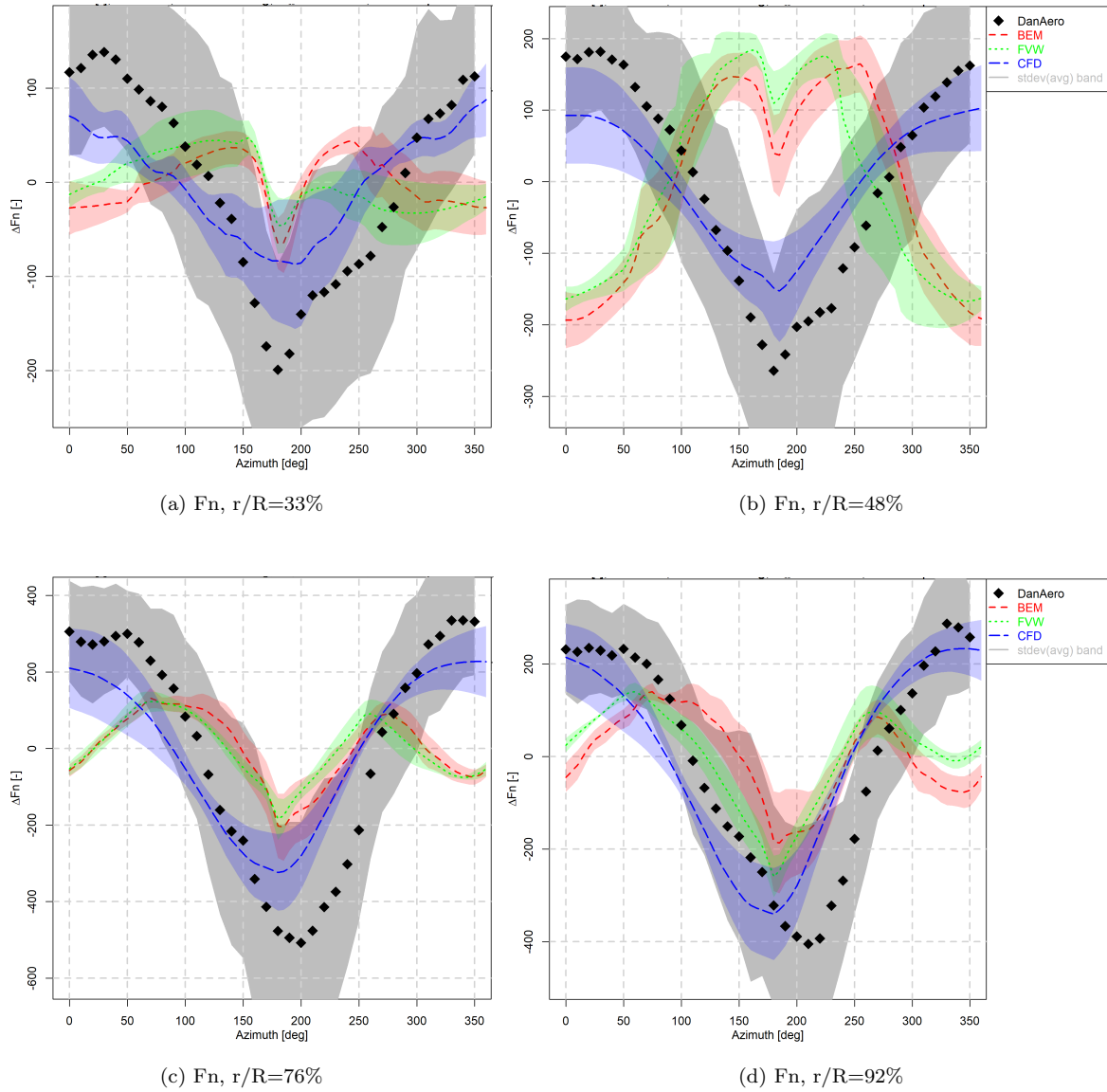
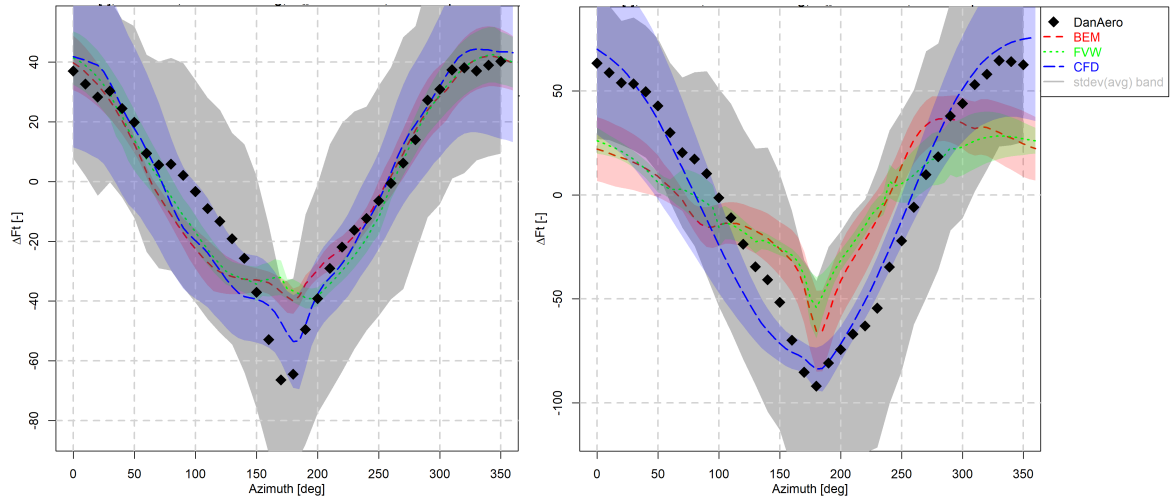
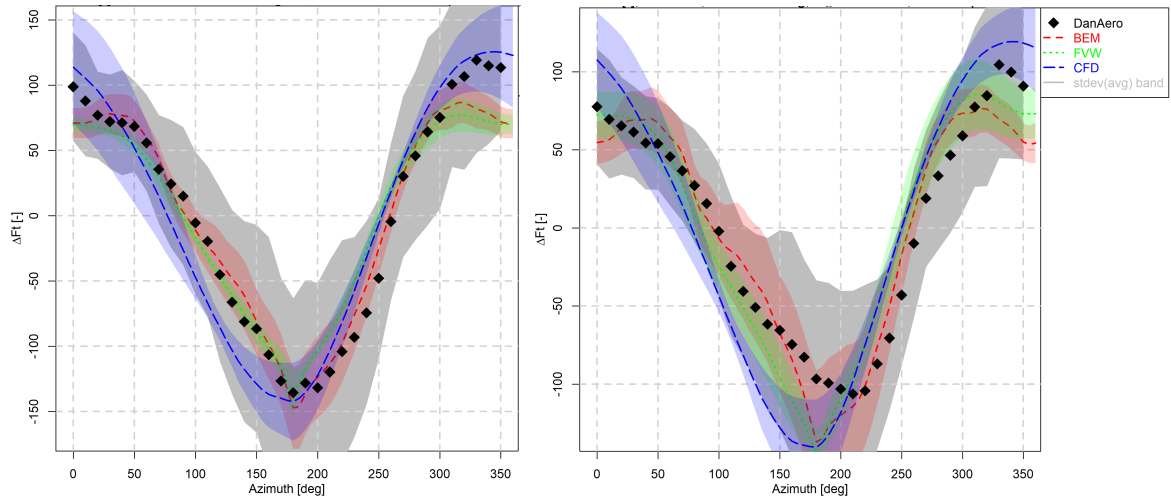


Figure 4.4: Normal force  $F_n$  variation by model types, Case IV.2.1



(a)  $r/R=33\%$

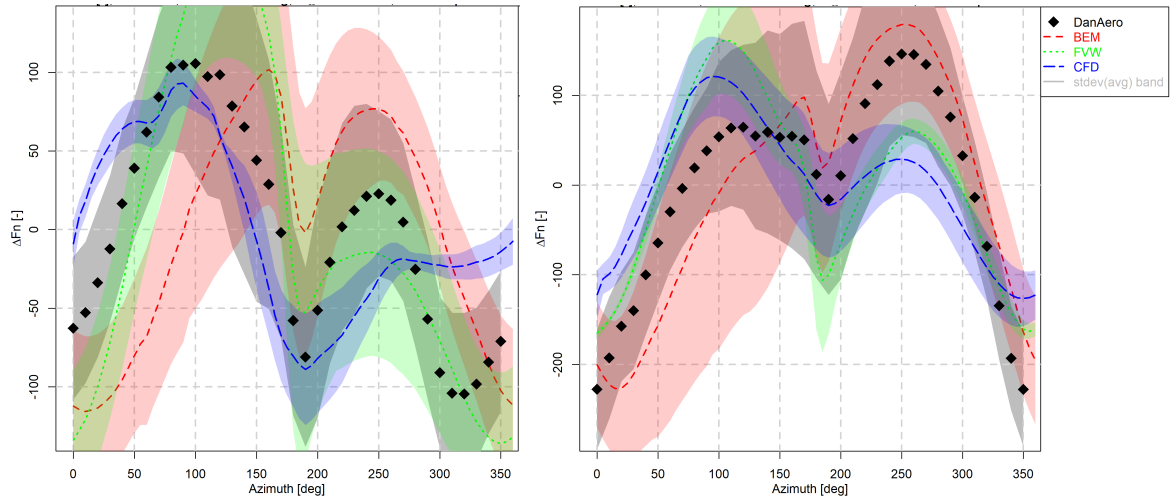
(b)  $r/R=48\%$



(c)  $r/R=76\%$

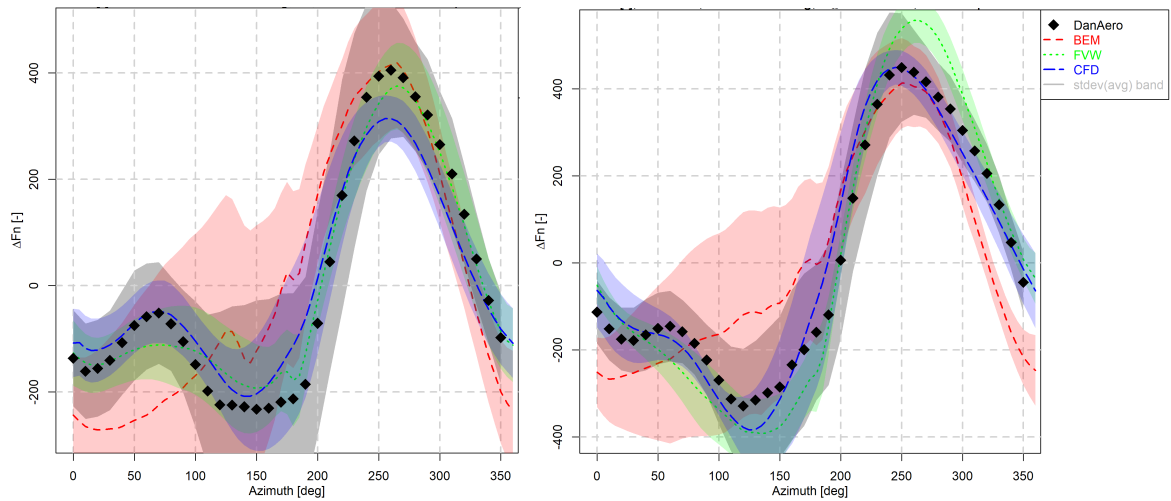
(d)  $r/R=92\%$

Figure 4.5: Tangential force  $F_t$  variation by model types, case IV.2.1



(a)  $F_n$ ,  $r/R=33\%$

(b)  $F_n$ ,  $r/R=48\%$

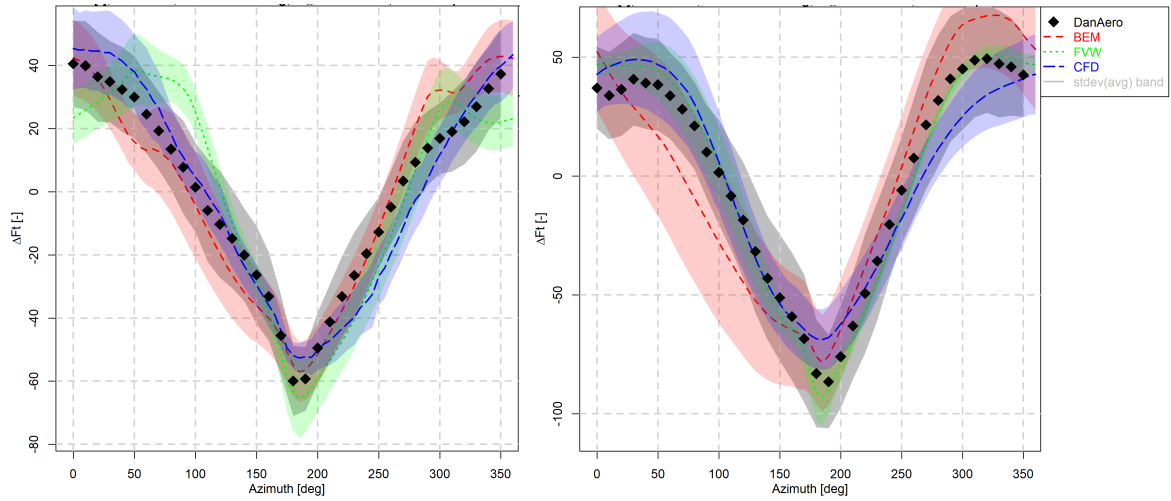


(c)  $F_n$ ,  $r/R=76\%$

(d)  $F_n$ ,  $r/R=92\%$

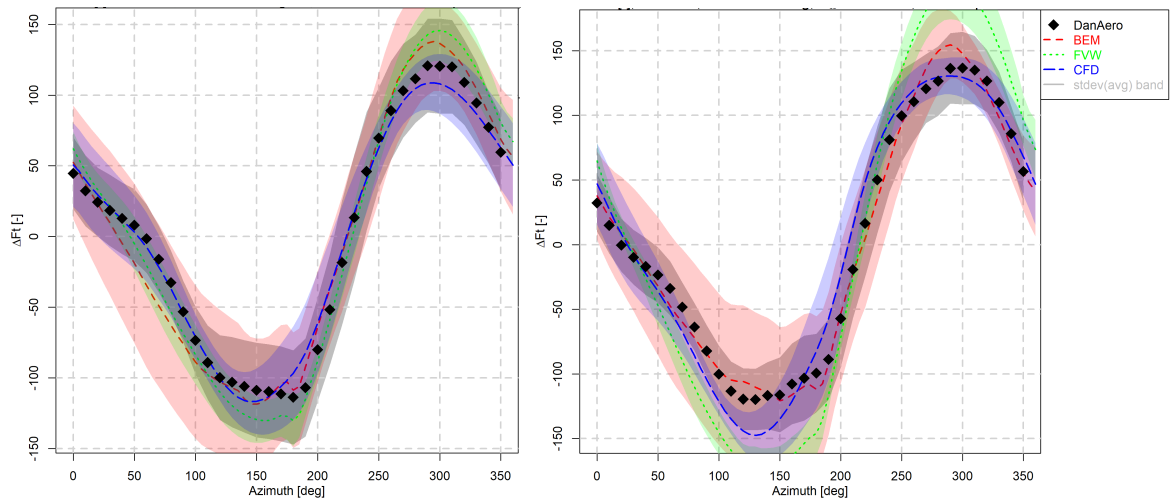
Figure 4.6: Normal force  $F_n$  variation by model types, Case IV.2.2





(a)  $r/R=33\%$

(b)  $r/R=48\%$



(c)  $r/R=76\%$

(d)  $r/R=92\%$

Figure 4.7: Tangential force  $F_t$  variation by model types, Case IV.2.2

# Chapter 5

## Task 3.1: Effects of Inflow Turbulence

G. Bangga, G. Guma, T. Lutz

### 5.1 Introduction

#### 5.1.1 Motivation and Goals

The present chapter reports the results from Task 3.1. In Task 3.1 the impact of inflow turbulence on the aerodynamic characteristics of a rotating rotor is studied at various flow conditions. In total, four reference cases are considered and the numerical results are compared with experimental data. From the assessments without inflow turbulence as described in chapter 4 for a uniform inflow, a sheared inflow and a case with combined shear and yaw, one realizes that the agreement between the engineering model codes and the experimental data deteriorates as the complexity of the case increases. It was also found that the mutual consistency between the simulation results from partners is affected strongly dependent on several important factors, with two most noticeable factors stem from the induction effect and the source of the polar data in case of engineering models (EM) like blade element momentum (BEM) or vortex lattice method (VLM) codes. This makes it difficult to draw the conclusion and to really assess the limit of each method for different cases.

Learning from the above experience, and ever since the present Task 3.1 includes an even higher complexity by introducing resolved turbulence, several aspects need to be fulfilled before the real assessment of the turbulence effects on aerodynamics can be done using various codes with varying fidelity level. To do so, the consistency between the codes has to be ensured. For CFD (computational fluid dynamics) based computations, a single source of the inflow data is defined, prepared and provided by USTUTT to all partners to promote consistent simulations. The turbulent inflow for the inflow plane of the computational domain has been provided. Then, each partner should perform empty box simulations (without rotor but including the wind shear) to ensure that the turbulence level, decay and velocity as well as turbulence intensity profiles are comparable. The frozen turbulence assumption in engineering model will not be able to reproduce the decay experienced in CFD results and in experimental data. Therefore, the timeseries of the turbulent inflow will be extracted from the empty box simulations at USTUTT at the rotor plane. Furthermore, there is a time delay between the extracted timeseries to the actual timeseries seen by the rotor due to reduced velocity effects by induction, and this is not yet considered in engineering models. The time delay is being quantified by monitoring the traveling speed of the turbulent structures with and without presence of the rotor according to [25, 26], albeit the studies were applied only to uniform (turbulent) inflow conditions. All of these preparations are carried out for the four investigated cases using various codes. As such one of the main objectives of Task 3.1 is to assess the consistency applying the above methods on the aerodynamic loads. The discrepancies will be assessed and suggestions for future improvements will be given.

## 5.1.2 Participants

The present studies are made possible due to collaborative works between 6 different institutions. The experimental results were provided by the Denmark Technical University (DTU) from the DanAero measurement campaign, see [19] and chapter 3. Two partners provide CFD results; the University of Stuttgart (USTUTT) using the FLOWer code and DTU using the EllipSys3D code. Six partners deliver engineering model computations; DTU using the HAWC2 code, IFP Energies nouvelles (IFPEN) using the AeroDeep and CASTOR codes, National Renewable Energy Laboratory (NREL) using the OpenFAST code, Office National d’Etudes et de Recherches Aeronautiques (ONERA) using the Puma code, The Netherlands Organisation for Applied Scientific Research (TNO) using the AeroModule code and USTUTT using the B-GO code. Table 5.1 lists all partners and the employed codes. More information on the codes can be found in Appendices B and C.

Table 5.1: List of contributing partners. CFD: Computational Fluid Dynamics, EM: Engineering Models, BEM: Blade Element Momentum, NW: Near Wake, VLM: Vortex Lattice Method.

Institutions	Abbreviation	Code Name / Type	
Denmark Technical University	DTU	EllipSys3D / CFD	CFD
University of Stuttgart	USTUTT	FLOWer / CFD	
Denmark Technical University	DTU	HAWC2 / BEM HAWC2 / BEM-NW	EM
IFP Energies nouvelles	IFPEN	AeroDeeP / BEM CASTOR / VLM	
National Renewable Energy Laboratory	NREL	OpenFAST / BEM OpenFAST / VLM	
Office National d’Etudes et de Recherches Aeronautiques	ONERA	Puma / VLM	
The Netherlands Organisation for Applied Scientific Research	TNO	AeroModule / BEM AeroModule / VLM	
University of Stuttgart	USTUTT	B-GO / BEM	

## 5.2 Test Matrix

### 5.2.1 Empty Box

As a first verification for the usage of different CFD solvers, empty box simulations were performed to compare the statistics and the required evaluation period. For the best consistency and to really enable further assessments of the employed codes, all CFD computations were performed utilizing the same inflow data generated in the Mann box generator PROFGEN at the IAG. The studies were carried out for four different selected cases as listed in Table 5.2. The cases contain four different wind speeds at the hub height ( $U_{hub}$ ), shear exponents ( $\alpha$ ), turbulence intensities ( $TI$ ), length scales ( $L$ ). It is noted that the cases EMPT-REF-1 and EMPT-REF-4 correspond to the cases IV.1.1 and IV.2.1 respectively from chapter 4 where the present cases include the effects of time varying wind speeds and the cases IV.1.1. and IV.2.1 are based on time averaged wind input data.

The inflow for all cases was generated for a Mann box size of 720 m in streamwise direction, represented by the generated inflow time ( $T_{Mann}$ ). To illustrate how the simulations are related to the real case including turbine (in the next comparison campaign given in Section 5.2.2), the rotational speed ( $n$ ) of the turbine is included. This is useful to better visualize how many turbine revolutions are included during the simulation period. For example, case EMPT-REF-1 that has a Mann box time of 118.032 is comparable to  $\approx 24$  rotor revolutions. In the studies, the time domain is transferred to the turbine revolution for a better and consistent comparison within the next campaign. All simulations were initialized over certain  $N_{init}$  to allow the turbulence develops before the evaluation was performed over  $N_{eval}$ . Note that if  $T_{Mann}$  is shorter than the actual total simulation time, the inflow is repeated as a cycle.

Table 5.2: Empty box cases for the first verification studies.

CASE Name	$U_{hub}$ [m/s]	$\alpha$ [-]	$TI$ [%]	$L$ [m]	$T_{Mann}$ [s]	$n$ [RPM]	$N_{init}$ [-]	$T_{init}$ [s]	$N_{eval}$ [-]
EMPT-REF-1	6.1	0.025	6.80	32.026	118.032	12.3	20	97.561	25
EMPT-REF-2	6.35	0.04	6.46	32.026	113.385	16.2	30	111.111	25
EMPT-REF-3	10.5	0.33	3.00	32.026	68.571	16.2	20	74.074	25
EMPT-REF-4	9.792	0.249	3.66	32.026	73.529	16.2	20	74.074	25

The generated turbulence field was injected at  $X = -320$  m using a momentum source term [27],

$$f_{Ei} = \frac{\rho u'_i}{\Delta x_n} \left( U_n + \frac{1}{2} u'_n \right)$$

with the subscript 'n' represents the normal component to the turbulence plane.

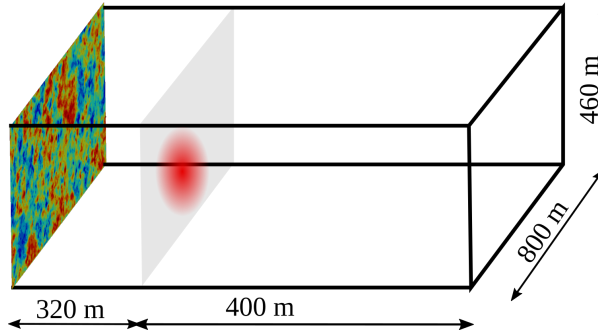


Figure 5.1: The Mann box domain size for the inflow generation. Note that the size of the actual computation domain is larger than the Mann box size. The turbulent flow signals generated by the Mann box will be imposed at  $-320$  m ( $\approx 8R$ ) upstream of the rotor.

The size of the Mann box to generate the turbulent flow signals in the cross flow directions ( $Y, Z$ ) are  $[800 \times 460] \text{ m}^2$  with the Mann-box grid spacing of 4 m. The size in flow direction ( $X$ ) determines the length of the wind file  $t = (N_u - 1) * \Delta_u / u_\infty$ . For all simulated cases, this is set to be  $\approx 18R = 720$  m as illustrated in Figure 5.1. The IEC61400-1 [28] provides reference values for the turbulence according to the wind turbine class. In this study the wind turbine class 1A was assumed. To match atmospheric conditions as required in IEC61400-1 a non-isotropic turbulence is created. Therefore, the stretching factor was chosen to be  $\Gamma = 3.9$  as recommended in [22] to approximate the Kaimal spectral model. The use of the rapid distortion theory ( $\Gamma > 0$ ) causes the vortex structures to become more elliptical, which alters the turbulence intensity. Therefore, a turbulence scaling factor  $SF_{Mann}$  is introduced. This turbulence scaling factor is the ratio of the target turbulence intensity to the actual  $TI$  level of the longitudinal turbulence in the Mann box as:  $SF_{Mann} = \sqrt{\sigma_{target}^2 / \sigma^2}$ , with  $\sigma_{target}^2$  specifies the target turbulence variance. Moreover, before using the turbulence field the axial velocity component is shifted by  $\Delta u$  to have zero mean velocity fluctuation in axial direction ( $u'_{mean} = 0$ ).

## 5.2.2 Rotor Simulations

As the second verification for the usage of different CFD and engineering model (EM) solvers, rotor simulations were performed. The studies were carried out for four different inflow cases, as listed in Table 5.2. The cases contain four different wind speeds at the hub height ( $U_{hub}$ ), shear exponents ( $\alpha$ ), turbulence intensities ( $TI$ ), length scales ( $L$ ). Detailed information about the flow conditions of the rotor simulations is listed in Table 5.3.

Table 5.3: Rotor cases for the first verification studies.

CASE Name	$U_{hub}$ [m/s]	$n$ [RPM]	Pitch [°]	Yaw [°]	Turbine Config [-]	$N_{init}$ [-]	$N_{eval}$ [-]
ROT-REF-1	6.1	12.3	0.15	-0.6	Pure rotor	20	25
ROT-REF-2	6.35	16.2	-4.75	-8.2	Pure rotor	30	25
ROT-REF-3	10.5	16.2	-4.75	-1.3	Pure rotor	20	25
ROT-REF-4	9.792	16.2	-4.75	-6.02	Pure rotor	20	25

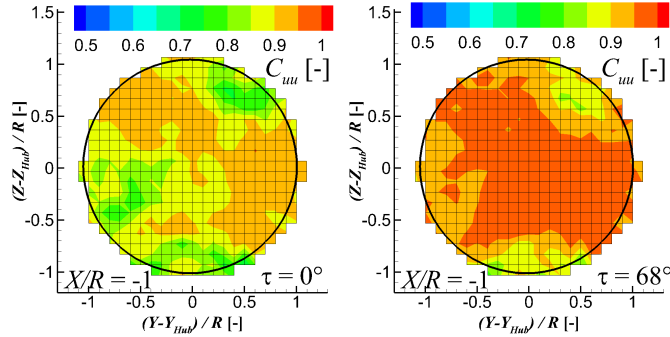


Figure 5.2: Time shift required for engineering model simulations (left) and the cross-correlation value of  $u$ -component without the time shift (middle) and by applying a time shift of  $68^\circ$  (right).

## CFD Solvers

For CFD solvers, the same inflow specifications as for the the empty box simulations were adopted, as listed in Table 5.2. The same approach was applied by imposing the turbulence fluctuations in the field at an upstream distance of -320 m from the rotor plane. The simulation strategy remains the same as for the empty box cases. All simulations were initialized over certain  $N_{init}$  to allow the turbulence develops before the evaluation was performed over  $N_{eval}$ . Note that if  $T_{Mann}$  is shorter than the actual total simulation time, the inflow is repeated as a cycle.

## Engineering Model Solvers

For engineering model solvers, a bit different approach was adopted. Turbulence is frozen in engineering models, therefore the turbulence decay over streamwise direction will not be accommodated directly. In this sense, it is reasonable to use the flow field from the CFD simulations of the empty box cases as the input data for these solvers. Despite that, as induction plays a role, the velocity reduces approaching the rotor. This causes turbulence to propagate at a slower rate but the turbulent structures are not significantly changed [25]. This aspect is not covered in the empty box simulations. As a way out of this dilemma, an approach was established at IAG by quantifying the required time shift by means of a cross-correlation of the flow field [25]. The cross-correlation level at  $X/R = -1$  for case ROT-REF-1 and the required time shift for every position upstream of the rotor for all cases are presented in Figures 5.2 and 5.3, respectively. To check the accuracy of the calculated time shift, the streamwise velocity over the time at  $Z = 57$  m (hub height 57.19 m) with and without applying the time shift is presented in Figure 5.4. One can observe that the streamwise velocity obtained from the empty box simulation (Empty) by applying the quantified time shift is better aligned with the extracted velocity from the simulation employing a rotating turbine (Rotor). In this sense, the required time shift exactly at the rotor plane can be estimated by extrapolating the data in Figure 5.2 using an exponential fit. All simulations were initialized over certain  $N_{init}$  to allow the turbulence develops before the evaluation is performed over  $N_{eval}$ . The length of the extracted data is exactly  $N_{init} + N_{eval} + \text{timeshift}$ . Therefore, there was no need to perform "data loop" in contrast with the CFD users.

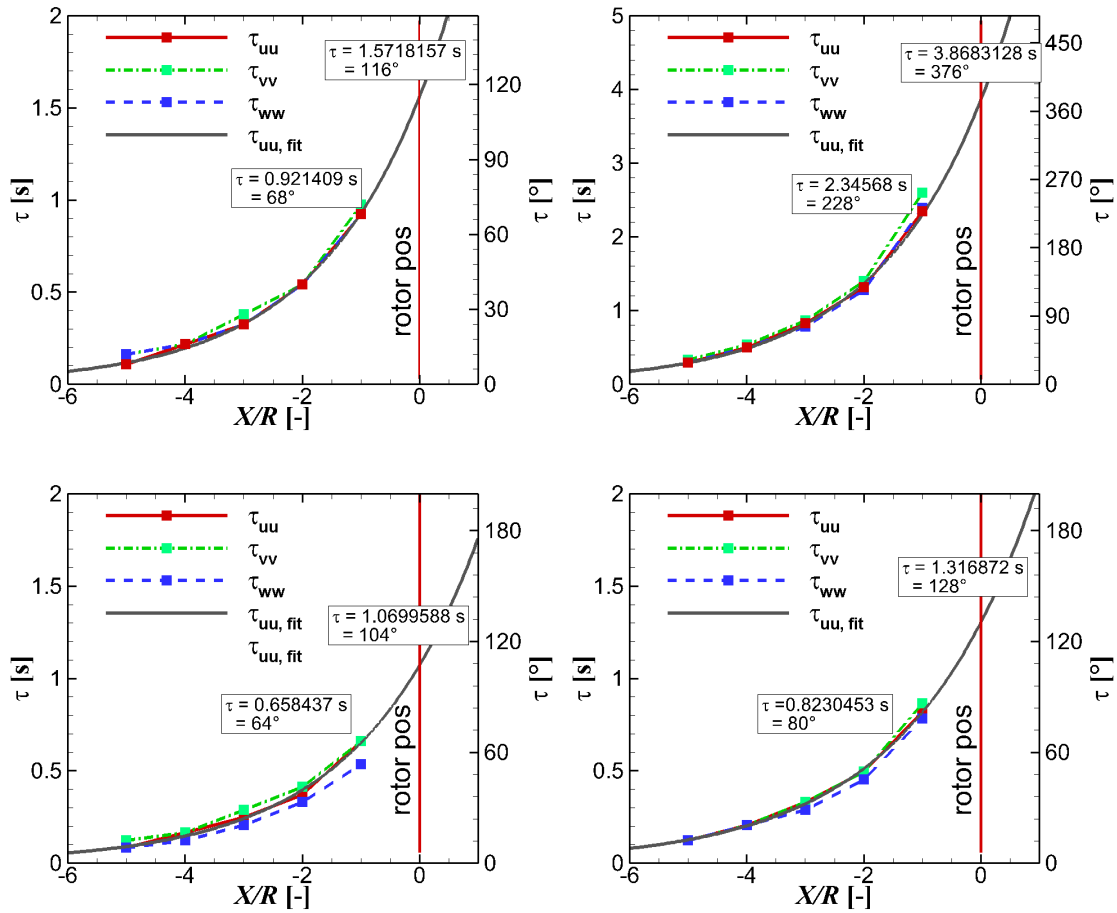


Figure 5.3: Time shift required for engineering model simulations for four reference cases. Subsequently from left to right: ROT-REF-1, ROT-REF-2, ROT-REF-3 and ROT-REF-4.

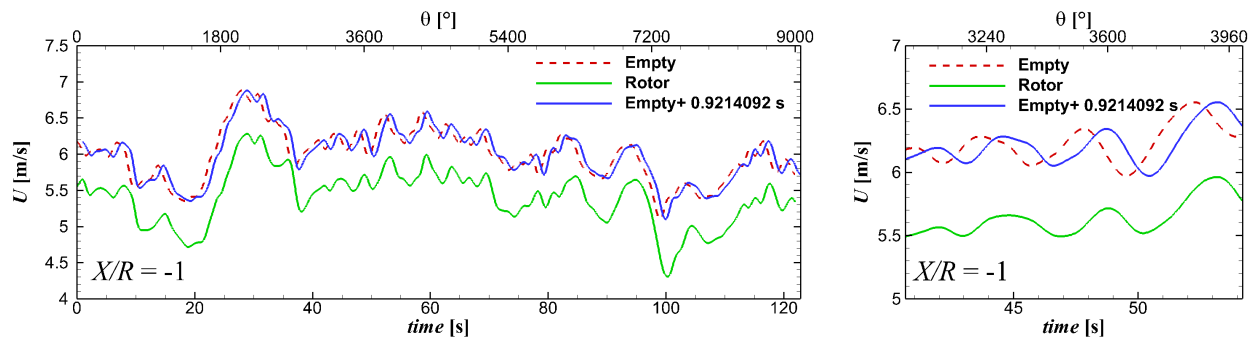


Figure 5.4: Streamwise velocity component over the time at  $Z = 57$  m and  $X/R = -1$  with and without adopting the time shift in comparison with the extracted velocity from the simulation employing a rotating turbine.

Furthermore, to encourage best consistency between engineering models and CFD, the polar data extracted from 3D CFD computations employing the azimuthal averaging method [24] were used. Note that the polar data contains already the tip loss effect. In that sense, the polar data from  $r/R > 0.9$  was replaced by the 2D measured polar data as recommended in [29]. This polar data is denoted as the "Hybrid 2D/3D Polar". Table 5.4 lists the main setup of the employed engineering models.

Table 5.4: General setup applied in the engineering model computations.

Institutions	Code	Polar	Turbulent Wake	Dynamic Stall	Yaw	Tip Loss
DTU	HAWC2	3D-P	DTU AD	BL modified	DTU AD	None
DTU	HAWC2-NW	Hybrid	DTU AD	BL modified	DTU AD	NW
IFPEN	AeroDeep-BEM	Hybrid	Ning	None	Blondel	Prandtl
IFPEN	CASTOR-VLM	Hybrid	None	None	None	None
NREL	OpenFAST-BEM	Hybrid	Glauert-Buhl	Minemma	Pitt-Peters	Prandtl
NREL	OpenFAST-VLM	Hybrid	None	None	None	None
ONERA	Puma	2D-PC	None	None	None	None
TNO	AeroModule-BEM	Hybrid	Wilson	BL	Schepers	Prandtl
TNO	AeroModule-VLM	Hybrid	None	Snel	None	None
USTUTT	B-GO	Hybrid	Spera	IAG-DS	IAG-Yaw	Prandtl

3D-P: 3D CFD polar data from USTUTT CFD

2D-PC: 2D measured polar data with 3D empirical correction

Hybrid: combined 3D CFD polar data from USTUTT CFD with 2D measured polar near the tip (from  $r/R > 0.9$ )

DTU AD: DTU Actuator Disc [30]

Glauert-Buhl: Glauert-Buhl turbulent wake state model [31]

Ning: Ning turbulent wake state model [32]

Spera: Spera turbulent wake state model [33]

BL modified: modified Beddoes Leishman model [34]

IAG-DS: IAG dynamic stall model [35]

Minemma: Minemma dynamic stall model [31]

Blondel: Blondel yaw model [36]

IAG-Yaw: IAG yaw model [37]

Pitt-Peters: Pitt-Peters yaw model [31]

Wilson: Wilson linear turbulent wake state model [38]

Snel: Snel first order dynamic stall model [39]

Schepers: Schepers yaw model [40]

NW: near wake model [34]

Prandtl: Prandtl tip loss model [41]

### 5.2.3 General Flow Conditions

The blade geometry of the DanAero wind turbine is used. The radius of the blade is 40m and since only the rotor is simulated without nacelle and tower, the three blades are simply connected in the root region. Note that a tilt angle of  $5^\circ$  is considered according to the turbine description in the experimental campaign. All structures are treated as rigid in all cases. The freestream air properties are density  $\rho = 1.22 \text{ kgm}^{-3}$ , temperature  $T = 288.15 \text{ K}$  and dynamic viscosity  $\mu = 1.8375 \times 10^{-5} \text{ kgm}^{-1}\text{s}^{-1}$ . Table 5.5 shows some basic parameters about the turbine and numerical setup.

Table 5.5: Basic properties of the simulations and turbine specification.

$N_{blade}$ [-]	$Z_{hub}$ [m]	Tilt [ $^\circ$ ]	$\rho$ [ $\text{kgm}^{-3}$ ]	$T$ [K]	$\mu$ [ $\text{kgm}^{-1}\text{s}^{-1}$ ]	Tower and Nacelle [-]
3	57.19	5	1.22	288.15	$1.8375 \cdot 10^{-5}$	No

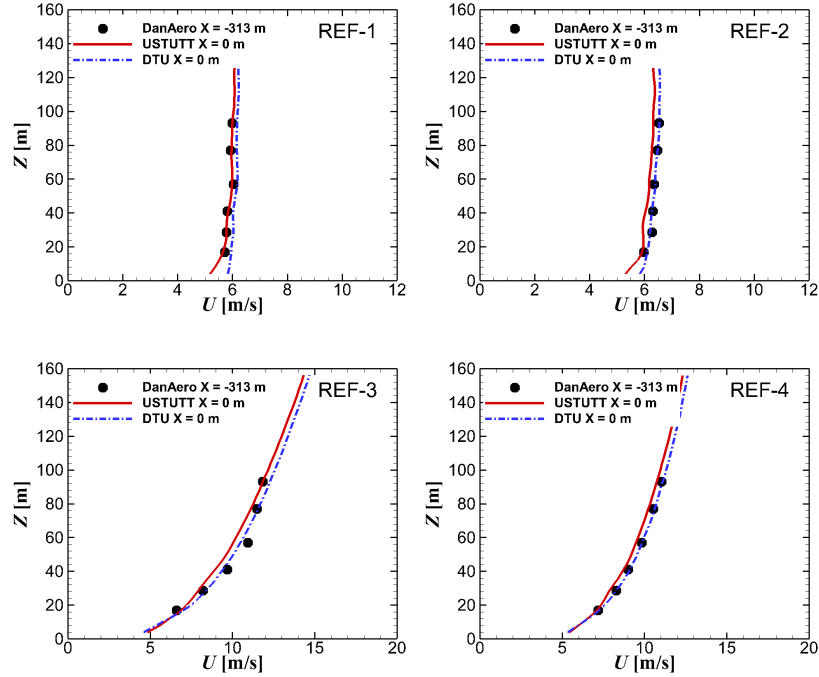


Figure 5.5: Velocity distributions at the designated rotor plane in comparison with the measured data upstream of the rotor location.

## 5.3 Results and Discussion

### 5.3.1 Empty Box Case

The results in terms of the velocity and turbulence intensity profiles at the designated rotor plane ( $X = 0$  m) calculated using CFD solvers are presented in Figures 5.5 and 5.6. Additionally, the turbulence intensity variation at hub height over the streamwise direction is presented in Figure 5.7. The values obtained at the met-mast during the DanAero measurement are displayed for comparison. The measurement was located at -313 m upstream of the rotor position. It can be seen clearly that the simulations are able to represent the measurement characteristics fairly well. The smaller turbulence intensity levels at the rotor plane for cases EMPT-REF-1 and EMPT-REF-2 are associated with the turbulence dissipation effect, both physically and numerically. In contrast, turbulence levels increase along  $X$  for cases EMPT-REF-3 and EMPT-REF-4, which can be attributed to wind shear influences.

One can see that the agreement between DTU and USTUTT results are good for most comparison plots. Some discrepancies are observed especially concerning the turbulence intensity level near the wall region for EMPT-REF-1 and EMPT-REF-2. The reason lies on the difference of the applied boundary condition on the wall of the computational domain. Note that for USTUTT a no-slip wall condition was applied while for DTU a slip condition was used. As a consequence, boundary layer development along  $X$  near the wall can be different. Despite that, as the level of shear exponent is increased to 0.33 and 0.249 for EMPT-REF-3 and EMPT-REF-4, respectively, the choice of the wall condition plays only a minor role because the boundary layer is strongly dictated by the imposed shear level itself.

### 5.3.2 Rotor Case

#### CFD Results

In the present section, the results with regards to the averaged azimuthal load variations for four different cases are presented. The corresponding measurement data from the DanAero experiment is included for



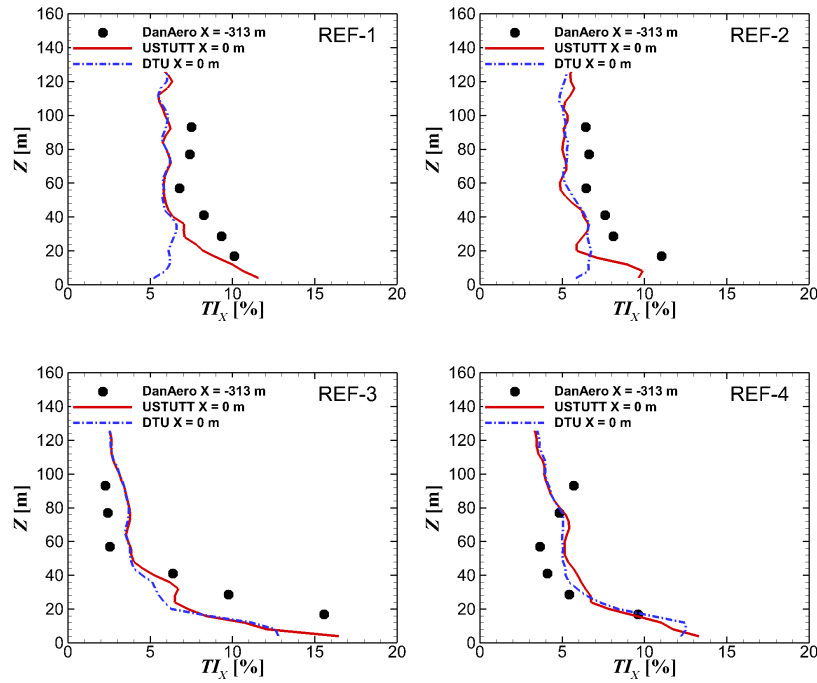


Figure 5.6: Turbulence intensity distributions at the designated rotor plane in comparison with the measured data upstream of the rotor location.

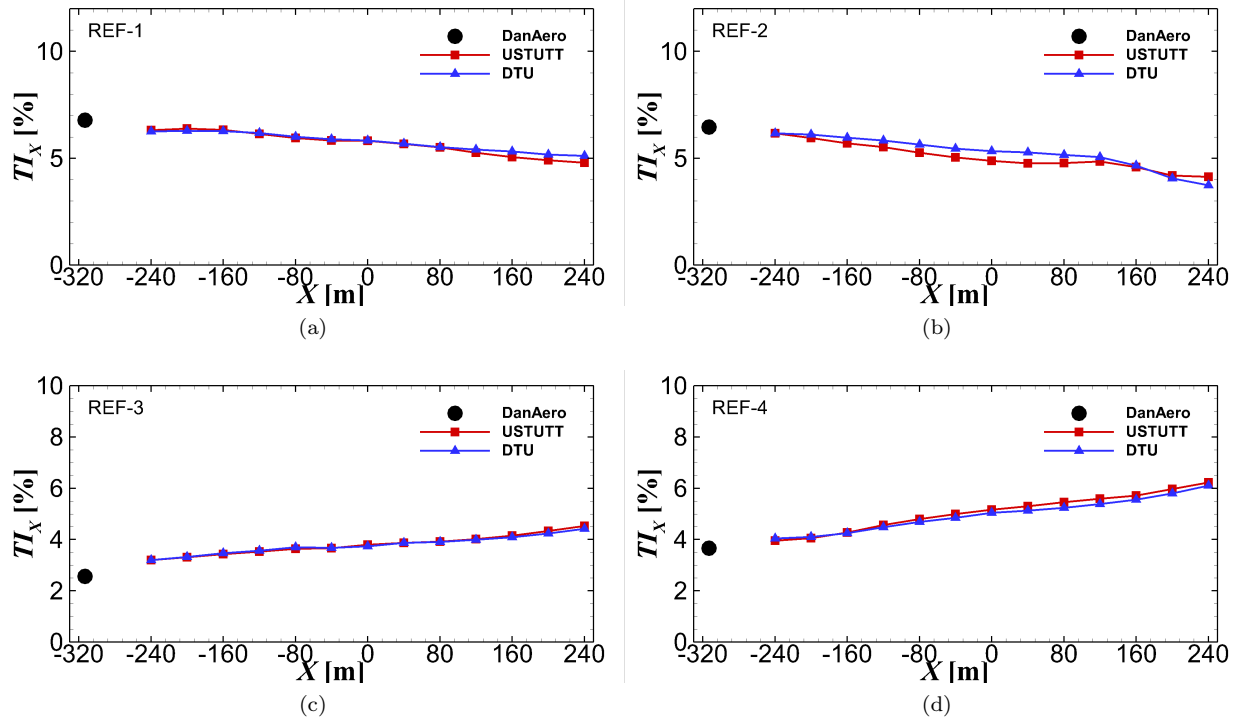


Figure 5.7: Turbulence intensity development along the streamwise direction.

comparison. Figures 5.8- present the normal loads (relative to chord) obtained from CFD computations delivered by USTUTT and DTU. The same inflow data and comparable numerical strategy as for the empty box cases in Section 5.3.1 were adopted. The evaluations were done by integrating the pressure distribution on the corresponding blade sections, both in CFD and experiment.

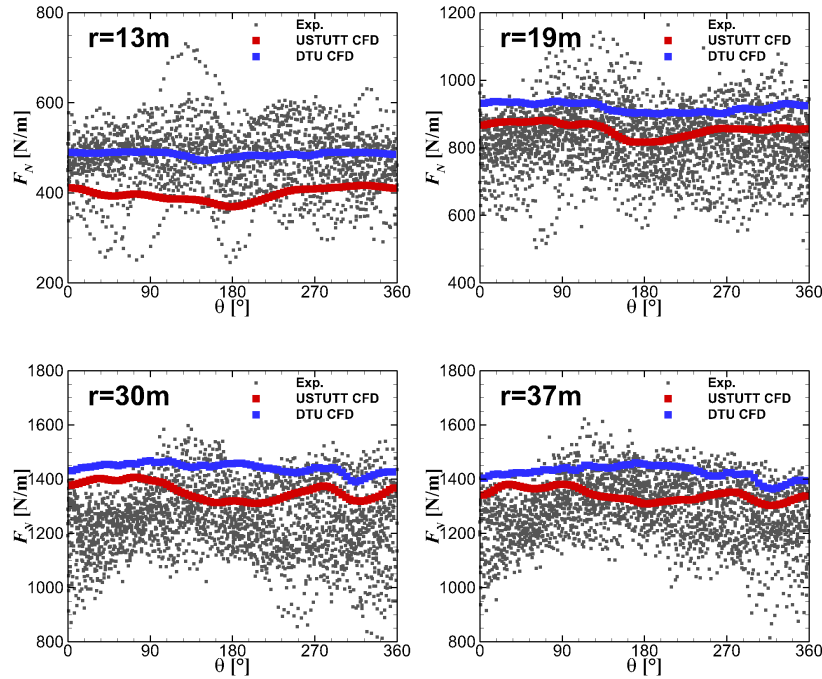


Figure 5.8: Azimuthal loads comparison between the CFD results against measurement data for ROT-REF-1.

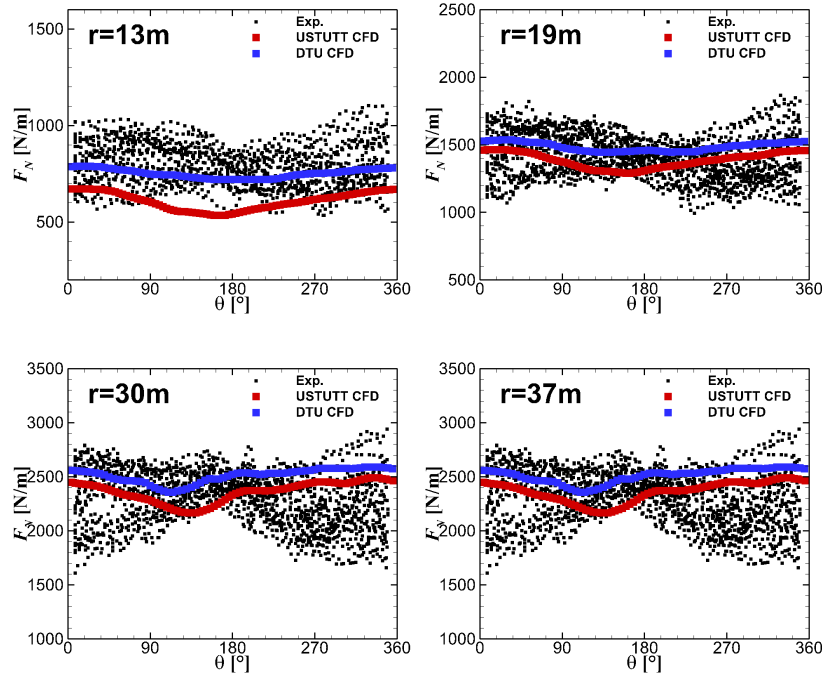


Figure 5.9: Azimuthal loads comparison between the CFD results against measurement data for ROT-REF-2.

For the first test case in Figure 5.8, both CFD results are in a good agreement with the experimental data. In the inboard region at  $r = 13$  m, USTUTT results seem to be a bit lower than the experimental data.

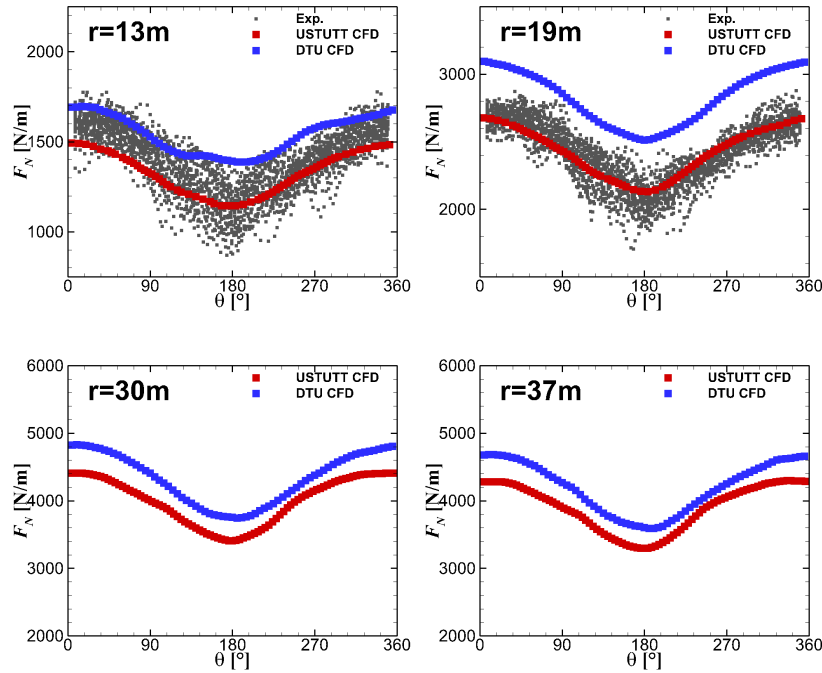


Figure 5.10: Azimuthal loads comparison between the CFD results against measurement data for ROT-REF-3.

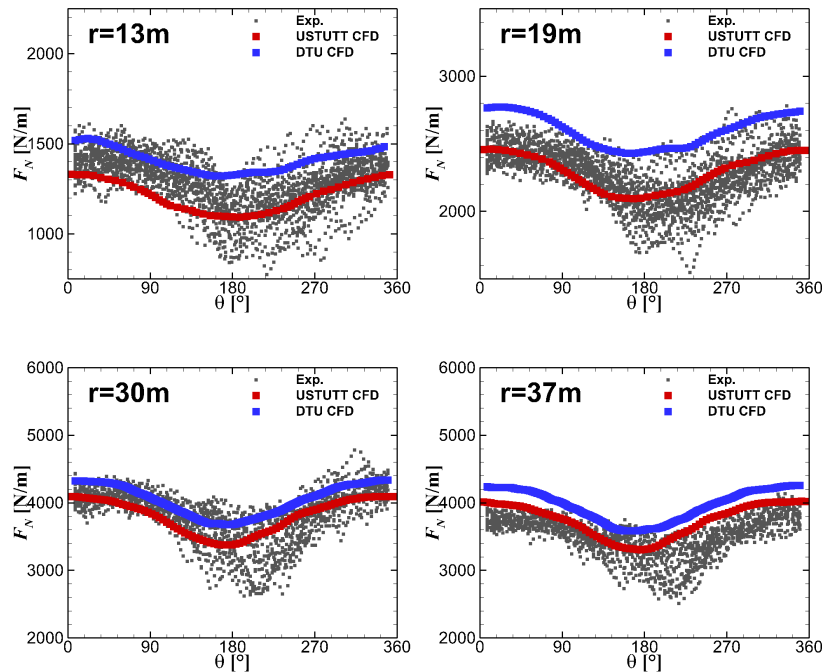


Figure 5.11: Azimuthal loads comparison between the CFD results against measurement data for ROT-REF-4.

On the other hand, DTU results at  $r = 30$  m is a bit higher than experiment. The difference in the applied wall boundary condition may contribute to the discrepancy. It should be noted as well that both CFD codes have different mesh requirements and numerical setup, which further contribute to increased uncertainty.

For the second case in Figure 5.9, a similar characteristic as in the first case in the inboard area is also observed. For the two outermost stations at  $r = 30$  m and 37 m, one can see that the trend of measured forces are not captured by both CFD codes. This is caused by the partial wake inflow effects during the measurement campaign.

For the third and fourth cases presented in Figures 5.10 and 5.11, the flow field is strongly dictated by the wind shear. Unfortunately, the sensors at  $r = 30$  m and 37 m for ROT-REF-3 were broken during the measurement campaign. Thus, comparison with experimental data is not possible to be done. In general, both USTUTT and DTU results for these two sheared cases are very similar and are in a good agreement with the measurement data. Some discrepancies are observed at  $r = 17$  m, where DTU results overshoot the USTUTT and experimental data. The reason might be attributed to the difference in the numerical setup and mesh resolution.

### Engineering Model Results

In this section, the results obtained from the engineering model computations will be compared with experimental data for four different test cases. Since there are several codes involved in this comparison round, the legends of the figures are plotted separately in Figure 5.12 for clarity.

In Figure 5.13, the comparison results for the first test case are presented. It can be seen that all engineering model results are in a good agreement with the experimental data. Despite that, the load predictions especially at  $r = 13$  m from ONERA are higher than the other codes. This occurs because the code used the 2D measured polar data with 3D empirical correction, in contrast with the other codes which employed the hybrid 3D/2D polar.

The second case presented in Figure 5.14 has a very similar flow condition as the first test case, but it includes yaw and a higher rotational speed, which further increase the induction factor. Furthermore, it was reported that this case contains partially wake inflow from the neighbouring turbines, which could potentially alter the experimental data. Despite the huge challenge experienced for this particular case, in general the results provided by all codes are in an acceptable agreement with the experimental data although the trend of the measured forces at the outboard regions are not captured. This can be attributed to the effects of aforementioned partial wake inflow. Note that CFD predictions in Figure 5.9 could not capture this effect as well.

The third case is dominated by shear and the results are presented in Figure 5.15. The agreement of all codes employing the hybrid 3D/2D polar are very good. One can see that the 2D corrected polar data

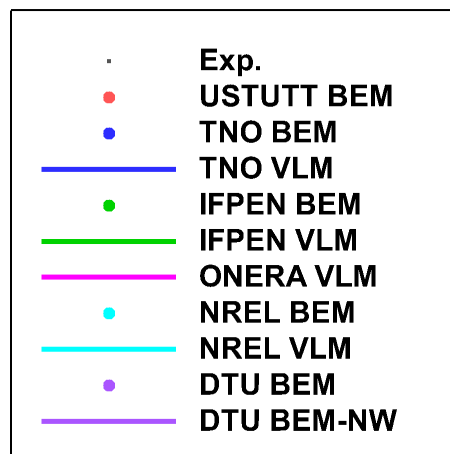


Figure 5.12: Legends used for Figures 5.13-5.16.

employed by ONERA is not able to reproduce the trend of the curve especially at  $r = 17$  m and 30 m. A similar observation can be seen for the fourth case in Figure 5.16. This raises further awareness that 3D rotational effects in the root area are important for correct modeling of the forces [42]. By considering the effects using 3D extracted CFD data, engineering model results can be improved as shown in the present report.

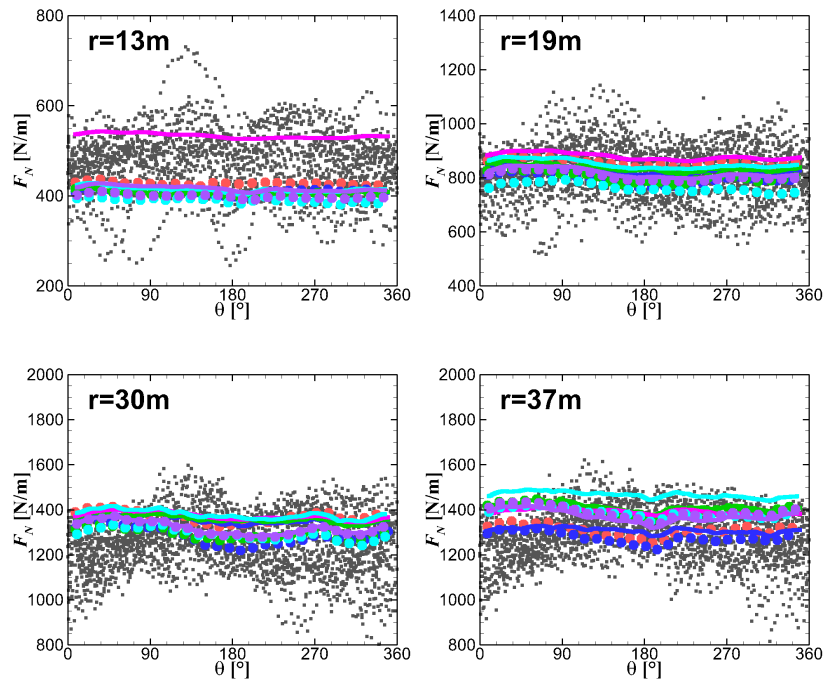


Figure 5.13: Azimuthal loads comparison between the engineering model results against measurement data for ROT-REF-1.

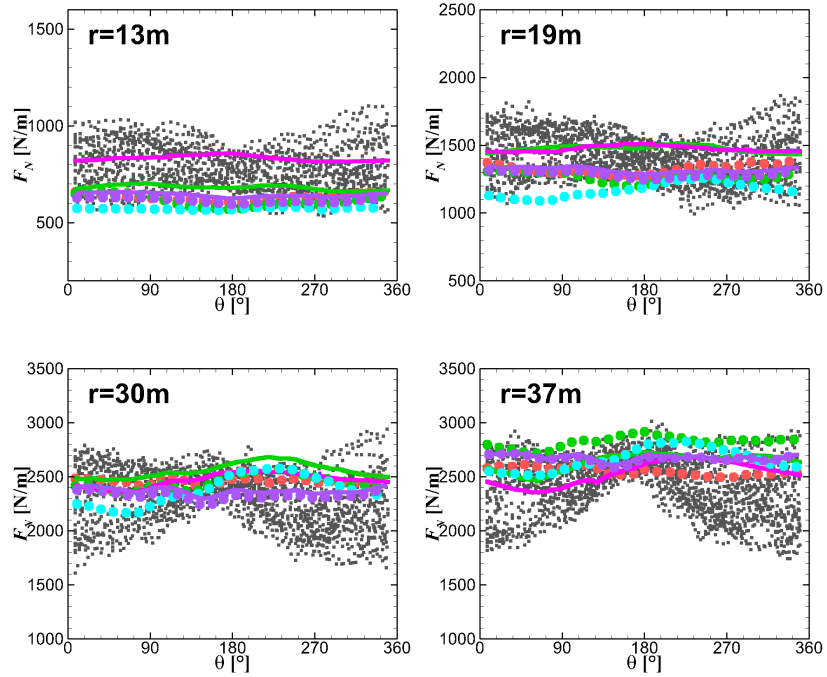


Figure 5.14: Azimuthal loads comparison between the engineering model results against measurement data for ROT-REF-2.

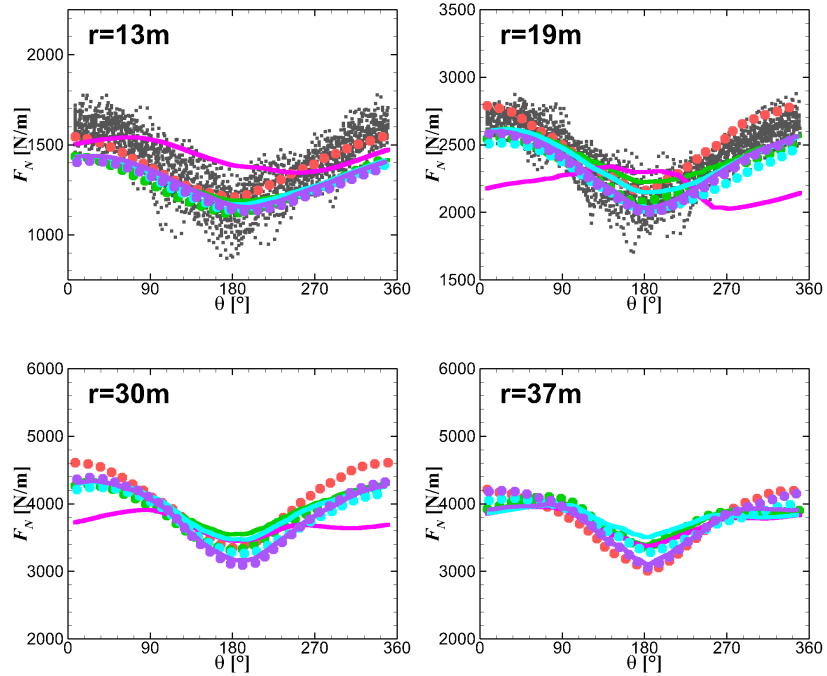


Figure 5.15: Azimuthal loads comparison between the engineering model results against measurement data for ROT-REF-3.

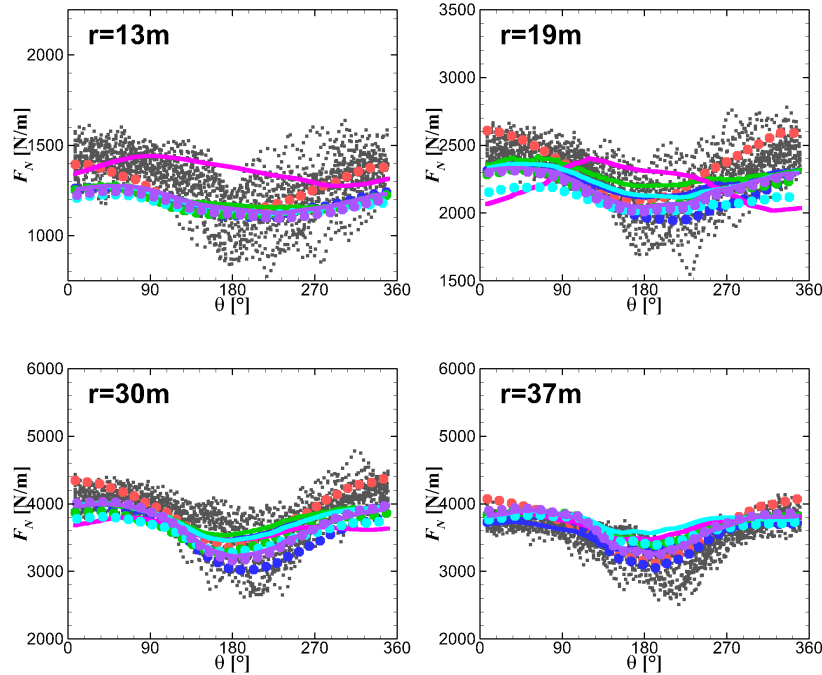


Figure 5.16: Azimuthal loads comparison between the engineering model results against measurement data for ROT-REF-4.

## 5.4 Concluding Remarks on Task 3.1: Effects of Inflow Turbulence

Comprehensive investigations on the aerodynamic responses to turbulent inflow under various flow conditions have been conducted. In total four different test cases were considered. The studies were performed by 6 different institutions, involving 2 CFD codes, 6 BEM codes and 4 VLM codes. To promote consistent simulations, the studies were performed by employing the same inflow data. For CFD solvers, the data was obtained from the Mann turbulence box generator at USTUTT. For engineering model solvers, a slightly different approach was adopted. The data was obtained from the empty box simulations carried out at USTUTT. For this purpose, the timeseries of the velocity field at the designated turbine location was extracted from the aforementioned empty box simulations. To further increase the consistency, the time delay experienced by the turbulent flow approaching the rotor was quantified and applied in the extracted flow data.

From the comparison round, the results demonstrate that both CFD codes predict comparable decay of the turbulence intensity along the streamwise direction. Some discrepancies are observed near the wall due to the difference on the applied boundary condition. However, when the degree of the wind shear increases, the impact of the boundary condition on the ground of computational domain is minor because the boundary layer is strongly dictated by the imposed shear level itself. Similarly, both CFD codes are able to predict the aerodynamic loads accurately in comparison with the measurement data. Some deviations are observed which might be attributed to the variations in mesh resolution and employed numerical approaches.

In contrast with the previous assessment in WP 2 (Shear and Yaw), not only the employed engineering models provide consistent agreement in the present Task 3.1, but they also predict the measured forces accurately. This is in contrast with the results obtained for WP 2 where the trend and the magnitude of the forces predicted by engineering models vary significantly. It has been demonstrated in the present report that the use of consistent inflow conditions and hybrid 3D/2D polar data is beneficial for improving the prediction quality of engineering model under turbulent inflow conditions.

For future research orientation, several aspects can be recommended. The studies can be extended by further assessment of the load statistics, loads alignment and wakes. Deeper analyses on the influence of

inflow turbulence can be done by artificially increasing the turbulence intensity for a specific test case. At last but not least, the underlying research activities might be used for further improving the reliability of engineering models and ultimately for an improved wind turbine design framework.



# Chapter 6

## Task 3.2: Yawed inflow

J.G. Schepers

The main aim of Task 3.2 is to model and understand yawed inflow of wind turbines. Most of the activities on this field took place in the evaluation of the comparison round IV.2.2, see chapter 4 where calculations from a large number of codes are compared with DanAero measurements at a yaw error of almost 40 degrees. From this evaluation it was concluded that such large yaw error is extremely difficult to model in particular by engineering models. The results from higher fidelity codes like CFD and FVW are generally closer to the measured results. The larger differences between measurements and calculations from engineering methods are mainly attributed to the challenges in modelling the azimuthal variation of the induced velocity. This variation in induced velocity is a consequence of the skewed wake geometry due to the yawed inflow.

Some further effort on the field of yaw engineering modelling was carried out by the Dutch Task 29 participants TNO, CWI, DNV-GL and Suzlon within the project WindTrue funded by the Topsector Energy Subsidy from the Dutch Ministry of Economic Affairs and Climate. The aim of this project was to build robust aero-elastic wind turbine models with a quantified level of uncertainty. Thereto model parameters and their probability distribution are calibrated with measurements.

Amongst others a calibration took place of the parameters in the model for the azimuthal variation of the induced velocity which is described in [1]. This model has been developed in 1998 and at that time it could be calibrated with a limited amount of wind tunnel measurements only. The lack of data with which the calibration was performed gives the underlying model parameters an unknown uncertainty. In order to determine these uncertainties a framework has been developed based on the uncertainty quantification toolbox UQLab [43] which was integrated with the TNO code AeroModule [44] in which the yaw model from [1] is implemented. In order to limit the number of parameters which need to be calibrated a sensitivity study was carried out to find the parameters which effect the model output most. This sensitivity study was based on the Sobol expansion approach, which decomposes the total variance of the quantity of interest (i.e. the model output) into contributions from individual parameters and their combinations.

Then a so-called Bayesian model calibration is performed for the most sensitive parameters. In Bayesian model calibration, a priori knowledge about the distribution of the selected parameters (e.g. physical bounds, previous calibrations) is used together with (measured) data to calibrate these parameters. However, Bayesian model calibration based on full non-linear aeroelastic models like AeroModule is computationally very time consuming, requiring thousands of model evaluations. For this reason, the AeroModule was replaced by a so-called ‘surrogate model’. The surrogate model is constructed by employing a limited number of smartly chosen conditions (‘nodes’), at which the aeroelastic simulations are performed.

The first calibration was carried out with DanAero measurements at yawed conditions, in particular the case which is reported in chapter 4. It turned out that more data points are needed than available in the DanAero database to determine the level of uncertainty in the model parameters. It was then considered to do the calibration with measurements from the so-called EWTW (ECN Wind Turbine Test Site Wieringermeer) database. This database contains measurements which are collected over a period of more than 7 years [45].

However, measurements were available of integrated blade and turbine loads only. These data hide the radial load distribution which made it difficult to calibrate the radial dependency of the yaw model parameters where this radial dependency is an essential characteristic of these models. A strong radial dependency of yawing phenomena is confirmed in the comparison round 2.2. which was discussed in chapter 4. There figure 4.6 showed the maximum in normal force at the outer part of the blade near an azimuth angle of 270 degrees where the maximum normal force at the inner part is near an azimuth angle of 90 degrees. The importance of this radial dependency made the EWTW measurements, even though they are taken over a long period not suitable for a calibration of yaw model parameters.

Eventually the calibration was carried out with data from the New Mexico wind tunnel experiment from Mexnext-III , see [46]. The amount of yawed measurements in this database was sufficient for a statistical reliable calibration but an obvious drawback is that these measurements are taken in a wind tunnel environment which differs from the full scale field environment. The results of the calibration are reported in [47].

It is noted that there is another challenge in modelling the wind turbine response at yaw. This second challenge is related to the fact that yaw goes together with angle of attack variations. This leads to dynamic stall which is a difficult phenomenon to model. Dynamic stall was also considered in WindTrue through a sensitivity study of parameters in the Beddoes-Leishman dynamic stall model [48]. The normal force at the outboard locations was found to be most sensitive to the time constant connected to vortex shedding, followed by the time constant connected to the airfoil leading-edge separation effect, see [49] and [50]

In summary the WindTrue project has led to an uncertainty assessment framework which is a great asset for future yaw model (and other model) calibration. At the same it was found that much more high quality measurements of local sectional loads on MW scale in the field are needed in order to determine the uncertainty of model parameters for MW scale turbines in atmospheric conditions.

# Chapter 7

## Task 3.3: Wake effects

S. Ivanell, H. Asmuth

### 7.1 Introduction

Wake flows have been investigated for many years with ambition to better understand the flow features in the turbine wake to estimate production losses and increased loads of downstream turbines. The task 3.3 was initialized to further study cases with an inflow of an upstream turbine. Within the task, unique possibilities exist to study the wake inflow, i.e., the flow of an upstream turbine and corresponding wake, due to the DanAero experiment database. The international expertise within the annex consortium has therefore gathered knowledge and model capacities to further investigate wake inflow situations. The task was led by University of Uppsala with contributions from various partners as described in the sequel.

#### 7.1.1 Motivation and Goals

The challenge of modeling the flow of a wake itself is very challenging. If one further on consider the interaction of two turbines, this is challenging today's state-of-the-art modeling capacity.

Farm modeling have been performed with excellent accuracy of the production of individual turbines [51], however, that is still challenging considering atmospheric conditions etc. The DanAero case do, however, provide unique set of data, since it does not only contain wind measurements and production data, but also extensive load and flow measurement of the downstream turbine.

Task 3.3 have fully concentrated on a benchmark on specific wake inflow cases of the DanAero experiment. The ambition was to compare different numerical approaches to assess how well today's state-of-the-art modeling possess capabilities to reproduce the flow of interaction turbines.

### 7.2 Participants and Models

In total six different numerical models of three different institutions participated in the benchmark including large-eddy simulations (LES), steady-state Reynolds-averaged Navier-Stokes (RANS) as well as dynamic wake meandering (DWM) models. A summary of the participating models is given in Tab 7.1. The three LES codes employed actuator line models (ALM) to represent the turbine. The RANS model utilized an actuator disk model (ADM).

For the main comparison all participants utilised a pre-generated synthetic inflow velocity field that was imposed at the inlet, see Section 7.3. An additional case using a precursor-generated inflow was submitted by the UU group (UU LES pc).

Table 7.1: Participants and methods.

Participant	Code	Method	Abbreviation
Uppsala University	elbe [52]	LBM-LES	UU LBM
		Steady-state RANS	UU RANS
	OpenFOAM	LES	UU LES
		LES-Precursor	UU LES pc
DTU	EllipSys3D	LES	DTU LES
	DWM code	DWM	DTU DWM
NREL	DWM code	DWM	NREL DWM

### 7.3 Case description

From the available measurements of the DanAero project two 10 minute bins were selected that entailed a full or partially waked inflow for the equipped wind turbine (WT2), with the wake being induced by WT1. The corresponding wind direction of about  $257^\circ$  implies mostly undisturbed measurements at the met mast, see Fig. 7.1. Apart from the wind direction, measurements were filtered for near-neutral atmospheric conditions as well as reasonably constant wind speeds throughout the bin. The selected case A refers to a period of normal operation, i.e. both turbines were operated using their default controller settings. In case B WT2 was operated at constant rotational speed as part of the DanAero experiments. Still, both turbines in the two cases were simulated with constant rotational speed, in order to reduce the amount of differences between the models. A summary of the two cases is given in Tab. 7.2.

Table 7.2: Cases description

Case	A	B
$\Omega_1$ [rpm]	16.11	15.50
$\Omega_2$ [rpm]	14.13	16.23
$Pitch_1$ [ $^\circ$ ]	0.00	0.00
$Pitch_2$ [ $^\circ$ ]	0.15	0.75
$U_H$ [m/s]	8.36	7.13
$D_H$ [ $^\circ$ ]	5.81	0.64
$TI_H$ [%]	6.98	12.10

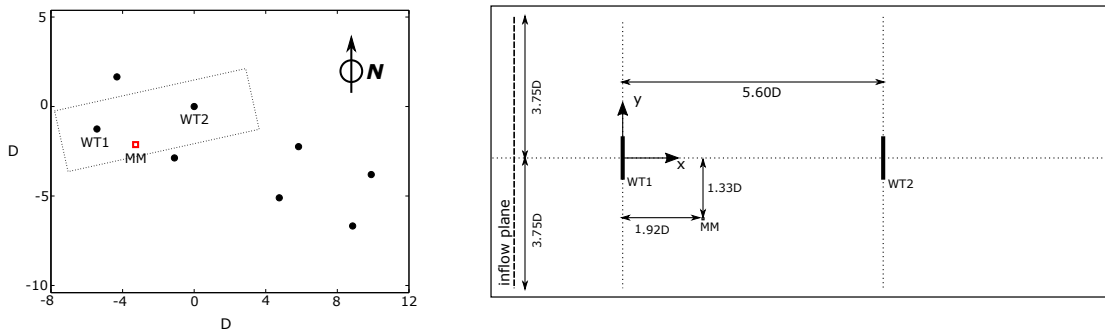


Figure 7.1: Skematic overview of the case set-up. Left: sketch of the Tjaereborg wind farm showing the global position of the upstream turbine (WT1), the downstream turbine (WT2) and the met mast (MM). Right: Close-up of the two simulated turbines including the definition of coordinates.

The inflow field was generated using the open-source toolkit PyConTurb [53]. PyConTurb generates a constrained synthetic turbulence field based on the Kaimal spectrum and the exponential coherence method. Time series of the three velocity components measured by the three sonic anemometers of the met mast (at

$z = \{17, 57, 93\}m$ ) served as the constraints. Hence, the turbulence characteristics at the met mast including larger transients of the bin could be incorporated in the inflow and used by all participants, regardless of the respective model. A special exception needs to be made for the stationary RANS simulation, in which a neutral ABL inlet condition is fixed. This condition, as well as the  $z_0$  value in the wall, depends on the velocity and TI at hub height extracted from the synthetic turbulence field. Moreover, fluctuations in the inflow used by the LES models had to be scaled by a factor of 2 in order to match the turbulence kinetic energy at the met mast.

## 7.4 Numerical Set-up

The specific numerical set-ups of all participants were chosen by the modellers in accordance with the model-specific best-practices and not further constrained by the benchmark definition. A summary of the key numerical parameters of the RANS/LES models and the DWM models is given in Tab. 7.3 and Tab. 7.4, respectively.

Table 7.3: Numerical configurations of the RANS and LES models: Sub-grid-scale (SGS) model; overall dimensions of the computational domain  $L_{x,y,z}^{out}$ ; dimensions of the finest (isotropic) grid region in the turbine and wake vicinity  $L_{x,y,z}^{ref}$  with corresponding grid spacing  $\Delta_x$ ; total number of grid points (cells); utilised bottom boundary conditions (stress BC implying the use of a wall function with corresponding aerodynamic roughness  $z_0$ ) and time step  $\Delta_t$ .

Participant	UU LBM	UU RANS	UU LES	UU LES pc	DTU LES
SGS model	Const. Smagorinsky	Realizable $k - \varepsilon$ [54]	One eq. eddy vis.	One eq. eddy vis.	Deardorff
$L_{x,y,z}^{out}$ [D]	$20.0 \times 10.0 \times 10.0$	$16.6 \times 10.0 \times 18.75$	$16.6 \times 10.0 \times 12.5$	$37.5 \times 37.5 \times 12.5$	$17.0 \times 7.5 \times 12.5$
$L_{x,y,z}^{ref}$ [D]	$12 \times 4 \times 4$	$16.6 \times 10 \times 18.75$	$16 \times 3.75 \times 1.9$	$16.6 \times 10 \times 1.9$	$11.2 \times 1.3 \times 1.4$
refined zone	$\Delta_x$ [D]	1/32	1/10, 1/20	1/16, 1/32	1/16, 1/32
	$\Delta_y$ [D]	1/32	1/10, 1/20	1/16, 1/32	1/16, 1/32
	$\Delta_z$ [D]	1/32	1/10, 1/20	1/16, 1/32	1/16, 1/32
grid points [millions]	14.48	0.91	6.19	9.61	11.73
Bottom BC	stress, $z_0 = 0.01m$	stress, $z_0 = 0.02m$	stress, $z_0 = 0.05m$	stress, $z_0 = 0.05m$	symmetry
$\Delta_t$ [s]	0.018	0.25	0.03	0.03	0.018

Table 7.4: Numerical configurations of the DWM models.

Participant	DTU DWM	NREL DWM
Initial deficit model	BEM wake [55]	BEM far wake [56]
Deficit modelling	eddy viscosity model [55]	eddy viscosity model [56]
Meandering modelling	Separate Mann box, 1Dx1D cells [55]	Low resolution Turbsim box, cell size: $\approx D/10$ [56]
Wake turbulence	Added wake turbulence model [55]	None

Further details of the ADM and ALM used in the RANS and LES models is given in Tab. 7.5.

Table 7.5: Wind turbine models configurations: Radial spacing of blade elements  $\Delta_r$ , smearing width  $\varepsilon$  and utilised tip correction model.

Participant	Model	D/ $\Delta_x$	$\Delta_r/\Delta_x$	$\varepsilon/\Delta_x$	Tip correction
UU LBM	ALM	32	2	1.5	-
UU RANS	ADM	20	2	2	Shen [57, 58]
UU LES	ALM	32	2	2	Shen [57, 58]
UU LES pc	ALM	32	2	2	Shen [57, 58]
DTU LES	ALM	60	1	2.5	Meyer Forsting et al. [59, 60]
DTU DWM	BEM [34]				Prandtl [34]
NREL DWM	BEM	25	0.6-1.5		Glauert

## 7.5 Results

### 7.5.1 Case A - Partial wake

In case A WT2 was subjected to a partially waked inflow due to the relative wind direction of  $5.81^\circ$  with respect to the  $x$  axis.

One challenge in the comparison of different models in terms of the wake flow is the comparability of the ambient flow. As mentioned earlier, the approach in this benchmark was to provide the same pre-generated inflow field to all participants. Still, differences, particularly in the turbulence kinetic energy (TKE), downstream of the inlet remain unavoidable. In the DWM models the imposed turbulence is simply propagated downstream, yet not affected by the solution of the wake flow. On the other hand, in LES the imposed turbulence evolves downstream as it becomes part of the overall solution of the flow field. This downstream evolution typically depends on the numerical dissipation, SGS model and grid resolution. The mean stream-wise velocity  $\bar{u}$  and TKE along the vertical at the met mast position are depicted in Figure 7.2. It can be seen that the TKE at hub height ( $z=57\text{m}$ ) agrees quite well between the different models and

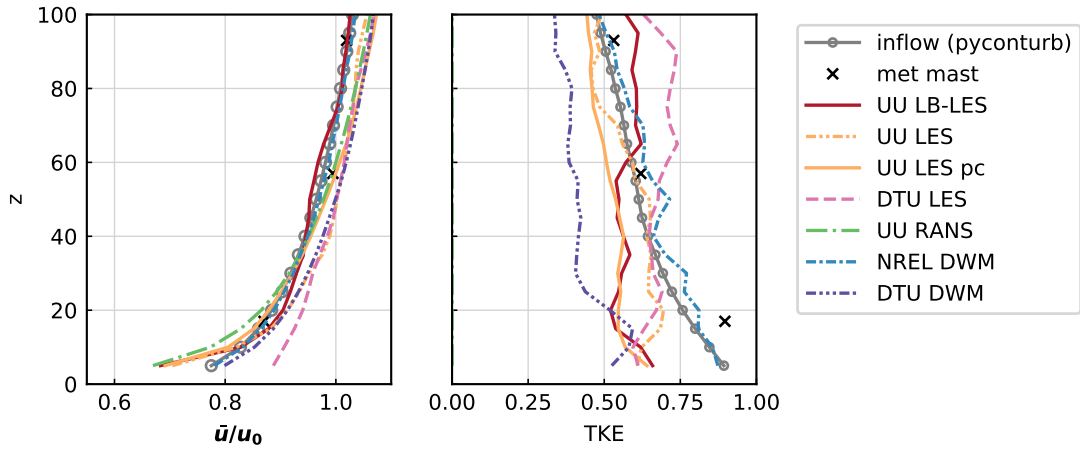


Figure 7.2: Case A; mean stream-wise velocity  $\bar{u}$  (normalised by the mean hub height velocity  $u_0$ ) and resolved turbulence kinetic energy (TKE) along  $z$  at the met mast position. Crosses mark the measurements of the sonics at the met mast. *inflow* refers the statistics of the synthetic inflow field generated by PyConTurb and used by most participants.

the measurements. Generally, the TKE in the LES solutions is rather constant with height not showing a negative shear as the imposed inflow.

A comparison of different wake characteristics is provided in Figure 7.3. The models are in rather close agreement in terms of the velocity, particularly in the far-wakes of the turbines (see  $x = \{-2D, -1D\}$  and  $x = 4D$ , respectively). But also the characteristic change from the typical near-wake profiles to post-transition Gaussian far wake profile is similarly predicted by the different model. An exception on that regard only states the UU RANS model. In terms of the  $Ti$  differences are more pronounced. Yet, particularly the LES models still show very similar characteristics throughout the entire domain. Furthermore, it can be appreciated that the DWM models also capture the characteristic peaks of the  $Ti$  in the near-wake related to the large-scale meandering of the velocity deficit.

The mean power of the turbines is compared in Figure 7.4. The power of the first turbine is consistently underestimated by the models. The closest agreement is found for UU LES with a difference of -1% while the largest refers to NREL DWM with -18%. Possible reasons for the underestimation are manifold. The most obvious reason for the consistent underestimation is the fixed rotational speed set in the models implying a sub-optimal operation. Secondly, differences in the mean wind speed apparent in the different model (as shown in Figure 7.2) will contribute to the differences between the models. As for the second turbine the magnitude of the relative differences towards the measurement are somewhat higher ranging from +8% for UU LB-LES to +26% for NREL DWM. The differences in power between the models show a large correlation

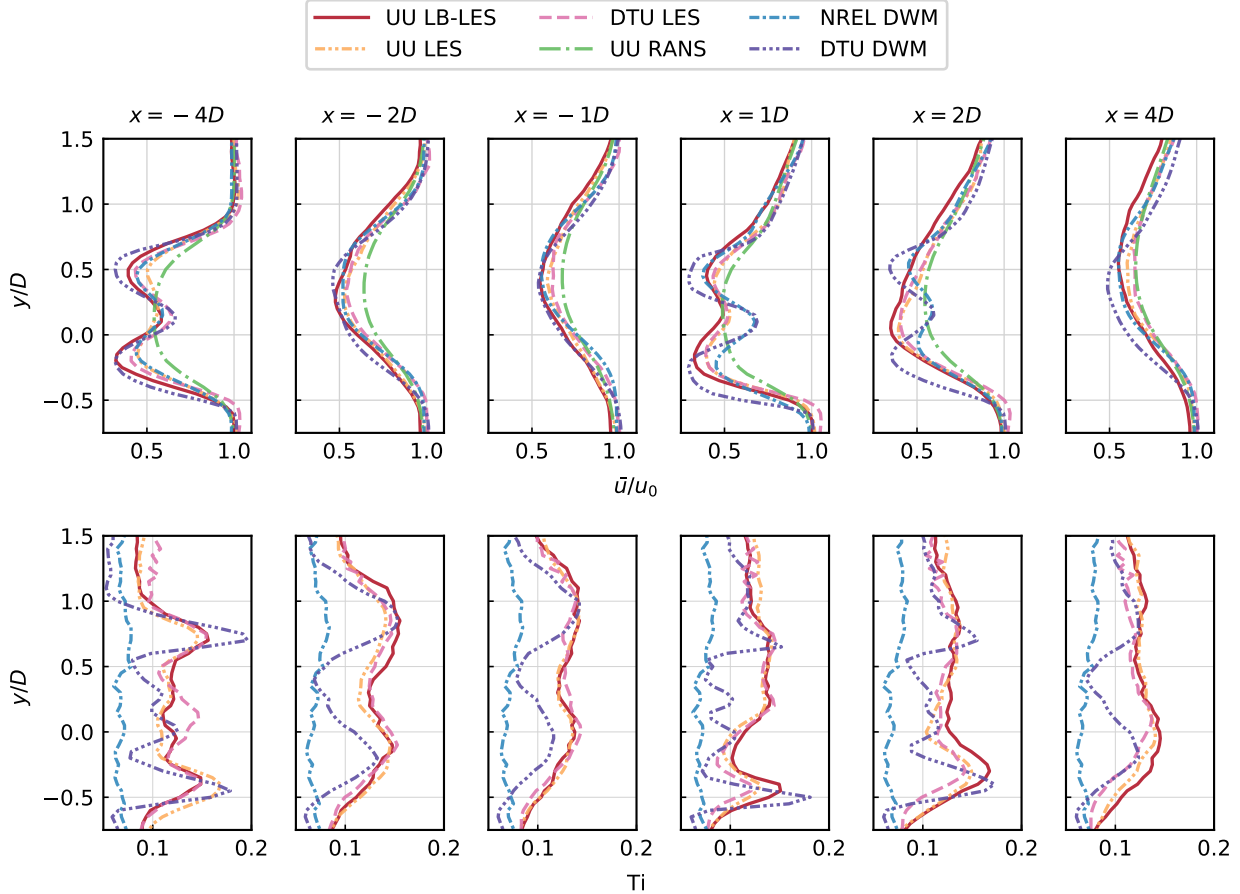


Figure 7.3: Case A; horizontal profiles of the mean stream-wise velocity (top) and turbulence intensity (bottom;  $Ti = \sqrt{2/3} \text{TKE}/u_0$ ) at hub height at different positions  $x$  relative to WT2.

with the upstream wake deficit. Thus, the differences in power and loads (as discussed later) mostly seem to originate from differences in the waked inflow rather than the different turbine models. Also, the variance of the power of WT2 is consistently lower in the simulations than in the measurement, yet similarly predicted by most models. The latter might indicate that the wake inflow in the measurements is characterised by higher large-scale fluctuations than modelled.

A more detailed impression of the interaction of WT2 with the inflow can be obtained from the mean forces along the blade illustrated in Figure 7.5. The mean tangential forces obviously show a similar trend in the agreement with the measurements as previously shown for the power. In terms of the normal forces, the models are in closer agreement than in the tangential component. Also note that the normal forces from the pressure distributions may suffer from a light inaccuracy as explained in section 3.9.4. It is furthermore recalled that the tangential force does not include the friction component

The azimuthal variation of the forces is given in Figure 7.6 allowing for more detailed indirect assessment of the wake inflow. In order to expose only the azimuthal variation we subtract the means of the forces at the respective radial position. First of all, the plots illustrate the overall effect of the partially waked inflow on the turbine. The maximum of the forces is found at  $\phi \approx 90^\circ$  when the blade is subjected to near-undisturbed inflow. On the other hand, in the minimum at  $\phi \approx 270^\circ$  the blade passes the center of the wake as can be inferred from Figure 7.3. This also shows that the azimuthal variation of the forces is dominated by the partial wake as opposed to differences related to shear (which would imply minima/maxima closer to  $0^\circ/180^\circ$ ). Furthermore, it is found that the LES models capture the azimuthal variation best. The magnitude of the azimuthal variation in the DWM results is consistently overpredicted. The magnitude of the variation

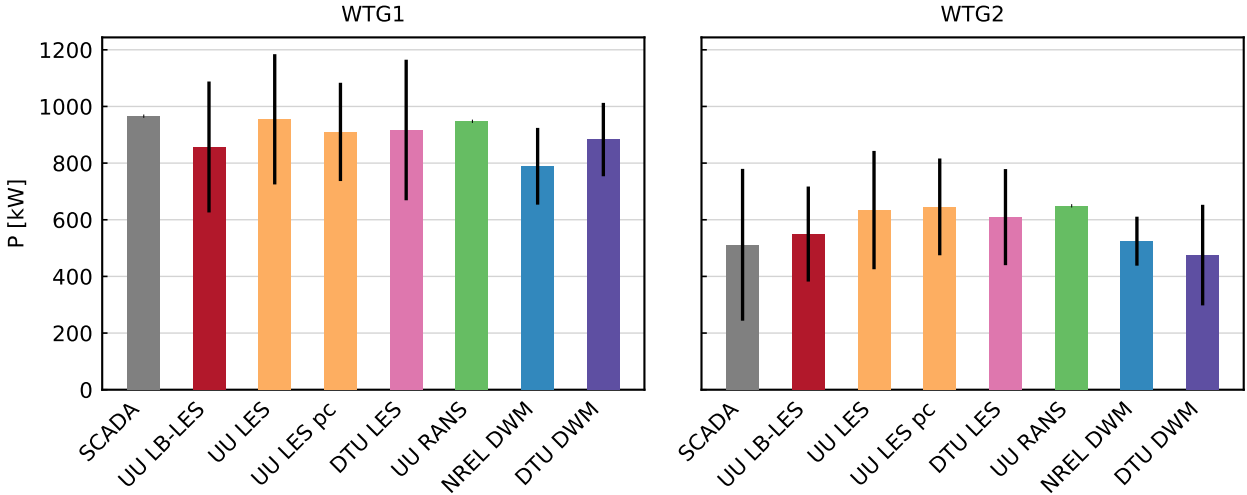


Figure 7.4: Case A; mean mechanical power  $P$  of WT1 (left) and WT2 (right). Error bars show the standard deviation. The mechanical power of the measurements was obtained from the electrical power logged by the SCADA system and the mechanical efficiency of the turbine determined during the measurement campaign.

predicted by the RANS model is somewhat close to the predictions of the LES models. Yet, both minima and maxima are slightly negatively shifted along  $\phi$ .

## 7.5.2 Case B - Full wake

The second test case differs in several crucial aspects from the previous. Firstly, as mentioned earlier, the mean wind direction was almost perfectly aligned with the two turbines resulting in a fully waked inflow for WT2. Secondly, this bin refers to a period where the control of WT2 was modified as part of the DanAero experiments. The turbine was operated at constant rotational speed. Hence, the fixed rpm set in the simulations no longer states a simplification facilitating the comparison to the measurements. Lastly, the mean wind speed is lower than in case A. This low wind speed in combination with the fixed rpm implies an untypically high TSR and  $C_T$  for WT2.

The spread of the wind statistics at the met mast is generally similar as in case A, see Figure 7.7. A further discussion thereof is thus omitted for the sake of brevity.

Also the agreement in the wake characteristics of WT1 is similar as in case A. A larger variation is found in the wake of WT2. The latter can be explained by the more significant spread in the distribution of the forces, as discussed later.

The power of WT1 predicted by the CFD models lies within  $\pm 10\%$  of the measurements, see Figure 7.9. In this case the NREL DWM and DTU DWM model predict a notably lower power of  $-25\%$  and  $-21\%$ , respectively. A similarly clear trend can not be observed for WT2. Moreover, the mean forces along the blade (Figure 7.10) indicate that a well-captured power not necessarily correlates with a correct prediction of the forces along the blade. Note, for instance, the peak in  $\bar{F}_t$  in UU LB-LES near the tip that states a clear over-prediction when compared to the measurements. At the same time it appears to correct for under-predictions of the tangential forces in the middle of the blade when it comes to the resulting power.

The azimuthal variation of the forces for case B is given in Figure 7.11. Even larger discrepancies between the models can be observed than for the mean forces, particularly, near the tip of the blade. UU LB-LES and DTU LES show only a small variation of the forces with  $\phi$ . On the other hand, UU RANS, UU LES and DTU DWM show a clear minimum and maximum near  $\phi = 180^\circ$  and  $\phi = 360^\circ$ , respectively. This not only agrees well with the measurements but also indicates a strong impact of shear on the force distribution. Lastly, the results by NREL DWM give an inverse picture of the force distribution. The latter might relate to a problem of the model arising from the large  $C_T$ .



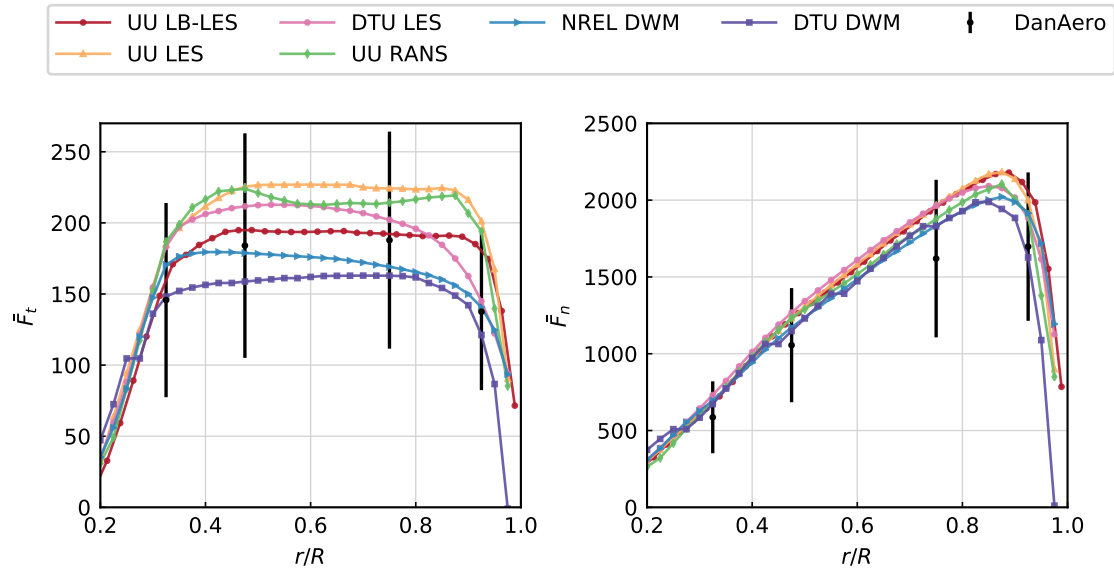


Figure 7.5: Case A; mean tangential force  $F_t$  (left) and normal force  $F_n$  (right) along the blade. Error bars of the measurements show the standard deviation.

## 7.6 Concluding remarks on Task 3.3: Wake effects

The benchmark results show good agreement considering the complexity of the study. The discussion has indicated limitations of the benchmark setup and indicated challenges when setting up a test case for different types of models and still ensuring that the comparison is as consistent as possible. The study do give an overview of state-of-the-art model limitations and challenges considering a turbine to turbine interaction case. The experience from this will be used in additional future work with the aim to present a full publication concluding additional cases where identified shortcomings of the benchmark setup is taken in to account.

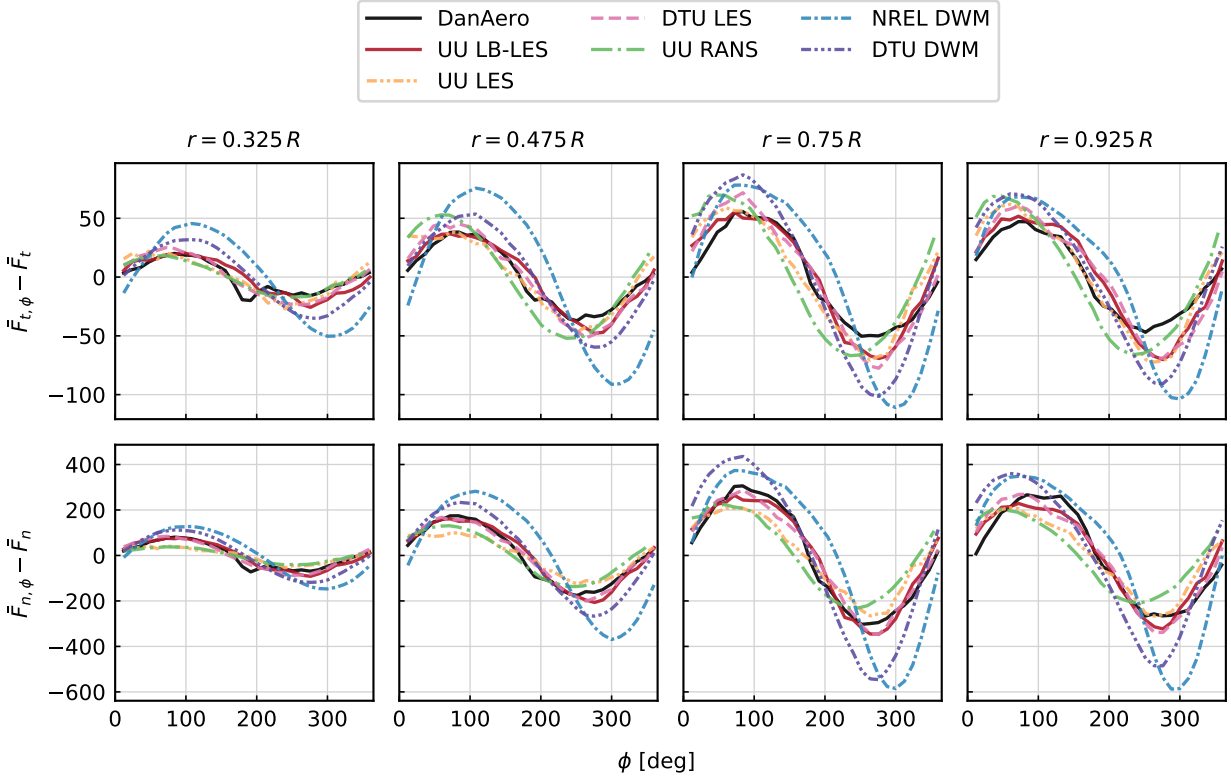


Figure 7.6: Case A; variation of the tangential force  $F_t$  (top) and normal force  $F_n$  (bottom) over azimuthal angle  $\phi$ . Means were obtained for 30 azimuthal bins.

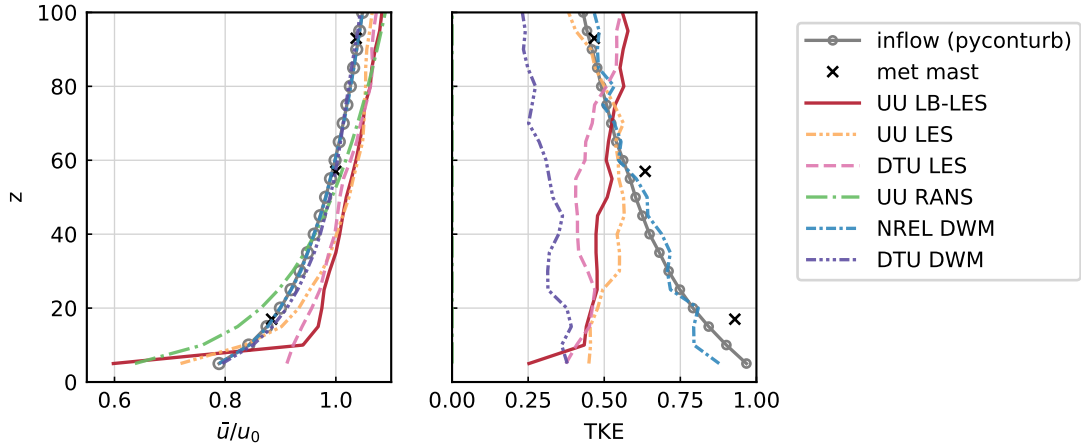


Figure 7.7: Case B; mean stream-wise velocity  $\bar{u}$  (normalised by the mean hub height velocity  $u_0$ ) and resolved turbulence kinetic energy (TKE) along  $z$  at the met mast position. Crosses mark the measurements of the sonics at the met mast. *inflow* refers the statistics of the synthetic inflow field generated by PyConTurb and used by most participants.

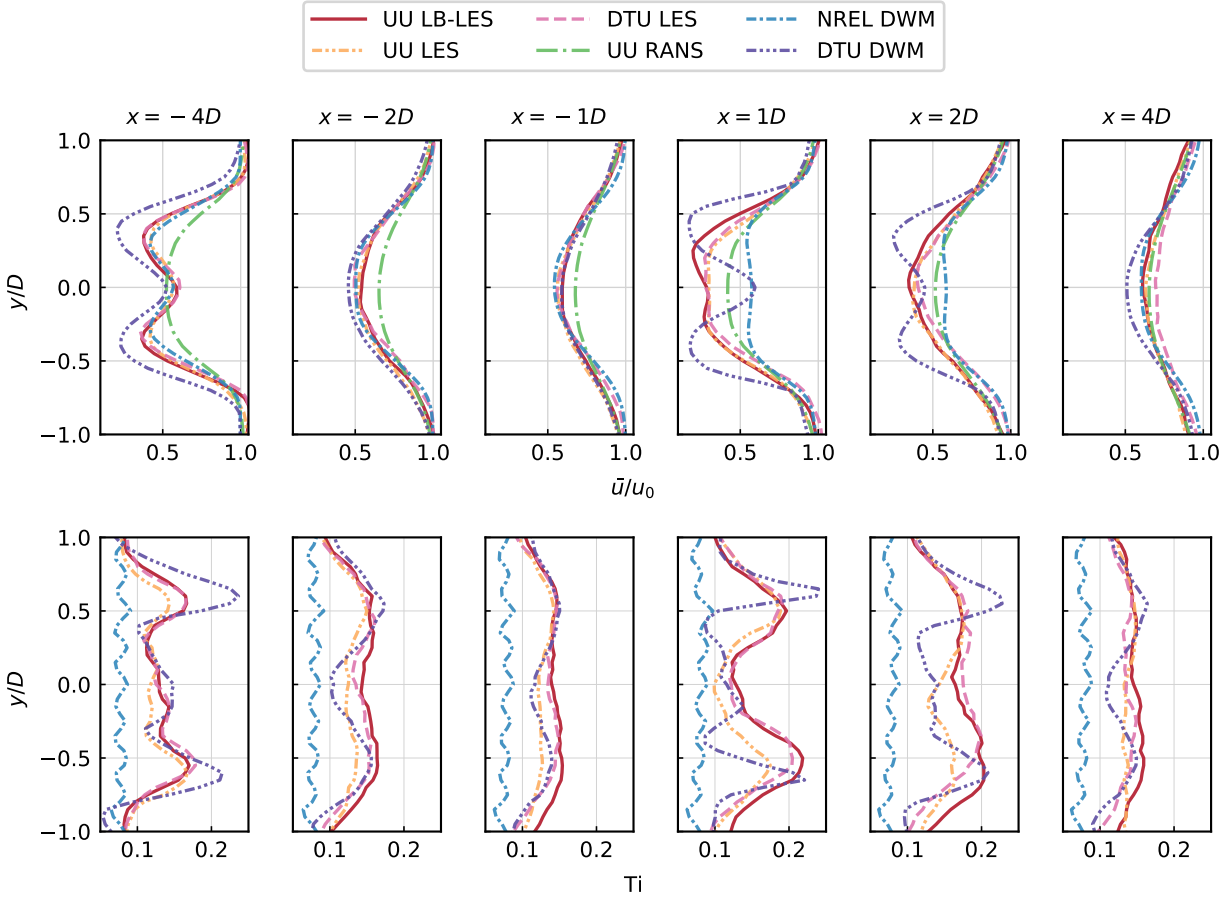


Figure 7.8: Case B; horizontal profiles of the mean stream-wise velocity (top) and turbulence intensity (bottom;  $Ti = \sqrt{2/3 \text{TKE}}/u_0$ ) at hub height at different positions  $x$  relative to WT2.

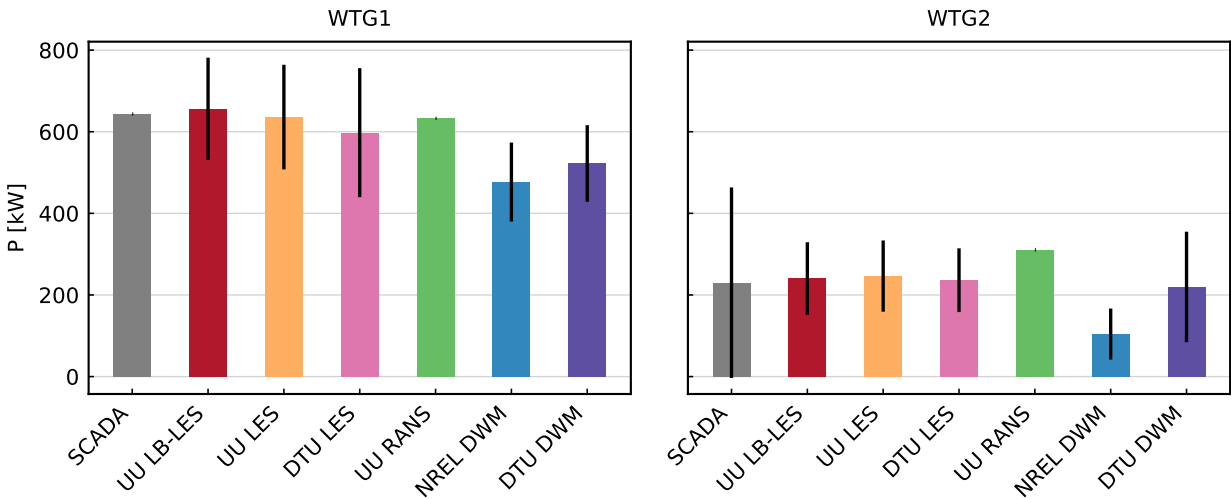


Figure 7.9: Case B; mean mechanical power  $P$  of WT1 (left) and WT2 (right). Error bars show the standard deviation. The mechanical power of the measurements was obtained from the electrical power logged by the SCADA system and the mechanical efficiency of the turbine determined during the measurement campaign.

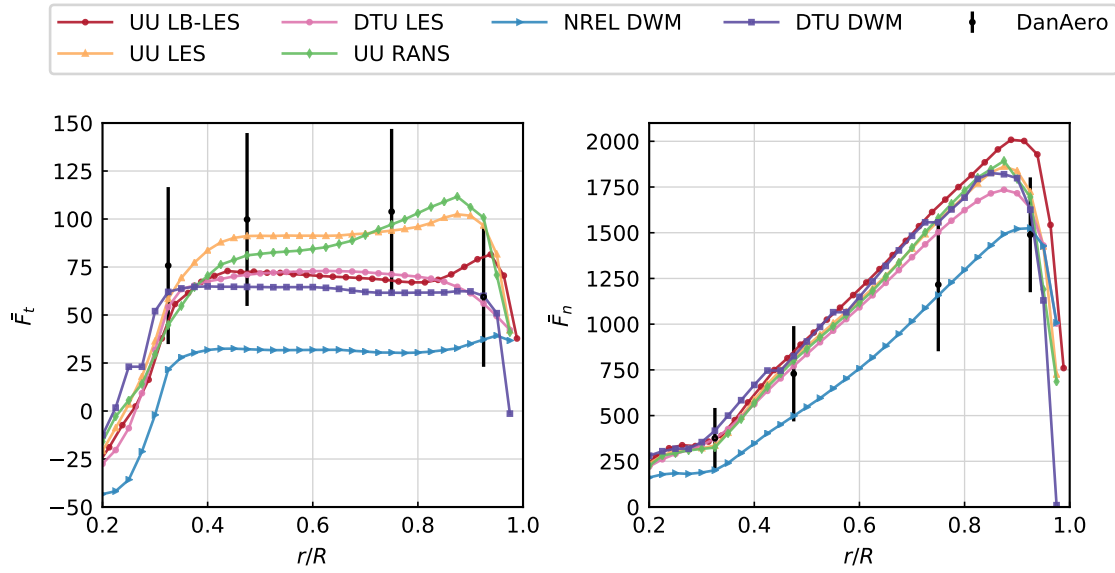


Figure 7.10: Case B; mean tangential force  $F_t$  (left) and normal force  $F_n$  (right) along the blade. Error bars of the measurements show the standard deviation.

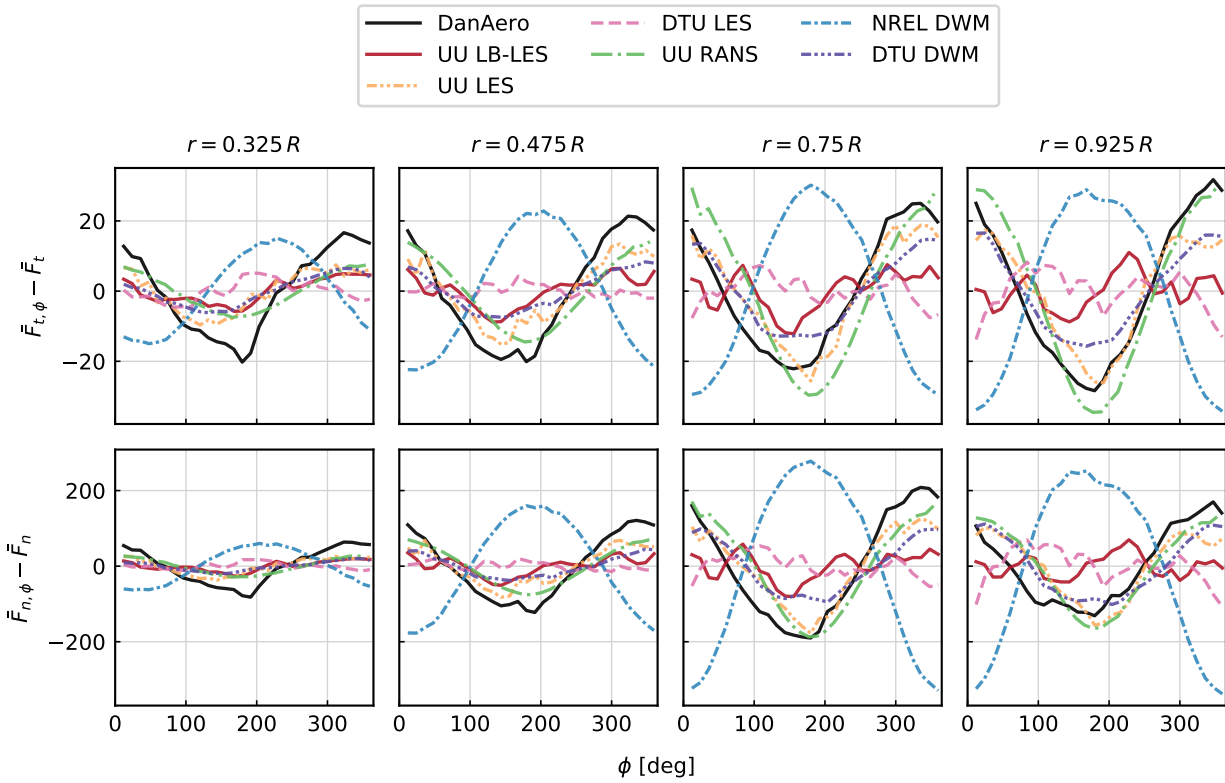


Figure 7.11: Case B; variation of the tangential force  $F_t$  (top) and normal force  $F_n$  (bottom) over azimuthal angle  $\phi$ . Means were obtained for 30 azimuthal bins.

# Chapter 8

## Task 3.4: 2D-3D airfoil characterization

T. Potentier, C. Braud, E. Guilmineau

### 8.1 Introduction

This part summarizes the work led by LHEEA lab. in France (T. Potentier, C. Braud, E. Guilmineau) with contributions from TNO in Netherland (G. Schepers) on 2D-3D airfoil characterization. For LHEEA lab. this work started in January 2020, with the PhD work of Thomas Potentier. To investigate differences between 2D and 3D flows from DANAERO database, an iBEM solver has been developed. The objective was to compare back-computed lift and drag aerodynamic coefficients from iBEM simulations using inputs from field measurements (fully 3D) with lift and drag coefficients from 2D wind tunnel experiments. Section 8.2 describes the iBEM solver and section 8.3 summarizes results and perspectives.

### 8.2 iBEM solver

#### 8.2.1 Description

1. **BEM formulation:** The main BEM (Blade Element Momentum) equations implemented are the classical momentum and blade element formulae [61]. Several corrections and filters on the BEM model and input data are implemented to ensure to remain within the BEM limits. The corrections applied are: Glauert high loading rotor, Prandtl root and tip factor, time travel correction between mast and turbine, azimuthal wind profile reconstruction, wake effect, yaw misalignment. The measured normal and tangential forces are used, along with the operating conditions of the turbine and SCADA data, to derive the local aerodynamic coefficients ( $C_L$  and  $C_D$ ) as well as the local induction.
2. **Blade discretization:** The blade is discretised in as many measurement points available, there are four instrumented sections on the blade.
3. **Airfoil data:** The aerofoil data is reconstructed based on the measurements and not given as input.
4. **Dynamic stall model:** There is no dynamic stall model implemented.
5. **Tip and root correction:** Prandtl root-loss and tip-loss correction are used as part of the induction modelling.
6. **Turbulent wake (i.e. momentum breakdown, high thrust correction):** The turbulent wake state is modelled using the equation from Madsen et al. [30], where the axial induction is modelled through a polynomial fit curve covering the low induction part (i.e.  $a \leq 0.5$ ) and the highly loaded rotor part (i.e.  $a \geq 0.5$ )

7. **Tower influence model:** The tower influence is either discarded by removing from the measured time series the data points located in the bottom half of the rotor or modelled through a tower shadow model [62].
8. **Yaw model:** The yaw model used is the model derived by Blondel et al. [36].
9. **Dynamic wake model:** Either a steady BEM code or an unsteady BEM can be used. The dynamic wake model is derived from Oye and described in [63].
10. **Drag in induction computation:** The drag is included in both the axial and tangential inductions.
11. **Miscellaneous remarks:** The Figure 8.1 shows in graphical format the steps described above.

### 8.2.2 Other information

1. **Wind modeling:** The wind is measured directly from the met mast at three heights (17m, 57m and 90m) by sonic anemometers. For each time step a power-law fitting is built taking into account the blade azimuthal position, so as to calculate the wind speed seen by the section at the time of the measurement.
2. **Time step:** N/A
3. **Simulation length:** The time series contains 21 000 data points which corresponds to 10min.
4. **CPU times:** Unsteady iBEM CPU time  $\leq$  5 min for 10 worth of data for a single section.
5. **Spanwise integration:** N/A

## 8.3 Results and perspectives

An iBEM solver has been developed and validated against CFD benchmark cases, provided by the IEA Task 29 members. The objective of the iBEM solver is to estimate the BEM modelling differences with lift and drag aerodynamic coefficients from 2D wind tunnel experiments. To do so, the iBEM solver takes as input the normal and tangential forces from the DANAERO field data (3D blade forces) and recompute the lift and drag aerodynamic coefficients using the BEM theory. The direct comparison is not possible as wind tunnel conditions are completely different from field tests (wind direction, intensity, wind inflow shears etc ...). A first operation was thus performed to keep conditions as close as possible as 2D wind tunnel tests. This is also mandatory to exclude effects that may introduce bias due to the BEM theory limitations. Methods were thus developed to filter out the boundary layer gradient and wakes from neighbouring turbines. Well-known BEM corrections were also implemented in the iBEM solver, including inflow vertical gradient profile, the wind inflow measurement location, the tangential measurement forces impact, aeroelastic deformation impact, yaw misalignment, dynamic wake and tower shadow effect.

Upon looking at the results presented in Figure 8.2, which shows the comparison of all different cases of the corrections and filters developed, it is apparent that the steady BEM equations are not sufficient to model accurately the expected behaviour of a wind turbine operating in the field. There is very little improvement in the  $C_L$  (both in trend and absolute values), compared to the reference wind tunnel data when using steady BEM (case 0 to case 5). Nevertheless, to ensure remaining within the BEM theory limits the application of the neighbouring wake filter is necessary. To account for more realistic inflow conditions, the mean vertical gradient velocity correction and the wind inflow location correction should be used. The use of the Unsteady iBEM method (case 6) highlights the importance of the unsteady part in a field data analysis. Firstly, in a physical analysis point of view, the addition of dynamic wake changes the  $C_L$  trend outcome thanks to the more accurate description of the inflow velocity. The lift coefficient evolution follows now the trend measured in a wind tunnel rather than the flat or even decreasing  $C_L(\alpha)$  relationship seen when using the steady BEM equations. We can also see that some rotational effects are present since the mean results hovers between the 2D and 3D corrected lift curves. The error bars show the dispersion in the results and most probably show the effect of transition location displacement, or the intermittent apparition of the flow separation,

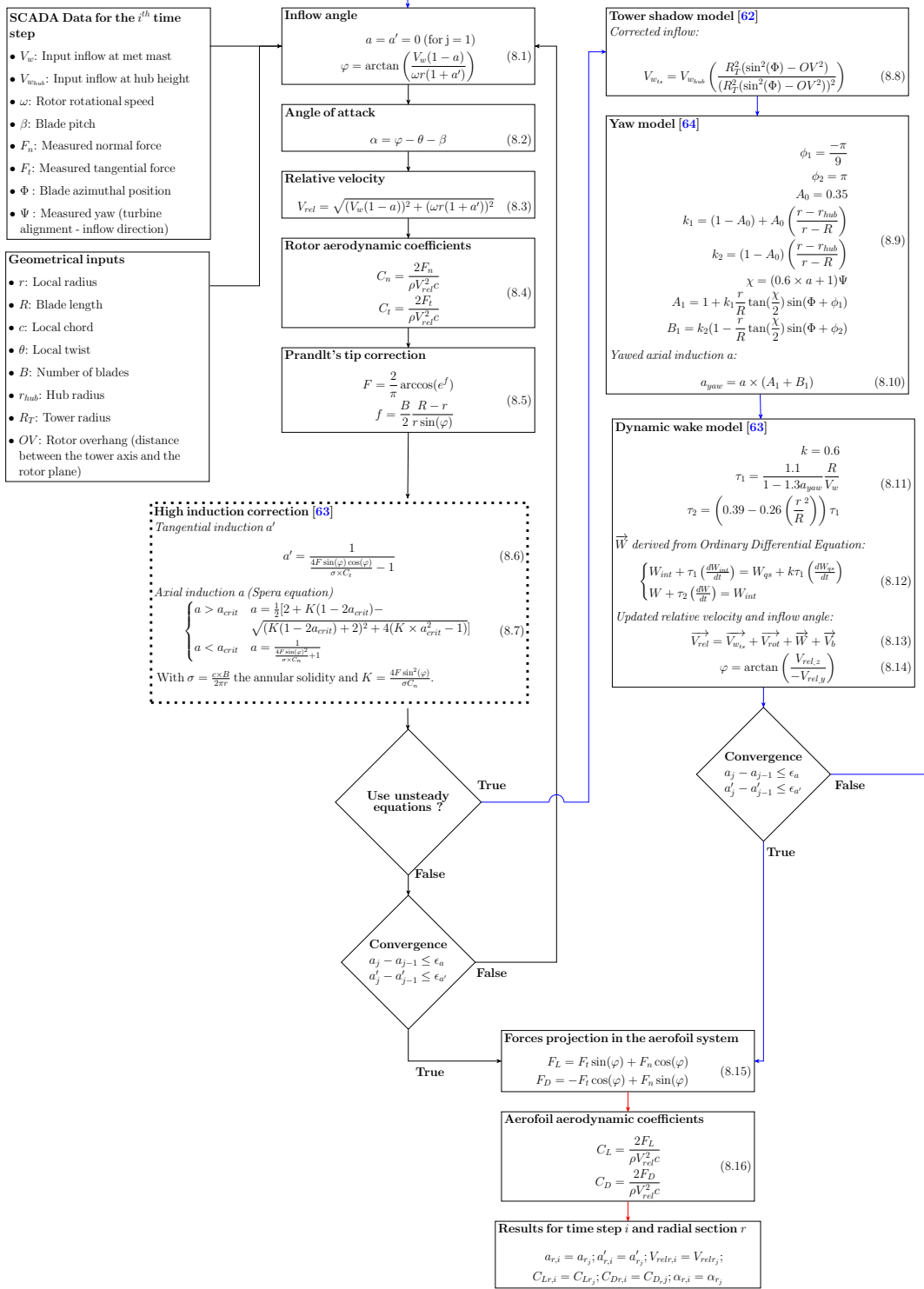


Figure 8.1: Diagram of the inverse Blade Element Momentum (iBEM) and Unsteady inverse Blade Element Momentum (UiBEM) method algorithm. The process is repeated until its convergence is reached for each time step of the acquired inflow velocity and for each blade section. The axial and tangential induction in the convergence loop are marked with subscript  $j$ . The black path shows the use of BEM equations, the blue path shows the use of unsteady BEM equations, the red path shows outputs of the present solver, which comprise of the measured forces projected in the aerofoil coordinates,  $C_L$  and  $C_D$ , the angle of attack  $\alpha$  and the converged axial and tangential induction. See [65] for more details.

both phenomena missing in the state-of-art of BEM models. Thanks to the tower shadow model and the yaw model a larger set of samples can be kept compared to the steady BEM equations. Figure 8.3a shows the number of samples converged using iBEM solver with the progressive application of filters and different corrections (from case 0 to case 5) at two radial locations. The sum of the transparent and opaque shaded area represents the total available number of samples to be analysed after the cumulative application of filters and correction models. The transparent shaded area is the non-converged part of the total number of samples. The converged number of samples decreases with the application of correction and filters (down to 10000 samples for  $r/R = 49\%$ ). It also highlights that the number of input samples and converged samples after the application of the unsteady BEM equations increase drastically. For the tip section the number of converged samples, when using the UiBEM method, is even greater than the raw analysis (see Figure 8.3b). For both sections, when using UiBEM, a maximum of 72% of the available dataset is analysed because of wake shadow effect between neighbouring turbines filter; out of which 85% have achieved convergence.

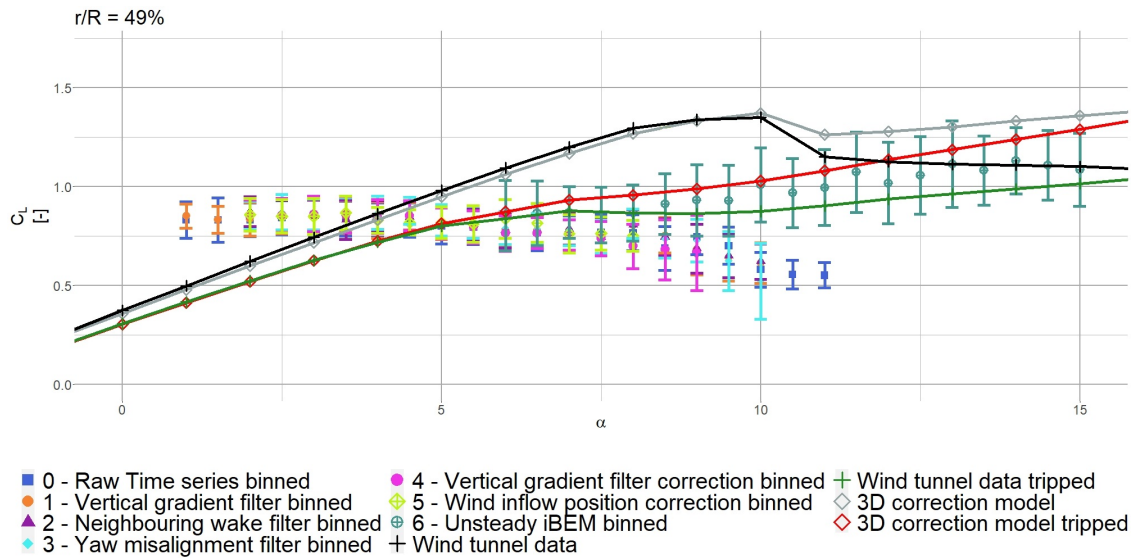


Figure 8.2: Binned averaged  $C_L$  comparison for the radial location  $r/R = 49\%$ . All the previously filters, corrections and BEM methods are overlaid. The black crosses show the clean 2D wind tunnel data, the grey crosses show the tripped 2D wind tunnel data. The error bars represent the  $C_L$  standard deviation in the analysed time series. The red diamonds show the 3D correction model applied to the clean 2D wind tunnel data, the green diamonds show the 3D correction model applied to the tripped 2D wind tunnel data. The error bars represent the  $C_L$  standard deviation in the analysed time series.

Figure 8.4 shows the results after applying the UiBEM method to all the sections. The inboard sections show a good agreement between the tripped wind tunnel conditions with the application of the 3D correction model and the calculated UiBEM  $C_L$ . The agreement is poorer when it comes to the outer sections, it may be attributed to the weakness of the BEM theory to capture both the tip vortex and the aeroelastic effects at those locations and needs dedicated investigations.

Previous data were presented using an angle of attack binning method. The blade azimuthal position impact were therefore compensated. In the following, the lift hysteresis is now investigated. The rapid variation of angle of attack during the blade rotation does not enable the flow around the aerofoil to reach a steady state organisation. In particular, dynamic stall can locally occur and may cause deviation from the mean  $C_L(\alpha)$  curve. Figure 8.5 shows the  $C_L(\alpha)$  evolution when the data is averaged by azimuthal position ( $\Delta\Phi = 5^\circ$ ). The dynamic stall behaviour is modelled using the adapted Beddoes-Leishman model from DTU [66]. Some parameters need to be chosen for this model: the reduced frequency  $k$  has been defined by the blade rotational speed (since the pitch is constant throughout the time series), the mean angle of attack  $\alpha_m$  is extracted from the UiBEM simulation of the considered time series, while the amplitude of the angle of attack oscillations  $\alpha_a$  is the difference between the highest quadrant averaged angle of attack and lowest mean angle of attack.



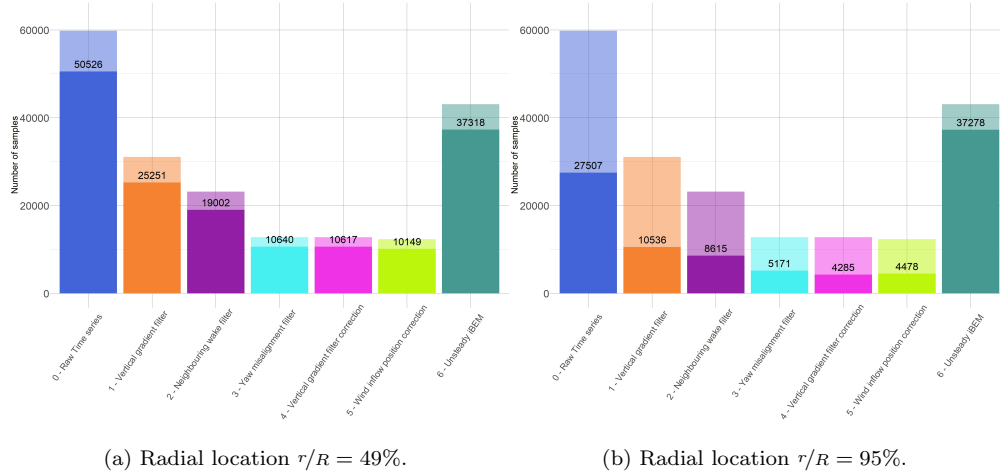


Figure 8.3: Effect on the data points converged of the filters, the corrections and unsteady BEM equations for different radial locations. The transparent shaded area represents the available data points after application of the filters, the opaque area represents the converged number of samples through the iterative iBEM procedure.

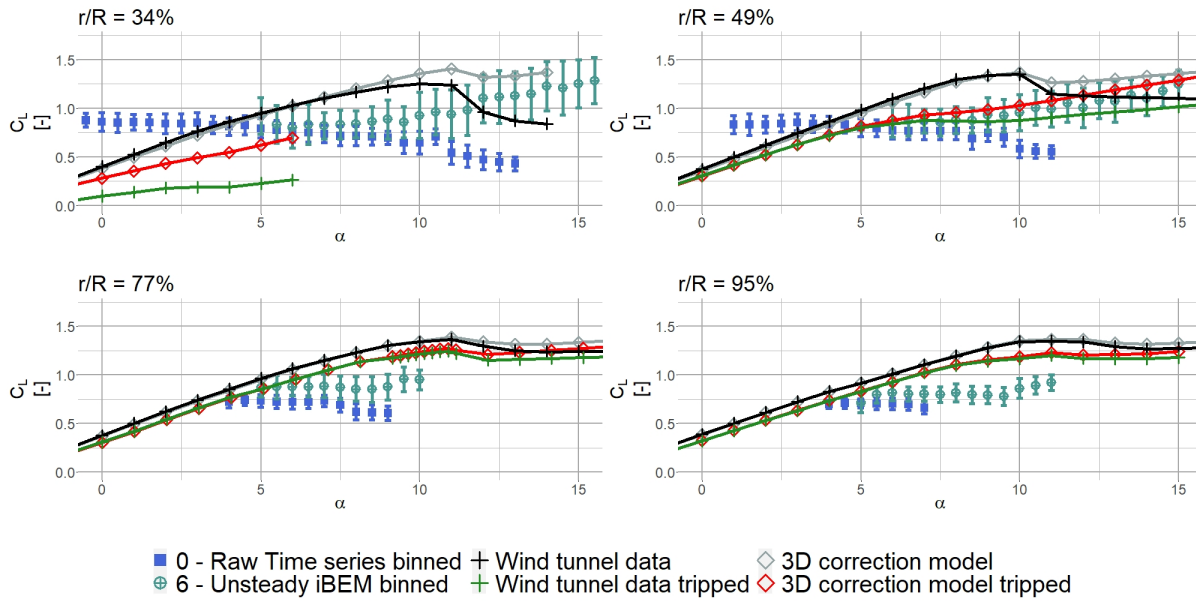


Figure 8.4: Binned averaged  $C_L$  comparison for all radial location. The square represents the average coefficient for the raw data, the crossed circles the average coefficients when the unsteady BEM equations are used. The black crosses show the clean 2D wind tunnel data, the grey crosses show the tripped 2D wind tunnel data. The error bars represent the  $C_L$  standard deviation in the analysed time series. The red diamonds show the 3D correction model applied to the clean 2D wind tunnel data, the green diamonds show the 3D correction model applied to the tripped 2D wind tunnel data. The error bars represent the  $C_L$  standard deviation in the analysed time series.

The quadrant average results follow the overall shape described by the instantaneous cloud of points. On Figure 8.5, the numbers written on the plot show some azimuthal blade position ( $0^\circ$  being the instrumented blade pointing upwards). We can clearly see the effect of the ABL vertical gradient, which decreases the angle of attack and the  $C_L$  when the blade is close to the ground (between  $90^\circ$  to  $270^\circ$ ). Then, the tower shadow effect is visible between  $90^\circ$  to  $180^\circ$ , because when the blade goes down, the angle of attack does not linearly change with the blade azimuth but loops back. Despite using a crude assumption for the reduced frequency, the dynamic stall model captures the essence of both the instantaneous data and the quadrant average data. The remaining dispersion of points are certainly to be attributed to the missing knowledge of the instantaneous wind inflow at the blade location. It may be different than the wind inflow at the mast location used in the present study and needs dedicated investigations.

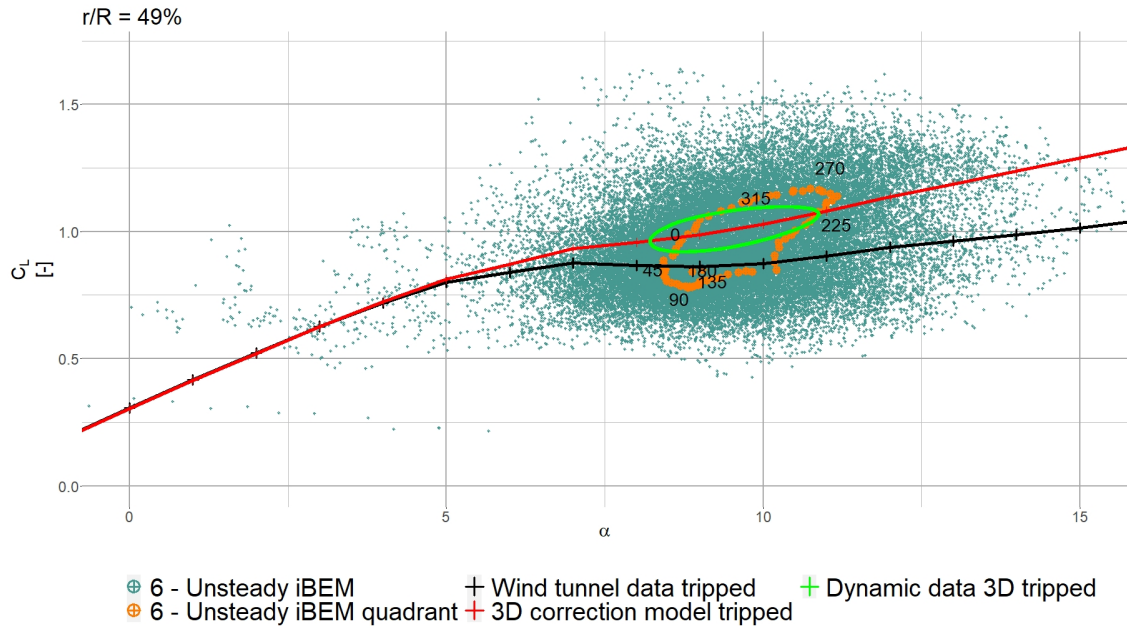


Figure 8.5: Quadrant averaged  $C_L$  comparison for the radial location  $r/R = 49\%$ . The green crossed circles the instantaneous coefficients when the unsteady BEM equations are used. The orange crossed circles the quadrant coefficients when the unsteady BEM equations are used. The error bars represent the  $C_L$  standard deviation in the analysed time series. The black crosses show the tripped 2D wind tunnel data. The red cross show the 3D correction model applied to the tripped wind tunnel data. The solid green line represents the dynamic data using the tripped 3D corrected wind tunnel data as input.

Also, in complement to the iBEM solver, CFD computations has been performed in 2D using an in-house solver of ECN-Nantes (ISIS-CFD [67]) and validated against EllipSys (see figure 8.6). Future work will include CFD simulations of the full rotor which will be used as an additional tool to compare 2D and 3D airfoil characteristics of the DANAERO database and also to contribute to the cross-comparison round of task 3.1.

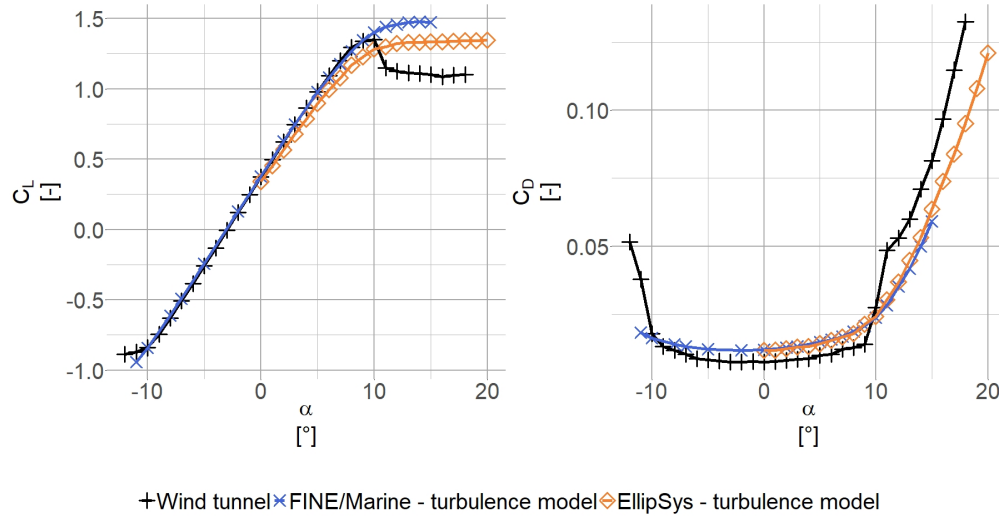


Figure 8.6:  $C_L$  and  $C_D$  comparison (Section  $r/R = 49\%$ ) between 2D wind tunnel experiments and 2D CFD computations ISIS-CFD (FINE™/Marine) from LHEEA lab. and EllipSys from DTU.

# Chapter 9

## Task 3.5: Aeroelastic analyses

A. Croce, S. Cacciola

This section describes aeroelastic analyses performed on the NM80 wind turbine model, within the Task 3.5. Goal of this task is to compare different wind turbine analysis codes in terms of aeroelastic behavior, including both response to steady wind conditions and turbine modal content (frequencies and damping factors).

The comparison considered both aeroelastic simulations and modal analysis of entire turbine or its sub-components in different conditions. Different tests of increasing complexity, ranging from single blade frequency computation to dynamic simulations, have been proposed to partners in order to assess, and possibly improve, the quality of their own simulation tools. Gradually increasing the complexity of the considered scenarios has the clear advantage of allowing one to early detect possible inconsistency in the modeling of turbine sub-components. Clearly, after verifying the correctness of the turbine assembly, which comprises both all sub-components and their coupling, it is possible to finally assess the goodness of those stability analysis tools, which typically complement the simulation codes for the evaluation of damping and of the proximity of flutter boundaries. In the case of wind turbines, the modal analysis deserves special attention. In fact, as long as non-rotating turbines are under investigation, standard stability analysis techniques developed for Linear Time Invariant (LTI) systems can be employed. On the other side, if one considers a rotating turbine, it is essential to adopt more sophisticated procedures compliant with the periodic nature of the system. Among all, one can mention those based on linearization and Coleman transformation [68], system identification [69] or simplified Floquet analysis [70]. All such procedures, although widely accepted, present some specific approximations which should be always checked.

This activity was supervised by the Department of Aerospace Science and Technology of Politecnico di Milano (A. Croce and S. Cacciola). With a significant amount of results, obtained with different simulation codes and analysis tools, seven partners, NREL, USTUTT, TNO, DTU, IFPEN, DNVGL and CNR-Insean, besides the supervising institution, POLIMI, participated to at least one comparison round.

This chapter is organized according to the following plan. At first, Sec. 9.1 deals with the description of the performed analyses, which have been used for performing all comparisons. The results of such a comparison are reported in Sec. 9.2. Finally, Sec. 9.3 finalizes the chapter by summarising the main conclusions.

Note that results are given anonymous.

### 9.1 Aeroelastic simulations and modal analyses

The following set of four different tests has been considered.

1. Computation of the natural frequencies and damping factors of a clamped, non-rotating blade, *in vacuo* and without gravity.
2. Computation of natural frequencies of the standstill wind turbine, non-rotating, *in vacuo* and without gravity.

- Derivation of the Campbell diagram of the entire turbine *in vacuo* and in air computed for different wind speed values from cut-in to cut-out. Blade pitch angles and rotor speed values are selected according to the control trim set points reported in Tab. 9.1.

Table 9.1: Conditions for Campbell diagram derivation.

<b>Wind speed</b> [m/s]	5.0	9.0	13.0	17.0	21.0	25.0
<b>Omega</b> [RPM]	9.91	17.83	19.08	19.08	19.08	19.08
<b>Pitch angle</b> [deg]	1.20	1.20	3.49	12.81	18.42	22.79

- Dynamic simulation in Nominal Wind Profile (NWP) conditions. For the same set points of Tab. 9.1, simplified dynamic simulations should be conducted excluding the control system by fixing the rotor speed and collective pitch angle. Moreover, the inflow should be set according to a Normal Wind Profile (i.e. exponential wind shear with  $\alpha = 0.2$ ) without tower shadow, turbulence and yaw misalignment angle).

With reference to the triads reported in Fig. 9.1 ([71]), at steady conditions, i.e. after a possible initial transitory, the mean value of the following sensor should be provided:

- Tower base bending moments  $M_x^{\text{base}}$ ,  $M_y^{\text{base}}$ ,  $M_{xy}^{\text{base}}$  and  $M_z^{\text{base}}$  (side-side, fore-aft, combined, torsion moments), in tower base fixed frame;
- Tower top bending moments  $M_x^{\text{top}}$ ,  $M_y^{\text{top}}$ ,  $M_{xy}^{\text{top}}$  and  $M_z^{\text{top}}$  (side-side, fore-aft, combined, torsion moments), in tower base fixed frame;
- Blade root pitchable bending moments  $M_x^{\text{blade}}$ ,  $M_y^{\text{blade}}$ ,  $M_{xy}^{\text{blade}}$  and  $M_z^{\text{blade}}$  (edge-wise, flap-wise, combined, torsion moments), in blade root pitchable frame;
- Blade(s) root hub-fixed bending moments  $M_x^{\text{hub}}$ ,  $M_y^{\text{hub}}$ ,  $M_{xy}^{\text{hub}}$  and  $M_z^{\text{hub}}$  (in-plane, out-of-plane, combined, torsion moments), in blade root fixed frame, which is formally equal to the pitchable frame but fixed in a position with null collective pitch angle;
- Hub center fixed force and bending moments  $F_x^{\text{rotor}}$ ,  $M_y^{\text{rotor}}$  and  $M_z^{\text{rotor}}$  (thrust, nodding and yawing), in rotor fixed frame;
- Blade(s) tip pitchable deflections  $s_x^{\text{blade-tip}}$ ,  $s_y^{\text{blade-tip}}$  (edge-wise, flap-wise), in blade root pitchable frame;
- Tower top deflections  $s_x^{\text{tower-top}}$ ,  $s_y^{\text{tower-top}}$  (fore-aft, side-side), in tower base fixed frame;

It is clear that, for the solution of the previous points 1 and 2, simple stability analysis for LTI technique can be employed. On the other side, solving point 3 requires a suitable treatment of the wind turbine periodicity. Finally, point 4 deals with a complete aeroelastic simulation of the whole turbine in normal wind shear but still without any coupled control system.

## 9.2 Results

### 9.2.1 Modes of isolated blade

In this section, the modal content of the isolated blade has been considered. All partners have been requested to provide the modal data (i.e. frequency and possibly damping factor) of the first ten blade vibratory modes, along with a “*name*”, which could describe the shape of each mode. Since the analysis is performed in *vacuo* and without gravity, the obtained results provide information related only to the inertial and structural properties of the blade.

Table 9.2 reports the frequencies of the first 10 blade modes, whereas Fig. 9.2 shows the uncertainty bar for each frequency (left), representing the spread in the results of all partners. Finally, Tab. 9.3 reports the damping factors.

From these results, it is clear that the agreement among partners’ predictions is excellent in terms of frequencies, if one considers the first four blade modes. As expected, the higher the frequency, the larger

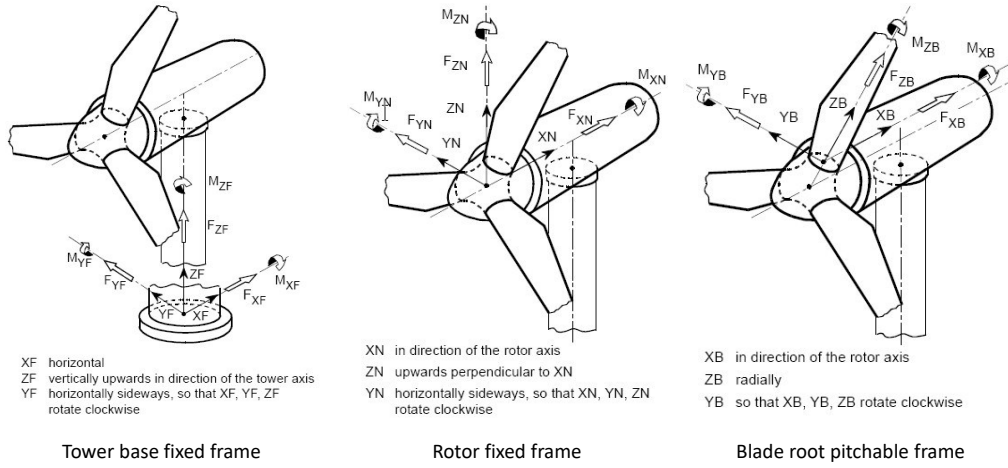


Figure 9.1: Sensor reference frames ( [71])

Table 9.2: Frequencies [Hz] of the first 10 modes of the isolated blade

Mode	Partners' results							
1 <sup>st</sup> flap	0.947	0.947	0.938	0.928	0.925	0.947	0.936	0.965
1 <sup>st</sup> edge	1.850	1.852	1.885	1.881	1.876	1.899	1.843	1.873
2 <sup>nd</sup> flap	2.685	2.708	2.688	2.643	2.653	2.651	2.651	2.672
3 <sup>rd</sup> flap	5.459	6.265	5.552	5.415	5.491	5.313	5.400	5.425
2 <sup>nd</sup> edge	6.312	6.315	6.729	6.707	6.822	6.958	6.263	6.213
4 <sup>th</sup> flap	9.361	10.718	9.696	9.452	9.729	8.848	9.274	9.364
3 <sup>rd</sup> edge	13.188	13.459	10.802	11.066	15.055	11.828	10.768	10.54
5 <sup>th</sup> flap	14.348	14.456	15.029	14.679	15.529	12.838	13.464	12.89
Combined vibrations	16.491	~	15.507	15.682	~	15.671	14.256	14.508
Combined vibrations	19.943	19.495	19.458		19.804	16.103	19.440	19.798
Combined vibrations		23.453			22.176	17.125		22.03

Table 9.3: Damping factors of the first modes of the isolated blade

Mode	Partners' results			
1 <sup>st</sup> flap	0.00695	0.0153	0.0153	0.0154
1 <sup>st</sup> edge	0.01526	0.0175	0.0175	0.01750
2 <sup>nd</sup> flap	0.02069	0.0434	0.0168	0.01699
3 <sup>rd</sup> flap	0.04495	0.0590	0.02	0.01800
2 <sup>nd</sup> edge	0.05435	0.0995	0.02	0.02033
4 <sup>th</sup> flap	0.08676	0.0997	0.02	0.02324
3 <sup>rd</sup> edge		0.1294	0.02	0.02459
5 <sup>th</sup> flap		0.1986	0.02	0.02699
Combined vibrations		~	0.02	0.03086
Combined vibrations		0.0181	0.02	0.03285
Combined vibrations		0.0355		

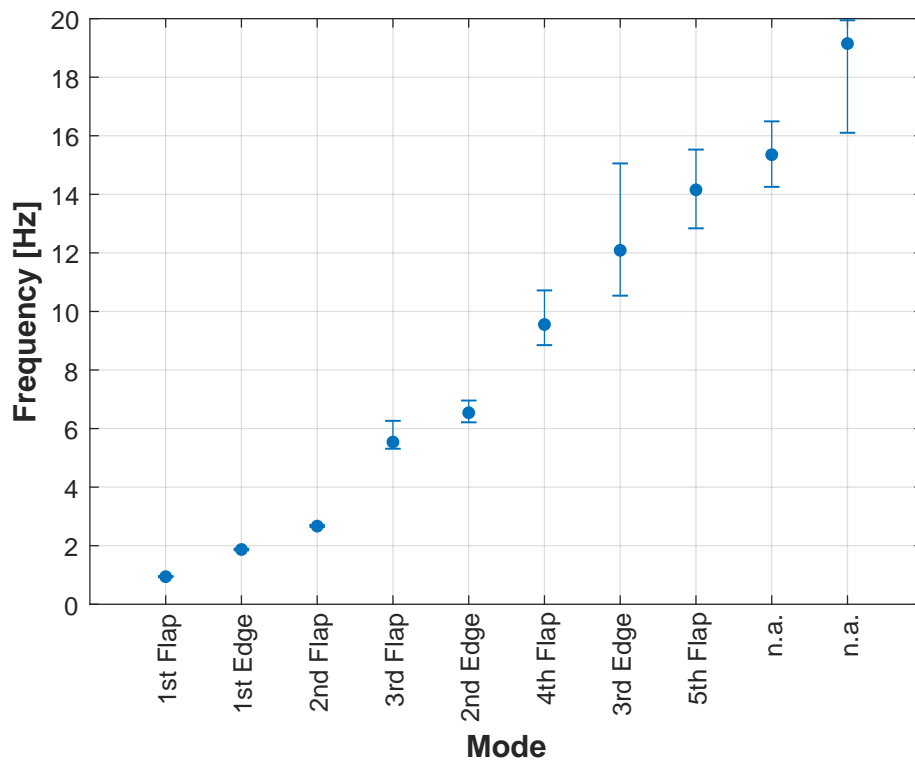


Figure 9.2: Frequencies of the isolated blade and spread of the results among partners. Points: mean values; bars: spread of the frequencies.

the spread. The apparent discrepancy in the prediction of higher modal frequencies is not surprising as the assumptions underlying the different implementations of beam models and the different procedures to extract the eigen-structure of the system may significantly impact on the estimation of the modal content. Since the frequency content of the wind is limited to the lower frequency range, having a good matching on blade frequency up to 10 Hz is more than acceptable.

Dealing with blade structural damping factors displayed in Tab. 9.3, it is possible to notice that there is a reasonable agreement among the results obtained by the four partners, that provided these values.

## 9.2.2 Modes of turbine at standstill

In this section, the modes of the entire turbine in standstill, i.e. in a parked condition, are investigated.

Similarly to the case of the isolated blade in § 9.2.1, standard stability analysis for LTI systems can be adopted to evaluate the modal characteristics of parked machine.

Table 9.4 reports the eigen-frequencies of the parked turbine *in vacuo*. The last column of the table is taken from [72] and refers to the frequencies extracted from real field vibratory data through peak-picking in the spectra of real field measured strain-gauge signals. The same data are also shown in Fig. 9.3, where the spread among Partners' results is indicated with light-blue bars, while the field estimations with dotted red markers. Finally, Tab. 9.5 reports the damping factors of the first turbine modes at standstill.

Table 9.4: Frequencies [Hz] of the first modes of the turbine at standstill

Mode	Partners' results								Field estimates (from [72])
1 <sup>st</sup> Tower Side-Side	0.454	0.428	0.468	0.482	0.414	0.4083	0.471	0.437	
1 <sup>st</sup> Tower Fore-Aft	0.470	0.449	0.481	0.504	0.416	0.4254	0.482	0.444	
1 <sup>st</sup> Drive-Train Torsion	0.666	0.669	0.667	0.675	0.654	0.6265	~	0.668	
1 <sup>st</sup> Rotor Yaw	0.893	0.94	0.871	0.850	1.018	0.8269	0.850	0.839	
1 <sup>st</sup> Rotor Tilt	0.949	0.947	0.941	0.914	1.018	0.8889	0.900	0.895	
1 <sup>st</sup> Rotor Collective Out-of-Plane	1.022	0.989	1.007	0.977	1.069	0.9707	0.994	0.955	
1 <sup>st</sup> Rotor In-Plane I	1.842	1.85	1.867	1.859	1.909	1.8059	1.870	1.838	
1 <sup>st</sup> Rotor In-Plane II	1.887	1.893	1.910	1.908	1.911	1.9051	1.920	1.853	
2 <sup>nd</sup> Rotor Yaw	2.297	2.608	2.250	2.254	2.002	2.0891	2.160	2.135	
2 <sup>nd</sup> Rotor Tilt	2.508	2.69	2.512	2.490	2.730	2.6340	2.500	2.401	
2 <sup>nd</sup> Rotor Collective Out-of-plane	2.763	2.707	2.754	2.696	2.786	2.7073	2.680		
2 <sup>nd</sup> Tower Fore-aft	3.988	3.986	3.983	4.243	4.298	3.9519			
2 <sup>nd</sup> Tower Side-side	4.129	4.289	4.040	4.278	4.300				

Apparently, the spread in the frequency computations is very low, especially for the first eight modes (i.e. up to 1<sup>st</sup> In-Plane II mode included).

The agreement becomes excellent if one considers the first tower, drive train and in-plane modes, as witnessed by the limited height in the error bars in Fig. 9.3. The same modes show also an excellent matching with the experimental results (red dots).

Surprisingly, the spread in the yaw, tilt and out-of-plane modes is higher but still acceptable. Similarly, the agreement with the experimental data is reasonable but not excellent, as an over-estimation of simulation models over field data is clearly visible in the plot.

As expected, the spread in Partners' results and errors with respect to field data increase for high-frequency modes.

As a final remark, there is a reasonable agreement among the results of the partners in terms of structural damping of the turbine at standstill, as reported in Tab. 9.5.



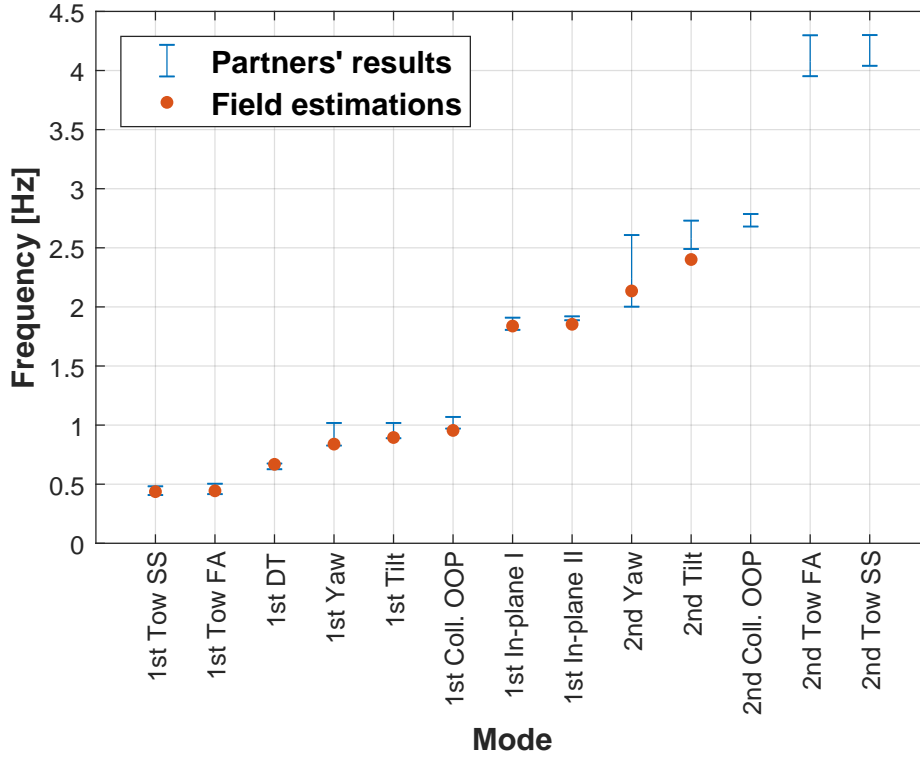


Figure 9.3: Frequencies of the turbine at standstill and spread of the results among partners. Points: estimations from field data (cf. Ref. [72]); bars: spread of the frequencies from partners' calculations.

Table 9.5: Damping factors of the first modes of the turbine at standstill

Mode	Partners' results		
1 <sup>st</sup> Tower Side-Side	0.0194	0.0045	0.0219
1 <sup>st</sup> Tower Fore-Aft	0.0212	0.0049	0.0207
1 <sup>st</sup> Drive-Train Torsion	0.0503	0.0010	0.0564
1 <sup>st</sup> Rotor Yaw	0.0153	0.0111	0.0213
1 <sup>st</sup> Rotor Tilt	0.0153	0.0144	0.0184
1 <sup>st</sup> Rotor Collective Out-of-Plane	0.0170	0.0156	0.0169
1 <sup>st</sup> Rotor In-Plane I	0.0175	0.0170	0.0277
1 <sup>st</sup> Rotor In-Plane II	0.0181	0.0176	0.0244
2 <sup>nd</sup> Rotor Yaw	0.0417	0.0134	0.0606
2 <sup>nd</sup> Rotor Tilt	0.0430	0.0156	0.0893
2 <sup>nd</sup> Rotor Collective Out-of-plane	0.0435	0.0170	0.0571
2 <sup>nd</sup> Tower Fore-aft	0.0621	0.0267	0.1496
2 <sup>nd</sup> Tower Side-side	0.0616	0.0229	

### 9.2.3 Campbell diagram of the entire turbine *in vacuo* and in air

The Campbell diagram is a plot of the eigen-frequencies of a rotating system as functions of the angular velocity of the rotor. As a rotating-bladed system, any wind turbine can be analyzed thanks to such a diagram.

In the case of wind turbines, often, since there is a linear dependency between rotor speed and wind speed in partial power region (region II), the diagram is expressed as a function of the wind speed itself instead of the rotor speed. This has also the advantage of allowing one to display the behavior of the system frequencies in the full power region (region III) with different collective pitch angles and constant rotor speeds.

The modal analysis of wind turbines in operating regimes presents a special feature, which is to be suitably considered: the system models are better characterized by periodic coefficients rather than invariant ones. Periodicity may arise for example from gravity, aerodynamics and tower-rotor interaction. It is important to stress that, even if we assume an ideal case without aerodynamics (*in vacuo*) and without gravity, the interaction among a flexible tower-nacelle group and the rotor blades represents a source of periodicity for the system, which is necessary to be considered to fully understand the so-called whirling modes [73].

Since the direct application of Floquet theory, which provides for a rigorous solution of the stability of LTP systems, is too computationally expensive especially for models with thousands of degrees of freedom, like modern multibody codes, it is preferable to employ different techniques.

Partners involved in the stability analysis have mainly used two procedures, one based on the Coleman transformation and the other on system identification.

Specifically, the procedure based on the Coleman (or multiblade) transformation follows this path. At first, the system is linearized about the steady periodic trajectory that the turbine reaches for constant inputs (wind and controls) after the initial transitory. The linearized periodic system is then converted in multiblade coordinates through the Coleman transformation, which is a simple periodic and known *a priori* transformation. It is possible to demonstrate that, if the rotor has three or more blades, such a transformation reduces dramatically the periodic content present in the multiblade-converted system matrices. Such a remaining periodicity can be then removed without losing the accuracy of the model. The final dynamical model turns out to be time-invariant and can be studied through a standard LTI technique, such that the Arnoldi algorithm, used to extract the lowest modes of a system without a direct solution of the eigenvalue problem. It is interesting to notice that removing the periodicity after the application of the Coleman transformation clearly generates an error in the computation of the modal characteristics. There is no rigorous procedure that can a priori estimate the upper bounds for such errors nor is there a demonstration that the simplification does not strongly propagate to system eigenstructure. However, extensive practice and comparisons performed with systems with few degrees of freedom show that Coleman-based algorithms generate frequency and damping estimates of high accuracy, providing that the linearization of the system be suitably performed. Additional material can be found in [68, 69] and references therein.

With identification-based approaches, one typically refers to non-intrusive methods which are applied directly to input-output time series generated through dynamic simulations. A linear time periodic input/output (I/O) model can be then fitted to the recorded time histories, yielding a reduced order periodic system, which can be analyzed through the Floquet theory. Clearly, if the reduced-order model has been suitably identified, its eigenfrequencies and damping factors are excellent approximations of those of the full model. As such, the methodology results model- and system-independent and does not require linearization. The clear disadvantage of this method is that the identification process cannot easily capture all highly damped modes, typically not visible in the system free response, and hence cannot provide the related frequencies and damping factors.

In the particular case of wind turbines, suitable input-output time histories can be obtained by perturbing the system from its periodic steady state regime through impulsive forces. Type and characteristics of the perturbation should be selected to neatly excite the mode of interest, while the output(s) to be recorded is to be chosen so as to see the vibrations related to those modes. As an example, a side-side impulsive force applied to tower top can be considered to excite tower side-side and whirling in-plane modes, all likely visible in the side-side tower root bending moment.

In the next section, the Campbell diagrams of NM80 *in vacuo* and in air are reported.

## NM80 Campbell diagram in vacuo

Figure 9.4 displays the Campbell diagram of the entire turbine in vacuo, in terms of the first eight modes. The wind speed, in the abscissa of the plot, does not refer to the inflow velocity, which is not included in the simulations, but to the couple rotor speed-pitch angle set according to Tab. 9.1. Each colored patch is related to a specific turbine mode and shows the spread in the location of the eigenfrequency predicted by partners. It is possible to notice how the different codes are able to capture the expected behavior of the frequencies and their behavior as functions of the rotor speed and pitch angle. The agreement between partners' results is acceptable, since the spread in predictions, even if certainly visible in the plot, is of a magnitude comparable to that of the standstill case (cf. 9.3).

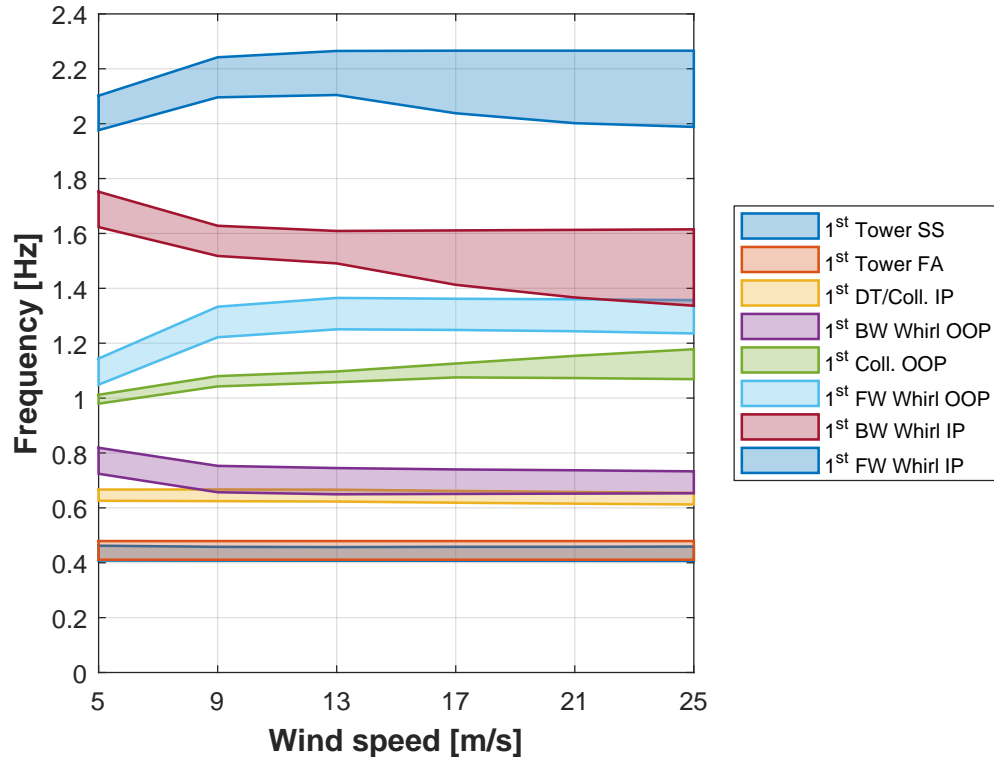


Figure 9.4: Campbell diagram of the wind turbine in vacuo and spread of the results among partners. Only first eight modes are displayed.

Figure 9.5 shows the damping factors of the eight first wind turbine modes in vacuo. All predictions for all modes stay in a range between 0 and 0.1, in line with what one would expect from simple structural damping.

## NM80 Campbell diagram in air

Figure 9.6 displays the Campbell diagram of the entire turbine in air, in terms of the first eight modes. The plot is arranged as in Fig. 9.4, with all patches indicating the spread in the results provided by the partners. Also in this case, there is a good agreement among partners' prediction, although the spread in the frequency location seems larger than the one obtained in the analysis in vacuo see above. This is especially true for the whirling modes, which, probably, are more affected by the details of the mathematical implementations of both the simulators and the tools performing the stability analysis.

Damping factors of the first eight modes of the turbine as functions of the wind speed are shown in Fig.9.7. As expected, out of plane and tower fore-aft modes undergo a significant increase in their damping factors due to the presence of the aerodynamics. In-plane whirling modes remain low-damped, as a demonstration of

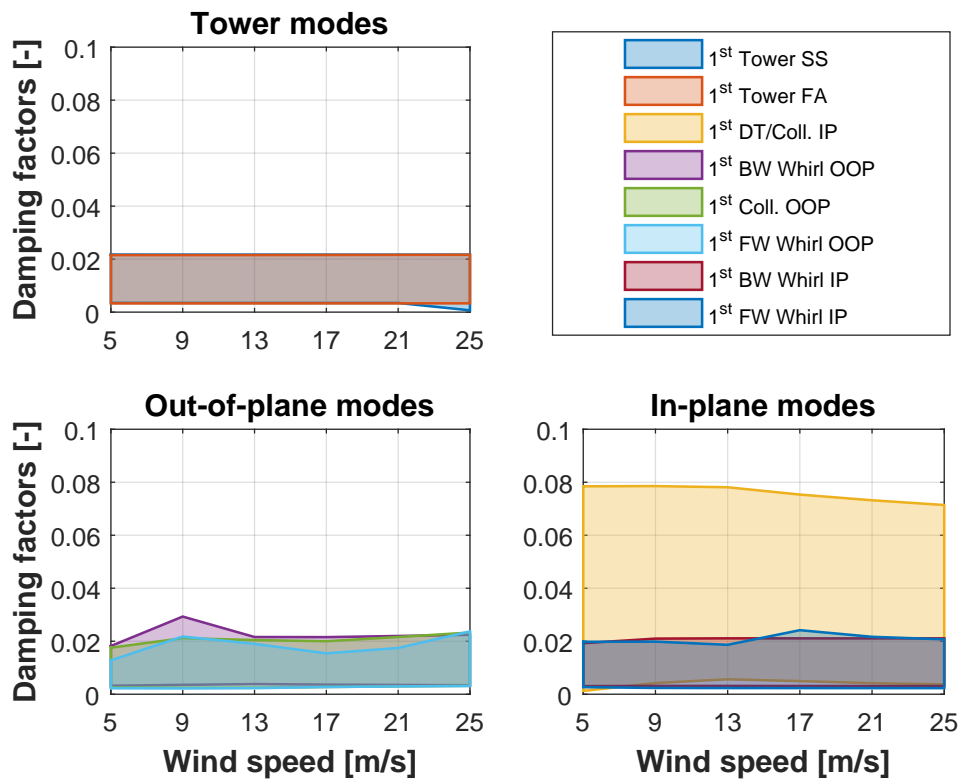


Figure 9.5: Damping factor of the first eight modes of wind turbine in vacuo and spread of the results among partners.

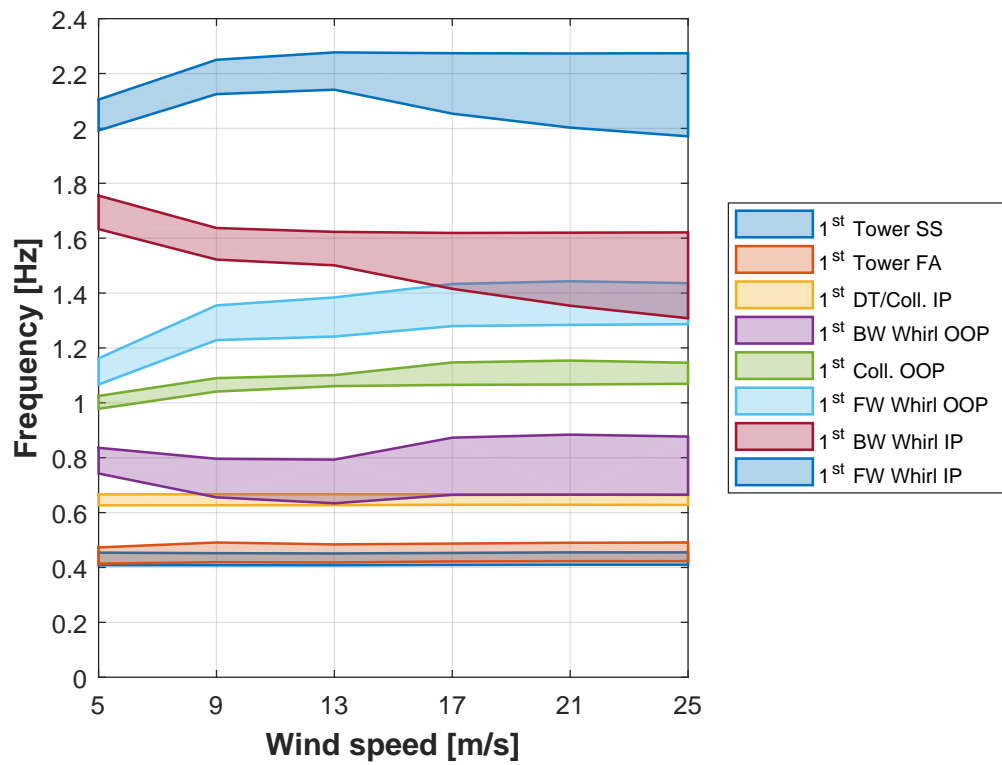


Figure 9.6: Campbell diagram of the wind turbine in air and spread of the results among partners. Only first eight modes are displayed.

the small impact of aerodynamics on in-plane vibratory characteristics. Finally, drive train mode experiences a progressive increase of damping in region III (full power region), due to the increase of the pitch angle entailing a larger inplane component of the lift of the blades.

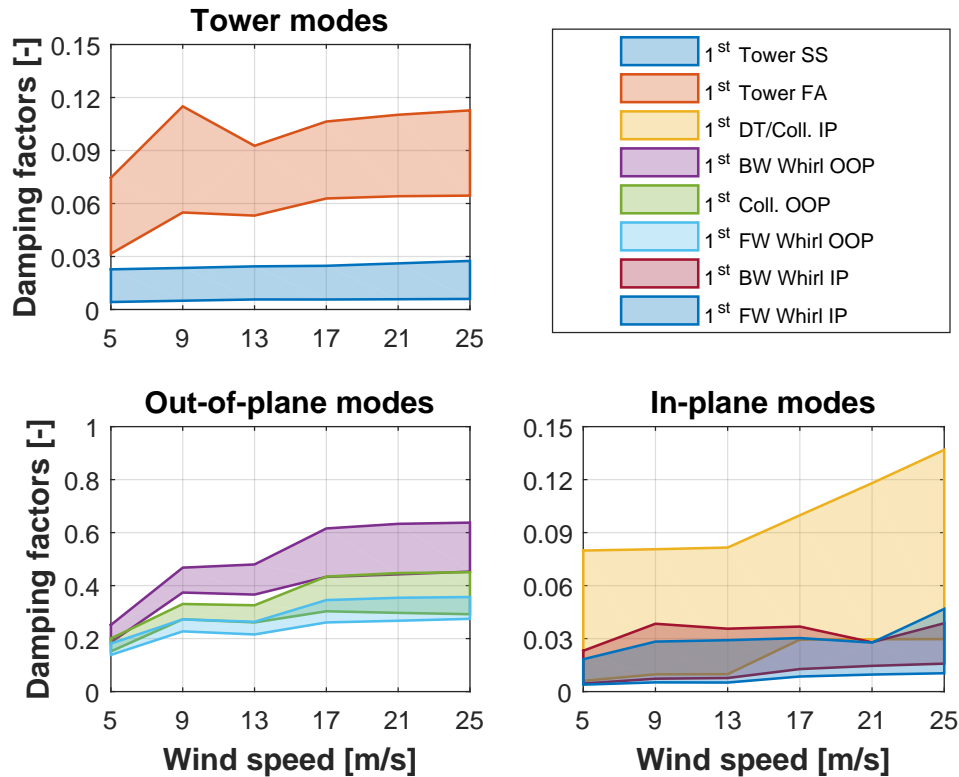


Figure 9.7: Damping factor of the first eight modes of wind turbine in air and spread of the results among partners.

To have a better understanding of the impact of aerodynamics in terms of modal damping, the difference between the damping factors in air and in vacuo has been computed. Clearly, subtracting or summing up directly damping factors, is not rigorous from the mathematical point of view, but can provide a rough estimation of how large is the contribution of what one could call “*aerodynamic-induced damping factors*”. Figure 9.8 show the aerodynamic-induced damping factor for the first eight modes. The plot makes it easier to evaluate how the aerodynamics affect the level of damping of the lowest turbine modes and to further verify the observation already derived from Fig. 9.7.

#### 9.2.4 Nominal Wind Profile (NWP) simulations

Full aero-elastic models have been finally used for performing time simulation of the turbine subject to a steady NWP wind. For different wind speeds within the operative range of the machine, the partners have been requested to provide the mean values of some variables of interest, according to the description reported in Sec. 9.1.

The comparisons among Partners’ results in terms of loads and displacements are shown from Fig. 9.9 to 9.14. Each figure refers to a set of loads reporting the different components as functions of the wind speed. Similarly to the previous analyses, the patches in the figure represent the spread in the Partners’ results.

Clearly, a good agreement on results has been obtained for all analyzed variables.

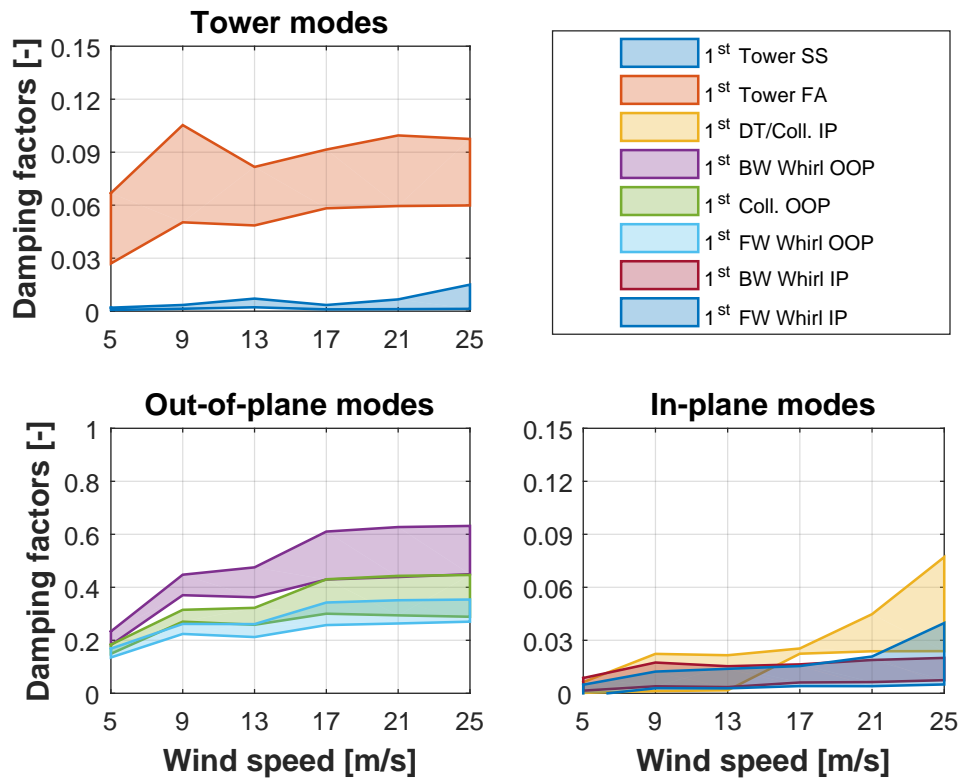


Figure 9.8: Aerodynamic-induced damping factor of the first eight modes of wind turbine in air and spread of the results among partners. Aerodynamic-induced damping is defined as the difference between the damping factors computed in air and in vacuo.

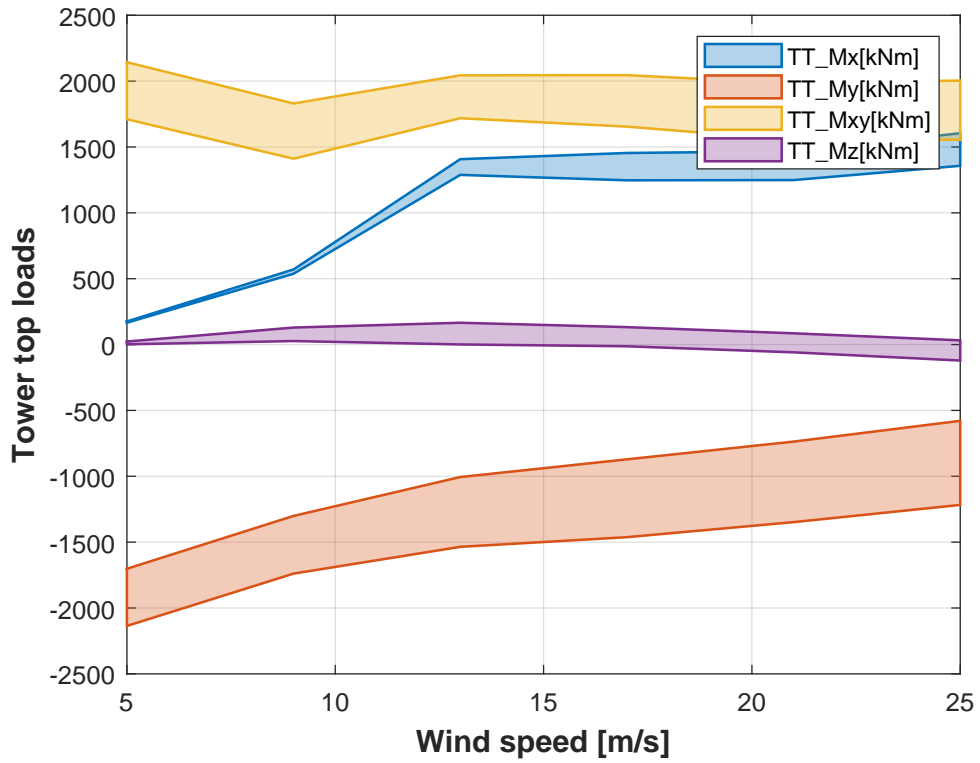


Figure 9.9: Mean tower top loads in NWP conditions as functions of the wind speed.

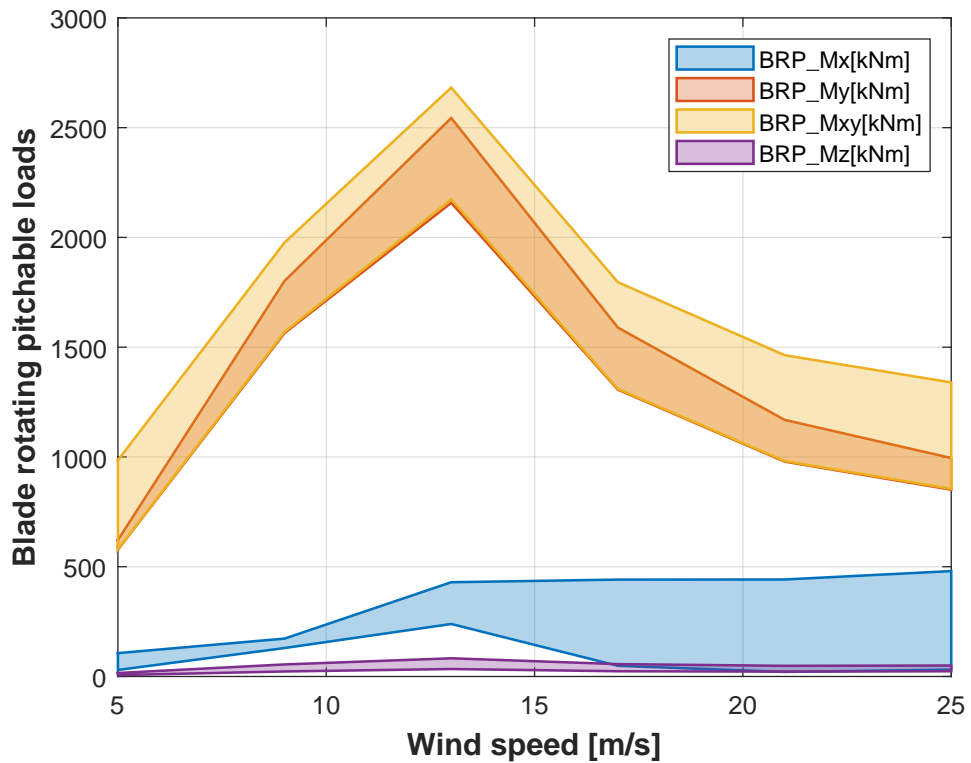


Figure 9.10: Mean blade rotating and pitchable loads in NWP conditions as functions of the wind speed.



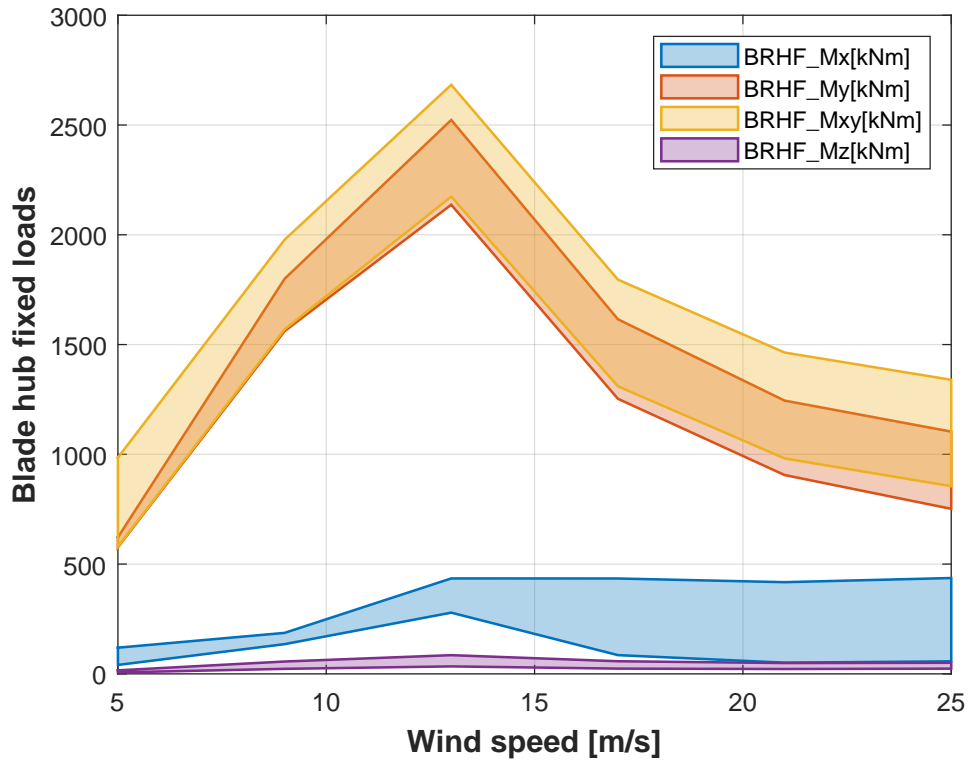


Figure 9.11: Mean blade hub fixed loads in NWP conditions as functions of the wind speed.

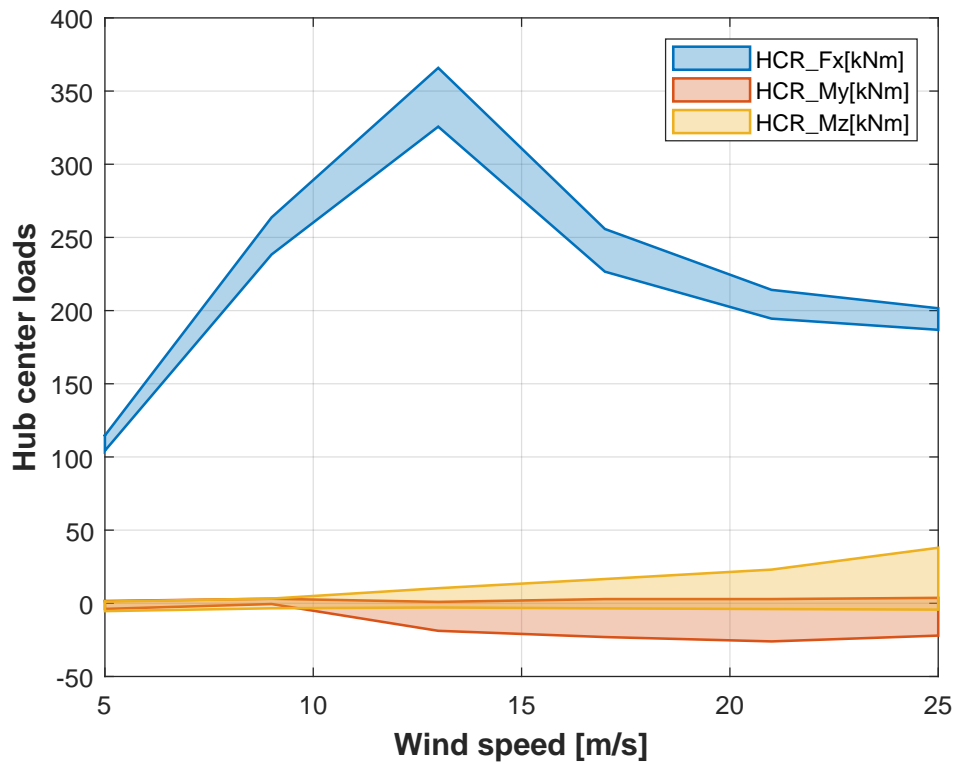


Figure 9.12: Mean hub center loads in NWP conditions as functions of the wind speed.

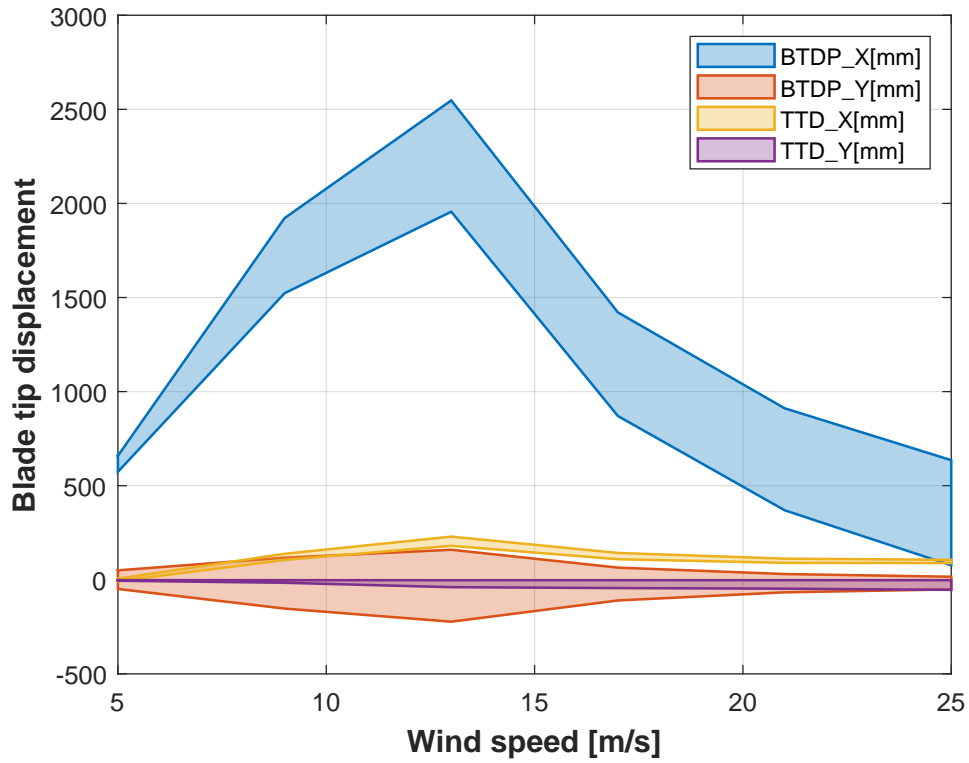


Figure 9.13: Mean blade tip displacements in NWP conditions as functions of the wind speed.

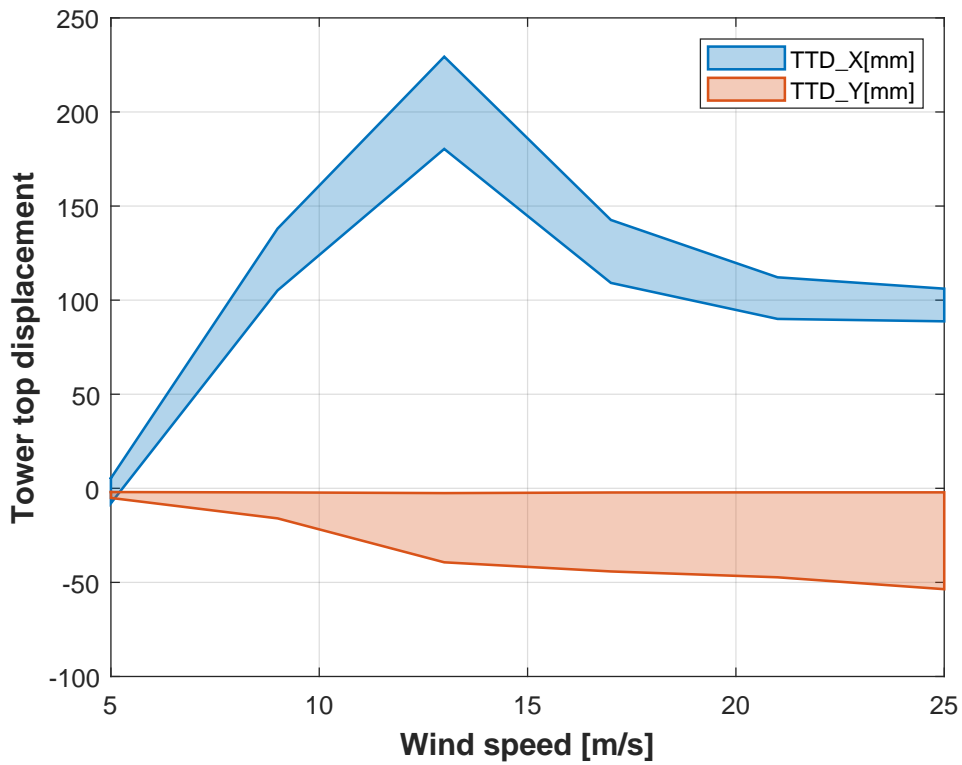


Figure 9.14: Mean tower top displacements in NWP conditions as functions of the wind speed.

### 9.3 Conclusions and comments on Task 3.5: Aeroelastic analyses

From the analysis conducted in Task 3.5, the following conclusions can be derived.

- The different codes and different analysis tools predict with a reasonable accuracy the modal characteristics of the wind turbine and of its blade.
- In terms of blade frequency, the agreement in the predictions is extremely satisfactory if one considers the lowest frequency modes, i.e. up to 7 Hz. This fact is of paramount importance as those blade modes are highly involved in the turbine dynamics and may affect its overall response. Computations of damping factors is more affected by the details of the beam model implementation inside the simulation codes. This fact is reflected on the higher level of spread, but absolutely acceptable, in the Partners' results.
- Similar conclusions can be derived for the modal characteristics of the turbine at stand still. Up to 2 Hz (a range of paramount importance for the aeroelastic response to realistic wind conditions), the agreement among Partners' results is excellent. Moreover, frequency predictions are in line with those obtained from a dedicated frequency estimation from field data. In terms of damping factors of the parked turbine, the comparison shows a reasonable agreement among Partners' estimations.
- Although the modal analysis of a rotating turbine is made more difficult due to the intrinsic periodic nature of the system, the predictions among partners are reasonably accurate especially for frequencies. With a mildly higher level of spread, also damping factors get predicted reasonably well.
- As expected from the good results obtained from modal analyses, loads and displacements computed from NWP dynamic simulations turn out to be reasonably accurate as witnessed by the low level of spread in the Partners' results.

# Chapter 10

## Task 3.6: Boundary Layer Transition

A. P. Schaffarczyk, B. A. Lobo, H.A. Madsen, Ö. S. Özcakmak

### 10.1 Introduction

In this chapter the work from Task 3.6 is described which is a combined activity of DTU Windenergy (H.A. Madsen and group) and Kiel University of Applied Science (KUAS) (B. A. Lobo and A.P. Schaffarczyk) on boundary layer transition on MultiMega watt turbines operating in the free atmosphere. A work plan for this task was defined which included the following items:

- Discussion about DAN-AERO (NM80) and aerodynamic glove (MM92) findings
- Targeted search for indications of by-pass transition
- Possibility to find a meaningful definition (and reasons) for a *low-pass* cut-off for *aerodynamic* inflow-turbulence in the range of 10 to 100 Hz
- Definition of CFD runs
- Possibilities for future experiments

To a certain amount this report may be regarded as a follow-up of [74].

### 10.2 Discussion of Results from DAN-AERO and Aerodynamic Glove on MM92 Experiments

#### 10.2.1 DAN-AERO

The analysis presented here is performed by using the data from the DAN-AERO project, see chapter 3 and [75] [76], where the LM-38.8 blade of the 2 MW NM-80 rotor placed in a wind farm was inspected. The blade section that is 36.8 meters from the hub is equipped with pressure taps and high-frequency microphones. The boundary layer transition is detected from the surface pressure fluctuations obtained from the high-frequency microphones. The inflow turbulence is also interpreted from the leading edge microphone in the laminar boundary layer. Moreover, DTU in-house CFD solver EllipSys3D [77] [78] [79] full rotor simulations are performed for comparison.

#### Background

The standard deviation method is used to detect transition where root-mean-square (RMS) values of the pressure fluctuations are obtained by integrating the power spectral density(PSD) in a particular frequency range. The data is filtered in 2 kHz to 7 kHz frequency range transition detection. A sudden chordwise

increase above a threshold value in standard deviations indicates the transition location on the surface. Figure 10.1 shows an example of the PSD vs frequency ( $f$ ) at different chordwise positions ( $x/c$ ) on the pressure side for the airfoil profile replicated from the LM-38.8 blade section tested in a wind tunnel at  $Re = 3 \cdot 10^6$ ,  $AOA = 0^\circ$ . The peak in the spectra, indicating a Tollmien-Schlichting (T-S) wave frequency, shows the natural transition process. The microphone at  $x/c=0.48$  (blue line) is under a transitional flow. The turbulent spectra can be observed from the PSD at  $x/c= 0.54$  (orange line).

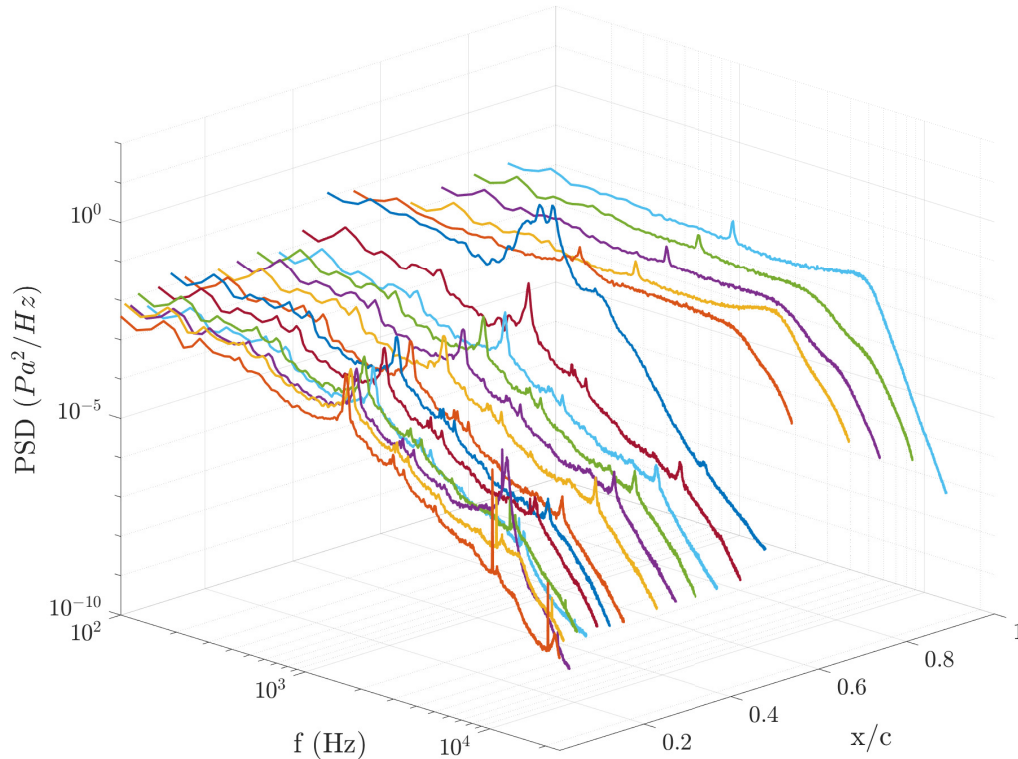


Figure 10.1: PSD at various chordwise locations on the pressure side,  $Re = 3 \cdot 10^6$ ,  $AOA = 0^\circ$  [80].

Furthermore, inflow turbulence characteristics are interpreted using a signal from a leading edge microphone at 0.2% chordwise position at a frequency range from 100 Hz to 300 Hz. At this chordwise position the boundary layer flow is laminar and the spectra of the pressure fluctuations will therefore correlate well with the inflow turbulence. Comparing now spectra from the rotor and from 2D wind tunnel flow, see Figure 10.2 it can be seen that from about 300 Hz and towards lower frequencies the energy content in the rotor spectra have increasingly higher energy content, except when comparing with wind tunnel flow with a turbulence grid inserted. A hypothesis is therefore that differences in transition between rotor and wind tunnel flow should be correlated with the differences in the energy contents below 300Hz. As mentioned above we have chosen to use the difference in energy between 100-300Hz but it could also e.g. be between 50-300Hz. However, at some low limit the boundary layer will only feel the impact of flow speed variation as unsteady flow.

Detailed information about the method and set-up can be found in previous publications [82] [83], [81]. The transition in EllipSys3D CFD simulation are modelled by a semi-empirical  $e^N$  model [84]. This model can be used together with bypass criteria in EllipSys3D. The Suzen and Huang [85] empirical model is used to simulate high turbulence intensity levels where bypass transition can be observed. The code checks the criteria for both natural and bypass transition simultaneously.

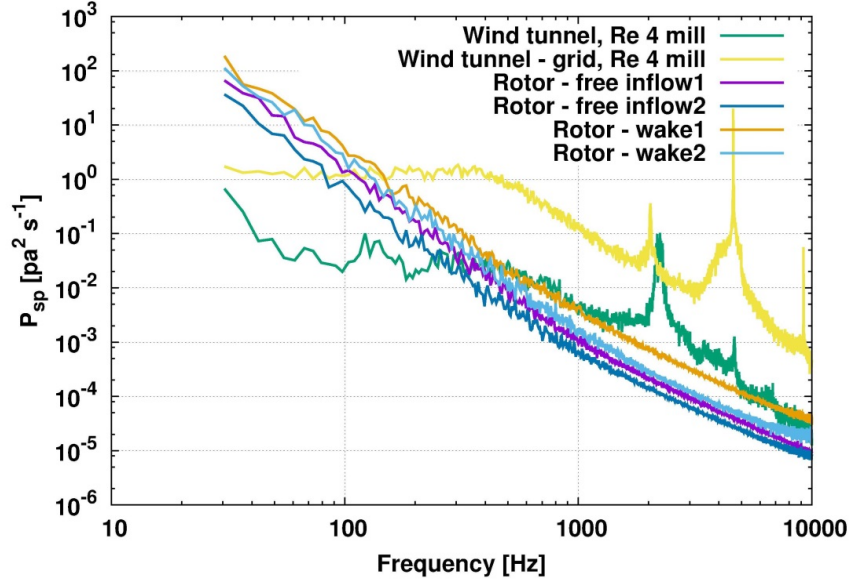


Figure 10.2: The power spectra of the signal from the microphone on the suction side at 0.2% chord from the LE (laminar boundary layer) for the airfoil section on the rotor and for the similar section in 2D wind tunnel flow. Figure from [81]

### Angle of attack and inflow turbulence effects on transition

The analysis presented here involves DAN-AERO experiments where the turbine was operated at two different pitch angle settings ( $1.25^\circ$  and  $4.75^\circ$ ). The free-stream velocity measured from the meteorological mast for the selected cases varies from 5 to 8.5 m/s. The turbulence intensities (TI) for the presented cases differ from 2.8% to 6.8%. In some of the cases, the turbine is operating partially under the wake of an upstream turbine. In EllipSys3D, several simulations are performed for different free-stream velocities and different amplification ratios ( $N=0.15$  to 7) for the natural transition model, and turbulence intensities for the bypass transition model.

The CFD results for the case with a pitch setting of  $4.75^\circ$ , with a free stream velocity of 7.2 m/s is presented in Figure 10.3. The amplification ratio ( $N$ ) of 3 is used for this simulation and the vorticity structures from the rotor colored by the axial velocity ( $w$ ) are shown at the top-left. The intermittency factor ( $\gamma$ ) which characterize the laminar, transitional and turbulent parts on the surface is shown for the blade section (top-right) and on pressure and suction sides (bottom) of the blade. The blue areas ( $\gamma=0$ ) show the laminar and the red parts ( $\gamma=1$ ) show the turbulent parts on the surface.

Figure 10.4 shows the experimentally detected transition positions on the pressure side of the blade section as a function of the blades azimuthal position during four revolutions. In this selected case, the rotor is operating at a pitch angle of  $4.75^\circ$ , at a free stream velocity of 8 m/s and turbulence intensity of 2.8% that corresponds to the  $N=0.15$  with Mack's [86] estimation. The decreasing angle of attack by the reduced relative velocity in the wake region causes experimentally detected transition locations to move around 20% of the chord. Furthermore, the regions where transition detected at 3% of the chord indicates the direct effect of the inflow turbulence on the transition location in addition to the decreasing angle of attack. This direct effect is analyzed in a previous study [81] by binning the transition locations according to the effective angle of attack on the blade. In this way, a direct correlation between the inflow turbulence and the detected transition points is established. The regions where the direct effect is visible indicates bypass type transition as defined by Morkovin [87]. It is seen that the experimental results match the numerical bypass transition model results in this region. Several EllipSys3D simulations are performed to cover these occurrences (both natural and bypass transition) as the measured blade is moving in an out of the wake region during a single revolution. It can be seen that these several simulations are able to cover most of the scenarios that the turbine is exposed to during a revolution.

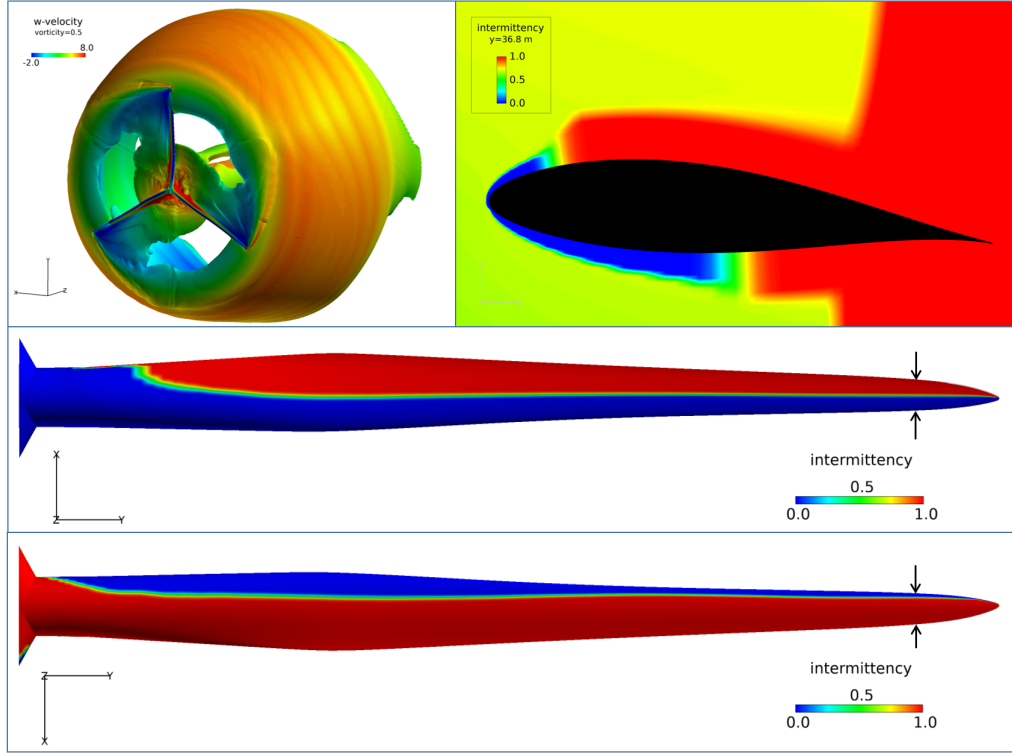


Figure 10.3: The vorticity iso-surfaces coloured by the axial velocity (top-left); intermittency( $\gamma$ ) at the blade section at  $y=36.8$  m from the hub(top-right); The  $\gamma$  values on the pressure (middle) and suction sides (bottom) of the blade for  $U_\infty=7.2$  m/s,  $N=3$ ,  $p=4.75^\circ$ . (Note that the free stream flow is in  $+z$  direction and the rotational speed in  $-x$  direction for the blade at azimuthal angle of  $0^\circ$ ). (The blade section that is analysed in the current study is highlighted by the arrows on the blade.) [82].

Analysis of several measurements from different days with various inflow velocity and turbulence conditions as well as two different pitch settings are collected in a single figure (Figure 10.5) that shows detected transition position as a function of angle of attack. The EllipSys3D results are also included by calculating the effective angle of attack. Moreover, wind tunnel experiment results obtained from the replication of the blade section profile tested in a controlled environment with high-frequency microphones are also included. EllipSys2D simulations for 5 million Reynolds number are included for comparison with the experiments.

It is seen that experimentally detected transition locations scattered along 44% of the chord on the pressure side during a single revolution when the wake influenced area of the rotor is large. On the other hand, when the rotor area affected by the wake is small, at low angle of attack values, the variation of the transition location along the chord during a single revolution drops to 5% [80]. These fluctuations in the transition location during one revolution is represented by EllipSys simulations conducted with different amplification factors( $N=0.15, 3$ , and  $7$ ) for natural transition and different turbulence intensity( $T.I.=2.8\%$ ,  $3.8\%$  and  $6.8\%$ ) values for the bypass transition model.

It is not easy to comment on the suction side as all the experimentally detected transition locations are in very close proximity to the leading edge (varying from 1% to 13%). Furthermore, analysis of the pressure tap measurements reveals surface bumps on the suction side which might be one of the factors affecting transition. The differences between wind tunnel conditions and field experiments are also observable mainly due to inflow turbulence and wake from an upstream turbine. The wake from an upstream turbine and inflow turbulence in real atmospheric conditions not only affect the relative velocity and angle of attack but also has a direct effect on transition. Several simulations from EllipSys3D, featuring different inflow scenarios, with  $e^N$  semi-empirical transition model, show agreement with low inflow turbulence cases where

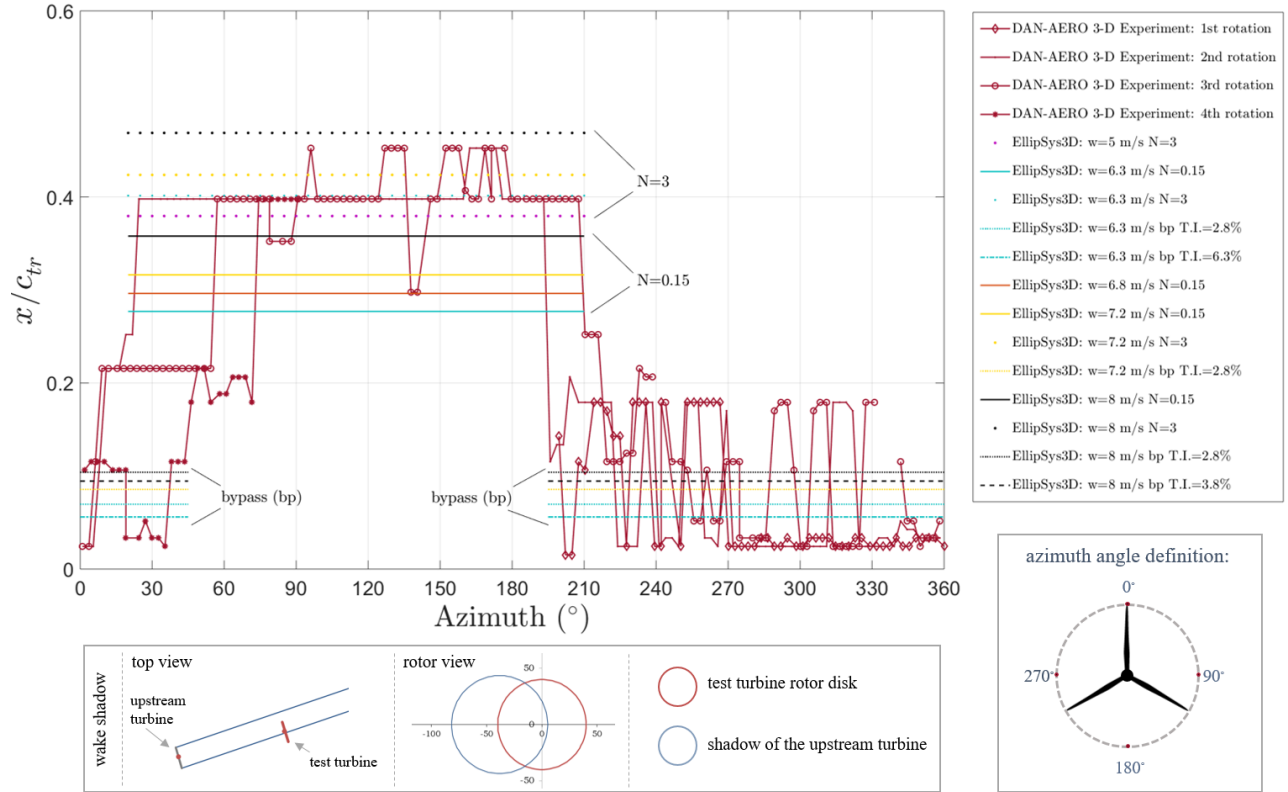


Figure 10.4: Experimentally detected transition points as function of azimuth angle and EllipSys3D simulations transition results for various different scenarios for the pressure side of the blade section. (The CFD results are labelled by colors for the different free-stream velocities ( $w$ ); i.e. black:  $w=8$  m/s, yellow:  $w=7.2$  m/s, orange :  $w=6.8$  m/s, turquoise:  $w=6.3$  m/s, purple:  $w=5$  m/s)(The wake region and azimuthal angle definition is given at the bottom) (Figure regenerated from [82]).

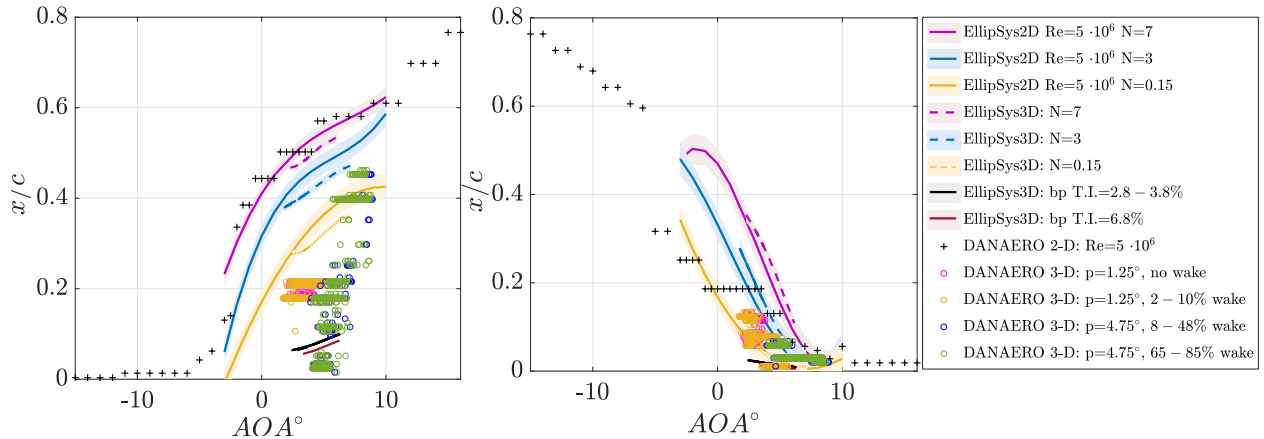


Figure 10.5: Detected transition points from the field and wind tunnel experiments and from the 2-D and 3-D CFD computations for the pressure side(left) and for the suction side(right). (The EllipSys 2-D and 3-D results are presented as a fitted line of the data. Shadows around the lines show the standard deviation of the fit.) [82].



we observe natural transition behavior. On the other hand, the bypass transition model of EllipSys3D shows an agreement with the high turbulence (wake affected inflow) cases where a bypass type transition behavior is observed in the experiments. It is seen that both natural and bypass type transition mechanisms can occur in a single revolution of the turbine.

### 10.2.2 Aerodynamic Glove

After preliminary investigation on a 15 m blade on an ENERCON E30 [88] blade, a similar measurement was undertaken on LM 43P blade mounted on a Senvion (REpower) MM92 [89]. Transition was intended to be detected by an array of microphones (like in the DanAero experiment) but enhanced by two teams (DLR Göttingen and Deutsche Wind Guard Engineering, Bremerhaven) who performed ground-based thermography. Due to the very short time of data compilation and a non-perfect surface preparation only a few data sets with large areas of mutable laminar boundary layer state could be recorded. Nevertheless, main finding was equal accuracy of microphones and thermography with regard to determination of transition location. The term *aerodynamic glove* was borrowed from Seitz [90].

## 10.3 Targeted search for a possible low-pass cutoff

### 10.3.1 Background

Transition onset sometimes (esp. in wind tunnels) can be related to turbulence intensity (TI). An example is Mack's (empirical) correlation [91]

$$N = 3.56 - 6.18 \cdot \log_{10}(100 \cdot TI) . \quad (10.1)$$

TI is determined by integrating a time-series (600 sec in most applications for wind turbines). But here is the problem: As most energy is close to the maximum (a frequency range of few mHz) taking this *load turbulence* seems to be not meaningful, as the boundary layer seems to be able to follow transient gusts up to several Hz. The question therefore is: Is there a low-frequency cut-off for wind turbulence which does **affect** laminar to turbulence transition and if so, how can it be determined? Similar questions arise in comparable investigation on wings of airplanes [92].

Unfortunately, so far no complete answer can be given. A first step towards an explanation is related to the connection of how much energy (as function of frequency) of the inflow turbulence penetrates into the boundary layer. These types of investigations were undertaken by B. A. Lobo and are described in more detail in section 10.3.2 as part of LES (Large-Eddy-Simulation) investigations for laminar-turbulent transition on wind turbine blades including turbulent inflow.

### 10.3.2 LES investigations

In July 2018, as part of the Aerodynamic glove experiment on the 2MW Senvion MM92 wind turbine, microphone and pressure sensor measurements together with thermographic imaging to study transition on a blade of 45 m length were collected as described in Section 10.2. A good agreement was found between the data from the microphones and the thermographic imaging technique [89]. However, the location of the laminar-turbulent transition in an associated Reynolds-Averaged Navier-Stokes (RANS) CFD simulation of the transitional flow using an  $N$ -factor with respect to Mack's correlation [91] and corresponding to the inflow turbulence intensity, deviated from the experimental results. It was therefore proposed to conduct wall-resolved large-eddy simulations (LES) to better understand the transition process within atmospheric turbulence and to look for a possible low-frequency cut-off as a procedure to possibly extend Mack's correlation as proposed in [88].

Wall-resolved LES combined with an inflow procedure relying on synthetically generated turbulence [93] and a source-term formulation [94] for its injection within the computational domain allow the investigation of relevant flow features such as separation bubbles, Tollmien-Schlichting (T-S) disturbances and streaks. The term streak refers to the velocity relative to the mean local mean,  $U(x, y, z, t) - \bar{U}(x, y) > 0$ .

Due to the high computational costs, the LES of the flow around a section of the blade with a relative thickness of 20 % corresponding to the profile at a radius of 35 m on the wind turbine blade corresponding

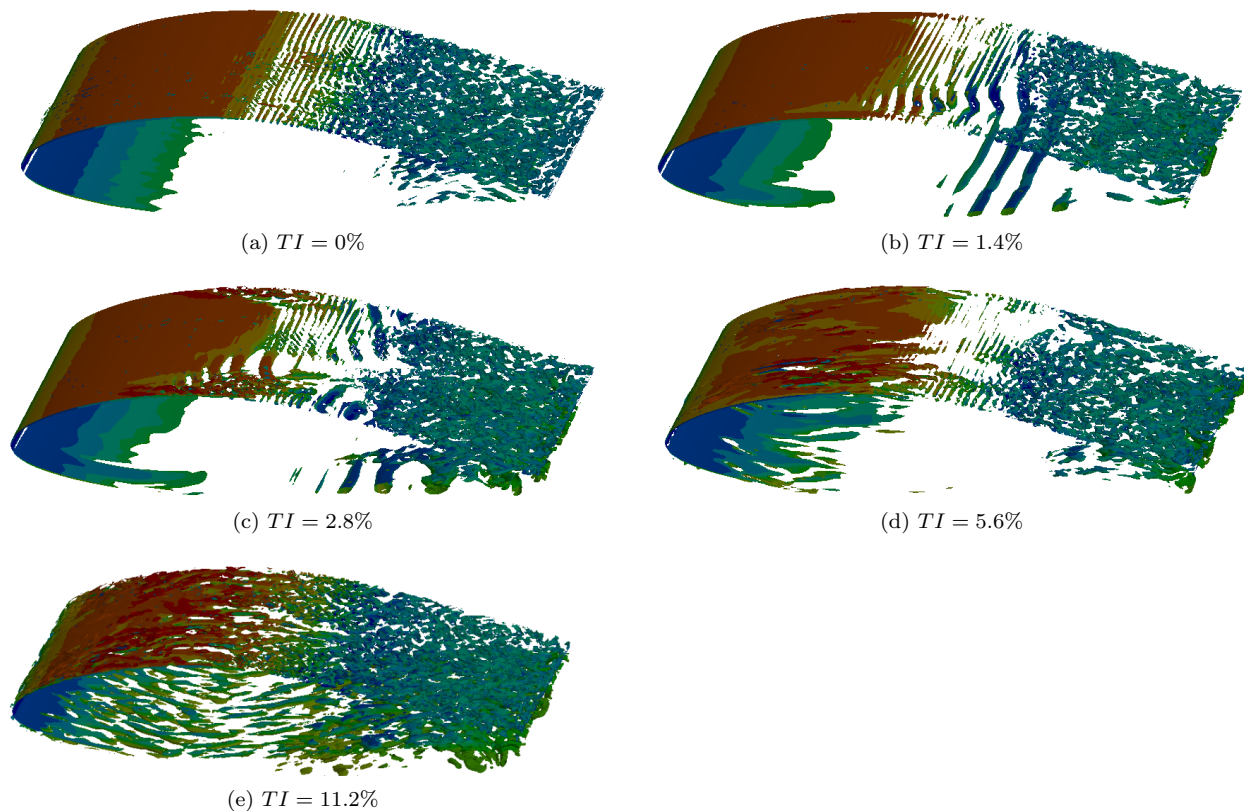


Figure 10.6: Instantaneous iso-surfaces of the  $Q$ -criterion ( $Q = 250$ ) colored by the mean streamwise velocity normalized by  $u_\infty^2/c^2$ . The  $Q$ -criterion is commonly used for vortex visualization and it defines vortices as areas where the vorticity magnitude is greater than the magnitude of the rate of strain [95].

to the aerodynamic glove experiment is conducted. On account of limited literature on the investigation of boundary layer transition around wind turbine blade sections with modeled inflow turbulence at high Reynolds numbers corresponding to the aerodynamic glove experiment, it was decided to step-up the chord Reynolds number incrementally beginning at a rather low Reynolds number of  $Re_c = 10^5$  through a PhD project. The results at this chord Reynolds number are included here. The study further focuses on the flow past this section at an angle of attack of  $\alpha = 4^\circ$  which lies within the range measured during the experiment. A parameter study with varying inflow turbulence intensities of  $TI = 0, 1.4\%, 2.8\%, 5.6\%$  and  $11.2\%$  was carried out. These incremental values were chosen to study the effects of increasing  $TI$  on the transition scenario.

Figure 10.6 shows instantaneous snapshots of the dimensionless  $Q$ -criterion normalized by  $u_\infty^2/c^2$  (with  $u_\infty^2$  being the far-field streamwise velocity and  $c$  being the chord-length) and colored by the mean streamwise velocity averaged along the spanwise direction and in time. In the absence of added inflow turbulence, i.e. an effective  $TI$  of  $0\%$ , cylindrical structures or rolls which are a characteristic for a Tollmien-Schlichting growth of disturbances are clearly visible. At their onset they are more or less two-dimensional, with slight three-dimensional effects seen as the flow progresses downstream.

With an increase in the inflow turbulence intensity to  $1.4\%$ , similar T-S structures are seen, albeit, occurring with relatively more three-dimensional effects. With a further increase in  $TI$  to  $2.8$  and  $5.6\%$  the influence of external streaks becomes more pronounced as will be made clear using the power spectral density plots of Figure 10.7 as will be described below. At the highest  $TI$  of  $11.2\%$  T-S rolls are no longer seen in Fig. 10.6 nor is any indication of their presence seen on the PSD plot which is not included here.

To investigate the mode and process of transition and to look for possible low-frequency influences of the turbulence energy spectra on the boundary layer receptivity in the case of bypass transition through the

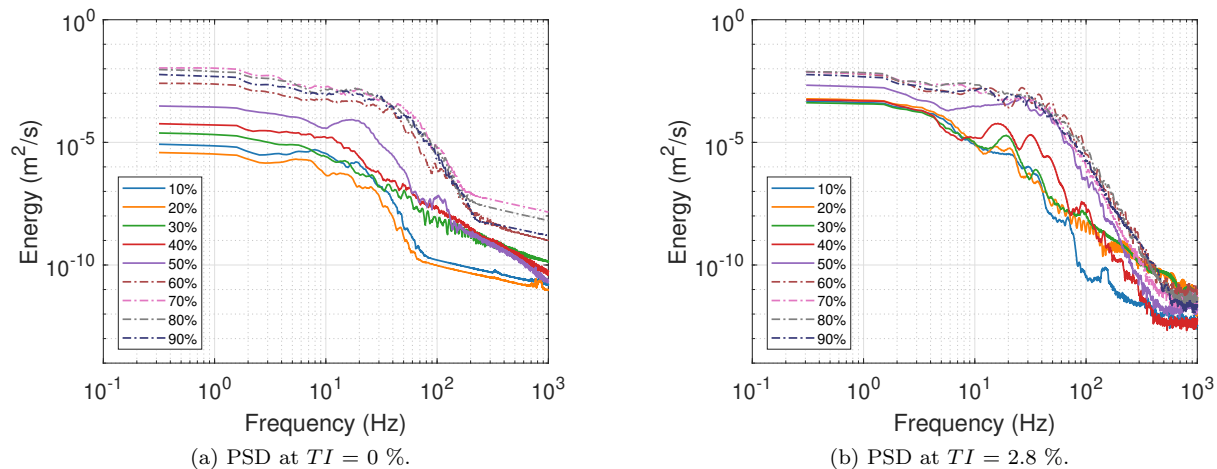


Figure 10.7: Power spectral density at different levels of the turbulence intensity determined at the height of the displacement thickness at the mid-span.

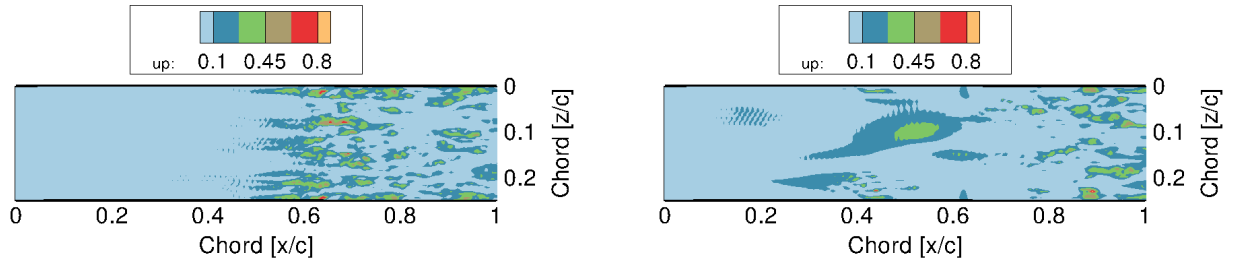
entry of boundary layer streaks, it was necessary to analyze the power spectral densities along the chord. Figure 10.7 shows the PSD plots generated using a Hann windowing function on the data which was collected at every 10 % chord. A total of  $2^{16}$  data points covering 3.28 dimensionless time units was used. In order to follow the transition process, even in the laminar separation region, data evaluations were carried out at the height of the boundary layer displacement thickness and at the mid-span.

At an inflow turbulence intensity of 0 % the growth of T-S disturbances beginning at about 30 % chord indicated by the continuous green line in Fig. 10.7a can be recognized by a clear increase in energy up to thousand Hertz. The T-S disturbances continue to grow in the downstream direction. This growth is seen at 40 % chord without any noticeable irregularity compared to the upstream location. However, at 50 % chord, a further increase in energy between approximately 70 and 150 Hz is found, indicated by the continuous purple line. This observation is attributed to the formation of streaks within the boundary layer at this location as seen in Fig. 10.8a.

For the sake of brevity, the case with an inflow  $TI$  of 1.4 % is not included as the effects seen in this case are also observed with an inflow  $TI$  of 2.8 %. At an inflow  $TI$  of 2.8 % the growth of T-S disturbances is visible at 20 and 30 % chord as seen in Fig. 10.7a. However, at 40 % chord, the entry of an external streak into the boundary layer is observed through an increase in energy in the low-frequency range up to approximately 100 Hz. Figure 10.8b illustrates the entry and development of a streak.

With an increase in  $TI$  to 5.6 % it is observed that external streaks intermittently enter the boundary layer right from the leading edge as indicated in Fig. 10.9. Due to the entry of multiple streaks into the boundary layer during the simulation, it was found necessary to isolate, extract and analyze data prior to the entry of the selected streak and compare the generated PSD plot to one generated on the passing of the streak through a point of interest. This is done in order to study the frequency characteristics of the streak. For this purpose data was extracted over 300,000 time steps covering an interval of 1.5 dimensionless time units. The data being sampled at every tenth time-step results in 30,000 data points, which is sufficiently large for the resolution of low-frequencies. According to this data, the streak begins to pass through 10 % chord at around the 12,000<sup>th</sup> data point. A comparison between the PSD plots at this location before and during the passing of the streak is shown in Fig. 10.10. A clear increase in energy up to 100 Hz is seen. Similar comparisons were made at downstream positions up to 50% chord after which the streak breaks down into turbulent flow. A similar result was observed at all locations.

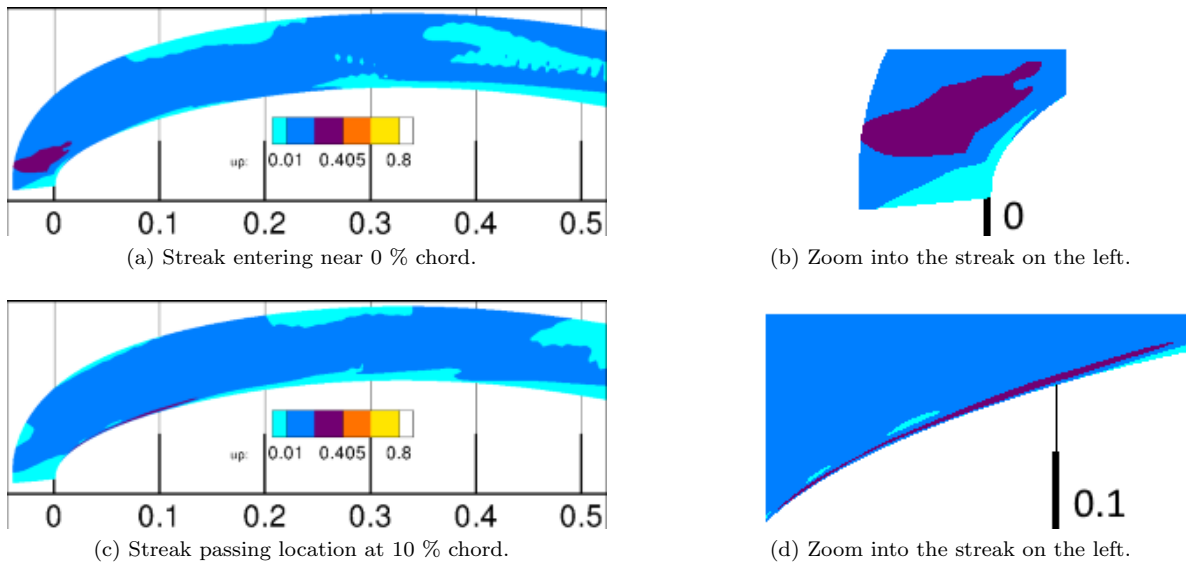
It is therefore concluded that at higher inflow turbulence intensities the transition scenario noticeably deviates from the T-S mode of transition observed for the lower inflow turbulence intensities with the influence of external streaks increasing with rising  $TI$ . External streaks enter the boundary layer and grow laterally and longitudinally before the flow turns fully turbulent. Accordingly, the influence of T-S disturbances



(a)  $TI = 0\%$ :  $u'$  streaks develop within the boundary layer at about 50 % chord.

(b)  $TI = 2.8\%$ : An external streak enters the boundary layer and grows laterally, passing through the data acquisition location at about 40 % chord at the mid-span.

Figure 10.8: Development of streamwise velocity fluctuations to visualize the entry of external streaks into the boundary layer. Slices are taken at a height equal to the displacement thickness corresponding to 50 % chord at the mid-span.



(a) Streak entering near 0 % chord.

(b) Zoom into the streak on the left.

(c) Streak passing location at 10 % chord.

(d) Zoom into the streak on the left.

Figure 10.9: Slices through the mid-span showing the entry of an external  $u'$  streak and its movement within the boundary layer at  $TI = 5.6\%$ . The horizontal axis displays the chord position  $[x/c]$ .

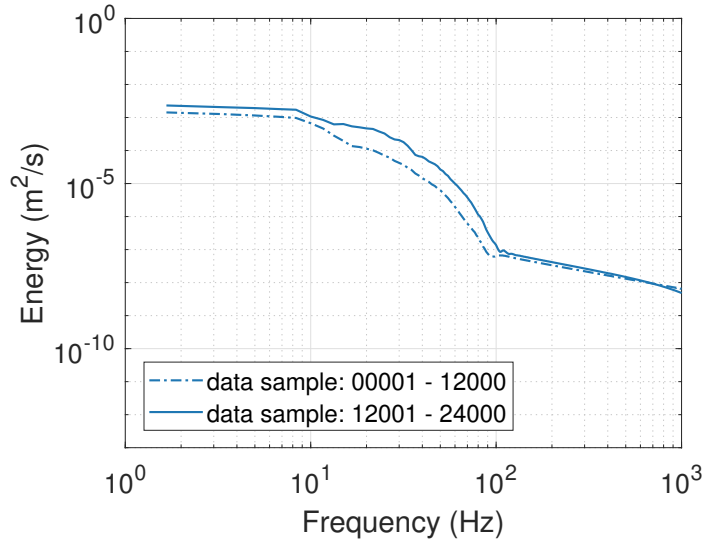


Figure 10.10: Change in the energy content on the entry of the relatively high velocity streak that was followed at 10 % chord ( $TI = 5.6$  %).

decreases with increasing  $TI$ , while the influence of external streaks increases. In such a scenario an increase in energy in the low frequency range is observed.

## 10.4 CFD runs

Only a very limited number of teams performed 3D-CFD runs including transitional modelling.

- DTU using EllipSys 3D
- IAG using FLOWer
- KUAS using FLUENT and a mesh prepared by FORwind/IWES

Fig. 10.11 summarizes the findings for the transition line for Case 1 ( $v_{in} = 6.1$  m/s and 12.3 RPM: Two groups of near-by results seems to be visible:

1. A group consisting of two applications of Menter's  $Re_{\vartheta} - \gamma$  model and
2. Drela's model and the *FLUENT Bra* case

The difference between FLUENT pre(liminary) and FLUENT Bra(ndon Lobo) is due to a much larger (50 k increased to 200 k) number of iterations despite the fact most of the residuals (mass flow, for example) seemed to be converged.

## 10.5 Summary and Conclusions of Task 3.6: Boundary Layer Transition

In WP 3.6 a set of 5 items have been defined to investigate 3D laminar to turbulent transition on a the LM38 blade used on the NecMicon 80 turbine. A number of important results have been found:

- Large scale experiments on two wind turbines (NM80 and MM92) clearly proved - highly transient - laminar parts on the boundary layer

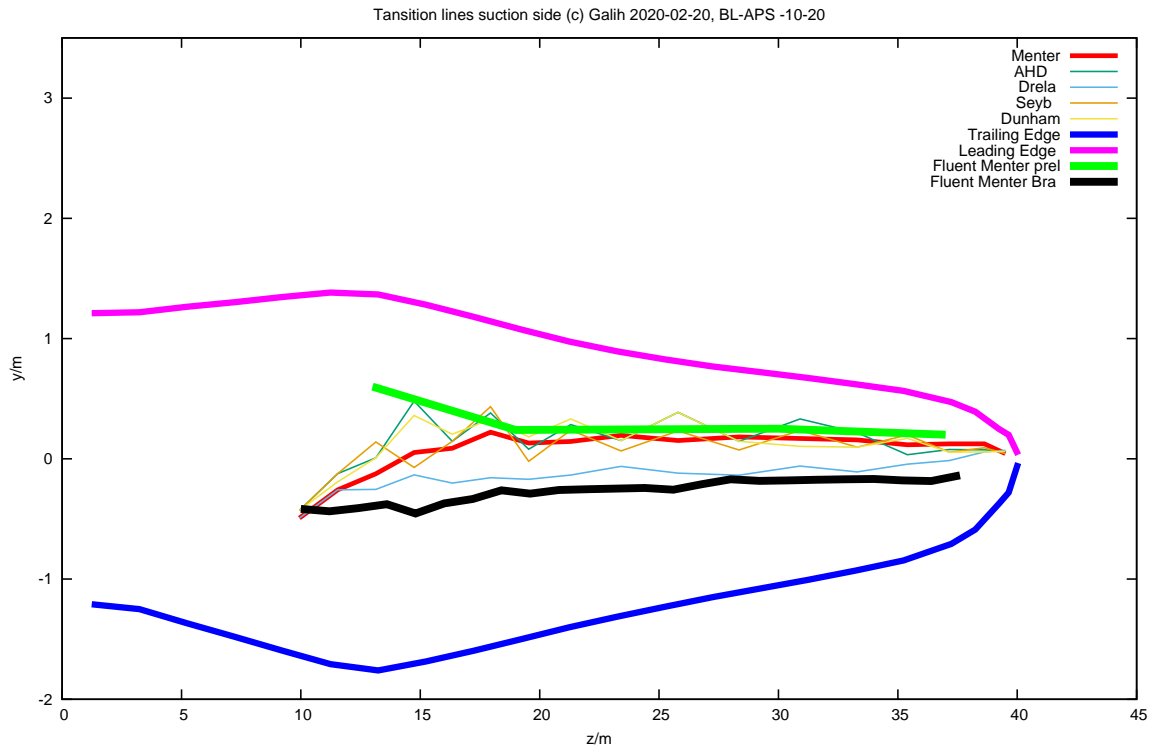


Figure 10.11: Calculated transition line for inflow velocity 6.1 m/s and 12.3 RPM using a variety of laminar to turbulent prediction methods. All computations except those labeled *FLUENT* have been performed by G. Bangga, IAG, University of Stuttgart, Germany.

- Due to the apparently high turbulence inflow the so-called by-pass scenario of transition is likely and first indications for an observation have been found both experimentally and by CFD
- The question of receptivity to distinguish between unsteadiness and turbulence is still under investigation (PhD thesis of Brandon Lobo)
- A first set of transitional CFD runs with a set of 5 transitional models have been performed, but the location of the transition line is still very much model dependent

## 10.6 Outlook to future experiments on boundary layer transition

From the summary above it is clear, that much more work has to be done for a clearer picture regarding laminar to turbulent transition on wind turbines under normal operating conditions. As explained in section 12 several countries have now started up new aerodynamic experiments and a cooperation on these experiments is established in the new IEA Task 47.

Also some local turbines may provide at least temporary access for transition measurements as this the case for the above mentioned MM92 in the North of Germany. A new project will improve the aerodynamic glove used in [89] and a new set of measurements will be performed in 2022/2023.

# Chapter 11

## Task 3.7: Acoustics

F. Bertagnoli

The work presented in this section is conducted in collaboration with IEA Wind Task 39-Quiet Wind Turbine Technology. The work is led by DTU (Franck Bertagnoli) who is also the Operation Agent of IEA Task 39. The aim is a benchmark of aeroelastic or aerodynamic wind turbine simulation codes that have the capability of modeling aerodynamic noise from the blades as well. The NM80 wind turbine investigated as part of the DANAERO project is used as a reference, much in the same way as conducted in other sub-tasks. The institutes involved so far in this benchmark are: DLR (Germany), DTU (Denmark), IAG (Germany), and TNO (The Netherlands). Further details about the different modelling approaches are given below.

In the present study, only turbulent inflow noise and trailing edge noise are considered, as these are recognized as the main contributions to aerodynamic noise from a wind turbine.

### 11.1 Test cases definition

This first round of the benchmark is focusing on the basics of wind turbine noise prediction and thus do not necessarily represent real atmospheric or operational conditions. The participants agreed on the definition of 4 initial test cases:

- Case 1.1: Same as Task 29 Case IV.1.1 and compare aerodynamic quantities (both integral, such as boundary layer thicknesses, and profiles, such as turbulent quantities across the boundary layer), surface pressure near TE and acoustic noise calculations. The specifications of Case IV.1.1 amounts to an axi-symmetric configuration (no-rotor tilt or yaw, not tower shadow, no wind shear, but 2.5deg coning and pre-bend are included) and a rigid rotor (i.e. no aeroelastic deformation of the blades)
- Case 1.2: Same as Task 29 Case IV 1.2 and compare aerodynamic quantities (see above), surface pressure near TE and acoustic noise calculations. The specifications of Case IV.1.2 are identical to Case IV.1.1, but for flexible blades.
- Case 1.3: Same as Case 1.1, but with different rotor speed.
- Case 1.4: Same as Case 1.1, but with wind shear.

In the future, it is envisaged that more realistic test cases will be defined and investigated. Note that the DANAERO experiment did not include noise measurements. Nevertheless, surface pressure was measured with high-frequency microphones at a spanwise blade section toward the tip of one of the blades. In addition, wind turbine certification included some noise measurements, and those may be used as well for code validation, provided that these data can made public, or at least shared with the Task's participants. These can be used to investigate trailing edge noise generation is more details as well as turbulent inflow noise, although the latter might prove more difficult.



## 11.2 Comparison of different wind turbine noise codes

At this stage of the study, 4 institutions have provided results for the benchmark test cases defined in the previous section: DLR (Germany), DTU (Denmark), IAG (Germany), and TNO (The Netherlands). The plan is to include the results from the OpenFAST code from NREL (USA) in the near future.

The different approaches for calculating aerodynamic noise are summarized below:

- DLR - Institute of Aerodynamics and Flow Technology (German Aerospace Center) using the PIANO CAA code (Note that only the TE noise is modelled). The trailing edge noise calculation is based on a boundary layer turbulence reconstruction techniques from RANS calculation. Turbulent inflow noise is not included in the model.
- DTU Wind Energy (Technical University of Denmark) using the HAWC2-Noise code which couples the aeroelastic code HAWC2 using the BEM method with a wind turbine aerodynamic noise prediction module using a TNO-Blake type model for trailing-edge (TE) noise and Amiet's model for turbulent inflow (TI) noise
- Institute for Aerodynamic and Gas Dynamics (University of Stuttgart, Germany) using the aerodynamic 3D CFD code Flower (using  $k-\omega$  SST turbulence model) and a TNO-Blake type TE noise models and Paterson and Amiet's model with Moriarty's thickness correction for the TI noise
- TNO - Wind Energy Technology (The Netherlands Organisation for Applied Scientific Research) using a BEM aerodynamic code and the BPM noise model for TE noise as well as Amiet for TI noise

Aerodynamic noise is largely dependent on the airflow around the turbine blades. A simplified study to confirm the good agreement between the different present contributions in terms of aerodynamic properties has been conducted. It is found that the agreement is fair and should not compromise the study of aerodynamic noise emissions conducted here.

## 11.3 Main results from the comparison benchmark

The results displayed below concentrates on some of the most significant findings achieved so far. Note that compared to the other sections in this report, trailing edge noise calculations require, for some of the modelling approaches, additional information regarding the turbulent boundary layer, such as velocity and turbulent kinetic energy profiles across the boundary layer in the vicinity of the trailing edge. To illustrate the various results, Figs. 11.1 and 11.2 display velocity, turbulent kinetic energy, dissipation and integral length scale across the boundary at a spanwise section located in the outer part of the blade (at a radius of 37 m) on suction and pressured sides, respectively. It is observed that the qualitative agreement is reasonable, but there are quite large quantitative discrepancies.

The main result of the analysis is the noise immission spectra calculated at a given receptor location. This is displayed in Fig. 11.3. It can be seen that the noise spectra are again in general good quantitative agreement, but similarly to the boundary layer profiles, there exist some qualitative discrepancies.

It is difficult to clearly identify which part of the different modelling approaches are responsible for the above noise level discrepancies, in particular to trace back the main factors that cause them. In order to evaluate the influence of the boundary layer quantities and the discrepancies between different approaches and models, a new step in this study is performed. Here, the aerodynamic inputs from the different participants are collected and processed, so that they can be used as inputs for a single noise modelling approach. The results are displayed in Fig. 11.4 for the institutes that could produce the necessary inputs for these calculations. It can be seen there are small discrepancies between the different results. It can be concluded that the large discrepancies observed earlier are due essentially to the acoustic modelling part of the different rotor noise models.

## 11.4 Conclusions on Task 3.7: Acoustics and outlooks

Although aerodynamics is the driving mechanism for aero-acoustic noise generation, the present study of various aero-acoustic modelling approaches for a wind turbine rotor shows that some quantitative

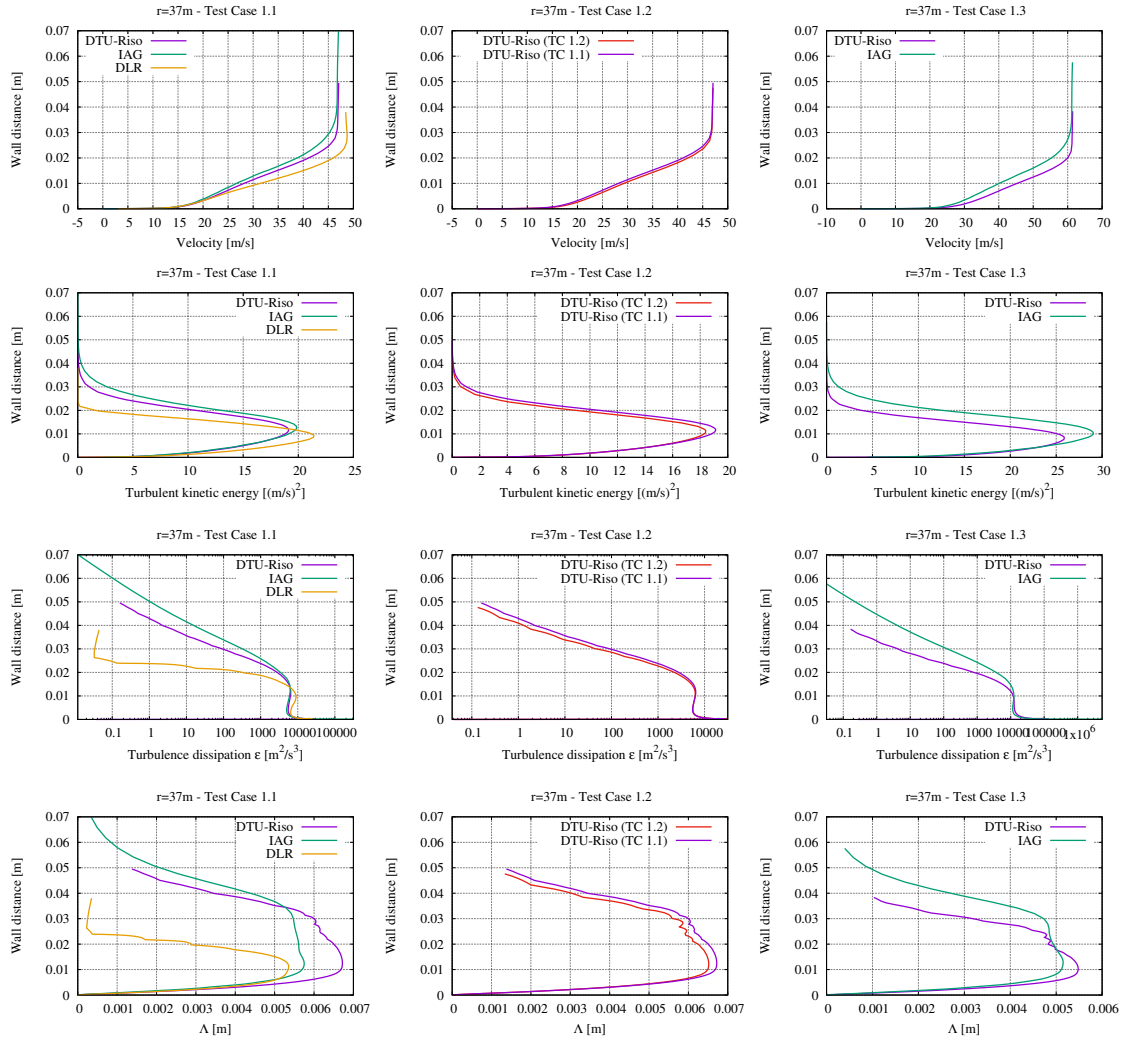


Figure 11.1: Boundary layer profiles of velocity, TKE, dissipation and integral length scale on the suction side at  $x/C = 93\%$  for different test cases (left to right).

discrepancies in the aerodynamic input data for the models (e.g. boundary layer profiles) may have a limited impact on the calculated noise levels. Thus, it is indeed the different acoustic modelling approaches that are responsible for the relatively large discrepancies observed between the different participants' calculation framework.

The next step is to investigate more detailed features of the acoustic emissions, such as rotor noise directivity, amplitude modulation, etc. Ultimately, it is the plan to confront the models to real wind turbine noise measurement data.

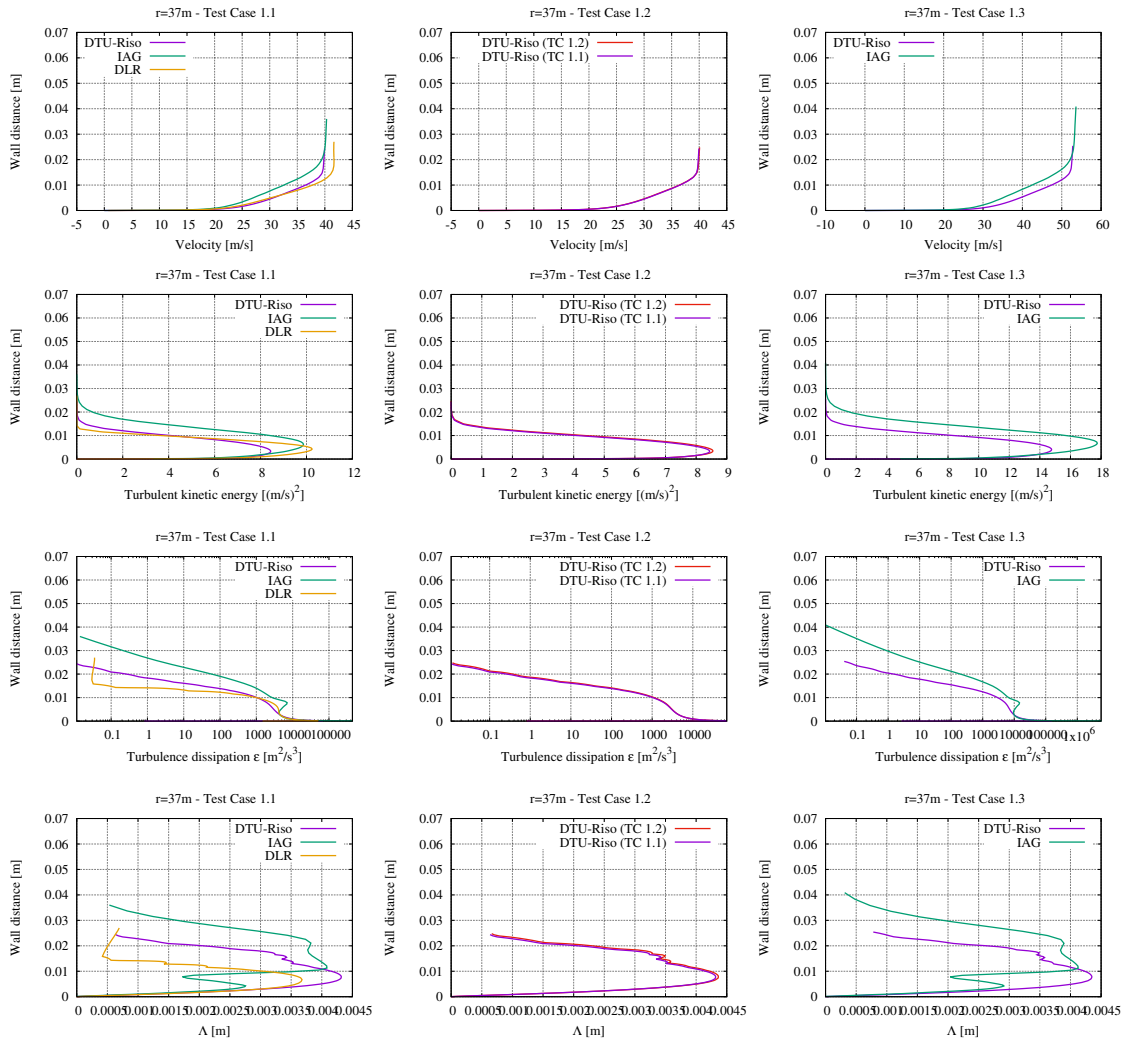


Figure 11.2: Boundary layer profiles of velocity, TKE, dissipation and integral length scale on the pressure side at  $x/C = 91\%$  for different test cases (left to right).

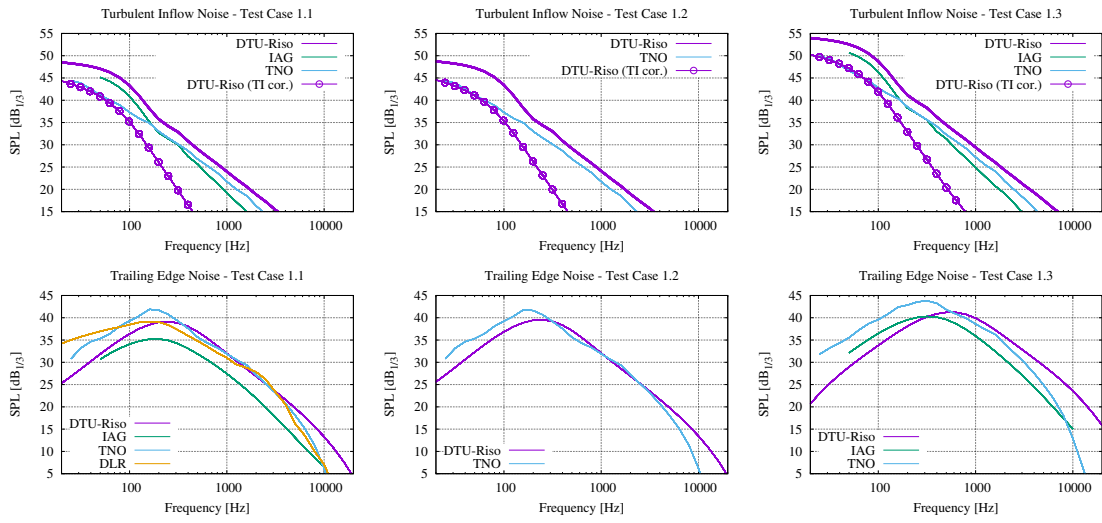


Figure 11.3: Sound pressure level spectra at ‘down-hub’ position for turbulent inflow (upper plots) and trailing edge noise (lower plots) for different test cases (left to right).

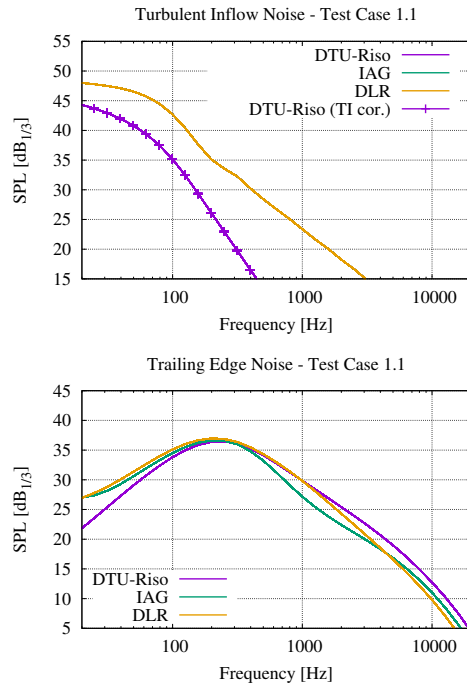


Figure 11.4: Sound pressure level spectra at ‘down-hub’ position for turbulent inflow (upper plots) and trailing edge noise (lower plots) for different test cases (left to right) with different aerodynamic inputs but the same acoustic modelling.

## Chapter 12

# WP4: New aerodynamic experiments

The data from the DanAero experiment which became publicly available in IEA Task29 Phase IV are seen as a great asset for the aerodynamic wind turbine society.

Still it should be realised that good measurement data in the wind energy society remain far too scarce. Amongst others the present project showed that a statistically valid calibration of aerodynamic model parameters with measurements requires much more data points than currently available. Also the scale of the DanAero experiment is still smaller than the scale of the wind turbines of 10 MW<sup>+</sup> which are entering the market now. Several examples can be given of aerodynamic problems which are scale dependant. This scale dependency is not only related to Reynolds number, but also to the changed relation between the scales in atmospheric inflow to the scales of the turbine (blades). An illustration of a modelling challenge for large wind turbines is given in figure 12.1 from [96]. It gives the extreme veer (i.e. the variation of wind direction with height) over the year 2015 at the location of Met Mast IJmuiden in the Dutch part of the North Sea. It shows that the maximum veer over the rotor plane of a 10 MW rotor (with diameter 220 meter) in this year is approximately 40 degrees! The modelling of such a large veer heavily violates the assumptions in the BEM theory. As a matter of fact BEM assumes no yaw misalignment at all and definitely no large variation of yaw angle over the rotor plane.

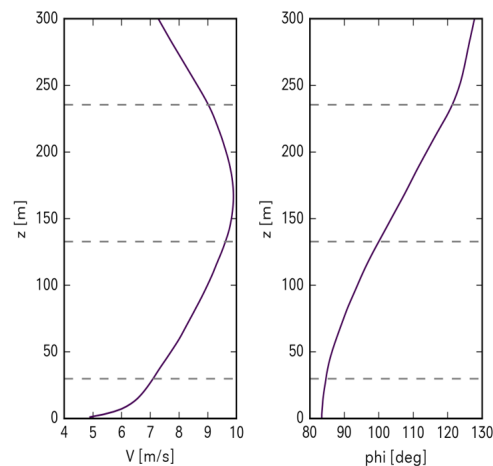


Figure 12.1: Shear (left) and extreme veer (wind direction as function of height, right) from the year 2015 at location of Met Mast IJmuiden in the North Sea (dashed lines indicate lower and upper part of rotor plane and hub height of 10 MW turbine), from [96]

Originally it was thought that within IEA Task29 Phase IV a public aerodynamic experiment could be designed on a large scale turbine. It was anticipated that this experiment would be carried out in a joined activity from the mondial aerodynamic wind turbine society (including the IEA Task 29 group). With this definition at hand it was expected that resources for such experiment could be found relatively easy.

However a main requirement for such experiment is that it should be public and it soon turned out that a main bottleneck lies in the confidentiality of the turbine data. Thereto it should be realised that public does not only mean that the measurement data may be released, but for validation purposes it is equally important that the underlying turbine model description is published as well. In the present context, the aerodynamic and aero-elastic blade data are most essential. Those data are protected and experience learned that they can be released only after very lengthy negotiations. This was already the case for the release of the DanAero blade data even though these blades were on the market for a relatively long time. The release of data from more recent designed blades is expected to be even more sensitive.

Therefore an alternative approach was discussed in which a tailor-made blade would be designed according to the wishes of the research society. Such blade is then built by a manufacturer but the ownership of the blade data remains at the research consortium by which the confidentiality issue from a commercial blade is overcome. Such blade could be placed on an existing turbine. A remaining problem might then still be confidentiality of the turbine design data (e.g. tower data, nacelle data etc) but these are less relevant for the present context where the focus lies on the aerodynamics and aero-elastics of blades. An exception could be the confidentiality of the control algorithm since the resulting pitch angle and rotor speed determine the aerodynamics to a large extent. However, even if the control algorithm cannot be released and a protection through NDA's is not possible either, a fall back scenario is formed by the use of the measured rotor speed and pitch angle as function of time and wind speed which will be sufficiently accurate input to assess the calculations of aerodynamic loads in comparison to measurements.

Hence although a common public large scale aerodynamic experiment along these lines could be a realistic option for the far future it was not expected to be feasible in the very near future.

This was even more true because several countries (e.g. the Netherlands, Denmark, France, Germany, Switzerland, Italy, USA) started up their own national projects, independent of Task 29, in which detailed aerodynamic measurement programs are carried out. In addition, as explained in section 10.6 some local turbines may provide at least temporary access for measurements of boundary layer transition.

This then makes it logical to wait with the design of a common large scale measurement project until the lessons from these national projects have been learned. These lessons can be on many fields: Drilling pressure holes non-intrusive in blades, choosing the right type of pressure transducers and data acquisition with the right frequency response and measurement range, connecting them to the data acquisition system, choosing the right locations for the sensors, powering the sensors, purging pressure tubes, protecting pressure tubes, cables and sensors against rain, vibrations and centrifugal forces, drift of sensors, calibration of sensors, limited access to sensors with small spaces and measurement uncertainties are just a few examples of aerodynamic measurement issues with which experience will be gained in the various national projects. Hence after these projects are finished a common follow-up experiment can be designed which includes the successful methods and techniques and avoids the non-successful methods and techniques. A cooperation between parties which are now starting up aerodynamic experiments is established in the new IEA Task 47 "Innovative aerodynamic experiment technologies and simulations on wind turbines in turbulent inflow" which will start on January 1<sup>st</sup> 2021. In this Task experiences on the specialistic field of detailed aerodynamic measurements will be shared. The new Task will advance the state of the art in Task 29 because some of these experiments are carried out on large scale wind turbines (up to 8MW) and they make use of new innovative measurement methods (e.g. high frequency fibre optic pressure sensors and LIDAR). The use of LIDAR for a detailed inflow characterisation is an important breakthrough since all validations until now rely on a crude inflow characterisation from mast measurements with a limited spatial resolution, where the masts are not even always upstream of the turbine.

## Chapter 13

# WP5: Integration and communication to other IEA Tasks and former phases

WP5 considers a cooperation/integration of results from IEA Task29 Phase IV and results from the previous Task 29 phases and other IEA Tasks. As explained in section 1.2 the previous phases of Task 29 were mainly built around wind tunnel measurements where IEA Task29 Phase IV is built around field measurements. It should be realised that wind tunnel and field measurements are complimentary. Measurements in the field can be done on representative full size turbines and as such the inevitable scaling effects in a wind tunnel environment are avoided where the atmospheric conditions are representative to the conditions which are experienced on a commercial wind turbine. On the other hand, the stochastic nature of atmosphere, though representative, makes interpretation of results more complicated where extremes and faulty conditions (e.g. extreme yaw) cannot be controlled but they need to be caught ‘by accident’. The best strategy to improve aerodynamic knowledge is then to combine the insights from full scale field measurements with those from wind tunnel measurements.

Although IEA Task29 Phase IV is mainly devoted to DanAero (field) measurements, some remaining activities on the wind tunnel measurements from the previous phases were carried out too. Amongst others the activities on yaw modelling and dynamic stall modelling as mentioned in chapter 6 make use of New Mexico experiments from the previous Task 29 phase. Moreover the differences between calculations and measurements in IEA Task29 Phase IV are compared with those in the previous phases. The fact that the differences in IEA Task29 Phase IV are larger is seen as an indication for the extreme challenges to model full scale wind turbines in atmospheric conditions which is one of the most important lessons of IEA Task29 Phase IV .

Also important is the communication to other IEA Tasks which work on different fields but which have overlap/connections to aerodynamics so that they can benefit from the knowledge created in IEA Task29 Phase IV and vice versa. The IEA tasks which were considered to have closest relation to aerodynamics are:

- IEA Task 19: “Wind Energy in Cold Climates” (The connection to Task 29 lies in the Task 29 models which can assess the aerodynamic effects of iced turbine blades)
- IEA Task 28: “Social Acceptance of wind energy projects” (The connection to Task 29 lies in the acoustic characterisation of wind turbine noise sources with associated aerodynamic modelling as described in section 11)
- IEA Task 30 “Comparison of Dynamic Computer Codes and Models for Offshore Wind Energy” (The connection to Task 29 lies in the fact that part of the Task 30 computer codes are aerodynamically driven)
- IEA Task 31, “Wakebench” (The connection to Task 29 lies in the near wake which is considered in Task 29 and which forms the starting point of the far wake considered in WakeBench. Moreover Task 29 will consider the turbine response to wake inflow with respect to loads where Wakebench considers the power output at wake inflow)

- IEA Task 37 “Wind Energy Systems Engineering: Integrated R, D&D” (The connection to Task 29 lies in the Task 29 aerodynamic models which are integrated into Task 37)
- IEA Task 39 “Quiet wind turbine technologies” (The connection to Task 29 lies in the improved understanding of aerodynamic noise as explained in section 11)
- Task 40 ‘Downwind turbine Technologies’ (The connection to Task 29 lies in the aerodynamic knowledge from Task 29 which can be used to model the wake of the tower)

Several joint activities with other IEA Tasks took place. In March 2019 a meeting was held together with Task 31 where results were shared. The most efficient way of cooperation was found to be through IEA Task 29 members which participate in other IEA Tasks as well. IEA Task 29 members participated in almost all Tasks mentioned above (with the exception of Task 28) and these members informed the Task 29 participants on the findings from these other Tasks during several meetings. As described in chapter 11, this even led to a common activity with Task 39 (Quiet noise technologies). The OA of Task 39 (also task leader of Task 3.7 in IEA Task 29) organised a common Task 29/Task 39 acoustic benchmark on the DanAero experiment. This Benchmark relied on the cases defined in Task 29. Calculations from various acoustic codes are compared. Since the results of acoustic predictions are partly driven by the aerodynamics this makes a cooperation between Task 39 and Task 29 very natural. As a matter it was found that the differences in acoustic calculations are inextricably connected to aerodynamic modelling so that the insights from Task 29 on differences between aerodynamic models helped Task 39 to understand the differences in acoustic results.

The same philosophy is followed in a new common Benchmark which is being defined in IEA Task 30 where the measurements from the EU project Unaflo are used as validation material to design codes. In the Unaflo project, [97] aerodynamic measurements are taken in the wind tunnel from PoliMi on an underground which simulates a floating wind turbine. The measurements will be simulated by Task 30 participants but Task 29 participants are invited too. Again the aerodynamic insights from IEA Task 29 will help IEA Task 30 and vice versa.



## Chapter 14

# Conclusions and recommendations

The overall objective of IEA Task29 Phase IV was to cooperate on the analysis of the measurements taken within the DanAero project. The analysis should result in improved aerodynamic understanding and models. This objective has been met. Over a period of 3 years, more than 20 leading institutes on the field of wind turbine aerodynamics cooperated closely. The main results and conclusions from IEA Task29 Phase IV are as follows:

- Within the project a documented database of high quality detailed aerodynamic measurements has been delivered by which a long wish from the aerodynamic wind community has been fulfilled, i.e. the wish to have detailed aerodynamic measurements taken on a large scale turbine under atmospheric conditions. Until now detailed aerodynamic field measurements were available from the IEA Tasks 14 and 18 only but these measurements were performed in the 1990's on outdated turbines with less advanced measurement techniques. The database is made available to the IEA Task29 Phase IV participants after signing a 'light NDA'.
- The cooperation within IEA Task29 Phase IV led to a thorough analysis of DanAero data by a large consortium with ample manpower. This enabled a critical scrutinization of the measurements. It was found that the mean load level was sometimes disturbed by a slightly wrong gain of pressure sensors but the load variations are measured reliably. The resulting insights on measurement quality are seen as a major benefit from the cooperation within this IEA Task. It also gives important learning experiences for new dedicated aerodynamic experiments which are currently set-up and which will form part of IEA Task 47.
- The availability of DanAero measurements enabled a high level validation of design codes which went far beyond a conventional validation. Such conventional validation is based on integrated loads like blade root bending moments where a good agreement can be a result of compensating errors so that misleading conclusions are drawn on the performance of codes. This is not the case in the present comparison which is based on the underlying sectional aerodynamic loads and pressure distributions.
  - Several validation rounds have been carried out where calculations are compared with DanAero measurements. The first calculational round considered a simple steady and axi-symmetric case defined at conditions close to a measurement case with little shear and little yaw. This was followed by a comparison case with a large shear and with a large yaw and shear. Calculations have been performed with high fidelity but time consuming Computational Fluid Dynamic (CFD) codes and with efficient but lower fidelity engineering Blade Element Momentum (BEM) methods as used by industry. Calculations with intermediate methods like free vortex wake (FVW) models and panel methods have been added too. Intermediate models are higher fidelity than BEM but less time consuming than CFD. Both BEM and FVW methods are lifting line methods, i.e. the modelling of the airfoil aerodynamics relies on tables with airfoil characteristics where CFD and panel methods model the airfoil aerodynamics directly.
  - Most of the simulations were done under steady time averaged conditions where the calculated results were compared with mean measured values. Some first evaluations were done in time domain. These evaluations were based on a mutual comparison between CFD and lifting line calculations. In order to do this a methodology has been developed which ensures a consistent input of background turbulence in the different codes. Thereto an empty box CFD wind field simulation was applied at the rotor position as input to the lifting line codes where the CFD empty box simulation was shifted in time to account for induction effects.
  - In order to facilitate the interpretation of differences between calculations and measurements the participants supplied model descriptions of their codes.

The following observations were made on the comparison between calculations and measurements:

- Generally speaking the mutual agreement between calculational results from the same model type is better than it was in the previous phases of Task 29, partly because the 'human factor' has become under control. The agreement between calculations and measurements however is sometimes poorer than the agreement found in the previous phases of Task 29. This is amongst

others true for the agreement in mean normal forces for the (almost) axi-symmetric case. This discrepancy is not only caused by a fundamental modelling deficiency but it is also a result of a slight measurement off-set. Other differences however are caused by fundamental modelling deficiencies, These deficiencies are related to the much more challenging conditions in IEA Task29 Phase IV where large turbines with aero-elastic deformations are modelled in atmospheric conditions with turbulent and inhomogeneous inflow in contrast to the relatively easy steady wind tunnel environment and small wind turbine with negligible aero-elastic effects as considered in the previous phases. The differences with measurements mainly appear in the results from the engineering BEM methods. It is encouraging to see that the results from higher fidelity codes like CFD and FVW often agree much better (though not perfect) with the measurements. More specifically the following can be mentioned:

- \* Large differences between results from engineering methods and measurement are found in the prediction of the yawed case where FVW methods show good results. This is most likely a result of the challenging induction modelling at yawed conditions. Yaw leads to a skewed wake geometry which induces an azimuthal variation of velocities. FVW methods model the wake geometry and resulting velocities in a physical way but engineering models do this in an empirical way with an inherent uncertainty. These differences are expected to become even more prominent at larger turbines since the veer (and so the yaw error) increase with size of the turbine.
  - \* The high shear case is also modelled poorly by the industrial engineering methods at least when they use the airfoil data as prescribed in the definition of the calculation case. These airfoil data rely on wind tunnel measurements, which is a standard procedure for engineering methods. CFD (and panel) methods predict the high shear case much better. If airfoil data are extracted from the CFD results and fed into the engineering methods the results from these methods also compare well with measurements. This indicates that the better prediction from CFD and panel methods is a result of the direct modelling of airfoil performance (in particular stall delay effects) which is physically more correct than the approach used by engineering models. Since the shear increases with size of the turbine, these discrepancies become more important for larger turbines. The generation of airfoil data with CFD methods can be done in a very efficient way. This then indicate that a hybrid CFD/engineering method offers potential for a much more accurate design calculation, without excessively increasing calculational effort.
- The more accurate results from the higher fidelity models confirms the soundness of an approach which is often applied in the wind energy society where engineering models are improved with results from academic high fidelity codes. It has now been proven that these high fidelity codes are higher fidelity indeed!
- In IEA Task29 Phase IV the available data have also been used for fundamental physical understanding of the until now hardly explored area of wind turbine aerodynamics in turbulent inflow. An important breakthrough is the improved physical understanding of boundary layer transition in the free atmosphere where significant differences in microphone spectra are found on the DanAero blade compared to the spectra on an airfoil in the wind tunnel. Until now most wind turbine design calculations rely on airfoil data taken at non-turbulent wind tunnel conditions but this indicates that the actual airfoil data at field conditions (in particular the drag) may be significantly different.
  - Together with IEA Task 39 an acoustic Benchmark was carried out. In this Benchmark noise calculations were performed on the DanAero turbine. It was found that part of the differences in acoustic modelling results find its origin in the aerodynamic modelling. However, the acoustic models themselves appear to have significant impact on the rotor noise predictions. More research is needed investigate the observed discrepancies, e.g. with respects to directivity effects, and confront the models to field noise measurements.
  - An important lesson learned for CFD modelling lies on grid refinement studies. Such studies are essential for a good outcome of these codes. It is found however that grid sensitive studies are code

dependant, e.g. the results for compressible codes differ from those for incompressible codes. This also means that the use of common grids to be used by all CFD codes in comparison rounds is not always feasible: A particular grid may be suitable for one code but not for other codes.

- Engineering model improvement was facilitated by a tool with which model parameters and the uncertainties of these parameters can be calibrated automatically. The tool was used to calibrate yaw model parameters. It was found that a statistical valid calibration requires more data points than available in the DanAero database which is the reason why the model calibrations were carried out with the New Mexico measurements, i.e. the measurements from the previous phase of Task 29. A drawback of this calibration was found to be the wind tunnel environment which differs from the representative atmospheric environment.
- IEA Task 29 led to a huge amount of publications, presentations and other dissemination activities. Apart from the ‘conventional’ dissemination by means of workshops, conference presentations, journal articles etc, the Task is characterised by the large amount of MSc and PhD students who actively participated in the project. After their graduation these students often found positions in the wind energy industry where they spread the Task 29 knowledge. In this way Task 29 contributes to the Human Capital Agenda. It is this outflow of knowledgeable students which is considered to be a very important dissemination form. It is estimated that at least 100 students worked largely or completely in the 4 phases of IEA Task 29 where approximately 25% of these students found positions in the wind industry after graduation. In addition there were students who found positions at other participants of IEA Task 29. The fact that Task 29 participants employ graduated students from other Task 29 participants is considered to be an important indicator of good cooperation in the Task.

The lessons learned (in particular the lesson that conventional measurements of e.g. blade root bending moments lack detail so that aerodynamic measurements of sectional loads are needed, with an additional lesson that very many data points are needed for a statistical valid calibration and the lesson that measurements are needed on representative scale) lead to the main recommendation from IEA Task29 Phase IV which is that much more detailed aerodynamic measurements are needed on an even larger scale. Another lesson learned is that such measurement are difficult to do. This leads to the recommendation that practical experiences from the few aerodynamic experiments which have been done should be shared. In this way problems can be prevented and successes can be copied so that the learning curve for future experiments is steepened. Steepening the learning curve of future aerodynamic experiments is a main objective of the new IEA Task 47 ”Innovative aerodynamic experiments and simulations on wind turbines in turbulent inflow” in which several parties cooperate which recently initiated aerodynamic field experiments. In many of these experiments the current state of the art is advanced amongst others through the larger scale which goes up to 8MW and the application of innovative measurement methods like LIDAR which gives much more detail on the rotor inflow than the currently used mast wind measurements. This supports another recommendation from Task 29 which is the development of a consistent comparison procedure in time domain between calculated and measured properties at turbulent inflow.

Hence the database which will be created in Task 47 and the associated knowledge is expected to be of even greater value than the outcomes of Task 29!

# Bibliography

- [1] J.G. Schepers. *Engineering models in wind energy aerodynamics, development, implementation and analysis using dedicated aerodynamic measurements*. PhD thesis, University of Delft, ISBN 978-94-6191-507-8, 2012.
- [2] J. G. Schepers and S. J. Schreck. Aerodynamic measurements on wind turbines. *WIREs Energy and Environment*, 8(1):e320.
- [3] J.G. Schepers, A. Brand, A. Bruining, J. Graham, M. Hand, D. Infield, H. Madsen, J. Paynter, and D. Simms. Final Report of IEA Annex XIV: Field Rotor Aerodynamics. Technical report, ECN-C-97-027, 1997.
- [4] J.G. Schepers et al. Final report of IEA Annex XVIII' Enhanced Field Rotor Aerodynamics Database. ECN-C-02-016, Energy Research Centre of the Netherlands, ECN, February 2002.
- [5] M.M. Hand, D.A. Simms, L.J. Fingersh, D.W. Jager, J.R. Cotrell, S. Schreck, and S.M. Larwood. Unsteady Aerodynamics Experiment Phase VI Wind Tunnel Test Configurations and Available Data Campaigns. NREL/TP-500-29955, National Renewable Energy Laboratory, NREL, December 2001.
- [6] S. Schreck. IEA Wind Annex XX: HAWT Aerodynamics and Models from Wind Tunnel Measurements. NREL/TP-500-43508, The National Renewable Energy Laboratory, NREL, December 2008.
- [7] J.G. Schepers and H. Snel. MEXICO, Model experiments in controlled conditions. ECN-E-07-042, Energy Research Center of the Netherlands, 2007.
- [8] K. Boorsma and J.G. Schepers. New MEXICO experiment. ECN-E -14-048, Energy Research Centre of the Netherlands, ECN, September 2014.
- [9] Schepers, J.G.; Boorsma, K.; Cho, T.; Gomez-Iradi, S.; Schaffarczyk, P.; Jeromin, A.; Shen, W.Z.; Lutz, T.; Meister, K.; Stoevesandt, B.; Schreck, S.; Micallef, D.; Pereira, R.; Sant, T.; Madsen, H.; Sorensen, N. Final report of IEA Task 29, Mexnext (Phase 1): Analysis of MEXICO wind tunnel measurements. ECN-E-12-004, Energy Research Center of the Netherlands, February 2012.
- [10] Boorsma, K.; Schepers, J.G.; Gomez-Iradi, S.; Schaffarczyk, P.; Madsen, H.A.; Sorensen, N.N.; Shen, W.Z. voorvoegsels; Lutz, T.; Schulz, C.; Herraez, I.; Schreck, S. Final report of IEA Task 29, Mexnext (Phase 2): Analysis of MEXICO wind tunnel measurements. ECN-E-14-060, Energy Research Center of the Netherlands, December 2014.
- [11] K. Boorsman and J.G Schepers and S. Gomez-Iradi and and I.Herraez and T. Lutz and P. Weihsing and L. Oggiano and G. Pirrung and H.A. Madsen and W.Z. Shen and H. Rahimi and A.P. Schaffarczyk. Final Report of IEA Task 29, Mexnext (Phase 3): Analysis of Mexico wind tunnel measurements. ECN-E -18-034, Energy Research Centre of the Netherlands, ECN, January 2018.
- [12] B. Stoevesandt, J.G. Schepers, Yuping, P. Fuglsang, editor. *Springer Handbook of Wind Turbine Aerodynamics*. Springer-Verlag, 2020.
- [13] H.A. Madsen and G. Pirrung. IEA Task 29, Phase IV DanAero database, corrections, updates Additional information, 2020.

- [14] J.G. Schepers. Minutes of the kick-off meeting of IEA Task 29, Phase IV held at PoliMi (Milano, Italy) on June 19 2018, June 2018.
- [15] J.G. Schepers. Minutes of the second meeting of IEA Task 29, Phase IV held at NREL (Boulder, USA) on March 13/14 2019, March 2019.
- [16] J.G. Schepers. Minutes of third meeting of IEA Task 29, Phase IV held at INSEAN/CNR (Rome, Italy) on February 4 and 5 2020, February 2020.
- [17] J.G. Schepers. Minutes of web meetings of IEA Task 29, Phase IV held on a 2 monthly basis since October 4 2019.
- [18] J.G. Schepers. Minutes of intermediate meeting of IEA Task 29, Phase IV held at University of Cork (Cork, Ireland) on June 21 2019, June 2019.
- [19] H Aagaard Madsen, C Bak, U Schmidt Paulsen, M Gaunaa, P Fuglsang, J Romblad, NA Olesen, P Enevoldsen, J Laursen, and Leo Jensen. The dan-aero mw experiments: final report. *Danmarks Tekniske Universitet, Risø Nationallaboratoriet for Bæredygtig Energi, available at: orbit.dtu.dk (last access: 13 November 2017)*, 2010.
- [20] H. A. Madsen, C. Bak, U. S. Paulsen, M. Gaunaa, N. N. Sørensen, P. Fuglsang, J. Romblad, N. A. Olsen, P. Enevoldsen, J. Laursen, and L. Jensen. The dan-aero mw experiments. *48th Aiaa Aerospace Sciences Meeting Including the New Horizons Forum and Aerospace Exposition*, pages 2010–0645, 2010.
- [21] N. Troldborg, C. Bak, H. Aa. Madsen, and W. Skrzypinski. *DANAERO MW II: Final Report*. April 2013.
- [22] T.J. Larsen and A.M. Hansen. How 2 hawc2, the user’s manual. Technical report, Risø National Laboratory, 2007.
- [23] N. Troldborg M. Gaunaa W. Skrzypinski A. Fischer U. Paulsen R. Møller P. Hansen M. Rasmussen C. Bak, H.Aa. Madsen and P. Fuglsang. DANAERO MW: Instrumentation of the NM80 turbine and meteorology mast at Tjæreborg. Report-I-0083, DTU Wind Energy, 2013.
- [24] Martin OL Hansen, Niels N Sørensen, and JA Michelsen. Extraction of lift, drag and angle of attack from computed 3-d viscous flow around a rotating blade. In *1997 European Wind Energy Conference*, 1997.
- [25] F Wenz, K Boorsma, T Lutz, and E Krämer. Cross-correlation-based approach to align turbulent inflow between cfd and lower-fidelity-codes in wind turbine simulations. In *Journal of Physics: Conference Series*, volume 1618, page 062005. IOP Publishing, 2020.
- [26] Koen Boorsma, Florian Wenz, Koert Lindenburg, Mansoor Aman, and Menno Kloosterman. Validation and accommodation of vortex wake codes for wind turbine design load calculations. *Wind Energy Science*, 5(2):699–719, 2020.
- [27] Niels Troldborg, Jens N Sørensen, Robert Mikkelsen, and Niels N Sørensen. A simple atmospheric boundary layer model applied to large eddy simulations of wind turbine wakes. *Wind Energy*, 17:657–669, 2014.
- [28] International Electrotechnical Commission et al. Iec 61400-1: Wind turbines part 1: Design requirements. *International Electrotechnical Commission*, pages 54–56, 2005.
- [29] Galih Bangga. Comparison of blade element method and cfd simulations of a 10 mw wind turbine. *Fluids*, 3(4):73, 2018.
- [30] H. Aagaard Madsen, Torben Juul Larsen, Georg Pirrung, Ang Li, and Frederik Zahle. Implementation of the blade element momentum model on a polar grid and its aeroelastic load impact. *Wind Energy Science*, 5:1–27, 2020.

- [31] P. J. Moriarty and A. Craig Hansen. Aerodyn theory manual. Technical report, National Renewable Energy Laboratory, December 2005. NREL/EL-500-36881.
- [32] Andrew Ning, Gregory Hayman, Rick Damiani, and Jason M Jonkman. Development and validation of a new blade element momentum skewed-wake model within aerodyn. In *33rd Wind Energy Symposium*, page 0215, 2015.
- [33] David A Spera. Wind turbine technology. 1994.
- [34] H. Aagaard Madsen, Torben Juul Larsen, Georg Raimund Pirrung, Li Ang, and Frederik Zahle. Implementation of the blade element momentum model on a polar grid and its aeroelastic load impact. *Wind Energy Science*, 5(1):1–27, 2020.
- [35] Galih Bangga, Thorsten Lutz, and Matthias Arnold. An improved second-order dynamic stall model for wind turbine airfoils. *Wind Energy Science*, 5(3):1037–1058, 2020.
- [36] Frédéric Blondel, Gilles Ferrer, David Teixeira, and Marie Cathelain. Improving a bem yaw model based on new mexico experimental data and vortex/cfd simulations. In *Congrès français de mécanique*. AFM, Association Française de Mécanique, 2017.
- [37] G Bangga. A simple unsteady modeling of wind turbine loads implemented in B-GO. Technical report, University of Stuttgart, Germany, 2020.
- [38] R.E. Wilson. Aerodynamic potpourri. In *Wind Turbine Dynamics, NASA Conference Proceedings 2185*, 1981.
- [39] H. Snel. Heuristic modelling of dynamic stall characteristics. In *Conference proceedings European Wind Energy Conference*, pages 429–433, Dublin, Ireland, October 1997.
- [40] J.G. Schepers. An engineering model for yawed conditions, developed on basis of wind tunnel measurements. Technical Report AIAA-1999-0039, AIAA, 1999.
- [41] Ludwig Prandtl and Albert Betz. *Vier Abhandlungen zur Hydrodynamik und Aerodynamik*, volume 3. Universitätsverlag Göttingen, 2010.
- [42] Galih Bangga. *Three-dimensional flow in the root region of wind turbine rotors*. kassel university press GmbH, 2018.
- [43] Marelli S and Sudret B. Uqlab a framework for uncertainty quantification in matlab. In *Swiss numerics colloquim*, 2013.
- [44] K. Boorsma, F. Grasso, and J.G. Holierhoek. Enhanced approach for simulation of rotor aerodynamic loads. Technical Report ECN-M-12-003, ECN, presented at EWEA Offshore 2011, Amsterdam, 29 November 2011 - 1 December 2011, 2011.
- [45] Boorsma, K. Validation of BEM and Vortex-wake models with full scale on-site measurements. TNO 2019 R11390, TNO, September 2019.
- [46] Boorsma, K.; Schepers, J.G.; Gomez-Iradi, S.; Herraiez, I.; Lutz, T.; Weihing, P.; Oggiano, L.; Pirrung, G.; Madsen, H.A.; Shen, W.Z.; Rahimi, H.; Schaffarczyk, P.;. Final report of IEA Task 29, Mexnext (Phase 3): Analysis of MEXICO wind tunnel measurements. ECN-E-18-003, Energy Research Center of the Netherlands, December 2014.
- [47] V.V. Dighe and B. Sanderse. Efficient bayesian calibration of aeroelastic wind turbine models using surrogate modeling. *Journal of Wind Energy*, 2021.
- [48] Leishman J.G. and Beddoes T.S. “A Generalised model for unsteady airfoil behaviour and dynamic stall using the indicial method”. In *42th Annual Forum of the American Helicopter Society Washington DC*, June 1998.

- [49] M. Caboni, M. Carrion, C. Rodriguez, G. Schepers, K. Boorsma, and Benjamin Sanderse. Assessment of sensitivity and accuracy of bem-based aeroelastic models on wind turbine load predictions. In *Journal of Physics: Conference Series*, September 2020.
- [50] Prashant Kumar, Benjamin Sanderse, K. Boorsma, and M. Caboni. Global sensitivity analysis of model uncertainty in aeroelastic wind turbine models. In *Journal of Physics: Conference Series*, September 2020.
- [51] K Nilsson, S. Ivanell, K.N. Hansen, R. Mikkelsen, J.N. Sørensen, S.-P. Breton, and D. Henningson. Large-eddy simulations of the lillgrund wind farm. *Wind Energy*, 18:449–467, 2015.
- [52] C. F. Janßen, D. Mierke, M. Überrück, S. Gralher, and Th. Rung. Validation of the GPU-Accelerated CFD Solver ELBE for Free Surface Flow Problems in Civil and Environmental Engineering. *Computation*, 3(3):354, 2015.
- [53] Jennifer M. Rinker. PyConTurb: An open-source constrained turbulence generator. *J. Phys.: Conf. Ser.*, 1037(6):062032, June 2018.
- [54] Tsan-Hsing Shih, William W Liou, Aamir Shabbir, Zhigang Yang, and Jiang Zhu. A new  $k - \varepsilon$  eddy viscosity model for high Reynolds number turbulent flows. *Computers & Fluids*, 24(3):227–238, 1995.
- [55] H. Aagaard Madsen, Gunner Chr. Larsen, Torben J. Larsen, Niels Troldborg, and Robert Flemming Mikkelsen. Calibration and validation of the dynamic wake meandering model for implementation in an aeroelastic code. *Journal of Solar Energy Engineering*, 132(4):041014, 2010.
- [56] J. Jonkman and K. Shaler. Fast.farm user’s guide and theory manual. Technical report, NREL, 2020.
- [57] Wen Zhong Shen, Robert Mikkelsen, Jens Nørkær Sørensen, and Christian Bak. Tip loss corrections for wind turbine computations. *Wind Energy: An International Journal for Progress and Applications in Wind Power Conversion Technology*, 8(4):457–475, 2005.
- [58] Ziyang Yu, Xing Zheng, and Qingwei Ma. Study on actuator line modeling of two nrel 5-mw wind turbine wakes. *Applied Sciences*, 8(3):434, 2018.
- [59] A. R. Meyer Forsting, G. R. Pirrung, and N. Ramos-García. *Actuator-Line-Smearing-Correction*. figshare, <https://doi.org/10.11583/DTU.9752285.v1>, Sep 2019.
- [60] A.R Meyer Forsting, Georg Pirrung, and Néstor Ramos García. Brief communication: A fast vortex-based smearing correction for the actuator line. *Wind Energy Science*, 2020.
- [61] M. O. L. Hansen. *Aerodynamics of Wind Turbines - Second Edition*. Earthscan, London, Sterling, VA, 2008.
- [62] Swagata Das, Neeraj Karnik, and Surya Santoso. Time-Domain Modeling of Tower Shadow and Wind Shear in Wind Turbines. *ISRN Renewable Energy*, 2011:1–11, October 2011.
- [63] Martin O. L. Hansen. *Aerodynamics of wind turbines*. Earthscan, London ; Sterling, VA, 2nd ed edition, 2008. OCLC: ocm86172940.
- [64] F. Blondel, G. Ferrer, M. Cathelain, and D. Teixeira. Improving a BEM Yaw Model Based on NewMexico Experimental Data and Vortex/CFD Simulations. page 14, 2017.
- [65] T. Potentier, C. Braud, E. Guilmineau, C. Le Bourdat, and A. Finez. Analysis of the DANAERO wind turbine field database to assess the importance of different state of the art bem correction models. *Energy Science and Engineering Journal*, accepted manuscript.
- [66] M.H. Hansen, Mac Gaunaa, and Helge Aagaard Madsen. *A Beddoes-Leishman type dynamic stall model in state-space and indicial formulations*. Denmark. Forskningscenter Risoe. Risoe-R, 2004.



- [67] E. Guilmineau, G. B. Deng, A. Leroyer, P. Queutey, M. Visonneau, and J. Wackers. Numerical Simulations for the Wake Prediction of a Marine Propeller in Straight-Ahead Flow and Oblique Flow. *Journal of Fluids Engineering*, page 021111, 2018-02-01.
- [68] M. H. Hansen. Aeroelastic stability analysis of wind turbines using an eigenvalue approach. *Wind Energy*, 7(2):133–143, 2004.
- [69] C.L. Bottasso and S. Cacciola. Model-independent periodic stability analysis of wind turbines. *Wind Energy*, 18(5):865–887, 2015.
- [70] P. F. Skjoldan and M. H. Hansen. Implicit floquet analysis of wind turbines using tangent matrices of a non-linear aeroelastic code. *Wind Energy*, 15(2):275–287, 2012.
- [71] Guideline for the certification of wind turbines. Hamburg: Germanischer Lloyd Industrial Services GmbH, 2010.
- [72] M. H. Hansen, K. Thomsen, P. Fuglsang, and T. Knudsen. Two methods for estimating aeroelastic damping of operational wind turbine modes from experiments. *Wind Energy*, 9(1-2):179–191, 2006.
- [73] G. Bir. Multi-blade coordinate transformation and its application to wind turbine analysis. In *Proceedings of the AIAA Wind Energy Symposium*, Reno, Nevada, 1 2008.
- [74] A.P. Schaffarczyk and R. Boisard and K. Boorsma and B. Dose and C. Lienard and T. Lutz H. Å Madsen and H. Rahimi and T. Reichstein and G. Schepers and N Sørensen and B. Stoevesand and P. Weihing. Comparison od 3d transitional cfd simulations for rotating wings with measurements. In *The Science of Making Torque from Wind*, Milan, Italy, 2018.
- [75] C. Bak, H.A. Madsen, U. S. Paulsen, M. Gaunaa, N.N. Sørensen, P. Fuglsang, J. Romblad, N.A. Olsen, P. Enevoldsen, J. Laursen, and L. Jensen. Dan-aero mw: Detailed aerodynamic measurements on a full scale mw wind turbine. *European Wind Energy Conference and Exhibition 2010, Ewec 2010*, 2:792–836, 2010.
- [76] N. Troldborg, C. Bak, Madsen H. Aa., and S Witold. Danaero mw: Final report. Technical Report No. 0027(EN), DTU Wind Energy, 2013.
- [77] Niels N Sørensen. *General Purpose Flow Solver Applied to Flow Over Hills*. PhD thesis, , Risø National Laboratory., 1995.
- [78] J.A. Michelsen. Basis3d - a platform for development of multiblock pde solvers. Technical report, Risø National Laboratory, 1992.
- [79] J.A. Michelsen. Block structured multigrid solution of 2d and 3d elliptic pde’s. Technical report, Technical University of Denmark, 1994.
- [80] Özge Sinem Özçakmak. *Laminar-Turbulent Boundary Layer Transition Characteristics of Wind Turbine Rotors: A numerical and experimental investigation*. PhD thesis, Denmark, 2020.
- [81] H. Aagaard Madsen, Özge Sinem Özçakmak, Christian Bak, Niels Troldborg, and Niels N. Sørensen. Transition characteristics measured on a 2mw 80m diameter wind turbine rotor in comparison with transition data from wind tunnel measurements. *Proceedings of the Aiaa Scitech 2019 Forum*, 2019.
- [82] Ö. S. Özçakmak, H. A. Madsen, N. N. Sørensen, and J. N. Sørensen. Laminar-turbulent transition characteristics of a 3-d wind turbine rotor blade based on experiments and computations. *Wind Energy Science*, 5(4):1487–1505, 2020.
- [83] Özge Sinem Özçakmak, Niels Nørmark Sørensen, Helge Aagaard Madsen, and Jens Nørkaer Sørensen. Laminar-turbulent transition detection on airfoils by high-frequency microphone measurements. *Wind Energy*, 22(10):1356–1370, 2019.

- [84] Mark Drela and Michael B Giles. Viscous-inviscid analysis of transonic and low reynolds number airfoils. *AIAA journal*, 25(10):1347–1355, 1987.
- [85] YB Suzen and PG Huang. Modeling of flow transition using an intermittency transport equation. *Journal of fluids engineering*, 122(2):273–284, 2000.
- [86] L. M Mack. Transition and laminar instability. Number No. NASA-CP-153203, California, 1977. NASA Jet Propulsion Laboratory.
- [87] M. V Morkovin. Bypass transition to turbulence and research desiderata. *NASA. Lewis Research Center Transition in Turbines*, pages 161–204, 1985.
- [88] A.P. Schaffarczyk and D. Schwab and M. Breuer. Experimental detection of laminar-turbulent transition on a rotating wind turbine blade in the free atmosphere. *WIND ENERGY*, 19, 2016.
- [89] T. Reichstein, A.P. Schaffarczyk, Chr. Dollinger, N. Balaesque, E. Schülein, C. Jauch, and A. Fischer. Investigation of laminar-turbulent transition on a rotating wind-turbine blade of multimegawatt class with thermography and microphone array. *energies*, 12, 2019.
- [90] A. Seitz and K.-H. Horstmann. In-flight investigation of tollmien-schlichtung waves. In *IUTAM Symposium on One Hundred Years of Boundary Layer Research, Proceedings of the IUTAM symposium held at DLR-Göttingen, Germany, August 12 - 14, 2004*, pages 115–124. Springer, 2006.
- [91] Leslie M. Mack. Transition and laminar instability. Technical Report NASA-CP-153203, JPL-PUBL-77-15, Jet Propulsion Laboratory, California Institute of Technology, Pasadena, California 91109, USA, 1977.
- [92] A.D Reeh and Tropea C. Behaviour of a natural laminar flow aerofoil in flight through atmospheric turbulence. *Journal of Fluid Mechanics*, 767:394–429, 2015.
- [93] M. Klein, A. Sadiki, and J. Janicka. A digital filter based generation of inflow data for spatially-developing direct numerical or large-eddy simulations. *J. Comput. Phys.*, 186:652–665, 2003.
- [94] S. Schmidt and M. Breuer. Source term based synthetic turbulence inflow generator for eddy-resolving predictions of an airfoil flow including a laminar separation bubble. *Computers & Fluids*, 146:1–22, 2017.
- [95] J. C. R. Hunt, A. A. Wray, and P. Moin. Eddies, streams, and convergence zones in turbulent flows. In *Proceedings of the Summer Program 1988*, pages 193–208. Center for Turbulence Research, 1988.
- [96] J.G. Schepers, P van Dorp, R. Verzijlbergh, and H Jonker. Aero-elastic loads on a 10 mw turbine exposed to extreme events selected from a year-long large-eddy simulation over the north sea. *Wind Energy Science*, 2020.
- [97] M. Caboni M. Cormier T. Lutz P. Schito S. Mancini, K. Boorsma and A. Zasso. Characterization of the unsteady aerodynamic response of a floating offshore wind turbine to surge motion. 2020.
- [98] J. N. Sørensen and W. Z. Shen. Numerical modeling of wind turbine wakes. *Journal of Fluids Engineering*, 124(2):393–399, 2002.
- [99] W. Z. Shen, W. J. Zhu, and J. N. Sørensen. Actuator line/navier–stokes computations for the mexico rotor: comparison with detailed measurements. *Wind Energy*, 15(5):811–825, 2010.
- [100] S. Øye. Flex simulation of wind turbine dynamics. In *State of the art of aeroelastic codes for wind turbine calculations*, Lyngby, Denmark, 1 1996.
- [101] W. J. Zhu, N. Heilskov, W. Z. Shen, and J. N. Sørensen. Modeling of aerodynamically generated noise from wind turbines. *Journal of Solar Energy Engineering*, 127(4):517–528, 2005.

- [102] M. Zhou, M. Sessarego, H. Yang, and W. Z. Shen. Development of an advanced fluid-structure-acoustics framework for predicting and controlling the noise emission from a wind turbine under wind shear and yaw. *Applied Sciences*, 10:7610, 2020.
- [103] Taeseong Kim, Anders M. Hansen, and Kim Branner. Development of an anisotropic beam finite element for composite wind turbine blades in multibody system. *Renewable Energy*, 59:172–183, 2013.
- [104] H. Glauert. *Airplane propellers, Division L*, volume 4. Julius Springer, Berlin, W.F. Durand (ed) edition, 1935.
- [105] H. Aagaard Madsen, Christian Bak, Mads Dossing, Robert Mikkelsen, and Stig Oye. Validation and modification of the blade element momentum theory based on comparisons with actuator disc simulations. *Wind Energy*, 13(4):373–389, 2010.
- [106] H. Aagaard Madsen and F. Rasmussen. A near wake model compared with the blade element momentum theory. *Proceedings*, pages 108–117, 2004.
- [107] Georg R. Pirrung, Helge Aagaard Madsen, Taeseong Kim, and Joachim Christian Heinz. A coupled near and far wake model for wind turbine aerodynamics. *Wind Energy*, 19(11):2053–2069, 2016.
- [108] Georg Pirrung, Vasilis Riziotis, Helge Aagaard Madsen, Morten Hansen, and Taeseong Kim. Comparison of a coupled near and far wake model with a free wake vortex code. *Wind Energy Science*, 2:15–33, 2017.
- [109] Ang Li, Georg Pirrung, Helge Aagaard Madsen, Mac Gaunaa, and Frederik Zahle. Fast trailed and bound vorticity modeling of swept wind turbine blades. *Journal of Physics: Conference Series*, 1037(6):062012, 2018.
- [110] Joachim C. Heinz, Niels N. Sørensen, and Frederik Zahle. Fluid–structure interaction computations for geometrically resolved rotor simulations using cfd. *Wind Energy*, 19(12):2205–2221, 2016.
- [111] J. C. Heinz. *Partitioned Fluid-Structure Interaction for Full Rotor Computations Using CFD*. PhD thesis, 2013.
- [112] Néstor Ramos-García, Matias Sessarego, and Sergio González Horcas. Aero-hydro-servo-elastic coupling of a multi-body finite-element solver and a multi-fidelity vortex method. *Wind Energy*, n/a(n/a).
- [113] Niels Troldborg, Jens Nørkær Sørensen, and Robert Flemming Mikkelsen. *Actuator Line Modeling of Wind Turbine Wakes*. PhD thesis, Technical University of Denmark, 2009.
- [114] A. R. Meyer Forsting, G. R. Pirrung, and N. Ramos-García. A vortex-based tip/smearing correction for the actuator line. *Wind Energy Sci*, 4(2):369–383, 2019.
- [115] Alexander Raul Meyer Forsting, Niels Troldborg, Andreas Bechmann, and Pierre-Elouan Réthoré. *Modelling Wind Turbine Inflow: The Induction Zone*. PhD thesis, DTU Wind Energy, Denmark, 2017.
- [116] Le Cunff C., Heurtier J.-M., Piriou L., Berhault C., Perdrizet T., Teixeira D., Ferrer G., and Gilloteaux J.-C. Fully Coupled Floating Wind Turbine Simulator Based on Nonlinear Finite Element Method: Part I - Methodology. Volume 8: Ocean Renewable Energy, 06 2013. V008T09A050.
- [117] Perdrizet T., Gilloteaux J.-C., Teixeira D., Ferrer G., Piriou L., Cadiou D., Heurtier J.-M., and Le Cunff C. Fully coupled floating wind turbine simulator based on nonlinear finite element method: Part ii - validation results. Volume 8: Ocean Renewable Energy, 06 2013. V008T09A052.
- [118] Bozonnet P., Caille F., Blondel F., Melis C., Poirrette Y., and Perdrizet T. A focus on fixed wind turbine tests to improve coupled simulations of floating wind turbine model tests. 2017.

- [119] Blondel F., Galinos C., Paulsen U., Bozonnet P., Cathelain M., Ferrer G., Madsen H.A., Pirrung G., and Silvert F. Comparison of aero-elastic simulations and measurements performed on NENUPHAR’s 600kw vertical axis wind turbine: Impact of the aerodynamic modelling methods. *Journal of Physics: Conference Series*, 1037:022010, jun 2018.
- [120] Betz A. Schraubenpropeller mit geringstem energieverlust. mit einem zusatz von l. prandtl. *Nachrichten von der Gesellschaft der Wissenschaften zu Göttingen, Mathematisch-Physikalische Klasse*, 1919:193–217, 1919.
- [121] Øye S. Dynamic stall simulated as time lag of separation. In *Technical Report, Technical University of Denmark*, 1991.
- [122] Snel H. and Schepers J.G. Joint investigation of dynamic inflow effects and implementation of an engineering method, 1995.
- [123] S. Andrew Ning. A simple solution method for the blade element momentum equations with guaranteed convergence. *Wind Energy*, 17(9):1327–1345, 2014.
- [124] R. Damiani and G. Hayman. The unsteady aerodynamics module for fast 8. Technical report, National Renewable Energy Laboratory, 2019. NREL/TP-5000-66347.
- [125] R. Damiani and J. Jonkman. DBEMT theory manual, rev.3. Technical report, National Renewable Energy Laboratory, 2017. Unpublished NREL report.
- [126] S. A. Ning, G. Hayman, R. Damiani, and J. Jonkman. Development and validation of a new blade element momentum skewed-wake model within aerodyn. Technical report, National Renewable Energy Laboratory, 2014. NREL/CP-5000-63217.
- [127] M. L. Buhl. A new empirical relationship between thrust coefficient and induction factor for the turbulent windmill state. Technical report, National Renewable Energy Laboratory, 2005. NREL/TP-500-36834.
- [128] H. Glauert. A general theory of the autogyro. Technical report, NACA Reports and Memoranda No. 111, 1926.
- [129] R. P. Coleman, A. M. Feingold, and C. W. Stempin. Evaluation of the induced-velocity field of an idealized helicopter rotor. *NACA ARR No. L5E10*, pages 1–28, 1945.
- [130] D. M. Pitt and D. Al. Peters. Theoretical prediction of dynamic-inflow derivatives. *Vertica*, 5:21–34, 1981.
- [131] H. Snel and J. G. Schepers. Investigation and modelling of dynamic inflow effects. Technical report, ECN-RX–93-029, 1993.
- [132] A. van Garrel. Development of a wind turbine aerodynamics simulation module. Technical Report ECN-C–03-079, ECN, 2003.
- [133] K. Shaler, E. Branlard, and A. Platt. Olaf user’s guide and theory manual. Technical report, National Renewable Energy Laboratory, 2020.
- [134] E. Branlard. *Wind Turbine Aerodynamics and Vorticity-Based Methods: Fundamentals and Recent Applications*. Springer International Publishing, 2017.
- [135] E. Branlard and A. R. Meyer Forsting. Assessing the blockage effect of wind turbines and wind farms using an analytical vortex model. *Wind Energy (under review)*, 2020.
- [136] J. Jonkman. Unofficial FAST Theory Manual. Technical report, National Renewable Energy Laboratory, Unpublished.
- [137] T. R. Kane and C. F. Wang. On the derivation of equations of motion. *Journal of the Society for Industrial and Applied Mathematics*, 13(2):487–492, 1965.

- [138] Q. Wang, N. Johnson, M. Sprague, and J. Jonkman. Beamdyn: A high-fidelity wind turbine blade solver in the fast modular framework. *33rd Wind Energy Symposium*, pages 17 pp., 17 pp., 2015.
- [139] J. Jonkman. The New Modularization Framework for the FAST Wind Turbine CAE Tool. Technical Report NREL/CP-5000-57228, National Renewable Energy Laboratory, 2013.
- [140] M. A. Sprague, J. M. Jonkman, and B. J. Jonkman. FAST Modular Framework for Wind Turbine Simulation: New Algorithms and Numerical Examples. Technical Report NREL/CP-2C00-63203, National Renewable Energy Laboratory, 2015.
- [141] M. Mudry. La théorie des nappes tourbillonnaires et ses applications à l’aérodynamique instationnaire. *PhD Thesis, Paris VI University*, 1982.
- [142] K. Boorsma, M. Hartvelt, and L.M. Orsi. Application of the lifting line vortex wake method to dynamic load case simulations. *Journal of Physics: Conference Series*, 753(2):022030, 2016.
- [143] C. Lindenburg and J.G. Schepers. Phatas-IV aeroelastic modelling, release ”dec-1999” and ”nov-2000”. Technical Report ECN-CX-00-027, ECN, 2000.
- [144] <http://www.wmc.eu/focus6.php>. 2016.
- [145] K Boorsma, L Greco, and G Bedon. Rotor wake engineering models for aeroelastic applications. *J. Phys. Conf. Ser.*, 1037:062013, 2018.
- [146] O.A. Bauchau, C.L. Bottasso, and Y.G. Nikishkov. Modeling rotorcraft dynamics with finite element multibody procedures. *Mathematical and Computer Modelling*, 33(10):1113 – 1137, 2001.
- [147] D.A. Peters and C.J. He. Finite state induced flow models — part ii: Three-dimensional rotor disk. *Journal of Aircraft*, 32(2):323 – 333, 1995.
- [148] S.R.J. Powles. The effects of tower shadow on the dynamics of a horizontal-axis wind turbine. *Wind Engineering*, 7(1):26–42, 1983.
- [149] O.A. Bauchau, C.L. Bottasso, and Trainelli L. Robust integration schemes for flexible multibody systems. *Computer Methods in Applied Mechanics and Engineering*, 192(3):395 – 420, 2003.
- [150] D. Schwamborn, T. Gerhold, and R. Heinrich. The dlr tau-code: Recent applications in research and industry. In *European Conference on Computational Fluid Dynamics*, 2006.
- [151] N.N. Sørensen. *General purpose flow solver applied to flow over hills*. PhD thesis, 1995.
- [152] M. Strelets. Detached eddy simulation of massively separated flows. *39th Aerospace Sciences Meeting and Exhibit*, 2001.
- [153] W.Z. Shen, J.A. Michelsen, N.N. Sørensen, and J.N. Sørensen. An improved simplec method on collocated grids for steady and unsteady flow computations. *Numerical Heat Transfer Part B: Fundamentals*, 43:221–239, 2003.
- [154] F. Zahle, N.N. Sørensen, and J. Johansen. Wind turbine rotor-tower interaction using an incompressible overset grid method. *Wind Energy*, 12(6):594–619, 2009.
- [155] Niels N. Sørensen. Hypgrid2d. a 2-d mesh generator. Technical report, Risø National Laboratory, 1998.
- [156] Frederik Zahle and Niels Sørensen. Rotor aerodynamics in atmospheric shear flow. *Ewec 2008 Conference Proceedings*, pages 120–124, 2008.
- [157] F.R. Menter. Zonal two equation kappa-omega turbulence models for aerodynamic flows. In *Proceedings of 24th AIAA Fluid Dynamics Conference*, 1993.
- [158] Torben Juul Larsen and Anders Melchior Hansen. How 2 hawc2, the user’s manual. page 69, 2015.

- [159] Mikhail L Shur, Philippe R Spalart, Mikhail Kh Strelets, and Andrey K Travin. A hybrid RANS-LES approach with delayed-DES and wall-modelled LES capabilities. *International Journal of Heat and Fluid Flow*, 29:1638–1649, 2008.
- [160] M.A. Sprague, S. Ananthan, G. Vijayakumar, and M. Robinson. Exawind: A multi-fidelity modeling and simulation environment for wind energy. In *Proceedings of NAWEA WindTech*, 2019.
- [161] M. A. Heroux, R. A. Bartlett, V. E. Howle, R. J. Hoekstra, J. J. Hu, T. G. Kolda, R. B. Lehoucq, K. R. Long, R. P. Pawlowski, E. T. Phipps, Á. G. Salinger, H. K. Thornquist, R. S. Tuminaro, J. M. Willenbring, A. Williams, and K. S. Stanley. An overview of the trilinos project. *ACM Transactions on Mathematical Software (TOMS) - Special issue on the Advanced Computational Software (ACTS) Collection*, 31:397–423, 2005.
- [162] H. C. Edwards, A. B. Williams, G. D. Sjaardema, D. G. Baur, and W. K. Cochran. Sierra toolkit computational mesh conceptual model. Technical Report SAND2010-1192, Sandia National Laboratories, 2010.
- [163] J. Sitaraman. Tioga, 2019.
- [164] S. J. Thomas, S. Ananthan, S. Yellapantula, J. J. Hu, M. Lawson, and M. A. Sprague. A comparison of classical and aggregation-based algebraic multigrid preconditioners for high-fidelity simulation of wind turbine incompressible flows. *SIAM Journal on Scientific Computing*, 41(5):S196–S219, 2019.
- [165] A Calabretta, M Molica Colella, L Greco, and M Gennaretti. Assessment of a comprehensive aeroelastic tool for horizontal-axis wind turbine rotor analysis. *Wind Energy*, 19(12):2301–2319, December 2016.
- [166] Testa C Greco L Salvatore F Leone, S. Computational analysis of self-pitching propellers performance in open water. *Ocean Engineering*, 64:122–134, 2013.
- [167] L Greco, R Muscari, C Testa, and A Di Mascio. Marine Propellers Performance and Flow-Field Features Prediction by a Free-Wake Panel Method. *J. Hydrodyn., Ser. B (English Ed.)*, 26(5):780–795, 2014.
- [168] L. Greco and C. Testa. Wind turbine unsteady aerodynamics and performance by a free-wake panel method. *Renewable Energy*, 164:444–459, 2021.
- [169] Veulliot J.-P. Cambier L. Status of the elsa cfd software for flow simulation and multidisciplinary applications. In *Proceedings of 46th AIAA Aerospace Science Meeting and Exhibit*, 2008.
- [170] Heib S.-Plot S. Cambier, L. The onera elsa cfd software: input from research and feedback from industry. *Mechanics and Industry*, 14(3):159–174, 2013.
- [171] NN. ANSYS FLUENT Theory Guide, Rel 15.0. Technical report, ANSYS Inc., November 2013.
- [172] C. Y. Özlem and O. Pires and X. Munduate and N. Sørensen and T. Reichstein and A.P. Schaffarczyk and K. Diakakis and G. Papadakis and E. Daniele and M. Schwarz and T. Lutz and R. Prieto. Summary of the Blind Test Campaign to predict High Reynolds number performance of DU00-W-210 airfoil. *AIAA 2017-0915*, 915, 2017.
- [173] N. Krimmelbein. Tau transition module (v9.30) user guide (v1.04). Technical report, DLR, (German Aerospace Association, Institute of Aerodynamics and Flow Technology), 2009.
- [174] Chr. Heister. CFD simulations of the MexNext rotor experiment using the DLR TAU code. In *IEA Task 11/29 MexNext Meeting*, January 2016.
- [175] M. Buhl. WT\_perf user’s guide. Technical report, NREL, December 2004.
- [176] Pascal Weihing, Johannes Letzgus, Galih Bangga, Thorsten Lutz, and Ewald Krämer. Hybrid RANS/LES capabilities of the flow solver flower—application to flow around wind turbines. In *Symposium on hybrid RANS-LES methods*, pages 369–380. Springer, 2016.

- [177] Thorsten Lutz, Christoph Schulz, Patrick Letzgus, and Andreas Rettenmeier. Impact of complex orography on wake development: Simulation results for the planned windfords test site. In *Journal of Physics: Conference Series*, volume 854, page 012029. IOP Publishing, 2017.
- [178] Levin Klein, Jonas Gude, Florian Wenz, Thorsten Lutz, and Ewald Krämer. Advanced computational fluid dynamics (cfd)–multi-body simulation (mbs) coupling to assess low-frequency emissions from wind turbines. *Wind Energy Science*, 3(2):713–728, 2018.
- [179] M Sayed, Th Lutz, E Krämer, Sh Shayegan, A Ghantasala, R Wüchner, and K-U Bletzinger. High fidelity cfd-csd aeroelastic analysis of slender bladed horizontal-axis wind turbine. In *Journal of Physics: Conference Series*, volume 753, page 042009. IOP Publishing, 2016.
- [180] Eva Jost, Annette Fischer, Galih Bangga, Thorsten Lutz, and Ewald Krämer. An investigation of unsteady 3-d effects on trailing edge flaps. *Wind Energy Science*, 2(1):241–256, 2017.
- [181] Galih Bangga, Thorsten Lutz, and Ewald Krämer. Active separation control on a very thick wind turbine airfoil—a URANS and DDES perspective. In *Journal of Physics: Conference Series*, volume 1037, page 022025. IOP Publishing, 2018.
- [182] Norbert Kroll, Cord-Christian Rossow, Klaus Becker, and Frank Thiele. The MEGAFLOW project. *Aerospace Science and Technology*, 4:223–237, 2000.
- [183] Galih Bangga, Amgad Dessoky, Thorsten Lutz, and Ewald Krämer. Improved double-multiple-streamtube approach for h-darrieus vertical axis wind turbine computations. *Energy*, 182:673–688, 2019.
- [184] Galih Bangga, Amgad Dessoky, Zhenlong Wu, Krzysztof Rogowski, and Martin OL Hansen. Accuracy and consistency of cfd and engineering models for simulating vertical axis wind turbine loads. *Energy*, 206:118087, 2020.
- [185] Ion Paraschivoiu. *Wind turbine design: with emphasis on Darrieus concept*. Presses inter Polytechnique, 2002.
- [186] Streiner S. *Beitrag zur numerischen Simulation der Aerodynamik und Aeroelastik großer Windkraftanlagen mit horizontaler Achse*. PhD thesis, University of Stuttgart, 2011.
- [187] Klein L. *Beitrag zur Modellierung tieffrequenter Emissionen von Windkraftanlagen*. PhD thesis, University of Stuttgart, 2018.
- [188] Uwe Jassmann, Joerg Berroth, Daniel Matzke, Ralf Schelenz, Matthias Reiter, Georg Jacobs, and Dirk Abel. Model predictive control of a wind turbine modelled in simpack. *Journal of Physics: Conference Series*, 524:012047, 06 2014.
- [189] Birger Luhmann, Homan Seyedin, and Po-Wen Cheng. Aero-structural dynamics of a flexible hub connection for load reduction on two-bladed wind turbines. *Wind Energy*, 20(3):521–535, 2017.
- [190] Florian R Menter. Two-equation eddy-viscosity turbulence models for engineering applications. *AIAA journal*, 32:1598–1605, 1994.
- [191] G Chesshire and William D Henshaw. Composite overlapping meshes for the solution of partial differential equations. *Journal of Computational Physics*, 90:1–64, 1990.
- [192] Antony Jameson, Wolfgang Schmidt, and Eli Turkel. Numerical solution of the euler equations by finite volume methods using runge kutta time stepping schemes. In *14th fluid and plasma dynamics conference*, 1981.
- [193] Galih Bangga, Thorsten Lutz, Eva Jost, and Ewald Krämer. Cfd studies on rotational augmentation at the inboard sections of a 10 mw wind turbine rotor. *Journal of Renewable and Sustainable Energy*, 9(2):023304, 2017.

- [194] Galih Bangga, Pascal Weihing, Thorsten Lutz, and Ewald Krämer. Effect of computational grid on accurate prediction of a wind turbine rotor using delayed detached-eddy simulations. *Journal of Mechanical Science and Technology*, 31(5):2359–2364, 2017.
- [195] Yusik Kim, Pascal Weihing, Christoph Schulz, and Thorsten Lutz. Do turbulence models deteriorate solutions using a non-oscillatory scheme? *Journal of Wind Engineering and Industrial Aerodynamics*, 156:41–49, 2016.
- [196] Yusik Kim, Eva Jost, Galih Bangga, Pascal Weihing, and Thorsten Lutz. Effects of ambient turbulence on the near wake of a wind turbine. In *Journal of Physics: Conference Series*, volume 753, page 032047. IOP Publishing, 2016.
- [197] Guang-Shan Jiang and Chi-Wang Shu. Efficient implementation of weighted ENO schemes. *Journal of computational physics*, 126:202–228, 1996.
- [198] Giorgia Guma, Galih Bangga, Thorsten Lutz, and Ewald Krämer. Aeroelastic analysis of wind turbines under turbulent inflow conditions. *Wind Energy Science*, 6(1):93–110, 2021.
- [199] Henrik Asmuth, Hugo Olivares-Espinosa, Karl Nilsson, and Stefan Ivanell. The Actuator Line Model in Lattice Boltzmann Frameworks: Numerical Sensitivity and Computational Performance. *J. Phys.: Conf. Ser.*, 1256:012022, July 2019.
- [200] Henrik Asmuth, Christian F. Janßen, Hugo Olivares-Espinosa, Karl Nilsson, and Stefan Ivanell. Assessment of weak compressibility in actuator line simulations of wind turbine wakes. *J. Phys.: Conf. Ser.*, 1618:062057, September 2020.
- [201] Henrik Asmuth, Hugo Olivares-Espinosa, and Stefan Ivanell. Actuator line simulations of wind turbine wakes using the lattice Boltzmann method. *Wind Energy Science*, 5(2):623–645, May 2020.
- [202] Martin Geier, Andrea Pasquali, and Martin Schönherr. Parametrization of the cumulant lattice Boltzmann method for fourth order accurate diffusion part I: Derivation and validation. *J. Comput. Phys.*, 348:862–888, 2017.
- [203] P. J. Mason and D. J. Thomson. Stochastic backscatter in large-eddy simulations of boundary layers. *Journal of Fluid Mechanics*, 242:51–78, September 1992.
- [204] Gonzalo P. Navarro Diaz, Matias Avila, and Arnau Folch. An annual energy production estimation methodology for onshore wind farms over complex terrain using a RANS model with actuator discs. *Journal of Physics: Conference Series*, 1037:072018, jun 2018.
- [205] E. GA Antonini, David A Romero, and Cristina H Amon. Optimal design of wind farms in complex terrains using computational fluid dynamics and adjoint methods. *Applied Energy*, 261:114426, 2020.
- [206] OpenFOAM, 2020.
- [207] Gonzalo P Navarro Diaz, A Celeste Saulo, and Alejandro D Otero. Comparative study on the wake description using actuator disc model with increasing level of complexity. In *Journal of Physics: Conference Series*, volume 1256, page 012017. IOP Publishing, 2019.
- [208] M. Paul van der Laan, Niels N. Sørensen, Pierre-Elouan Réthoré, Jakob Mann, Mark C. Kelly, and Niels Troldborg. The  $k-\varepsilon$ - $fp$  model applied to double wind turbine wakes using different actuator disk force methods. *Wind Energy*, 18(12):2223–2240, 2015.
- [209] Richard JAM Stevens, Luis A Martínez-Tossas, and Charles Meneveau. Comparison of wind farm large eddy simulations using actuator disk and actuator line models with wind tunnel experiments. *Renewable energy*, 116:470–478, 2018.
- [210] RC Storey, SE Norris, and JE Cater. An actuator sector method for efficient transient wind turbine simulation. *Wind Energy*, 18(4):699–711, 2015.



- [211] Jörn Nathan, Christian Masson, Louis Dufresne, and Matthew J Churchfield. Analysis of the swepted actuator line method. In *E3S Web of Conferences*, volume 5. National Renewable Energy Lab.(NREL), Golden, CO (United States), 2015.
- [212] Matias Avila, Abel Gargallo-Peiró, and Arnau Folch. A CFD framework for offshore and onshore wind farm simulation. *Journal of Physics: Conference Series*, 854:012002, may 2017.
- [213] Avinaash Murali and RG Rajagopalan. Numerical simulation of multiple interacting wind turbines on a complex terrain. *Journal of Wind Engineering and Industrial Aerodynamics*, 162:57–72, 2017.
- [214] Matthew J Churchfield, Sang Lee, John Michalakes, and Patrick J Moriarty. A numerical study of the effects of atmospheric and wake turbulence on wind turbine dynamics. *Journal of turbulence*, (13):N14, 2012.
- [215] Jörn Nathan, Christian Masson, and Louis Dufresne. Near-wake analysis of actuator line method immersed in turbulent flow using large-eddy simulations. *Wind Energy Science*, 3(2):905, 2018.
- [216] J Nathan, Alexander Raul Meyer Forsting, Niels Troldborg, and C Masson. Comparison of openfoam and ellipsys3d actuator line methods with (new) mexico results. In *Journal of Physics: Conference Series*, volume 854, page 012033, 2017.
- [217] Ulrich Schumann. Subgrid scale model for finite difference simulations of turbulent flows in plane channels and annuli. *Journal of computational physics*, 18:376–404, 1975.

## Appendix A

# Comparison Round Data Format and Test Cases

This section describes the data format and test cases for the purpose of the comparison between calculations and measurements (chapter 4).

## A.1 First round: Uniform inflow

# IEA Task 29, Phase IV: Definition of first round of calculations on DanAero experiment (Case IV.1)

J.G. Schepers, H.A. Madsen, K. Boorsma, G. Pirrung  
December 17th 2018

Revision December 17<sup>th</sup> versus October 3 2018

- CFD model is uploaded
- Flapwise and edgewise moments were mentioned in the text as output properties but they were not in the file format. They are now taken out.
- The CFD chapter erroneously included a section 3.2.2 on Velocities. This has now been taken out and replaced with section 3.2.3 which specifies output of flow velocities at the four 5 hole probes.

## 1. Description of the wind turbine and experiment

Information based on references [1] to [6]

The first cases of IEA Task 29 Phase IV (denoted as Case IV.1.1 and IV.1.2) aim to check the model descriptions of the participants and they do not include a comparison with measured results. Still they are a preparation for such comparison at a later stage. For this reason the conditions are taken as much as possible in agreement to the conditions of a measured case with little shear, yaw and turbulence (section 2). Moreover the output properties are as much as possible compatible to the measurement signals from the DanAero experiment.

The turbine data can be found digitally in an Excel sheet on [https://share.dtu.dk/sites/IEA-Task-29\\_293350/Lists/News/DispForm.aspx?ID=4&Source=https%3A%2F%2Fshare%2Edtu%2Edk%2Fsites%2FIEA-Task-29\\_293350%2FSitePages%2FHome%2Easpx&ContentTypeId=0x0104004B5A174D68045141B59E64500460A769](https://share.dtu.dk/sites/IEA-Task-29_293350/Lists/News/DispForm.aspx?ID=4&Source=https%3A%2F%2Fshare%2Edtu%2Edk%2Fsites%2FIEA-Task-29_293350%2FSitePages%2FHome%2Easpx&ContentTypeId=0x0104004B5A174D68045141B59E64500460A769) but **for the first cases tilt angle, and tower shadow effects are neglected. Pre-Bend is included!**

To make sure that everybody uses the same input, the airfoil coefficient data sets are prescribed in the Excel sheet (also see DANAERO\_3DA\_pc\_hama\_38.CL.eps) For the CFD modellers please use the supplied CAD files from the Sharepoint site which you find on:

[https://share.dtu.dk/sites/IEA-Task-29\\_293350/The%20DanAero%20Data%20Base/Forms/AllItems.aspx?RootFolder=%2Fsites%2FIEA-Task-29\\_293350%2FThe%20DanAero%20Data%20Base%2FTurbine%20model%2FCFD%20modelling&FolderCTID=0x01200010776225236F1A48B82AE11B7D12512A&View=%7BB05E01CB-C5F6-4D9F-A3AD-9CF0B959D925%7D](https://share.dtu.dk/sites/IEA-Task-29_293350/The%20DanAero%20Data%20Base/Forms/AllItems.aspx?RootFolder=%2Fsites%2FIEA-Task-29_293350%2FThe%20DanAero%20Data%20Base%2FTurbine%20model%2FCFD%20modelling&FolderCTID=0x01200010776225236F1A48B82AE11B7D12512A&View=%7BB05E01CB-C5F6-4D9F-A3AD-9CF0B959D925%7D) with:

- Design geometry of the blades as supplied by DTU, Please note that the blade geometry does not yet include the pitch angle.

- Note that tower and nacelle effects are neglected

## **2. Description of case IV.1.1 and case IV.1.2.**

Under the umbrella of case IV.1 (i.e. the calculational case which aims to check the model description of the Task 29 participants) two ‘sub’ cases are defined denoted as **case IV.1.1, and case IV.1.2**. The difference between these two sub-cases lies in the fact that case IV.1.1 is modelled in a **rigid** way where case IV.1.2 includes **flexibilities**. They are a preparation for the simulations of a measured case with little yaw and little shear which was calculated in AVATAR already by a limited number of participants (see AVATAR deliverables D2.6 and D4.2).

The output format is largely based on the format which has been used in the former Mexnext phases.

It is noted that within Task 3.5 (aero-elasticity) a separate aero-elastic check is carried out, mainly based on eigenfrequencies and dampings.

- Case IV.1.1 (Axi-symmetric)
  - Rigid construction
  - No tilt, no tower shadow
  - Pre-bend is included
  - Pitch angle: 0.15 degrees to feather (constant)
  - Rotor speed: 12.3 rpm (constant)
  - Wind speed 6.1 m/s
  - Air density  $\rho = 1.231 \text{ kg/m}^3$
  - Yaw angle: 0 degrees
- Case IV.1.2 (Axi-symmetric with flexibilities)
  - As Case IV.1.1 including flexibilities

## **3. Results to be supplied:**

**Those participants who calculating the stiff case IV.1.1 only please provide zeros for the data of case IV.1.2**

### **3.1 Lifting line codes:**

The comparison of results from lifting line codes (e.g. BEM codes) mainly focusses on the local aerodynamic forces and the angle of attack at several radial stations. In addition the blade root bending moments and deflections in flapwise and edgewise direction are calculated. Most of these properties will eventually be compared with the measured values in follow-up cases. It is noted that accelerations have been measured too so they can be added in a later stage. For the present case they are zero. Moreover the axial force and rotorshaft torque as integrated from the local loads at the instrument locations are added too.



Note that this makes the total number of rows to be  $n + 3$   
 (1 (header) + 1 (axial force) + 1 (torque) +  $n$  radial locations)

### 3.1.2 Lifting line variables

- Requested data and units
  - For a minimum of 10 (preferably more) radial locations:
    - $V_{eff}$  (i.e. the resultant incoming velocity at the blade section) [m/s]
    - $\alpha$  Angle of attack [deg]
    - $u_i$ , the local axial induced velocity [m/s]  
 The sign is positive pointing in upwind direction.
    - $u_{tan}$ , the local velocity induced in tangential (rotational) direction [m/s]  
 The sign is positive pointing opposite to the direction of rotation.
    - $c_n$  aerodynamic normal force coefficient =  
 $F_{n,c}/(0.5 \rho V_{eff}^2 c)$  [-]  
 Orientation in agreement with  $F_{n,c}$  from loads (section 3.1.1)
    - $c_t$  aerodynamic tangential force coefficient =  
 $F_{t,c}/(0.5 \rho V_{eff}^2 c)$  [-]  
 Orientation in agreement with  $F_{t,c}$  from loads (section 3.1.1)
- Files to be supplied:
  - Please supply the data in one plain ASCII file which should contain the data for both cases.
  - Format: Each row contains 14 columns, separated by tabs or blanks. The first row gives the identification of data. The next rows give the data for both cases at the chosen radial locations (a total of  $n$ ), increasing from root to tip. Hence, the format is as follows:

```

r  V_eff1.1  alpha1.1  ui1.1  utan1.1  Cn1.1  Ct1.1  V_eff1.2  alpha1.2  ui1.2  utan1.2  Cn1.2  Ct1.2  Ct24
r1  --      --      --      --      --      --      --      --      --      --      --      --      --

| |      | |      | |      | |      | |      | |      | |      | |      | |      | |      | |      | |
| |      | |      | |      | |      | |      | |      | |      | |      | |      | |      | |      | |

rn  --      --      --      --      --      --      --      --      --      --      --      --      --
  
```

Note that this makes the total number of rows to be  $n + 1$   
 (1 (header) +  $n$  radial locations)

### 3.2 CFD codes

It is anticipated that many CFD (and panel) codes calculate the pressure distributions and from that the (aerodynamic) loads and moments along the blades and possibly deflections. Moreover it is anticipated that the velocities at the probe positions can be calculated. In the next cases these results can be compared with the measured data.

### 3.2.1 Loads and deflections

See the format specification of the file in section 3.1.1.

### 3.2.2 Pressure data

- Requested data and units.
  - For all instrumented sections: Pressure data in dimensional form [Pa] **relative to the ambient pressure** as function of x (along the chord) and y (perpendicular to the chord). Note that (x=0,y=0) is at the nose of the airfoil. Positive y at the suction side. Units of x and y are [m]. Note that x and y do not necessarily need to coincide with the position of the sensors.
- Files to be supplied
  - For the 4 instrumented sections (r=13121/19064/30219/36775 mm from the rotor center) and every case a separate (ASCII) file needs to be supplied. Hence a total of 4 (radial positions) \* 2 (cases) = 8 files need to be supplied. For those participants who calculate case IV.1.1 only it is sufficient to supply 4 files.
  - Format: Three columns with pressures as function of x (along the chord) and y (perpendicular to the chord) starting at the trailing edge, then going along the suction side to the leading edge and then back to the trailing edge along the pressure side. Separate the columns by tabs or blanks. The format is as follows:

x[m]	y[m]	Pressure [Pa]
chord (t.e.)	0	--
--	positive	usually negative
0(l.e.)	0	--
--	negative	usually positive
Chord(t.e.)	0	--

### 3.2.3 Output of velocities at the five hole probess

For the four radial positions (14.54 m, 20.34 m, 31.04 m, 36.04 m from the rotor center) of the five hole pitot tubes extract flow velocities in the rotor plane coordinate system and the inflow angle IA [deg], side slip angle SLA [deg] and relative velocity Vrel [m/s] (see the sheet "Output sensors for simulations" in "IEA-Task-29-IV-NM80-turbine definition\_hama\_Dec\_17-2018\_v4.xlsx") and store them in an ASCII file (ident\_flowsensor.dat) as:



Radius       $u_n$  [m/s]  $u_t$  [m/s]  $u_r$  [m/s]   IA [deg]   SLA [deg]   Vrel [m/s]

## References

- [1] H.Aa. Madsen, C. Bak, U.S. Paulsen, M. Gaunaa, P. Fuglsang, J. Romblad, N.A. Olesen, P. Enevoldsen, J. Laursen, and L. Jensen. *The DAN-AERO MW Experiments Final report*. Technical Report RISO-R- 1726(EN), Technical University of Denmark, 2010.
- [2] C. Bak, H.Aa. Madsen, P. Hansen, M. Rasmussen, P. Fuglsang, J. Romblad, N.A. Olesen, *Danaero MW Measurement campaigns on the NM80 2.3 MW Wind Turbine at Tjaereborg 2009* Technical Report RISO-I- 3046(EN), Technical University of Denmark, 2010.
- [3] N. Troldborg, C. Bak, H. Aa. Madsen, W. Skrzypinski *DANAERO MW: Final Report* DTU Wind Energy E-0027, April 2013
- [4] C. Bak, H. Aa. Madsen N. Troldborg M. Gaunaa, W. Skrzypinski A. Fischer, U.S. Paulsen, R. Moller, P. Hansen, M. Rasmussen, P. Fuglsang *Danaero MW Instrumentation of the NM80 turbine and meteorology mast at Tjaereborg*, DTU Wind Energy report I-0083, May 2013

Additional information can be found from the following AVATAR deliverables:

- [5] H.Aa.Madsen, Joachim Heinz, S. Voutsinas, N. R. García, G.Pirrung, Niels N. Sørensen, N. Troldborg *Aerodynamics of Large Rotors, Validation of advanced models against measured data* AVATAR Deliverable 4.2, August 2016
- [6] N. N. Sørensen, N. Ramos García, S. Voutsinas, E. Jost, T. Lutz *Effects of complex inflow for the AVATAR reference rotor*, Deliverable D.2.6, September 2017

## A.2 Second round: Shear and Yawed flow

# IEA Task 29, Phase IV: Definition of second round of calculations on DanAero experiment (Case IV.2)

K. Boorsma J.G. Schepers, H.A. Madsen, G. Pirrung  
June 03 2019

## Revision

- 1, April 16
- 2, May 14
- 3, May 23
- 4, May 27
- 5, June 3

## 1. Description of the wind turbine and experiment

Information based on references [1] to [6]

The second cases of IEA Task 29 Phase IV (denoted as Case IV.2.1 and IV.2.2) aim to compare rotor aerodynamics in yaw and vertical shear between codes and experiment. The output properties are as much as possible compatible to the measurement signals from the DanAero experiment.

The turbine data can be found digitally in an Excel sheet on the sharepoint site ([Turbine data excel sheet](#)) and contrary to the first cases, for the second cases **flexibility, tilt angle, and tower shadow effects are included. Pre-Bend is included as well** (here it is noted that the 5 degree tilt angle will increase tower clearance on the lower half of the rotor plane for this upwind rotor). It is anticipated that for many CFD contributions this is not manageable (a rigid and tilted rotor without the tower effect will suffice for CFD), but the main priority here is comparison to the measurements. Fortunately, a recent investigation using a stiff and flexible aeroelastic model of the NM80 turbine in simulations with the HAWC2 code indicates that the flexibility has very small impact on the aerodynamic forces on the blade<sup>1</sup>

To make sure that all lifting line codes use the same input, the airfoil coefficient data sets are prescribed in the Excel sheet (also see ANAERO\_3DA\_pc\_hama\_38.CL.eps) For the CFD modellers please use the supplied CAD files from the sharepoint site ([CFD rotor model](#)), which is the design geometry of the blades as supplied by DTU. Please note that the blade geometry does not yet include the pitch angle. At a later stage the mesh files for CFD will be prescribed as well.

## 2. Description of case IV.2.1 and case IV.2.2.

---

<sup>1</sup> See the note "HAWC2-model-set-up-NM80-turbine.pdf" on the sharepoint site in the folder "The DANAEERO data base".

Under the umbrella of case IV.2 two ‘sub’ cases are defined denoted as **case IV.2.1, and case IV.2.2**. The difference between these two sub-cases lays in the fact that case IV.2.1 is in **sheared** inflow where case IV.2.2 is in **yawed** inflow (although it also has a considerable shear).

The output format is largely based on the format which has been used in the former Mexnext phases in yaw, where results were given as a function of rotor azimuth angle. Here an azimuth angle of 0 degree is defined as blade 1 pointing upwards. Positive rotation is in clockwise direction whilst looking downwind.

- Case IV.2.1 (shear)

All below parameters are constant

- Pitch angle: -4.75 degrees (i.e. negative pitch means larger AOA)
- Rotor speed: 16.2 rpm
- Hub height wind speed 9.792 m/s @ 57.19 m
- Shear exponent 0.249
- Air density  $\rho = 1.22 \text{ kg/m}^3$
- Yaw angle: -6.02 degrees, see Figure 1 for yaw angle convention.
- Ambient pressure: 1005 Pa

- Case IV.1.2 (yaw)

All below parameters are constant

- Pitch angle: -4.75 degrees (i.e. negative pitch means larger AOA)
- Rotor speed: 16.2 rpm
- Hub height wind speed 8.429 m/s @ 57.19 m
- Shear exponent 0.262
- Air density  $\rho = 1.22 \text{ kg/m}^3$
- Yaw angle: -38.34 degrees
- Ambient pressure: 1020 Pa

### **3. Results to be supplied:**

#### **3.1 Lifting line codes:**

The comparison of results from lifting line codes (e.g. BEM codes) mainly focuses on the local aerodynamic forces at the 4 instrumented sections. In addition the flapwise blade root moments are compared. The axial force and the torque will be deduced from the sectional forces at the 4 station using a post-processing script. Apart from that several lifting line variables are compared mutually.

##### **3.1.1 Loads**

- Requested data and units as a function of bin averaged rotor azimuth angle [deg] between 0 and 360 deg. Preferably in steps smaller than 5 deg azimuth.
  - $M_{\text{flap}}$ : Flapwise blade root moment of blade 1 [Nm] at  $r=3.04$  m from the rotor center (not perpendicular to the rotorplane but co-rotating with the pitch angle).
  - For the 4 instrumented radial locations ( $r=13121/19064/30219/36775$  mm from the rotor center) (we will use these exact locations in all future comparisons):
    - $F_{\text{normal}}$  (i.e. the force normal to the local chord, positive pointing in downwind direction) [N/m]

- $F_{\text{tangential}}$  (i.e. the force parallel to the local chord, positive pointing from trailing to leading edge) [N/m]. [To compare with the measurements this should be the ‘pressure’ tangential force without skin friction \(CFD only\).](#)
- Files to be supplied:
  - Please supply the data in two ASCII files which should contain the data for the two cases (case IV.2.1 and IV.2.2).
  - Format: Each row contains 10 columns with data containing flapwise blade root moment, and normal and tangential forces at 4 sections. Separate the columns by tabs or blanks. The first row gives the identification of data. The next rows give the data at the specified azimuth positions (a total of n) between 0 and 360 deg. Hence, the format is as follows

```
Azi Mflap Fnr1 Ftr1 Fnr2 Ftr2 Fnr3 Ftr3 Fnr4 Ftr4
Azi1 - - - - - - - - - -
| | | | | | | | | |
| | | | | | | | | |
Azin - - - - - - - - - -
```

Note that this makes the total number of rows to be  $n + 1$   
(1 (header) + n azimuth positions)

### 3.1.2 Lifting line variables

- Requested data and units as a function of bin averaged rotor azimuth angle [deg] between 0 and 360 deg. Preferably in steps smaller than 5 deg azimuth.
  - For the 4 instrumented radial locations ( $r=13121/19064/30219/36775$  mm from the rotor center):
    - $V_{\text{eff}}$  (i.e. the resultant incoming velocity at the blade section) [m/s]
    - $\alpha$  Angle of attack [deg]
    - $u_i$ , the local axial induced velocity [m/s]  
[The sign is positive pointing in upwind direction.](#)
    - $u_{\text{tan}}$ , the local velocity induced in tangential (rotational) direction [m/s]  
[The sign is positive pointing opposite to the direction of rotation.](#)
    - $c_n$  normal force coefficient =  $F_{\text{normal}} / (0.5 \rho V_{\text{eff}}^2 c)$  [-]  
[Orientation in agreement with  \$F\_{\text{normal}}\$  from loads \(section 3.1.1\)](#)
    - $c_t$  tangential force coefficient =  $F_{\text{tangential}} / (0.5 \rho V_{\text{eff}}^2 c)$  [-]  
[Orientation in agreement with  \$F\_{\text{tangential}}\$  from loads \(section 3.1.1\)](#)
- Files to be supplied:
  - Please supply the data in two plain ASCII files which should contain the data for the three cases (case IV.2.1 and IV.2.2)

- Format: Each row contains 25 columns, containing the 6 variables at 4 radial stations. Separate the columns by tabs or blanks. The first row gives the identification of data. The next rows give the data at the specified azimuth positions (a total of n) between 0 and 360 deg. Hence, the format is as follows:

```

Azi  Veffr1  αeffr1  uir1  utanr1  cnr1  ctr1  Veffr2  αeffr2  ----  utanr4  cnr4  ctr4
Azi1  -      -      -      -      -      -      -      -      -      -      -      -
|      |      |      |      |      |      |      |      |      |      |      |
|      |      |      |      |      |      |      |      |      |      |      |
Azin  -      -      -      -      -      -      -      -      -      -      -      -

```

Note that this makes the total number of rows to be  $n + 1$   
(1 (header) + n azimuth positions)

### 3.2 CFD codes

CFD (and possibly panel) codes will model the pressures distributions (and resulting loads) around the blades which can be compared with the measured data as well.

#### 3.2.1 Loads

See the format specification of the file in section 3.1.1.

#### 3.2.2 Pressure data

- Requested data and units.
  - For all instrumented sections: Pressure data in dimensional form [Pa] **relative to the ambient pressure** as function of x (along the chord) and y (perpendicular to the chord) for 4 different azimuth angles (0 degrees (12 o'clock), 90 degrees (3 o'clock), 180 degrees (6 o'clock) and 270 degrees (9 o'clock)). Note that (x=0,y=0) is at the nose of the airfoil. Positive y at the suction side. Units of x and y are [m]. Note that x and y do not necessarily need to coincide with the position of the sensors.
- Files to be supplied
  - For every instrumented section and every sub case a separate (ASCII) file needs to be supplied. Hence a total of 4 (radial positions at r=13121/19064/30219/36775 mm from the rotor center) \* 2 (cases) = 8 files need to be supplied.
  - Format: Ten columns with pressures as function of x (along the chord) and y (perpendicular to the chord) starting at the trailing edge, then going along the suction side to the leading edge and then back to the trailing edge along the pressure side. Separate the columns by tabs or blanks. The format is given below: It starts with 2 columns with x and y of the pressure points, then the first azimuth angle (0 degrees) followed by the pressures, then the azimuth angles and the pressures at the remaining azimuth angles. We explicitly ask you to specify the azimuth angle to assure that the pressures are supplied for the correct azimuthal position. We recall that pressures should be supplied in Pascal relative to ambient pressure.

x[m]	y[m]	Azi <sub>0</sub>	P <sub>azi0</sub> [Pa]	Azi <sub>1</sub>	P <sub>azi1</sub>	Azi <sub>2</sub>	P <sub>azi2</sub>	Azi <sub>3</sub>	P <sub>azi3</sub>
chord (t.e.)	0	0	--	90	--	180	--	270	--
--	positive	0	negative *)	90	--	180	--	270	--
0(l.e.)	0	0	--	90	--	180	--	270	--
--	negative	0	positive **)	90	--	180	--	270	--
Chord(t.e.)	0	0	--	90	--	180	--	270	--

\*) Usually suction (negative) pressures \*\*) Usually positive pressures

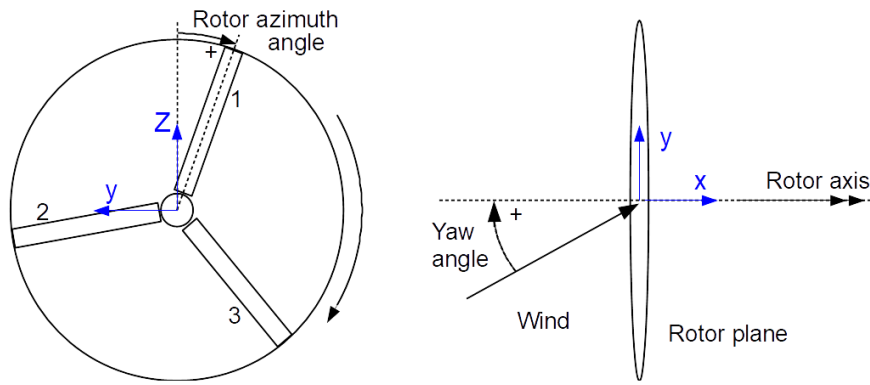


Figure 1: Front view looking downwind (left) and top view looking downward (right), defining azimuth and yaw angle



## References

- [1] H.Aa. Madsen, C. Bak, U.S. Paulsen, M. Gaunaa, P. Fuglsang, J. Romblad, N.A. Olesen, P. Enevoldsen, J. Laursen, and L. Jensen. *The DAN-AERO MW Experiments Final report*. Technical Report RISO-R- 1726(EN), Technical University of Denmark, 2010.
- [2] C. Bak, H.Aa. Madsen, P. Hansen, M. Rasmussen, P. Fuglsang, J. Romblad, N.A. Olesen, *Danaero MW Measurement campaigns on the NM80 2.3 MW Wind Turbine at Tjaereborg 2009* Technical Report RISO-I- 3046(EN), Technical University of Denmark, 2010.
- [3] N. Troldborg, C. Bak, H. Aa. Madsen, W. Skrzypinski *DANAERO MW: Final Report* DTU Wind Energy E-0027, April 2013
- [4] C. Bak, H. Aa. Madsen N. Troldborg M. Gaunaa, W. Skrzypinski A. Fischer, U.S. Paulsen, R. Moller, P. Hansen, M. Rasmussen, P. Fuglsang *Danaero MW Instrumentation of the NM80 turbine and meteorology mast at Tjaereborg*, DTU Wind Energy report I-0083, May 2013

Additional information can be found from the following AVATAR deliverables:

- [5] H.Aa.Madsen, Joachim Heinz, S. Voutsinas, N. R. García, G.Pirrung, Niels N. Sørensen, N. Troldborg *Aerodynamics of Large Rotors, Validation of advanced models against measured data* AVATAR Deliverable 4.2, August 2016
- [6] N. N. Sørensen, N. Ramos García, S. Voutsinas, E. Jost, T. Lutz *Effects of complex inflow for the AVATAR reference rotor*, Deliverable D.2.6, September 2017

## Appendix B

# Lifting line code description

## B.1 DNV GL - Bladed - Code description

Marina Carrion, Steven Parkinson, Edoardo Cicirello

The results provided by DNV GL are based on the new BEM code developed for Bladed. The model is based on classical BEM theory where the axial and tangential Glauert momentum equations are expressed in dimensional form instead of non-dimensional factors. Further the dynamic models (dynamic wake, dynamic stall, skew wake correction) are fully expressed in state-space form allowing combined direct integration of structural and aerodynamic states. The aerodynamic and structural states are integrated with a 4th order variable step Runge-Kutta integrator.

The following engineering correction models are applied in the BEM model:

1. Oye Dynamic wake model
2. Incompressible Beddoes-Leishman dynamic stall model in state-space format, modified to also include the vortex lift terms on lift and moment coefficient.
3. Glauert skew wake correction method.
4. Prandtl tip correction and Glauert corrections for highly loaded rotors.

## B.2 DTU - EllipSys3D/Actuator Line/FLEX5 - Code description

Wen Zhong Shen (DTU Wind Energy)

The flow past a wind turbine is modelled with the actuator line (AL) method introduced by Sørensen and Shen [98], which is implemented in DTU's in-house finite volume code EllipSys3D. EllipSys3D is developed by the cooperation of the Department of Mechanical Engineering at DTU and the Department of Wind Energy at Risø National Laboratory. The AL method [98] [99] represents the aerodynamic loads of wind turbine blades by using a body force distributed along rotating lines. The body force imposed in the Navier-Stokes equations is computed by the aero-elastic code FLEX5 [100]. The coupling of FLEX5 and AL methods is performed in both ways. The flow data at the blades from EllipSys3D/AL are fed into FLEX5 to calculate the angle of attack and relative velocity including blade deformation/motions. Then, aerodynamic loads on the blades are obtained by using tabulated airfoil lift and drag vs angle of attack (AoA) data. These loads are then fed into EllipSys3D/AL as a body force on the moving actuator lines. In this approach, the actuator line coordinates are determined from FLEX5, which includes the effect of blade bending and motion of the rotor (up/down/side-to-side/rotations). In a standard aero-elastic code, these effects and motions are calculated based upon using the blade momentum theory (BEM) as the aerodynamic model. Here, a Navier-Stokes AL method is used to solve the fluid-structure interaction problem instead. To calculate the noise emission from the blades, the BPM code [101] is used. The variables of angle of attack, airfoil boundary layer parameters, and relative velocity are called from FLEX5 and fed to BPM. A flow chart of the combined EllipSys3D/AL, FLEX5 and BPM framework is shown in the figure below.

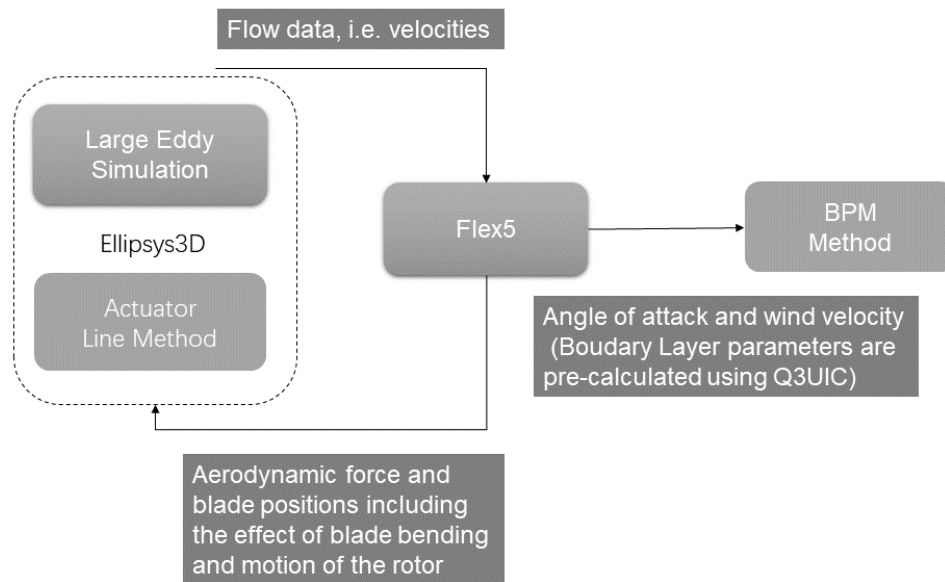


Figure B.1: Flow chart of the combined EllipSys3D/AL, FLEX5 and BPM program.

In EllipSys3D, the solution to the incompressible Navier Stokes equations is advanced in time using an iterative time-stepping method. The equations are solved iteratively in each global time-step, with the usage of under-relaxation. First, the code uses the momentum equations as a predictor so that the solution can be advanced in time. The pressure correction equation, i.e., the rewritten continuity equation to satisfying the local mass conservation in discretized form, is used as a corrector making the predicted flow field satisfy the

continuity constraint. This is a two-step procedure corresponding to a single sub-iteration, and the process is repeated until the solution becomes convergent with sub-iterations. The variables are then updated after the convergent solution is updated, and then followed by the next time step. The aero-elastic code FLEX5 is designed to simulate the wind turbine's dynamic behavior regarding different wind conditions. FLEX5 operates in the time domain, and the output is the time-series of simulated loads and deflections. The acoustic prediction BPM model [101] used in this work takes the detailed geometrical and flow information into account, e.g., tip shape, blade geometry as well as wind direction. The velocity at each blade segment is computed by accounting for the induction effect and the vibration velocity of the blade. Furthermore, the geometry contours of airfoil sections at different blade segments are also included in the prediction as important inputs.

In the computation rounds, a mesh of  $192 \times 192 \times 512$  in the transversal, vertical and streamwise directions, respectively, is used with a resolution of 30 cells per rotor radius in the rotor plane and 18 cells per rotor radius uniformly distributed from 1D in front of the turbine to 11D behind the turbine. The airfoil data used in the computations were provided from the IEA Task 29 consortium. To take into account the dynamic stall effects, the Øye dynamic stall model is used as this is part of FLEX5. The tower is not considered in the computations. For more details about the code and computations, the reader is referred to [102].

## B.3 Description of DTU - HAWC2 codes

H. Aa. Madsen, G. R. Pirrung, Christian Grinderslev and A. Meyer-Forsting (DTU Wind Energy)

### B.3.1 Introduction

The computational codes from DTU are build up around two basic codes: the HAWC2 aeroelastic code and the 3D CFD code EllipSys3D. Below the different versions of the codes are briefly described

### B.3.2 The HAWC2 code

The HAWC2 code has been developed at Risoe National Laboratory of Denmark (now DTU Wind Energy) over the last more than 15 years. Its available on a commercial basis with a license and is widely used within the wind industry and at several research institutes. For research cooperation a reduced or fee license can be provided.

Over the last few years the HAWC2 code has been further developed into a framework where the code can be run with aerodynamic modelling of different fidelity's presented below after the description of the structural part.

### B.3.3 The structural part of HAWC2

The structural part of the code is a multibody formulation based on the roating frame of reference method as described in [103]. In the particular formulation of the code, the turbine structure is subdivided into a number of bodies where each body has its own coordinate system. Within each body, the structure consists of an assembly of linear Timoshenko beam elements. The nonlinear effects of the body motion (rotations and deformations) are accounted for in the coupling constraints in between the individual bodies, ensuring small deflections within the linear beam elements. This means that effects of large rotations and deflections are included using a proper subdivision of a blade to a number of bodies. The suggested method has been validated with another existing nonlinear multibody formulation with the classical spin-up maneuver example [103].

### HAWC2 BEM

In the basic version of the HAWC2 The aerodynamic part of the code is based on the blade element momentum (BEM) theory [104], however implemented in a way that is comparable with an actuator disc approach [105], [30], which means that the induction at each time step is computed in a number of points distributed over the swept area in order to respond to instantaneous changes in loading from shear and turbulence in the inflow. In particular the induction response to turbulence will with this implementation have the same same frequency characteristics as the turbulent inflow which means peaks at 1p, 2p etc. In general an increased dynamic induction reduces the dynamic loads from turbulence which seems in line with computations with higher fidelity codes.

The present BEM implementation has a further advantage that rotor designs where the swept surface deviates from a plane circular disc like coned rotors or rotors with wing lets can be analyzed if induction characteristics can be imported from a CFD based actuator disc simulation [105].

### HAWC2-NW

The HAWC2-NW is a hybrid BEM and lifting line code developed over almost the same time interval as the HAWC2 code. The overall idea with the model [106] is to use a fast lifting line (LL) model to compute the induction from the near part of the trailed vorticity from the individual blades. The big advantage is that the induction at one position on the blade is influenced by the trailed vorticity along the whole blade so that strong variations in loading on the blade like at the tip region is modelled more accurate. Also the near wake dynamic induction is modelled more accurately with the NW model as no external time constants are used for the near wake.

Since the first formulation of the NW model in 2005 [106] the model has been developed much further [107] [108] and recently extended to model swept blades [109].

### **HAWC2-EllipSys3D**

A partitioned coupling between HAWC2 and EllipSys3D enables high-fidelity fluid-structure interaction (FSI) simulations. The coupling between aerodynamics (EllipSys3D) and structure (HAWC2) is loose, such that only one corrector step is conducted for each timestep. This was found sufficient for wind turbine aero-elasticity in [110], due to the high mass ratio between wind turbine and air.

HAWC2 does 2nd order accurate predictions of deformations, which are propagated to the CFD surface mesh. The volume mesh is deformed through a volume blending based on grid line distance to the surface. EllipSys3D then computes the flowfield through inner sub-iterations and new forces are calculated. These are transferred to HAWC2 which calculates the actual deformation, and then predicts the deformation for the coming timestep. The HAWC2CFD framework is presented in [110–112].

### **HAWCStab2**

Another important tool using the same input files as HAWC2 is HAWCStab2 which is a tool for stability analysis. It computes both structural and aeroelastic frequencies and damping for the whole turbine as well as for the blade only.

Finally, a range of pre- and post processing tools can be downloaded from the same site as where the HAWC2 and HAWCStab2 also are shared, . Several references relating the codes are also available from that site.

### **B.3.4 EllipSys3D-AL**

The actuator line (AL) [98] is a lifting line (LL) representation of aerodynamic surfaces in Eulerian computational fluid dynamics (CFD) applications. The actuator line model, unlike the actuator disc, captures transient physical features like shed and trailed vorticity (including root/tip vortices) by distributing the blade forces - computed from 2D airfoil polars - in the flow domain. The chosen EllipSys3D implementation employs a three-dimensional Gaussian force projection, following the original formulation of Sørensen and Shen [98]. The smearing length scale is twice the grid size as recommended by Troldborg [113] to guarantee numerical stability. The force smearing leads to over-predictions in the blade forces, which is counteracted by the correction of Meyer Forsting *et al.* [59,60,114]. To ensure the blade tip to remain inside a single cell during one time step  $\Delta t < 2\Delta x/(\Omega D)$  - with mesh spacing  $\Delta x$  and rotational speed  $\Omega$ .

The numerical domain for the rotor simulations is discretised in a verified, standard manner [113,115]. It consists of a box with  $25R$  side length that contains an inner box with a uniformly spaced refined mesh of  $3.2R$  edge length at its centre surrounding the rotor. The mesh spacing in this region is connected to the number of blade sections of the AL -  $\Delta x = R/40$ . In total 192 cells discretise the flow domain along each dimension, resulting in  $7 \times 10^6$  degrees of freedom. The boundaries off the main flow direction are of the Symmetry type, whereas the inflow and outflow faces obey Dirichlet and Neumann conditions, respectively.

## B.4 IFPEN DeepLines Wind<sup>TM</sup> solver

F. Blondel, P. Bozonnet (IFPEN)

### B.4.1 DeepLines Wind<sup>TM</sup> aero-elastic model

DeepLines Wind<sup>TM</sup> is an aero-hydro-servo-elastic solver ([116], [117]) able to model floating wind turbines, accounting for aerodynamic and hydrodynamic loads as well as the elasticity of the various structural components. It has already been successfully applied to the simulation of horizontal [118] and vertical [119] axis wind turbines.

DeepLinesWind is based on a finite-element solver using Timoshenko beams, thus including flapwise and edgewise bendings, traction/compression and torsion. The blades, the tower and the shaft are modelled with beam elements and lineic mass distribution. Whereas the nacelle and the hub are modelled using rigid-bodies, associated with punctual mass and inertia matrix. Structural damping on the beam elements is included with Rayleigh formulation. As regards time integration a semi-implicit Newmark scheme is implemented. Coupling with the aerodynamic library is performed through a loose coupling: the aerodynamic library is called at each time step, but no iteration is made. Several aerodynamic libraries can be used with DeepLinesWind<sup>TM</sup>, including AeroDeeP (BEM) and CASTOR (vortex), introduced below.

### B.4.2 AeroDeeP: Blade Element Momentum (BEM) model

The first model used during the DanAero benchmark is a BEM-based model, that includes several corrections.

#### Mean induction model

*AeroDeeP* is based on a mean induction model that includes the effect of rotor misalignment and a Turbulent Wake State (TWS) correction adapted to yaw.

Under low induction conditions ( $a \leq \beta$ , with  $\beta \approx 0.35$  in the present simulations), the following relation between the axial induction and the thrust coefficient holds (Glauert, [104]):

$$C_{T,MOM} = 4aF\sqrt{1 + a^2 - 2a\cos(\gamma)}, \quad (\text{B.1})$$

with  $\gamma$  the rotor misalignment angle (that includes both yaw and tilt effect).

For higher inductions (TWS,  $a > \beta$ ), relation B.1 is not valid anymore. We use the correction proposed by Ning et al. [32]. The thrust coefficient is approximated using a second-order polynomial expression:

$$C_{T,TWS} = k_0 + k_1a + k_2a^2, \quad (\text{B.2})$$

with:

$$\begin{aligned} k_0 &= f_1 - k_1 - k_2, \\ k_1 &= f'_0 - 2k_2\beta, \\ k_2 &= \frac{f_1 - f_0 - f'_0(1 - \beta)}{(1 - \beta)^2}, \\ f_1 &= 2, \\ f'_0 &= \frac{dC_{T,MOM}}{da} \quad \text{with } (a = \beta), \\ f_0 &= C_{T,MOM} \quad \text{with } (a = \beta). \end{aligned} \quad (\text{B.3})$$

#### Tip and hub loss model

The Prandtl model [120] is used to account for both tip and root vortex influence:

$$F = \frac{2}{\pi} \arccos \left( \exp \left( -\frac{\frac{B}{2} \left(1 - \frac{r}{R}\right)}{\frac{r}{R} \sin(\phi)} \right) \right) \times \frac{2}{\pi} \arccos \left( \exp \left( -\frac{\frac{B}{2} \left(\frac{r}{r_{hub}} - 1\right)}{\frac{r}{R} \sin(\phi)} \right) \right), \quad (\text{B.4})$$



with  $\phi$  the inflow angle,  $r_{hub}$  the hub radius,  $R$  the rotor radius,  $r$  the current element radius (from the rotor center),  $B$  the number of blades and  $F$  a factor that scales the thrust coefficient as  $C_{T,loss} = \frac{C_T}{F}$ .

### Rotor misalignment model

Rotor misalignment models (or yaw models) are used to account for the interactions between the wake and the blades under misaligned rotor plane conditions. In our implementation, a global misalignment angle  $\gamma$  that includes both yaw and tilt effect is used. The model presented in Blondel et al. [36] is used in this benchmark. The model accounts for both tip and root vortex effects, keeping a low number of parameters and two constant phases. The azimuthal distribution of the axial induction is obtained as follows:

$$a_{yaw} = a \left( 1 + k_1 \frac{r}{R} \tan(\chi/2) \sin(\psi + \phi_1) + k_2 \left( 1 - \frac{r}{R} \right) \tan(\chi/2) \sin(\psi + \phi_2) \right). \quad (\text{B.5})$$

In equation B.5,  $\phi$  are phase angles, that take the following values:  $\phi_1 = 0$ ,  $\phi_2 = \pi$ . With  $A_0 = 0.35$  a constant of the model, the shape functions take the following forms:

$$\begin{aligned} k_1 &= (1 - A_0) + A_0 \frac{r - r_{hub}}{R - r_{hub}}, \\ k_2 &= 1 - A_0 \frac{r - r_{hub}}{R - r_{hub}}, \end{aligned} \quad (\text{B.6})$$

with  $R$  the rotor radius,  $r_{hub}$  the hub radius, and  $r$  the current element radial position with respect to the hub center. The misaligned rotor correction is applied after the convergence of the induced velocities.

### Dynamic stall modelling

Dynamic stall is likely to occur in the considered cases. The model of Øye [121] is used in the present study. It integrates some modifications, has suggested in [36].

The lift is modeled using the following relation:

$$C_{l,dyn} = f_d C_{l,fa} + (1 - f_d) C_{l,fs}, \quad (\text{B.7})$$

with  $f_d$  the dynamic attachment degree function, the subscript *dyn* indicating dynamic lift, *fa* fully-attached lift, and *fs* fully-separated lift coefficients. The fully-attached lift coefficient is computed using the static lift curve slope at an attack angle of zero degree:

$$C_{l,fa} = \left. \frac{\partial C_l}{\partial \alpha} \right|_{\alpha_0} (\alpha - \alpha_0). \quad (\text{B.8})$$

This expression of the fully-attached lift coefficient is used to compute the static attachment degree function, using the Kirchhoff flow theory:

$$C_l \simeq \left( \frac{1 + \sqrt{f}}{2} \right)^2 C_{l,fa}. \quad (\text{B.9})$$

Then, the fully-separated lift coefficient can be calculated, since we have  $C_l = f C_{l,fa} + (1 - f) C_{l,fs}$ . The dynamic attachment degree function is based on a first order ordinary differential equation:

$$\frac{df_d}{dt} = \frac{(f - f_d)}{\tau}, \quad (\text{B.10})$$

with  $\tau = A_1 c / |u|$ ,  $A_1$  being a constant usually set to  $A_1 = 4$ ,  $c$  the airfoil chord, and  $|u|$  the norm of the airfoil relative velocity. In the present implementation, dynamic stall is applied within the convergence loop of the BEM algorithm.

## Dynamic inflow modelling

Another dynamic correction is applied to the BEM through the so-called “dynamic inflow” models. This model represents the time lag observed on the rotor loads when a change of inflow condition (or rotor state) is present. Such changes can be due to a varying wind velocity, a change in pitch angle, or even a sheared inflow. Dynamic inflow time scales are rather high compared with dynamic stall time scales, which distinguishes the two corrections.

The dynamic inflow model derived by Øye (as described in [122]) is used. In this model, the dynamic induced velocity  $w_{dyn}$  is computed using based on a system of two first-order differential equations, involving an intermediate induced velocity  $w_{int}$  and the steady one  $w_{qs}$ :

$$\begin{aligned}w_{int} + \tau_1 \frac{dw_{int}}{dt} a &= w_{qs} + k\tau_1 \frac{dw_{qs}}{dt}, \\w_{dyn} + \tau_2 \frac{dw_{dyn}}{dt} &= w_{int},\end{aligned}\tag{B.11}$$
$$\tau_1 = \frac{1.1}{1 - 1.3a} \frac{R}{|v|},$$
$$\tau_2 = \left(0.39 - 0.26 (r/R)^2\right) \tau_1,$$

with  $|v|$  the norm of the wind vector relative to the considered blade element. In the current implementation, the relative velocities that are due to the rotor misalignment (i.e. advancing and retreating blade effect) are excluded from the calculation of the dynamic stall. To do so, a first BEM algorithm is run under fully aligned flow conditions (only the norm of the wind projected in the hub direction is kept, the others are set to zero). Then, the axial, dynamic induced velocity is calculated and the offset with respect to the quasi-steady velocity is stored ( $\Delta w_{aligned} = w_{dyn} - w_{qs}$ , with  $w_{qs}$  the quasi-steady induced velocity of the fully aligned simulation). Finally, the dynamic induced velocity of the “standard”, non fully-aligned BEM is computed:  $w_{dyn,misaligned} = w_{qs,misaligned} + \Delta w_{aligned}$ .

The dynamic inflow correction is applied after the convergence of the induced velocities.

### B.4.3 CASTOR: Free-wake lifting-line vortex filaments flow solver

CASTOR is a free-wake vortex filament lifting-line solver based on the generalized Prandtl lifting-line theory. In order to reduce the computational cost, CASTOR is based on a hybrid *OpenMP* / *GPU* implementation, thereby reducing the computational times up to two orders of magnitude when compared to sequential *CPU* implementations. The wake can be discretized using vortex filaments and/or vortex particles. In the present simulations, only filaments are used. A modified Øye dynamic stall model, as described in section B.4.2, has been used during the simulations.

### B.4.4 DanAero simulations setup

#### Wind model

In the present simulations, uniform and constant wind without turbulence has been used.

#### Airfoil data

The five provided airfoil polars have been linearly interpolated along the blade. These polars are already corrected for three-dimensional effects, thus no additional corrections have been used.

#### Spanwise integration

Axial and torque are integrated using a trapezoidal rule applied to each blade element.

### **Time stepping**

An automatic time step setting is used, with a maximum value of  $\Delta t = 0.05sec$ . It corresponds to a rotation of the blades of approximately 3.7 degrees per time step for the axial flow cases and 4.85 degrees per time step for the sheared and yawed flow cases. The simulated physical time is set to approximately 120sec. For the vortex solver, 15 full wake rotations are kept in the wake in the axial flow case while 20 full rotations are kept in the sheared and yawed cases. The result averaging is based on the complete wind turbine rotations included between physical times  $t_{start} = 80sec$  and  $t_{end} = 120sec$ .

### **Model discretization**

In the present simulations, there are 238 degrees of freedom or nodes in the model. The tower and the blades are respectively discretised with 54 (equally-spaced) and 34 (cosine-spaced) beam elements.  $\beta$  coefficients for the structural Rayleigh damping are set to 1.e-5, 0 and 0.02 respectively for the blades, shaft and tower.

### **CPU times**

Using the *BEM* model, the global simulation time is approximately 2 minutes. Using the vortex solver on one single *GPU*, the simulation time is approximately 7 hours (using the aforementioned 15 full rotations in the wake and a blade rotation of 4.85 degrees per time step).

## B.5 NREL OpenFAST - Code description and simulation setup

E. Branlard and J. Jonkman (NREL)

### B.5.1 BEM

1. **BEM formulation:** The momentum and blade element formulae are combined and expressed using the flow angle as a variable, leading to a constraint equation that is solved using a root finding method [123]. The BEM equations are applied locally, using the local inflow, without using azimuthal averaging or a grid. The equations are applied in the blade cross section coordinate system. The different models are applied in the following order: 1) Quasi steady induction; 2) Dynamic inflow; 3) Yaw correction; 4) Dynamic stall. The models are documented in [31, 124–127]. A reformulation of the algorithm is likely to occur in the near future.
2. **Blade discretization:** 40 stations along the blade span from root to tip, calculation points are at the stations.
3. **Airfoil data:** The 5 polars provided (which already include 3D corrections), were linearly interpolated to each blade stations based on the thickness distribution.
4. **Dynamic stall model:** The Minemima/Pierce variant of the Beddoes-Leishman dynamic stall model was used. The input parameters (see [124])  $\alpha_0$ ,  $\alpha_1$ ,  $\alpha_2$ ,  $C_{n,\alpha}$ ,  $C_{n,1}$ ,  $C_{n,2}$ ,  $C_{d,0}$ ,  $C_{m,0}$  were computed based on the interpolated polar data. Other parameters of the models were kept at their default values (e.g. time constants). For the cases simulated in this report, the dynamic stall model has a moderate influence on the results for the first half of the blade span, and very limited impact for the outer part of the blade.
5. **Tip and root correction:** Glauert tip and hub loss corrections are used (that is, Prandtl tip-loss correction adapted such as to use the local flow angle) [104]. The radial distance is computed using the hub radius for the hub correction, and from the tip for the tip correction. The hub correction has very limited impact on the results.
6. **Turbulent wake (i.e. momentum breakdown, high thrust correction):** The Glauert/Buhl correction is used for axial inductions above 0.4. The correction is found in [127].
7. **Tower influence model:** The tower influence is accounted for using a flow model that relies on the potential flow about a 2D cylinder (see e.g. [61]). A smooth transition is done for values above the tower.
8. **Yaw model:** The skew wake model of Glauert [128]/Coleman [129] is used, with the constant in front of the sinusoidal term taken by default as:  $15\pi/32 \tan(\chi/2)$  (from Pitt and Peters [126, 130]).
9. **Dynamic inflow model:** The implementation relies on Øye’s dynamic inflow model (also referred to as TUDK model in [131]). The differential equations are integrated assuming a linear variation of the right hand side of the equation [125], a method different from the one presented by Hansen [61].
10. **Drag in induction computation:** The drag is included in both the axial and tangential inductions. For the cases studied in this report: including the drag in the tangential induction results in negative tangential induced velocities towards the root; including drag in the axial induction results in an increased axial induction at the root.

### B.5.2 Lifting line vortex methods

1. **Blade representation:** A lifting line model is used, following the implementation of van Garrel [132, 133].
2. **Blade discretization:** 40 stations along the blade span from root to tip, equally distributed from the root to 90% of the span, and with twice the resolution for the remaining tip values. Calculation points are located in between stations, following the full-cosine approximation of van Garrel [132].

3. **Wake:** A free vortex-lattice wake is used. In this work, the time step was chosen to correspond to a 6 degrees azimuthal discretization. A sub-cycling method is implemented, allowing for a larger time step than the elastic solver. The wake consists of three regions: near-wake, free far-wake, and frozen far-wake, respectively of length corresponding to 6, 2 and 7 rotor revolution(s). The near-wake has the same spanwise discretization as the blade. The far wake consists only of a root and tip vortex, which positions and intensities are set from the last values of the near wake. The frozen far-wake convects at the average velocity over the free far-wake. This configuration leads to approximately 40.000 wake points. The vorticity is regularized using the Vatistas kernel. The initial regularization parameter for the wake and the blades is taken at half the discretization distance along the blade span. A core spreading method is used to increase the regularization parameter with wake age. The model from Squire is applied, with an eddy viscosity parameter of 3000. Additional details on the models mentioned are found in [133,134].
4. **Convergence:** No discretization study was performed to analyse the convergence, but attention was put on the time derivative of the induction at the rotor as the wake extends downstream. The loads on the rotor were seen to have converged after approximately 90s for the cases selected. The wake was chosen to extend for 15 revolutions downstream, corresponding to approximately 4 to 5 diameters. This distance was chosen based on the following consideration:, for a vortex cylinder wake, a wake length of  $3.5D$  accounts for 99% of the induction compared to a wake of infinite length [135].
5. **Airfoil data:** The 5 polars provided (which already include 3D corrections), were linearly interpolated to each blade stations based on the thickness distribution.
6. **Dynamic stall model:** No dynamic stall was used.
7. **Tower shadow model:** The tower shadow models of OpenFAST can be used in conjunction with the vortex code. For the current study, the potential flow model is used. There are two options for the vortex code: the tower shadow model affects the lifting line velocity only, or, the tower shadow model affects the lifting-line and the wake velocity. For this study, the former option was used.
8. **Miscellaneous remarks** OpenMP parallelization is used to parallelize the Biot-Savart computation, and a Fast multipole tree-code is used to reduce the computational complexity.

### B.5.3 Structural modeling

1. **Elastic components:** blades, tower, and shaft were modeled as elastic. The yaw bearing was assumed rigid.
2. **Elastic modeling:** Two main elasticity modules of OpenFAST were used, ElastoDyn and BeamDyn. Two configurations are used in this study. In one configuration, ElastoDyn models the tower shaft and blades. In another configuration, ElastoDyn models the tower and shaft, while the blades are modelled with BeamDyn. ElastoDyn relies on a limited set of carefully selected degrees of freedom, which are taken as shape functions for flexible bodies. Flexible bodies are hence modelled using a Rayleigh-Ritz approach, where the equation of motions are derived using Kane’s method (i.e. the virtual work principal) (see e.g. [136, 137]). ElastoDyn further includes some geometric nonlinearities, valid for moderate deflection. Only flap and edge wise bending are modelled, no torsion is included. BeamDyn uses a geometrically exact beam theory that is discretized using Legendre-spectral finite elements [138]. BeamDyn includes full geometric nonlinearity, and models all beam deformations: bending, shear, axial, torsion. OpenFAST uses a modular framework [139, 140] with a loose coupling, such that each module integrates its states, and communication and extrapolation of inputs and outputs is taken care by the glue-code. The blade is discretized using 36 elements, and the tower using 40 elements.
3. **Degrees of freedom (DOF):** ElastoDyn uses 3 DOF per blade (2 flap and 1 edge shape functions), 4 DOF for the tower (2 in fore-aft and 2 in side-side direction), and 2 DOF for the shaft (shaft rotation and torsion). BeamDyn’s number of DOF depends on the user inputs. For the current study, one element is used, with 7 nodes, and 23 quadrature points, leading to 42 DOF per blade. For the

ElastoDyn only configuration, the total number of DOF is 15 (counting the shaft rotation). For the BeamDyn configuration, the total number of DOF is 132.

#### 4. Structural damping:

For the ElastoDyn blade, the dampings for the two flaps and edge modes are set respectively as: 0.2435, 0.2785, 0.2674, where the values are in percent of critical damping, and corresponds to the following values of percent log. decrements: 1.53, 1.68, 1.75. BeamDyn using stiffness proportional damping. The damping factors for the flap and edge direction were selected as:  $\beta_{fl} = \frac{2\zeta_{fl}}{\omega_{fl}} \approx 0.00082$  and  $\beta_{ed} = \frac{2\zeta_{ed}}{\omega_{ed}} \approx 0.00047$ . Similar values was set for the corresponding shear directions, giving:

$$\beta_{\text{BeamDyn}} = [0.00082, 0.00047, 0.00047, 0.00047, 0.00082, 0.00047] \quad (\text{B.12})$$

The tower damping values were adjusted so that the 1st modes FA-SS of the full structure reaches 2% log decrement, leading to the 1.11% of critical damping for all tower modes. It is noted that the tower was tuned with a longer length to account for the fixity of the foundation (see “miscellaneous notes” below). The drive train torsional damping was set to 0.99 MN-m/(rad/s), such as to give 0.8% of damping ratio (5% log. decrement).

5. **Mass distribution:** The blade and tower mass is distributed along the span (that is, projected onto the shape function for ElastoDyn). The blade mass was not tuned (integrated mass being 9.6t), but the stiffness was lowered to match the natural frequencies. The nacelle mass (taken from the last element provided in the HAWC2 definition), is added to the shaft mass, and their combined center of mass and  $y$  inertia is computed and given as inputs to the “nacelle” properties of OpenFAST. The hub mass and inertia was computed by integrations of the hub elements provided and lumped at the rotor center.
6. **Solution method:** Time integration of the elastic modules is performed using a second-order Adams-Bashforth-Moutlon algorithm for ElastoDyn simulations, and a generalized alpha algorithm for BeamDyn. The BEM module (AeroDyn), contains no continuous states, and hence only a constraint equation is solved for, using the same time-step as the one from the glue-code (and the elastic modules). For simulations using the vortex code, the vortex code integrates its states using a first order Euler algorithm. A sub-cycling method is used when coupled to the elastic solver, such that the right hand side (RHS) of the vortex code state equation is only evaluated every  $n$  steps of the global (and elastic) solver. Yet, the vortex code constraints (finding the circulation) are solved for at each steps, and, the states are integrated at each steps using the proportion  $1/n$  of the RHS of the state equation. Correspondingly, the outputs (velocities and loads at the lifting line) are evaluated at each steps.
7. **Miscellaneous notes:** The tower was tuned compared to the HAWC2 model given: it was extended further below the ground to model the foundation using an apparent fixity length approach. This avoids the large variations of stiffness and mass that were otherwise specified in the HAWC2 model.

### B.5.4 Other information

1. **Wind modeling:** Wind is modelled using the Inflow wind module of OpenFAST which supports, amongst other, shear and turbulence. The same wind module is used for the BEM and vortex code computations.
2. **Time step:** For case IV.1,  $dt = 0.01\text{s}$  ( $0.75^\circ$ ) for the glue-code, elastic and BEM modules, while  $dt_{VC} = 0.08\text{s}$  ( $6^\circ$ ) for the vortex code. For case IV.2,  $dt = 0.01\text{s}$  for the glue-code, elastic and BEM module, while  $dt_{VC} = 0.06\text{s}$  ( $6^\circ$ ) for the vortex code. Cases using BeamDyn, required a time step of  $dt = 0.0001\text{s}$ , resulting in a evaluation of the RHS of the state equation of the vortex code every 600 steps.
3. **Simulation length:** Simulations were run for 120s. For case IV.1, averaging was done over the last 2 rotor revolutions, using the azimuthal values (instead of the time values) to perform averages over exact integer number of revolutions. For case IV.2, azimuthal values were bin-averaged based on the

azimuthal position, using time values between 90s and 120s. It is noted that these procedures are not strictly necessary since periodic steady states were obtained after 90s for both cases.

4. **CPU times:** ElastoDyn+BEM: 60s (1 CPU) . ElastoDyn+Vortex code: 4h (4 CPU).  
BeamDyn+BEM: 3.5h (1 CPU). BeamDyn+Vortex code 36h (4 CPU)
5. **Spanwise integration:** Axial forces integrated using 40 spanwise stations, using the line to point mapping of the mesh mapping library of OpenFAST. Trapezoidal integration is used.

## B.6 ONERA - PUMA - Actuator Line/Free Wake - Code description

Ronan Boisard (ONERA)

The PUMA (Potential Unsteady Methods for Aerodynamics) code, which is developed at ONERA since 2013, is based on a long lasting knowledge about free wakes methods for helicopter aerodynamics. It is built on a coupling between an aerodynamic module and a kinematic module. The aerodynamic module relies on a free wake model and a lifting line approach. The free wake model is based on Mudry theory [141] which rigorously describes the unsteady evolution of a wake modeled by a potential discontinuity surface. The lifting line method relies on 2D airfoils characteristics and can handle some 3D corrections for blade sweep and 2D unsteady aerodynamics effects through dynamics stall models. Moreover, different time discretization options are available in order to balance between accuracy, scheme stability and computational time. Concerning the kinematic module, it is based on a rigid multi-body system approach using a tree-like structure with links and articulations. In order to reduce computational time, the code has been parallelized using OpenMP and the Multilevel Fast Multipole Method has been implemented for the computation of the velocities induced by each wake panel on any element. PUMA is extensively used at ONERA for any aerodynamic study which requires low computational cost or a large amount of parametrical investigation like pre-design studies. It has been successfully applied on quite a lot of different fixed wings and rotating wings configurations like propellers, counter rotating open rotors, helicopter rotors and more recently wind turbines in the MexNext project. A careful look at PUMA numerical parameters has been carried out at the beginning of this investigation through a wide parametric study, which turned out to be essential to define the most appropriate values for the more meaningful parameters listed below:

- 45 radial stations for wake emission using sinusoidal distribution along the span;
- 25 revolutions kept in the wake to compute induced velocities;
- 10° time steps;
- 35 revolutions computed to ensure perfect convergence;
- nacelle and tower influence neglected;
- no dynamic stall model.
- No modeling of the blade flexibility
- Used provided airfoil datas without any corrections
- Not accounting for nacelle and tower

The PUMA tool was used for CaseIV.1.1 (Axi-symmetric) and also for Case IV.2.1 (Shear), and IV.2.2 (yaw) and for the Task3.1. For the cases which include the turbulent boundary layer modeling, the workflow was slightly adapted. The flowfield surrounding the wind turbine was provided from each time step by USTUTT using an empty box computation. This ?undistributed? flowfield was then provided to the PUMA modeling of the wind turbine at each time step to compute the wind turbine wake. Induced velocities from the wind turbine wake are then added to the provided flowfield in order to compute the correct loads on the wind turbine blade and update the wake shading and displacement. Due to numerical issues and to the specificity of this kind of computation , the numerical parameters used for the first computation round were slightly modified:

- Computation time step: 5 degrees
- Number of radial stations for blade definition : 25
- Number of wake revolutions kept for induced velocity computations: 15



## B.7 TNO Aero Module

Koen Boorsma

### B.7.1 Model

The Aero Module [26, 44, 142] is an assembly of rotor aerodynamic models. It includes both BEM as well as a lifting line free vortex wake formulation, allowing the same external input (e.g. wind, tower, airfoil data) to be used for both models. The BEM formulation is based on PHATAS [143], including state of the art engineering extensions which have matured over decades of research in wind turbine rotor aerodynamics. The free vortex wake method is based on the AWSM code [132].

The Aero Module has been coupled to the PHATAS code (available from the FOCUS6 simulation software [144]) that solves the structural dynamics of a wind turbine. The resulting full aero-elastic model is denoted PhatAero. The coupling scheme is implicit, which means the PHATAS code typically calls the Aero Module around 10 times per time step.

#### BEM specific implementation

In order not to average out the effect of inflow variations (e.g. shear, turbulence) on local induction, an unsteady formulation is implemented. Here the momentum equation is evaluated locally for each blade instead of balancing the aggregate of all blade element forces within the annulus with the momentum of a full annulus. A skewed wake model is used in yawed inflow, based on wind tunnel measurements and described in [40]. To correct for the Prandtl effect in the BEM simulations, a Prandtl factor has been calculated and applied to root and tip regions. For axial induction factors exceeding 0.38 the momentum line (or  $C_t$ - $a$  curve) has been replaced by a straight line tangent to  $a=0.38$  as proposed by Wilson [38]. Drag has been excluded from contributing to the induction calculation. The ECN dynamic inflow model [122] has been implemented to add another term to the axial momentum equation to account for the aerodynamic rotor ‘inertia’ in the case of pitch action, rotational speed variation or wind speed variation. The term is proportional to the time derivative of the annulus averaged axial induction and has a dependency on the radial position.

### B.7.2 Settings

The number of elements per blade used for both simulation types is around 20. The airfoil data was prescribed as defined by DTU for this round, already containing 3D corrections. Hence the 3D correction model in the Aero Module was switched off. However the model of Snel [39] has been used to account for the effects of dynamic stall on airfoil data. For the first round about 15 rotor revolutions are calculated at a timestep equivalent to a  $10^\circ$  azimuth step which for AWSM takes around 20 minutes on a 40 node cluster with a resolved free and total wake length of around 3 rotor diameters. For the second round about 20 rotor revolutions are calculated at a timestep equivalent to a  $2^\circ$  azimuth step which for AWSM takes around 120 minutes on a 40 node cluster with a resolved free and total wake length of respectively 2 and 3 rotor diameters. Here it is noted that from a distance of approximately 0.5 diameter downstream of the rotor, the streamwise wake resolution is coarsened by a factor of 5 as reported in [145]. The results are averaged or bin-averaged with azimuth angle over the last revolution for the first and second cases respectively. For the second round the tower influence is accounted for using a flow model that relies on the potential flow around a semi-infinite dipole.

## B.8 POLIMI Codes Description

A. Croce, S. Cacciola

This section describes the PoliMI aero-servo-hydro-elastic code *Cp-Lambda* and the system identification tool, both used in the Task 3.5.

### B.8.1 The Cp-Lambda code

The *Cp-Lambda* has been developed at the Department of Aerospace Science and Technology of the Politecnico di Milano over the past 20 years, inspired and partially based on a software tool that was originally developed for rotorcraft applications. The code has been widely used for industrial and research projects by research institutes and by wind energy companies for the design and the certification of their wind turbines and/or rotor blades. It may be also available on a commercial basis with an appropriate license or within a more wide research program.

*Cp-Lambda* is a finite element based multibody formulation, more thoroughly described in Reference [146]. It includes specific features useful for the modeling of wind turbines. One of the main highlights of the code is its generality: in fact, no assumption is made a priori about the topology of the model. Rather, one can assemble the model by connecting elements from a library that includes body models (beams and rigid bodies), mechanical joints (including the lower pairs, unilateral contact conditions, and flexible joints), actuators (including prescribed displacements and rotations within joints, first order and second order actuator dynamics models, generator models, etc.). Since each element from the library can be connected to any other element, even by forming closed loops, wind turbine generators of arbitrary topology can be modeled.

The multibody formulation is based on the full finite element method, which means that no modal based reduction is performed on the deformable components of the structure. Cartesian coordinates are used for the description of all entities in the model, and all degrees of freedom are referred to a single inertial frame; this avoids the introduction of multiple floating frames, and leads to a geometrically exact formulation, i.e. a formulation that handles arbitrarily large three dimensional rotations.

The turbine blades and tower are modeled by beam elements. The element models beams of arbitrary geometry, including curved and twisted reference lines, and accounts for axial, shear, bending and torsional stiffness.

Joints are modeled through holonomic or non-holonomic constraints, as appropriate, which are enforced by means of Lagrange multipliers using the augmented Lagrangian method. All joints can be equipped with internal springs, dampers, backlash, and friction models.

Lifting lines can be associated with beam elements and are described by three dimensional twisted curves, which do not necessarily coincide with the associated beam reference lines. The lifting lines are based on classical two-dimensional blade element theory and use local profile aerodynamic characteristics, accounting for the aerodynamic center offset, twist, sweep, and unsteady corrections. Lifting lines are here used to model the aerodynamic characteristics of the blades, but also of the tower and of the nacelle. An inflow element can be associated with the blade lifting lines to model the rotor inflow effects; presently, the Peters-He [147] and the dynamic Pitt-Peters wake models [130] are implemented in the code.

Wind is modeled as the sum of a steady state mean wind and a perturbation wind, accounting for turbulence and/or gusts. The deterministic component of the wind field implements the transients, as, for instance, specified by International Regulations (such as [71], the exponential and logarithmic wind shear models, and the tower shadow effects, which include the potential flow model for a conical tower, the downwind empirical model based on Reference [148], or an interpolation of these two models. The stochastic component of the wind field is computed according to the Von Karman and Kaimal turbulence models. The turbulent wind is pre-computed before the beginning of the simulation for an assigned duration of time and for a user-specified two-dimensional grid of points. During the simulation, the current position of each airstation is mapped to this grid, and the current value of the wind is interpolated in space and time from the saved data.

The multibody formulation used in this effort leads to a set of non-linear partial differential algebraic equations. Spatial discretization of the flexible components using the finite element method yields a system of differential algebraic equations in time, which are solved using an implicit integration procedure which is

non-linearly unconditionally stable. The implicit nature of the scheme allows for the use of large time steps and is more appropriate than explicit schemes for the typical dynamics of rotor systems. At each time step, the resulting non-linear system of equations is solved using a quasi-Newton scheme. The time step length is adjusted based on an error indicator. Ad hoc procedures are used for refining the step during intermittent contact events, for example when a backlash contact model is present in a joint.

The proof of non-linear unconditional stability of the integration stems from two physical characteristics of multibody systems that are reflected in the numerical scheme at the discrete level: the preservation of the total mechanical energy and the vanishing of the work performed by constraint forces. Numerical dissipation, which is important when dealing with stiff differential algebraic systems and with high frequency unresolved modes, is obtained by letting the solution drift from the constant energy manifold in a controlled manner in such a way that at each time step, energy can be dissipated but not created. More details on these non-linearly stable schemes can be found in the bibliography of Reference [146] and in [149].

The code can perform several different analysis types. A static analysis solves the static equations of the problem, obtained by setting all time derivatives to zero, yielding the deformed structural configuration under steady loads. The steady loads include prescribed external forces, steady aerodynamic loads or inertial loads due to rotation of elements of the system at constant prescribed angular velocity. An eigenanalysis can be performed about the deformed equilibrium configuration, to yield the natural frequencies and eigenmodes of the linearized system response about this configuration.

Typically, a static analysis is used for computing consistent initial conditions for a subsequent dynamic analysis. The user can specify a number of sensors on the virtual prototype of the turbine, which provide output information for the analysis. The same sensor outputs can also be fed as inputs to the on-board controllers, which in turn operate the system actuators. Controllers, which can include supervision logics and feedback controllers, are implemented as user-defined routines that are linked with the rest of the code.

Finally, the model preparation and data interpretation phases are supported by various graphic procedures, including animations and time history plots, and other post-processing operations such as the determination of fatigue loads by a rainflow analysis and the Campbell diagram.

## B.8.2 Periodic stability analysis through system identification

In order to perform a stability analysis for wind turbine compliant with the periodic nature of such systems, a dedicated tool, written in Matlab, has been developed to be used synergistically with the standard eigenanalysis present in `Cp-Lambda`. Reference [69] provide a thorough description of all details of this periodic stability analysis.

The periodic stability analysis is based on system identification from input-output time histories directly computed through suitable turbine dynamical simulations. From this point of view, the analysis can be regarded as model- and system-independent as it can be employed using data coming from any simulator of arbitrary complexity, in principle applicable to real turbine data. In the context of wind turbine analysis, the very same tool can be used for performing stability analysis for the entire wind turbine in closed- or open-loop operations or even for its sub-parts such as the isolated blade.

Given a set of simulated time histories of specific loads, where the modes of interest are visible, a simplified Single-Input Single-Output discrete periodic model of the PARMAX (Periodic Auto-Regressive Moving-Average model with exogenous input) type is identified through the minimization of the prediction error, by applying standard *equation* and *output error* methods. The equation error is typically less efficient than the output error method, but it can be solved in closed-form. Hence, the model identified with the equation error is typically given as initial guess for the output error, which involves an iterative process. The quality of the identified models is generally verified by looking at the matching between the predicted output and the virtual measurements. With such an identified model, one has obtained a reduced-order system able to approximate the relevant dynamics of the turbine in a specific condition.

The Floquet theory is then used to study the reduced-order identified model, providing frequency, damping factors and participation factors of all modes well visible in the simulation data, which were fed to the identification process. Additionally, since the identified model is periodic, the entire approach is compliant with the periodic nature of the wind turbine system and generates the desired results in a reasonable time, i.e. dozens of seconds.

Similarly to any system identification based activity, the generation of suitable input-output time series

deserves a special attention. To this end, one has to select a specific set of loads where the modes of interest are visible, e.g. tower base side-side mode to see tower side-side modes and in-plane whirling.

Then, one has to introduce in the dynamical simulations an impulsive perturbation to excite the low damped tower, whirling and blade modes. As an example, a tower top lateral impulsive force can opportunely excite the tower and whirling modes. The loads of interest are recorded after the end of the perturbation to consider only the free-response of the machine in the identification. Filtering, trimming and re-sampling are typically required to ease the identification process.

With such an approach the low-damped modes of an operating turbine (tower side-side and fore-aft, drive-train, forward and backward in-plane whiling and the blade edgewise modes) are typically well captured.

# Appendix C

## CFD and panel codes descriptions

### C.1 Description of the simulations for the comparison rounds IV1.1 (axial inflow), IV2.1 (shear) and IV2.2 (yaw) with the DLR TAU code

Manfred Imiela

#### C.1.1 Flow Solver TAU

The aerodynamic simulations were conducted using the DLR TAU-Code [150]. It solves the compressible, three-dimensional Reynolds-Averaged Navier-Stokes (RANS) equations in the integral form using a finite volume formulation. A cell-vertex formulation with a dual-grid approach was adopted for the spatial discretization. The solver module contains a central scheme as well as several upwind schemes for the discretization of the inviscid fluxes. Viscous terms are computed with a second-order central scheme. Artificial damping is added by scalar or matrix dissipation. For the simulation of turbulent flows several one- and two-equation turbulence models are implemented. Time integration is achieved using either an explicit Runge-Kutta type time-stepping scheme or an implicit LU-SGS (lower-upper symmetric Gauss-Seidel) algorithm. Time-accurate simulations are performed with a dual-time stepping approach. For accelerating the convergence of the flow equations among various multi-grid type cycles can be chosen. In case of multi-block meshes arbitrary motions can be prescribed for each mesh block by the motion module. The chimera technique additionally allows for overlapping of different mesh blocks and therefore eases the mesh generation process.

#### C.1.2 General Set-up

The aerodynamic simulations for the comparison rounds were carried out with no turbulent fluctuations in the incoming flow. The closure of the Navier-Stokes equation is accomplished by Menter's two equation k-SST model. The spatial discretization is realized with a second order central scheme stabilized by applying matrix dissipation. An implicit LUSGS algorithm is used to advance the solution in time. All cases were simulated fully turbulent regarding the flow on the blade surface. While the axial flow case allows for a steady computation because it is fully axisymmetric, the other flow cases need to be treated as unsteady. In the latter case the dual time stepping method is used in order to advance the simulation in time. The difference in the inflow properties not only affects the timewise simulation method but also the mesh setup. One goal of the MexNext comparison rounds is to compare the results among various aerodynamic codes. In order to make a proper comparison it was necessary to run the codes on identical or at least very similar meshes. Therefore Galih Bangga from IAG Stuttgart provided the meshes, since all codes are capable of running on structured meshes.

### C.1.3 Axial Flow (Case IV.1.1)

Since the axial flow case is fully axis-symmetric only one blade needs to be meshed and embedded in a periodic background grid as depicted in Figure C.1. As can be seen the background grid comprises a  $1/n$ -th cylinder segment with  $n$  being the number of blades therefore reducing the simulation time enormously. The rotor is positioned in the grid center ( $x,y,z = 0,0,0$ ) perpendicular to the rotor axis that is parallel to the  $x$ -axis.

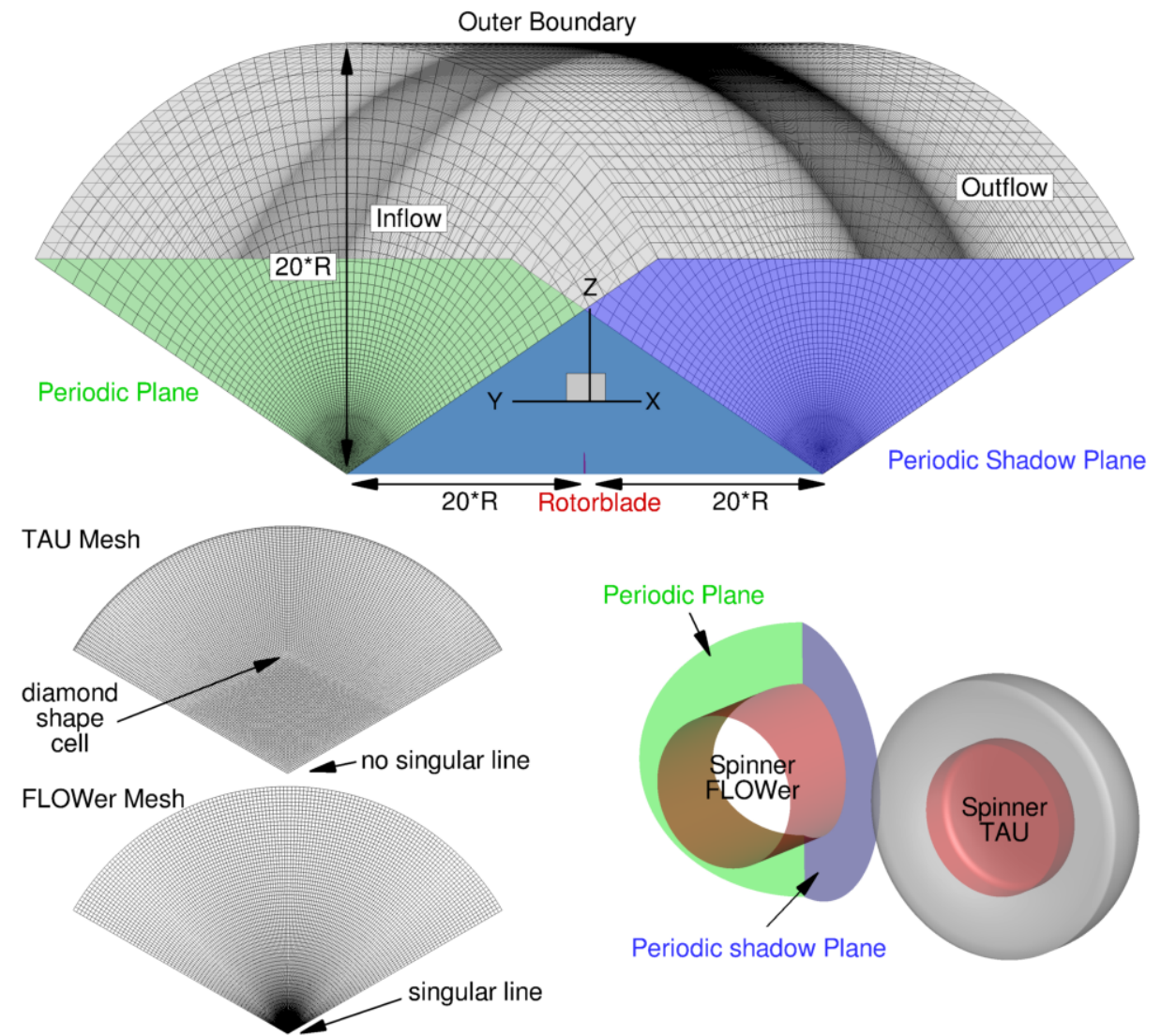


Figure C.1: Mesh setup for the axial flow case

The Inflow, Outflow and Outer Boundary were treated as farfield boundaries allowing for in- and outflow depending on the characteristics. The periodic boundary condition was used for the lateral boundaries and the blade and spinner surface were defined as no-slip walls. While the blade mesh could be adopted to TAU without any changes (for a detailed description of the blade mesh see chapter C.8), the background grid and the spinner grid had to be slightly adjusted. As shown in Figure C.1 the original mesh contains a singular line being identical to the rotor rotation axis ( $x$ -axis). Since TAU cannot handle singular lines, a “butterfly mesh” was created as can be seen in Figure C.1 “shifting” the singular line from the rotor center in the direction of the outer boundary. The remaining properties of the background grid were kept as close to the IAG design as possible resulting in 12.5 Mio. points. Another requirement of TAU for periodic meshes is

Case	Yaw [°]	Tilt [°]	$V_{wind}[\frac{m}{s}]$	$\rho_{inf}[\frac{kg}{m^3}]$	$P_{inf}[Pa]$	$\eta_{inf}[\frac{kg}{ms}]$	$T[K]$
IV.1.1	0	0	6.1	1.2285	1033.56	1.81411e-5	293.15

Table C.1: Aerodynamic reference conditions for case IV.1.1

Cell Size [m]	Streamwise extension	Lateral extension	Ground normal extension
0.5	-40 — 256	-80 — 80	128
1.0	-348 — 448	-128 — 128	192
2.0	-448 — 512	-192 — 192	256
4.0	-576 — 576	-320 — 320	320
8.0	-768 — 768	-384 — 384	384
16.0	-1024 — 1024	-1024 — 1024	1024

Table C.2: Extension of the equidistant meshes

that the periodic plane and its shadow plane each only contain one marker. This makes the use of the IAG Spinner impossible for TAU (since there will be two markers on the periodic plane: one from the background grid and one from the spinner). Since the boundaries of the spinner mesh must not touch or penetrate the periodic boundaries of the background mesh, the easiest way of closing the rotor surface was a simple round cap as depicted in Figure C.1. Since all the meshes were combined using the Chimera technique, the spacing on the hub cap was adjusted to the spacing at the root of the blade in order to be similar. The total mesh then consisted of 12.5 Mio. (background mesh), 8.9 Mio. (blade mesh) and 0.45 Mio. (spinner mesh) a total of 21.9 Mio. points. For the axis-symmetric case a constant inflow velocity of 6.1 m/s was chosen. No tilt and no yaw angle were imposed and the rotor was considered as rigid. Only the prebend was included in the blade mesh. All rotor blades were pitched 0.15° to feather and the rotor rotates at a constant speed of 12.3 rpm. All aerodynamic reference conditions are summarized in Table C.1.

#### C.1.4 Sheared and Yawed Flow (Case IV.2.1, Case IV.2.2)

For the sheared and yawed flow case no periodic mesh can be used. In order to be able to compare the results with simulations with turbulent inflow, only the rotor is modelled, this time embedded in a prismatic background grid. The chimera technique is applied in order to account for the rotating rotor in the stationary background grid. The following meshes from IAG could be adopted without any changes: rotor blade mesh (same as in the axial flow case), spinner mesh and a local refinement mesh in the vicinity of the rotor. The background mesh had to be redesigned because in the original version it contains hanging grid nodes which cannot be handled by TAU. As shown in Figure C.2 the new background mesh is also made up of a mesh sequence of equidistant meshes ranging from a mesh resolution of 0.5m for the innermost grid to 16m for the outermost grid. The domain sizes of the various grids are shown in Table C.2. The grids are connected by small connector grids comprised of regular tetraeders. In 2D each connector mesh has a width of 4 times the inner grid spacing. As can be seen the domain size is equal to [2048 x 2048 x 1024] m<sup>3</sup> in streamwise, lateral and normal to the ground direction. As in the axial flow case the boundary conditions for the inflow, outflow and outer boundary are set to farfield conditions. For the comparison rounds also the lateral boundaries are chosen to be farfield. Only the ground surface is set to no-slip wall. In total the mesh contains 129 Mio. points (background mesh: 98.4 Mio., blade mesh: 8.9 Mio., spinner mesh: 0.27 Mio., local rotor refinement: 2.4 Mio.).

The turbine is located at  $X = 0$  m. The rotor is centered laterally, yawed according to the case (see Table C.3), shifted 57.19 m vertically and tilted 5° around its new center. The three rotor blades are connected by a simple spinner. All blades extend 40 m in radial direction and are pitched 4.75° away from feather (which means that the incidence angle is increased). The rotor blade surface is set to a no-slip wall and the rotor rotates with 16.2 rpm.

During the unsteady simulation a constant boundary layer profile is imposed at the inlet of the domain. The same reference profile is also used to initialize the whole flow field in order to speed up convergence. The aerodynamic reference conditions are summarized in Table C.3.

At first both simulations are advanced in time using a quite coarse timestep equivalent to 2° azimuth.

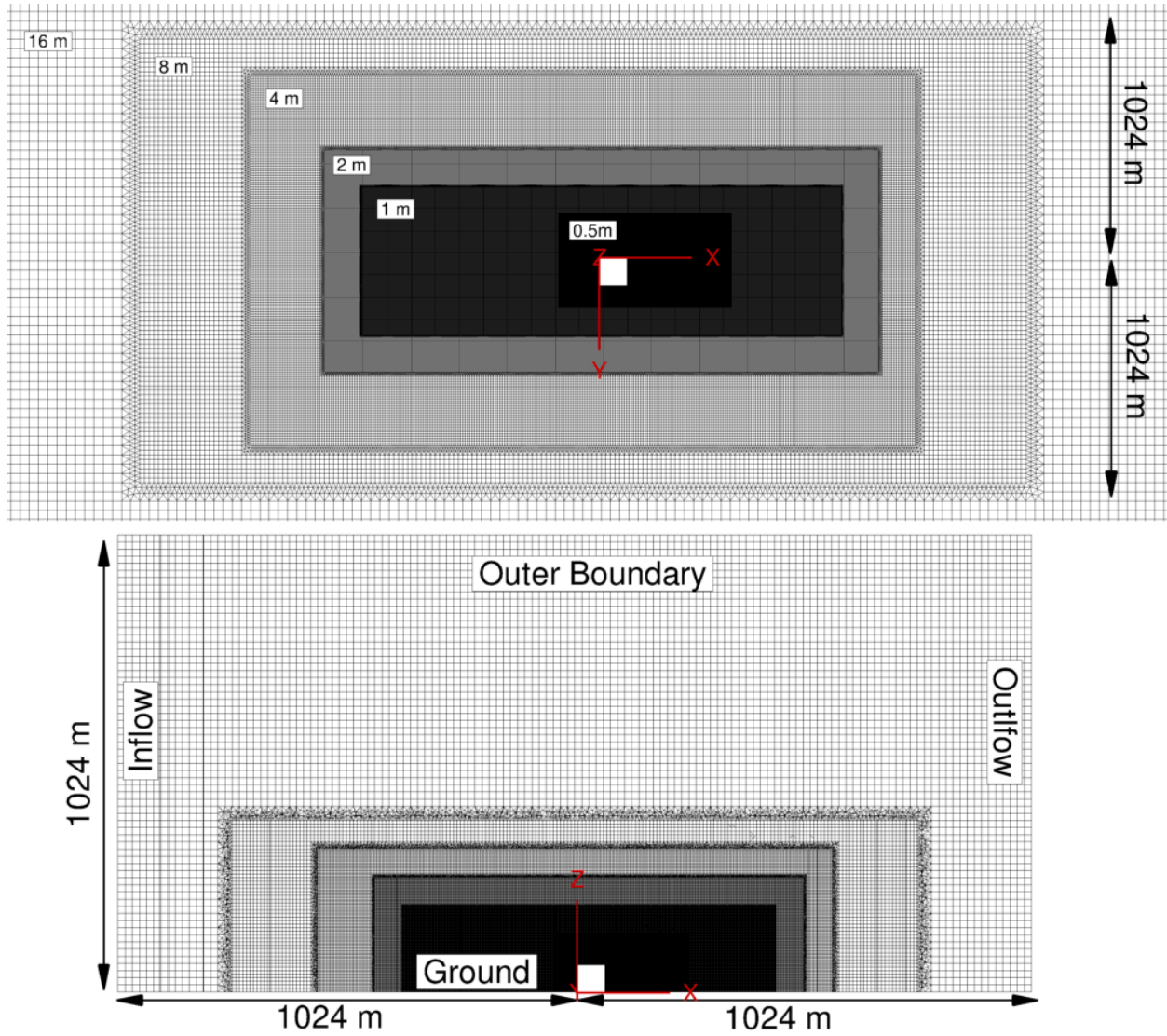


Figure C.2: Background mesh for unsteady simulations

Case	Yaw [°]	$V_{wind}[\frac{m}{s}]$	$expShear$	$\rho_{inf}[\frac{kg}{m^3}]$	$P_{inf}[\text{Pa}]$	$\eta_{inf}[\frac{kg}{m \cdot s}]$	$T[\text{K}]$
IV.2.1	-6.02	9.792	0.249	1.22	1005	1.78465e-5	287.028
IV.2.2	-38.34	8.429	0.262	1.22	1020	1.80530e-5	291.312

Table C.3: Aerodynamic reference quantities for the sheared and yawed flow case



This way the wake behind the rotor builds up quicker than with a small timestep. On the other hand the large timestep prevents a satisfactory convergence of the simulation. Therefore the timestep is reduced to a timestep equivalent to  $0.1^\circ$  azimuth after 20 revolutions. The simulation is then carried out for four further revolutions. The requested quantities (pressure distributions at  $0^\circ$ ,  $90^\circ$ ,  $180^\circ$ ,  $270^\circ$  and loads for one revolution) are extracted from the last revolution. The normal and tangential force for each radial cut has been obtained by transforming the force contribution of each chordwise surface element from the wind tunnel to the airfoil coordinate system. In a second step the force contribution of all chordwise elements of the corresponding radial cut are integrated and smeared over the element length. The integrated loads contain only the pressure part of the force. With respect to the level of convergence it has to be mentioned that the computation at the time of extracting the desired quantities is not fully converged. Unfortunately the computations could not be continued due to the long turn around times. Each computation was carried out on 1280 AMD EPYC 7601 processors. The turnaround time for the first twenty revolutions ( $\Delta t = 2^\circ$ , inner Iterations = 50) was approximately 7 days. The same turnaround time was necessary for two revolutions using  $\Delta t = 0.1^\circ$  with 20 inner Iterations.

### C.1.5 Acknowledgement

Special thanks to Galih Bangsa (IAG) for providing the meshes and for numerous very fruitful discussions.

## C.2 DTU - EllipSys3D - Code description and simulation setup

Christian Grinderslev, Niels N.Sørensen

### C.2.1 Flow solver

EllipSys3D [78, 79, 151] solves the incompressible-flow Navier-Stokes equations in structured curvilinear coordinates using the finite-volume method with a collocated grid arrangement. For closure, turbulence is calculated through Reynolds-averaged-Navier-Stokes (RANS) or large-eddy-simulation (LES) capabilities. The code is parallel and highly scalable using Message Passing Interface (MPI) and multi-block decomposition, multi-grid method and grid sequencing. Multiple convective schemes are available, and in the present study the Quadratic Upstream Interpolation for Convective Kinematics (QUICK) scheme is used for steady inflow simulations. For turbulent inflow cases, with Improved Delayed Detached Eddy Simulation (IDDES) turbulence modelling, a mix of QUICK and the fourth order central difference scheme is used in accordance to the mask approach by Strelets [152].

For pressure correction, an improved version of the the SIMPLEC algorithm [153] is used to couple the velocity and pressure. Rhie-Chow interpolation is used to avoid odd/even pressure decoupling. Overset capabilities, including grid hole-cutting, are implemented internally in the code [154].

### C.2.2 Computational grids

In this setup, the overset grid approach is chosen, as separate meshes can be constructed for each purpose and then overlapped, connected through interpolation algorithms. In the present study, three mesh groups are used and overlapped. Near the rotor, an O-O type mesh is grown from the blade surface mesh, extruding through 128 cells  $\approx 15\text{m}$  from the surface using HypGrid [155]. The first cell adjacent to the rotor surface has a height of  $1 \times 10^{-6}\text{m}$  to ensure a  $y^+$  of less than 1. Each blade is resolved in 128 cells spanwise and 256 cells chordwise. Around the rotor mesh a cylindrical disc mesh is constructed with pre-cut holes around the blades. This mesh rotates along with the rotor mesh, which creates a simplified holecutting procedure. To avoid the disc mesh penetrating the ground boundary when tilting the rotor, the last third of the disc mesh downstream is narrowed linearly.

For flexible rotor simulations, deformations are propagated to the rotor mesh via a blending factor, such that the volume deformation is kept within cells located inside the hole region of the overlapping disc mesh. This is done to avoid the need of updating donor and fringe cells within the rotor and disc mesh, as the two rotate together.

For the farfield domain, a semi-cylindrical shape is chosen ensuring a good compatibility between overlapping grids. The farfield domain expands 2km in the flow direction, with the rotor placed 800m,  $\approx 10D$ , from the inlet. Cells are stretched far from the rotor, but refined near the rotor to resolve the wake behind the rotor. Across the flow direction, the domain radius is 500m  $\approx 6.25D$  in each direction, with the rotor placed in the center. Ground conditions are ensured 57.2m below the hub, using a symmetry boundary condition, which constrains the flow perpendicular to the boundary. Parallel to the flow, the symmetry condition works as a slip condition, as no development of the input wind flow profile is desired.

#### Grids for steady inflow (Case IV.1.1, Case IV.2.1 and Case IV.2.2)

The combined grids consists of a total of 39.26M grid cells. Here, domain cells are stretched toward the in- and outlets and squeezed together near to rotor, to obtain a good match to the overlapping disc mesh.

#### Grids for turbulent inflow cases (Case IV.3.1)

For turbulent inflow, a higher resolution in the domain is needed to resolve the turbulent features. This is obtained through a refined domain mesh, with refinement in the range  $[-340:250]\text{m}$ , in which the resolution in the flow direction is decreased to  $\approx 1\text{m}$ . The domain alone consists of  $\approx 36.1\text{M}$  cells. Combined with disc and rotor mesh, a total of  $\approx 54.5\text{M}$  cells is used.

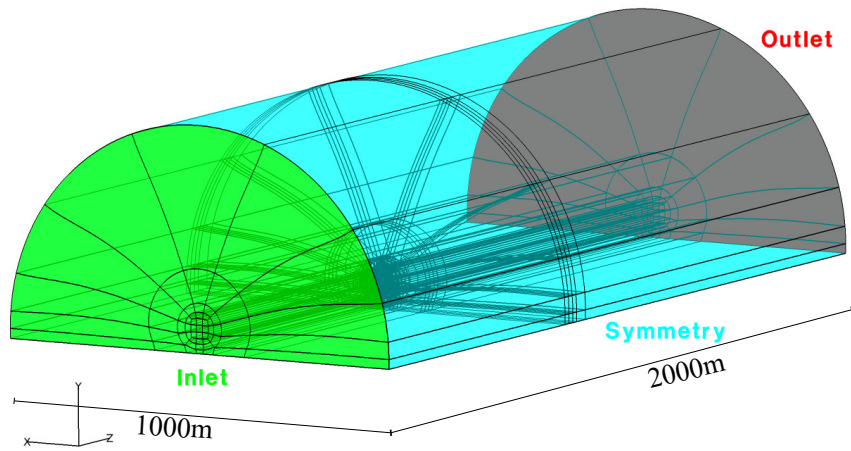


Figure C.3: Computational domain with prescribed boundary conditions

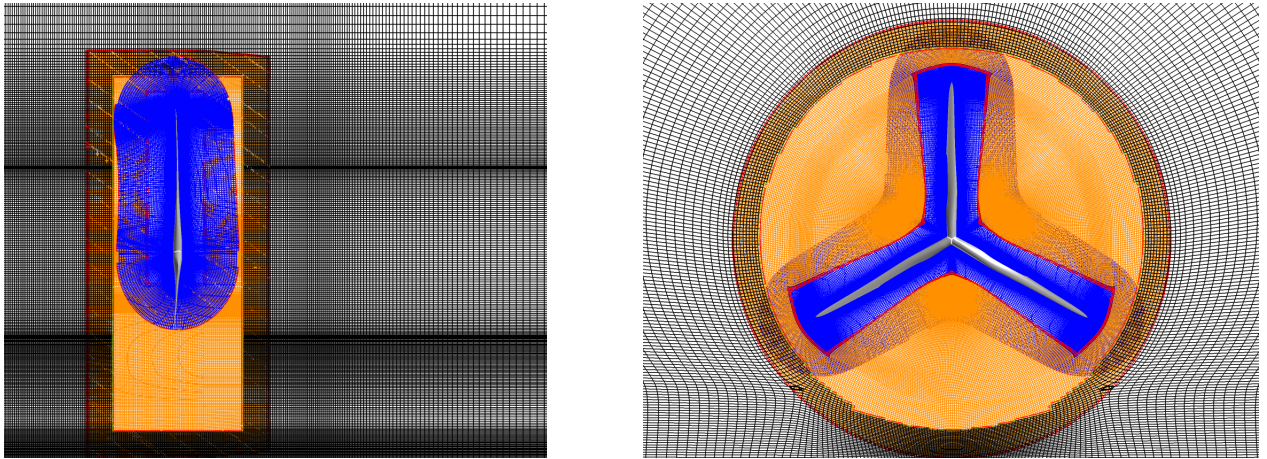


Figure C.4: Grids used for simulations without inflow turbulence. Left: side view, right: front view. Red cells show fringe cells of overlapping grids. Blue: rotor grid, orange: disc grid, black: background grid. Entire background grid is not shown.

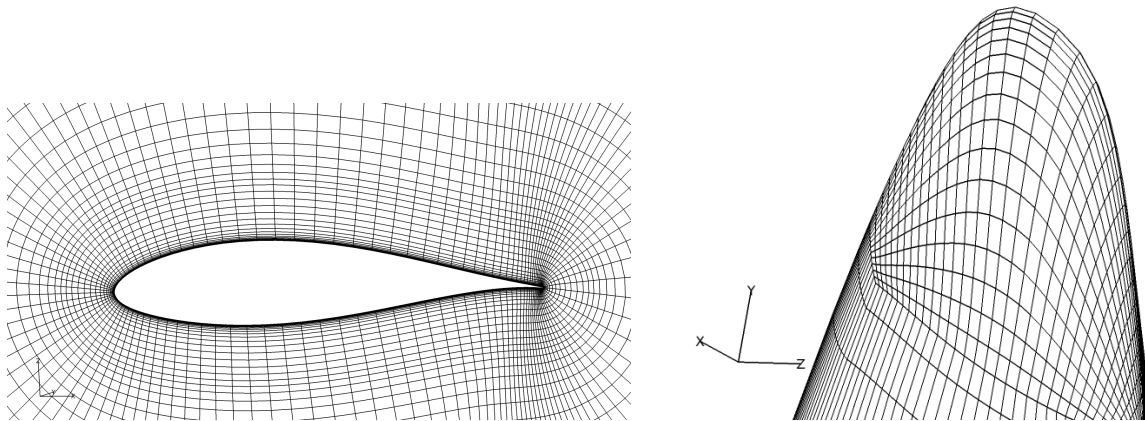


Figure C.5: Near rotor mesh and surface discretization at tip. Only every second line shown

### C.2.3 Simulation setups

#### Steady inflow (Case IV.1.1, Case IV.2.1 and Case IV.2.2)

For sheared inflow, a power law corresponding to that found from measurements is used as an inlet condition and initial flow field in the domain. To constrain the profile in the domain, a maximum of 12 m/s and a minimum of 4 m/s is used such that a cutoff is made on the profile, as presented in [27] and [156]. All simulations are conducted as fully turbulent unsteady RANS (URANS) simulations using the  $k - \omega$  SST turbulence model [157]. Time steps are reduced through the simulations until time step insensitivity in thrust and torque is obtained at  $6.43 \times 10^{-4}$  sec (0.0625 deg/sec). All simulations have been run for +25 revolutions to develop the wake and converge in thrust and power.

#### Flexible simulations

For all steady inflow cases, the influence of considering flexibility of the rotor is studied through the DTU coupling framework. Here, EllipSys3D is coupled to the aeroelastic solver HAWC2 [34, 158], replacing the usual BEM based aerodynamics.

The framework is partitioned and loosely coupled such that HAWC2 does 2nd order accurate prediction of deformations, which are propagated to the CFD surface mesh. The volume mesh is deformed through a volume blending based on gridline distance to the surface. EllipSys then computes the flowfield through sub-iterations and new forces are calculated. These are transferred to HAWC2 which calculates the actual deformation, and then predicts the deformation for the coming timestep. The FSI framework is presented in [110–112].

#### Turbulent inflow (Case IV.3.1)

For turbulent inflow cases, shear is applied as described for steady flow cases, while turbulent fluctuations are applied on top of the profile through immersed boundary force planes as described in [27]. A turbulence plane is inserted 320m upstream of the rotor with cross span of 640x360m, meaning that outer edges of the provided turbulence plane has been omitted in order to fit the plane in the domain. The turbulence is immersed using a Gaussian smearing normal to the turbulence plane, with a smearing parameter  $\epsilon=3.0$ , and inflow turbulence fluctuations are up-scaled with a factor in all directions, to circumvent the immediate loss of turbulence intensity happening when introducing the turbulence. This up-scaling was calibrated to fit the IAG turbulence intensity (TI) at the first comparison point ( $x=-240$ m) to better compare TI decay along the the domain. Scaling of 1.05 for cases Rot-REF1 and Rot-REF2, 1.1 for Rot-REF3 and finally 1.15 for Rot-REF4 were used. Same factors apply for their empty box counterparts. For turbulent inflow cases, the Improved Delayed Detached Eddy Simulation (IDDES) [159] turbulence model is used.

#### Assumptions and uncertainties

In this work, the tower, nacelle and spinner are not modelled. The rotor geometry is based on the theoretical geometry of the rotor, meaning that no irregularities on the actual rotor surface are modelled.

## C.3 NREL - Exawind - Code description and simulation setup

Ganesh Vijayakumar, Shreyas Ananthan, Michael. A. Sprague

### C.3.1 Flow solver

ExaWind is an open-source modeling and simulation environment for wind energy. The primary physics codes of ExaWind are Nalu-Wind<sup>1</sup>, AMR-wind<sup>2</sup> and OpenFAST<sup>3</sup>. Nalu-Wind is a wind-focused computational fluid dynamics (CFD) code that is coupled to the whole-turbine simulation code OpenFAST. The modeling and simulation environment was created under U.S. Department of Energy funding to achieve the highest-fidelity simulations of wind turbines and wind farms to date, with the goal of enabling disruptive changes to turbine and plant design and operation.

Nalu-Wind [160] solves the incompressible form of Navier-Stokes equations, on generalized unstructured grids, with appropriate RANS or LES models for turbulence closure. The codebase uses an implicit backward-difference-formula (BDF) family of timestep algorithms with an approximate pressure-projection algorithm. Nalu-Wind uses the linear upwind differencing scheme (LUDS). Nalu-Wind contains the infrastructure for discretization of the underlying models, and it heavily utilizes the Trilinos [161] Sierra Toolkit (STK) [162] providing an unstructured mesh in-memory, parallel-distributed database. Overset hole-cutting capabilities are implemented through the TIOGA library [163]. For overset simulations, each equation is solved using a single global linear system where the overset coupling between the meshes are introduced as linear constraint rows. The momentum and scalar transport equations are solved using solvers from Trilinos (Belos, Ifpack2) and the pressure-Poisson system is solved using solvers from *hypra* ([164] GMRES with BoomerAMG preconditioner). Four Picard iterations are used within each timestep to minimize the error from approximate pressure projection algorithm.

### C.3.2 Computational grids for steady inflow (Case IV.1.1, Case IV.2.1 and Case IV.2.2)

The boundary-layer resolving, near-body O-O mesh grown from the blade surface was embedded in a structured, hexahedral-element-only, cylindrical wake-capturing mesh with an O-H (or “butterfly”) topology. For the purpose of consistency, we use the same near-body O-O mesh provided by DTU described in Sec. 3.4.3. The cylindrical mesh extended half a rotor diameter upstream and 4 diameters downstream. The section of the cylindrical mesh around the near-body mesh had constant spacing in the flow direction up to half a diameter upstream and downstream, and mesh stretching was introduced in the flow direction further downstream. The wake-capturing mesh was embedded inside a fully unstructured mesh that covered the rest of the domain that had extended 10 diameters upstream, 15 diameters downstream and 10 diameters in lateral directions. The combined grids consists of a total of 39.31M grid cells.

---

<sup>1</sup><https://github.com/Exawind/nalu-wind>

<sup>2</sup><https://github.com/Exawind/amr-wind>

<sup>3</sup><https://github.com/OpenFAST/openfast>

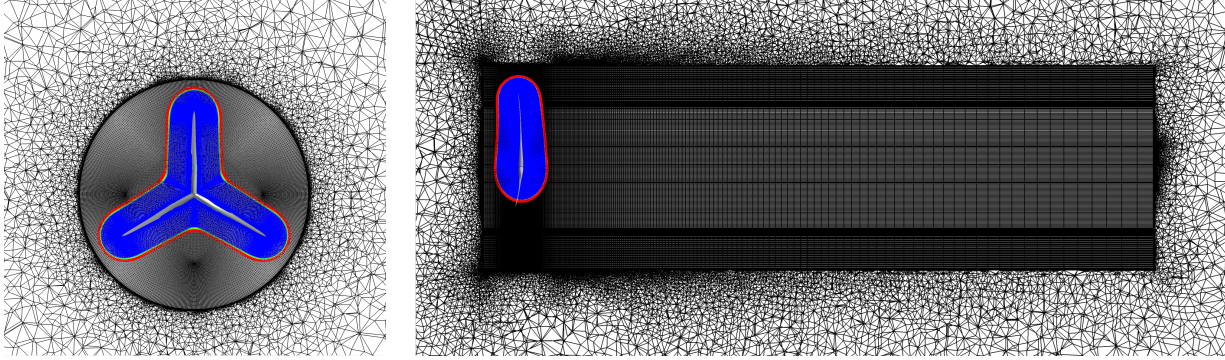


Figure C.6: Grids used for Nalu-Wind simulations. Red cells show fringe cells of overlapping grids. Blue: rotor grid, black: background grid. Entire background grid is not shown.

### C.3.3 Simulation setup for steady inflow (Case IV.1.1, Case IV.2.1 and Case IV.2.2)

For sheared inflow, a power law corresponding to that found from measurements is used as an inlet condition and initial flow field in the domain. For purposes of consistency, we constrain the velocity profile between a maximum of 12 m/s and a minimum of 4 m/s as described by DTU in Appendix C.2.3. We use the fully turbulent approximation for all simulations using the unsteady RANS (URANS)  $k - \omega$  SST turbulence model [157]. A time step of  $1.69 \times 10^{-3}$  seconds corresponding to 0.125 degrees/timestep is used to obtain converged torque and thrust. All simulations are run for atleast 25 revolutions to develop the wake and obtain convergence in thrust and power.

#### Assumptions and uncertainties

The effect of the tower, nacelle and spinner on the aerodynamics are assumed to be negligible compared to that of the rotor geometry and are hence not modeled. The rotor surface is assumed to be clean and the flow around the rotor is assumed to be fully turbulent.

## C.4 ForWind-IWES-HSEmden/Leer - Description of OpenFOAM simulations

Khaled Yassin, Leo Höning, and Bernhard Stoevesandt

### C.4.1 General Description

OpenFOAM<sup>®</sup> is an open source software for Computational Fluid Dynamics that is widely used around the world in different applications including Wind Energy. Using this software, the three-dimensional, unsteady Reynolds-Averaged Navier-Stokes equations (RANS), Large Eddy Simulations (LES), and hybrid RANS-LES equations can be solved using Finite Volume Method (FVM) by employing a wide variety of numerical schemes. In this task, a hybrid Spalart-Allmaras, Improved Delayed Detached Eddy Simulations (SA-IDDES) turbulence model was applied to combine the benefits of using both LES for far-field and RANS simulations close to the walls (Blades, hub, tower and Ground).

#### In-house codes

To benefit from the fact that OpenFOAM is an open source software, some in-house pre- and post-processors were used during this task.

- bladeBlockMesher and windTurbineMesher:

The provided blade, hub, and tower geometries were used to generate in-house turbine grids to be more suitable and computationally stable for OpenFOAM to simulated task VI.2. The first step was to use bladeBlockMesher. BladeBlockMesher is a code implemented within OpenFOAM framework that is able to generate high-quality, hyperbolic, and fully structured cells for the blade. The second step is to fit such a mesh into a background mesh using the in-house code windTurbineMesher.

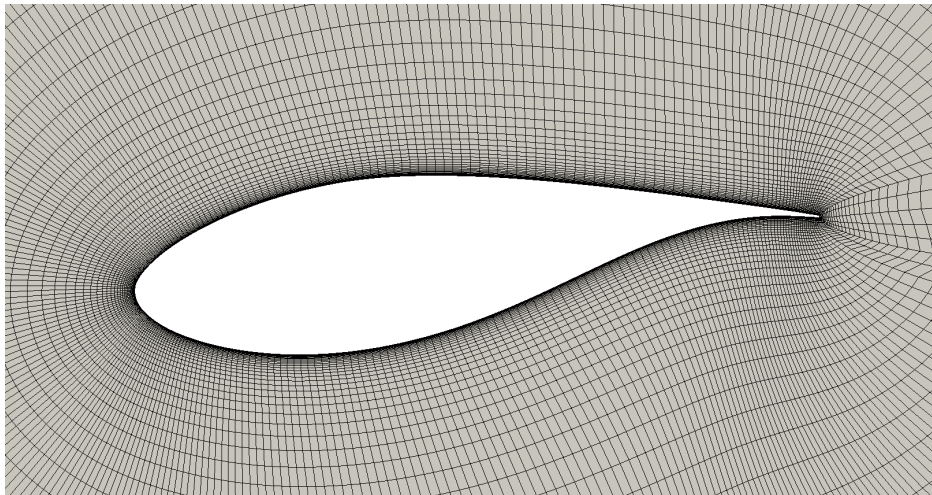


Figure C.7: Cross section of blade mesh generated by bladeBlockMesher

- BeamPimpleDyMFoam:

BeamPimpleDyMFoam is a beam solver that applies the Geometrically Exact Beam Theory (GEBT) to simulate FSI of wind turbine blades and to change the surrounding mesh according to the blade's flapwise, edgewise and torsional deflection. Also included in this solver turbinePerformance post-processor which is a run-time post-processor to export different turbine performance parameters like overall generated power and torque. It can also calculate forces, deflections, and Angles of Attack (AoA) of given blade sections.

## C.4.2 Simulation tasks' description

During IEA task 29 IV, three different sub-task were simulated using OpenFOAM namely: Tasks IV.1, Tasks IV.2 , and preliminary sub-tasks of Task IV.3.

### Cases IV.1.: Turbine rotor

According to the task IV.1. description document, is divided into two sub-tasks: rigid and flexible blade simulation of the given rotor. Both cases have axial, laminar, uniform inflow with wind speed = 6.1 m/s and rotational speed of the rotor = 12.3 rpm.

This case was simulated using steady-state  $k-\omega$  SST turbulence model (accordingly, fully turbulent flow was assumed). In this task, Computational grid provided by DTU was used to simulate the performance of the turbine. This grid is spherical domain grid with around 14 Million hexahedral, structured cells. Since the domain in this case is in a spherical form and includes only the turbine rotor, the Moving Reference Frames (MRF) technique was used simulate the rotation of the rotor instead of rotating the rotor itself. The domain boundaries in this case were treated as inlet-outlet boundaries (equivalent to zero gradient but with fixed value in inlet faces). While all walls had no-slip condition for velocity and zero pressure gradient. Convergence was noticed after  $4 \times 10^4$  iterations. This took about  $1.5 \times 10^5$  s using 120 CPU's.

### Cases IV.2.: Shear and yaw

These cases focus on the simulation of performance of the Mexico wind turbine under shear and yaw operation cases. For case IV.2.1, the rotor was simulated at inlet wind speed of 9.792 m/s at a hub height = 57.19m, shear exponent = 0.249, and about  $-6^\circ$  yaw angle. On the other hand, case IV.2.2 was simulated at inlet wind speed of 8.429 m/s at a hub height = 57.19m, shear exponent = 0.262, and  $-38.37^\circ$  yaw angle.

These two tasks were simulated using Spalart-Allmaras IDDES. The mesh has about  $29 \times 10^6$  hybrid cells. The new in-house generated mesh is a rectangle mesh with 1200m x 560m x 337m domain. The turbine hub is located 400m from the inlet patch, 280m from the side patches and 57.7m (hub height) from the ground patch. Each blade consists of 257 cells spanwise and 256 cells chordwise as shown in figures C.8 and C.9.

In each case, a rectangular domain was used with fixed value inlet, zero gradient outlet, symmetric upper boundary and no slip lower boundary to simulate the ground. Laminar, sheared inflow was simulated in these two cases. To ensure that the flow has the proper sheared flow with the indicated shear exponent in the case description, the flow injected from the inlet patch is varying with the variation of the height to mimic wind shear. Also, the ground was assumed to have a no-slip condition to sustain the given wind shear.

### Cases IV.3.: Turbulent inflow

The main goal of this cases is to simulate the effect of turbulent inflow on wind turbine performance. Turbulent inflow was injected to the field using fields provided by USTUTT and then converted to momentum sources using an in-house code. These simulations used in an empty domain with LES WALE turbulence model to simulate the induced turbulence effect on the domain.

The computational grid of this domain was generated in accordance to the dimensions and cell sizes provided by USTUTT in their report circulated during this task. This domain is shown in figures C.11 and C.10.



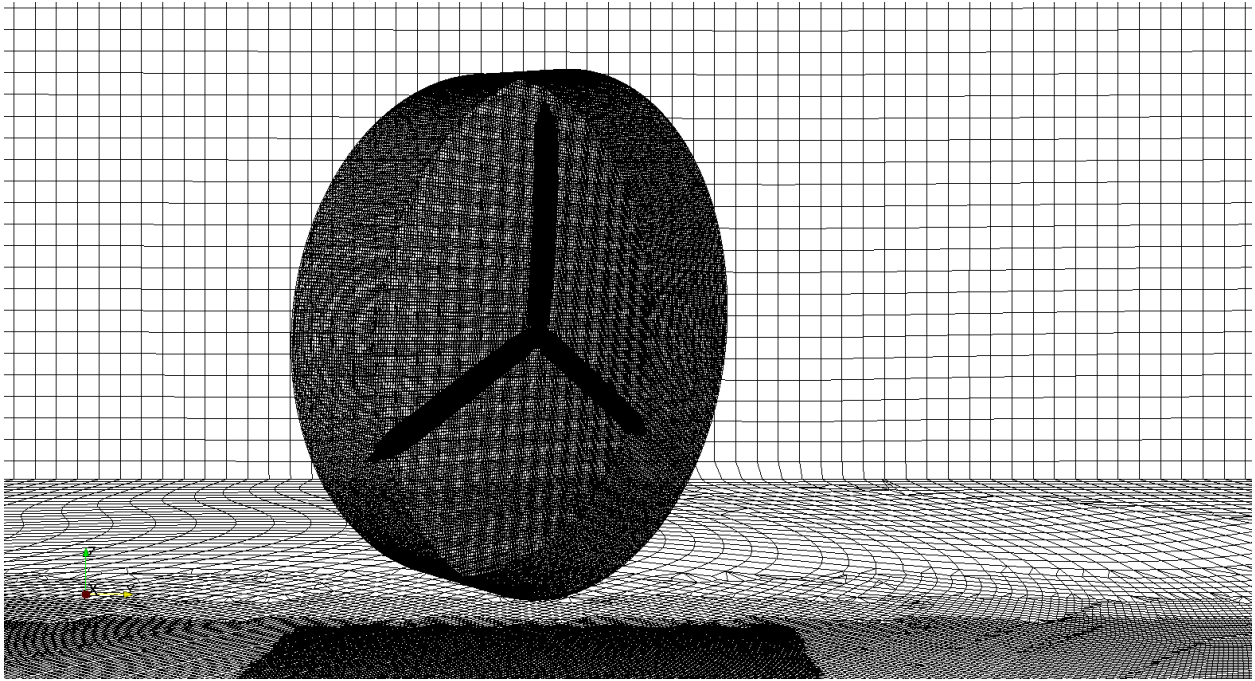


Figure C.8: Rotor cells of the yawed case

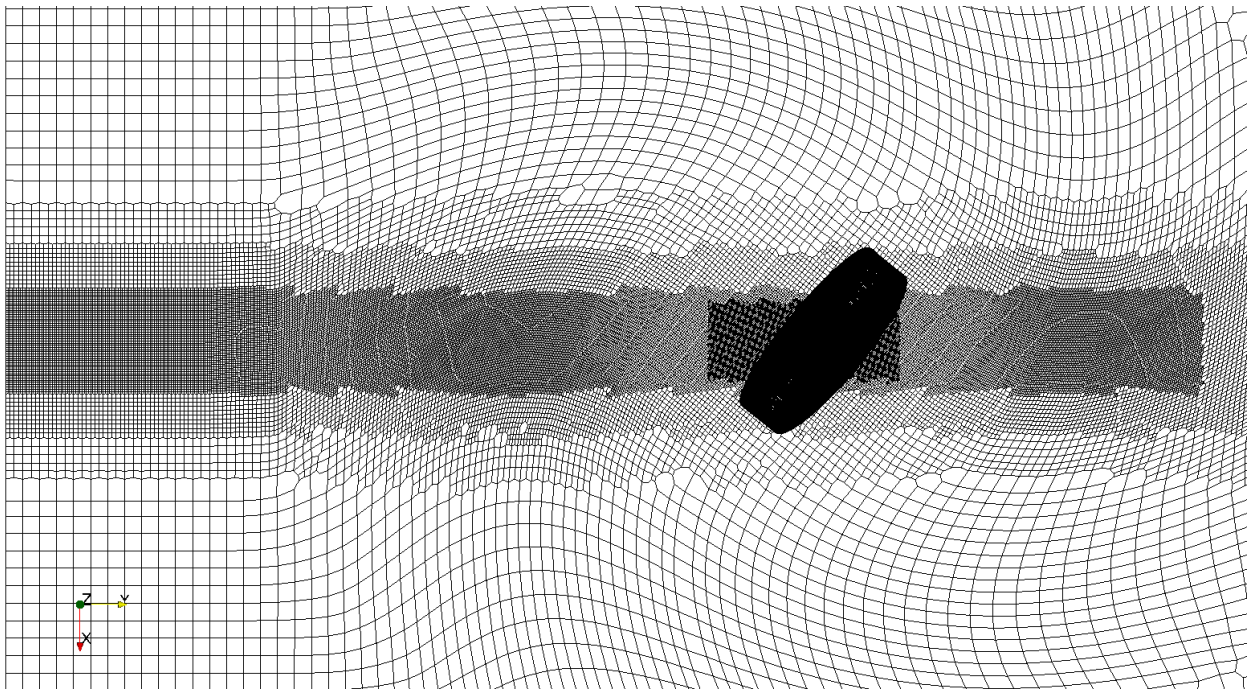


Figure C.9: Plan view of yawed rotor cells

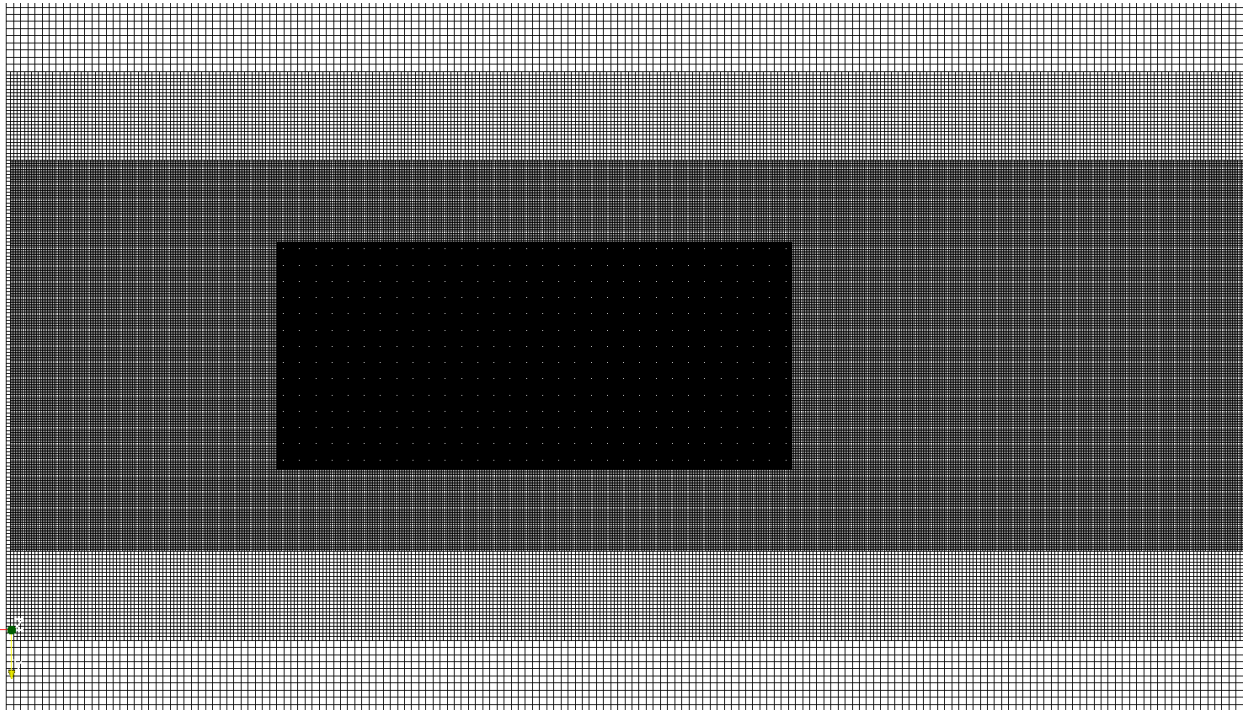


Figure C.10: Ground patch of empty domain in task IV.3.1

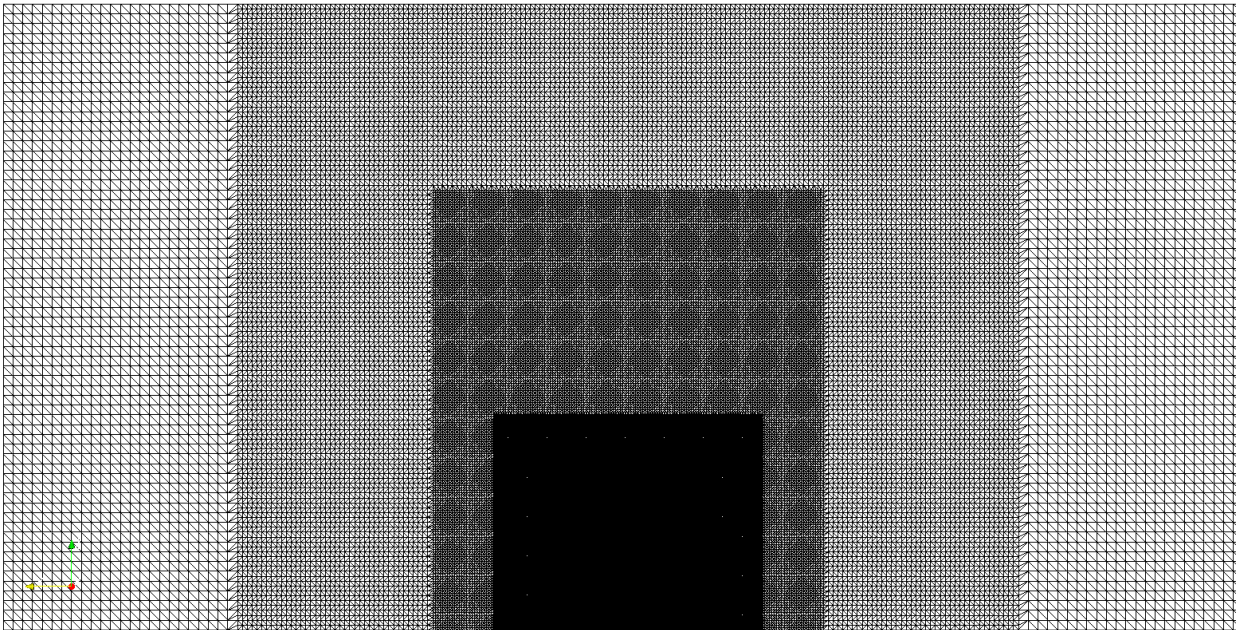


Figure C.11: Side section of empty domain in task IV.3.1

## C.5 CNR-INM, FUNAERO: code description and simulation setup for rounds IV1.1 (axial inflow), IV2.1 (shear) and IV2.2 (yaw)

Luca Greco, Claudio Testa, Francesca Magionesi

### C.5.1 General model description

CNR-INM Free-wake UNsteady AEROdynamics (FUNAERO) code features an aerodynamic formulation based on the Boundary Element Method (BEM) to predict the behaviour of a wind turbine operating in a spatially uniform/nonuniform inflow. FUNAERO is a 3D unsteady free-wake panel method for rotating blades. It is based on the assumption of incompressible, inviscid, attached and irrotational flows. Viscous effects on blade loads are (roughly) estimated by assuming that, locally, the boundary layer of each blade section behaves like that over an equivalent flat plate whose Reynolds number matches the blade operating conditions. The wake shape is not known a priori but is part of the aerodynamic solution. A consistent approach to tackle this problem is to consider wake points aligned to the local flow, that is, moving with the wind and convected by the local fluid velocity due to the rotor blades and their wakes (self-induced effect). FUNAERO has been thoroughly assessed in the past considering different turbine models or marine propellers ([145, 165–167]). It has been recently validated using the three-bladed model-scale Mexico rotor tested in the large open jet facility of the German Dutch Windtunnels DNW. A detailed analysis can be found in [168]. A view of the predicted three-dimensional shape of the wake Fig. C.12, reveals the well-known curled-wake mechanism, i.e., the formation of a counter-rotating vortex pair in the wake of a turbine under highly yawed conditions.

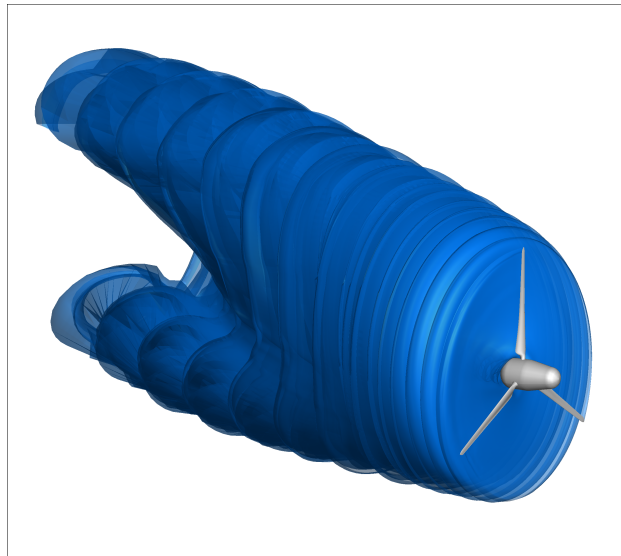


Figure C.12: Yawed flow: predicted three-dimensional shape of rotor wake

### C.5.2 Simulation setup

The simulations for the comparison rounds IV1.1 (axial inflow), IV2.1 (shear) and IV2.2 (yaw) have been performed modelling rotor blades and nacelle, whilst the presence of the tower has been neglected. The origin of the geometrical description of the rotor is the IGES file provided to all the partners. This includes the full three-dimensional shape of rotor blades specially placed accordingly to the real turbine configuration. Starting from this geometrical input, a zero-th order BEM is used to solve the aerodynamic problem: blades, nacelle and wake surfaces are discretized into surface quadrilateral panels. The code uses a structured mesh.

The DANAERO rotor was simulated using 32 chordwise and 80 spanwise panels along the blade, whilst 96 wake panels per revolution are used along 10/14 wake revolutions and 4/5 D wake length. Boundary conditions are imposed on blade, nacelle and wake surfaces for the well-posedness of the problem. Specifically, the impermeability condition on blades/nacelle surfaces and the absence of pressure discontinuity and fluid particles motion throughout the wake define these boundary conditions. The BEM formulation yields a linear set of algebraic equations for the velocity potential over the blade. This system of equations is solved by classical LU factorization techniques. Then, pressure distribution upon the blade(s) is further computed by the Bernoulli equation and blade loads are obtained through the surface integration of the elemental forces contribution due to the pressure field and stresses (tangential and normal) associated with viscosity. The solution seeking of the wake shape is a nonlinear process that is solved by a predictor/corrector-based finite difference method (Heun scheme). For steady-state simulations a pseudo time step is used. The nonlinear wake alignment procedure is iterated until a periodic solution is achieved. The RMS of wake nodes position at the end of each revolution is compared with the previous one and converged is obtained for differences within a required accuracy. Typically, assuming  $N$  wake revolutions, convergence is reached after  $2N + 1$  rotor revolutions.

The aerodynamic simulation has been run considering only rigid blades undergoing uniform axial flow, yaw or shear. No turbulence effects were included. The azimuth angle step used in the aerodynamic simulations is  $3.75^\circ$ , corresponding to a time step of about 0.04 sec. The aerodynamic simulations covered about 52 seconds and the solution computed for last revolution was considered as converged in the case of unsteady simulation. No averaging procedure was applied. FUNAERO is a research code so it is not fully optimized. Anyhow, the code is able to run in parallel on shared memory machines. The CPU time of the computations was about 72 wall-clock hours on a single machine with 76 CPUs. Blade and rotor loads are obtained through the surface integration of the elemental forces contribution due to the pressure field. In order to comply with the calculation round requirements, normal and tangential forces results do not contain the contribution of friction.

### C.5.3 Rotor and tower structural modelling

Rotor and tower structural modelling is applied to predict the turbine behaviour *in vacuo*, without aerodynamic loading. In this case the modelled wind turbine components are the blades, nacelle and tower. The structural dynamics solver is based on a finite element formulation, where each section of the blade is a linear Timoshenko beam element with non-uniform cross-section characteristics. The initial geometry is interpolated using modified Akima piecewise cubic Hermite interpolation. The blade elements are modelled using Timoshenko theory and discretized using the commercial FE solver Comsol Multiphysics. 2315 elements are used to discretize the whole structure (about 10 cm length for each element). Flapwise, edgewise and torsion of the blade are modelled with a total of degrees of freedom equal to 9200. Beam parameters (density, moment of inertia, E, G, etc..) are distributed along the length of the structure. Different interpolation technique have been implemented in the model: nearest neighbour, linear, cubic and cubic spline.

## C.6 ONERA - ELSA - Code description

Ronan Boisard (ONERA)

The mesh used is the one provided by DTU which was also used for EllipSys3D solver. It only includes the blades without tower or nacelle. The computations was performed with elsA Reynolds-averaged Navier-Stokes (RANS) flow solver, co-owned by Airbus, Safran and ONERA [169] [170]. ElsA solves the RANS equations in a finite volume cell-centered formulation on multi-block structured body grids. The simulations are performed using a 2nd order AUSMP scheme, with a time integration ensured by a Backward Euler 2nd-order scheme with a scalar LUSSOR method. The chosen turbulence model is  $k-\omega$  Wilcox with Menter correction, Zheng limiter and SST correction. Adiabatic walls using low Reynolds approach was used for blade surfaces and non reflecting far field boundary condition was applied on external mesh faces. ElsA solver was only used for Case IV.1.1 (Axi-symmetric) which allows performing steady computations in absolute velocity formulation in the relative reference frame. Flexibility was not included in the computation.

Origin	Extension	Size/M	Blocks	Interface
DTU	360°	14.1	1	no
IAG/DLR	360°	29.2	3	chimera
FORwind/IWES	120°	24.5	3	AMI

Table C.4: Meshes prepared for CFD models.

## C.7 Code description ANSYS FLUENT, used by Kiel UAS

A.P. Schaffarczyk, Kiel University of Applied Sciences (KUAS)

### C.7.1 Code description

FLUENT is a commercial CFD code, developed since the 1980ies and now available from ANSYS. We used Release 19.0. There exist numerous theory guides with extensive descriptions of how and what kind of flows can be simulated [171].

### C.7.2 Solution Methods

The main properties for solving the Navier-Stokes-Equations we used are:

- Pressure-Velocity-Coupling: SIMPLE
- Spatial Discretization: 2nd order (upwind)
- Algebraic Multigriding (Gauss-Seidel)

### C.7.3 Mesh

Unfortunately, it was only possible to convert DTU and FORWind/IWES' mesh to FLUENT. The original DTU mesh (see table C.4 for some properties of the computational domain as well mesh size) did not converge however, probably due to high aspect-ratio cells close to the blade's wall. IAG/DLR's mesh uses a Chimera technique with overlapping volumes. AMI (= arbitrary mesh interfaces) couples/interpolates different blocks at close but different 2D-interfaces. As a consequence, although a lot of effort was spent, it was not possible to convert and to configure IAG/DLR's chimera mesh for use with FLUENT. So, we were left with FORwind/IWES' mesh prepared by. Leo Höning. Finally we were left with FORwind/IWES' mesh. No resources were available to construct an own mesh.

### Turbulence and Transition modeling

As a turbulence model we used Menter's SST- $k-\omega$  and to model laminar-to-turbulent transition Menter's  $Re_\theta - \gamma$  transitional model [171] based on transport equations was used. It is well known that  $e^N$  models are superior, see [172]. Nevertheless to use, for example, tau's transition module [173] so far only for the Mexico blade has been reported [174].

### Results

Table C.5 gives a short overview of results for global values like  $c_T$  and  $c_P$ . Data from other groups were collected mainly from the presentation at the 2019 meeting at NREL, Boulder, CO, USA. It has to be noted that [21] reports transitional simulations as well. Three groups (LM, DTU and Siemens) were mentioned. There an average  $c_P = 0.482 \pm 0.015$  can be deduced including transition and  $c_P = 0.445 \pm 0.005$  for fully turbulent flow. See chapter 14 of [21] for details. It has to be noted, that convergence in terms of residuals is very different, see Fig. C.13. Residuum for mass seems to stagnate at a level of about  $4 \cdot 10^{-4}$ , those for velocities decrease very slowly down to  $10^{-5}$  for the first 38 k iterations

Solver	Mesh	$c_P$	$c_T$
BEM (wt-perf)	(-)	0.429	0.820
EllipSys3D	DTU	0.483	0.824
tau	IAG/DLR	0.483	0.821
FLOWer	IAG/DLR	0.471	0.820
openFOAM	FORwind/IWES	0.441	0.798
FLUENT ft	FORwind/IWES	0.417	0.763
FLUENT tr	FORwind/IWES	0.433	0.774

Table C.5: Numbers for  $c_T$  and  $c_P$  from various computation. wt-perf (see C.10 for a short description) is an outdated BEM-code from NREL [175] for aerodynamics (power, thrust, bending moment) only. These values have been incorporated for reasons of comparison only. ft means fully turbulent and tr transitional.

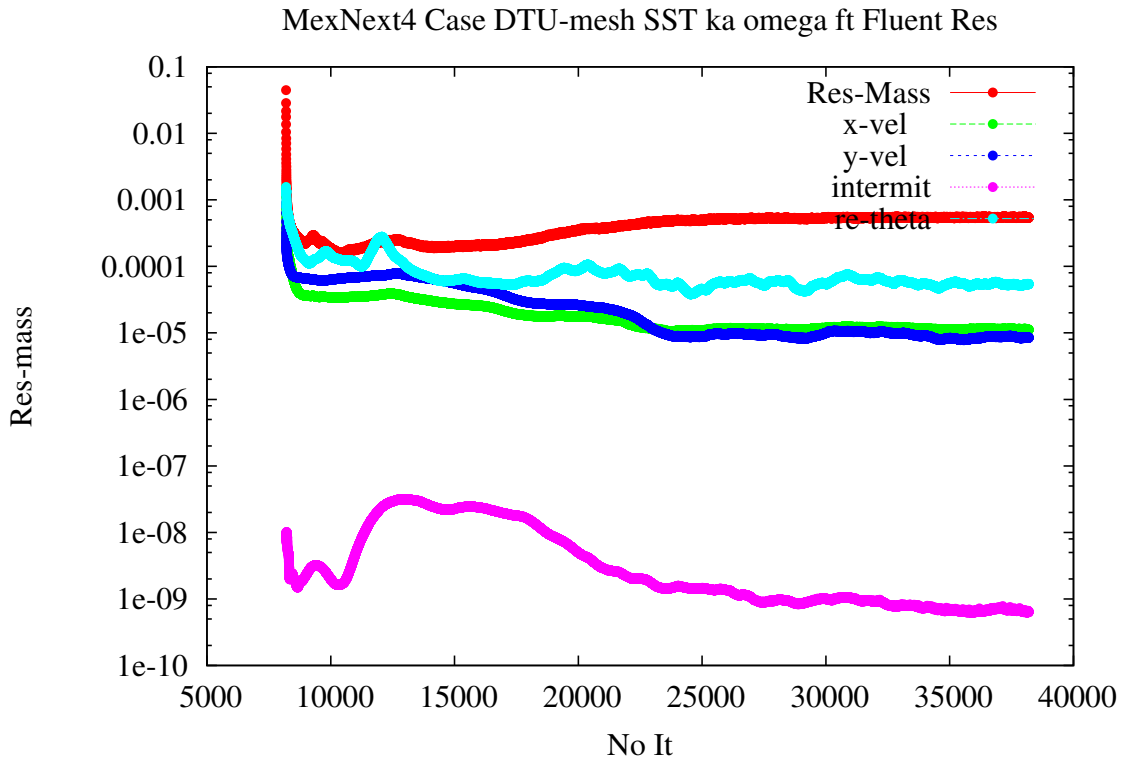


Figure C.13: Residuals for a typical transitional FLUENT job using FORwind/IWES' mesh and Menter's  $Re_\theta - \gamma$  transitional model. As the location of the transition line was not smooth after 50 k iterations about 200 k more were added.

### C.7.4 Discussion

From table C.5 it is clearly seen, that the overall performance prediction with FLUENT is visibly (almost 10%) smaller than from other (EllipSys3D, tau and FLOWer) codes. A slight mismatch in pitch (of about  $0.4^\circ$ ) was found, but was discarded as the main reason for under-prediction, because BEM-calculations showed that a change of about 1% would result only. So, unfortunately, up to now it remains open what causes this rather big difference.

### C.7.5 Resources

Jobs were run on resources from HLRN, The North German Supercomputing Alliance. We used 3 nodes with 96 processors each. In 12 wall-clock hrs about 36 k iterations could be performed. In total about 260 k iterations had to be performed, which only then resulted in a stable transition line, see section 10.4.

### C.7.6 Acknowledgement

Computations were performed with resources provided by the North-German Supercomputing Alliance (HLRN). Special thanks go to Galih Bangsa (IAG) and Leo Hönig (FORwind/IWES) for numerous discussions and trials on mesh conversion.



## C.8 USTUTT Code description and setup

Galih Bangga, Giorgia Guma and Thorsten Lutz

### C.8.1 FLOWer Code

This study was conducted based on the process chain for the simulation of wind turbines, which was developed at the Institute of Aerodynamics and Gas Dynamics (IAG, USTUTT) in the last years, e.g. for high fidelity RANS/LES modelling, flow in complex orography, aeroelastic effects, and active flow control by flap and actuator jet [176–181]. The main part of the chain is the CFD code FLOWer, which is complemented by different pre- and post-processing tools. The basic version of the CFD code FLOWer was developed by the German Aerospace Center (DLR) within the MEGAFLOW project [182] in the late 1990s. It is a compressible code and solves the three-dimensional Navier-Stokes equations in an integral form with several turbulence models available. The numerical scheme is based on a finite-volume formulation for block-structured grids. The ROT module allows body motions in translating/rotating reference frames for unsteady wind turbine simulations. Time integration is accomplished by an explicit multi-stage scheme. Time accurate simulations use the dual time stepping method as implicit scheme. The turbulence model equations are solved separately from the main flow equations using a full implicit time integration method. FLOWer is optimized for parallel computing and uses Message-Passing Interface (MPI).

### C.8.2 B-GO

The momentum code B-GO has been developed at USTUTT for the purpose in improving the consistency between low order simulation tools and high fidelity CFD model. B-GO was used especially for Task *Task 3.1: Effects of Inflow Turbulence*. B-GO adopts a full local implementation approach, where the induction is calculated exactly on the blade element location. This allows the code to model the induction variations in response to complex inflow conditions such as wind shear, yaw and turbulence. The code was firstly introduced in [29] for HAWT operating under stalled flow conditions. The code was further extended for VAWT in [183,184] employing a well known double-multiple streamtube (DMS) approach [185]. An extended version of the DMS model, namely the improved double-multiple streamtube (IDMS) approach, has been introduced in B-GO [183,184], which revises the formulation for the flow curvature and wake expansion effects.

Figure C.14 illustrates the calculation accuracy of B-GO in comparison with the CFD results and measurement data of the DanAero turbine. The comparison round is for the highly sheared flow in combination with large yaw (Task 2.2) in Chapter 4. It can be seen that B-GO accurately predicts the azimuthal normal force acting on four different radial stations. Overall the code is validated and justified for the use in comparison round in Task 3.1.

### C.8.3 SIMPACK Software

The elastic response of the DanAero wind turbine was calculated by the creation of a SIMPACK model starting from the provided data of the HAWC2 model. SIMPACK is a commercial software from Dassault Systemes for the simulation of Multi-Body-Systems. A Multi-Body-System consists of rigid and flexible bodies interconnected by force and joint elements that impose the kinematic and dynamic constraints. Each body, represented by one or more markers, may then have three translational and rotational displacements as result of deformation and motion. The body motion is described by a set of Differential-Algebraic Equations (DAEs), a combination of differential motion equation and algebraic constraint. SIMPACK has a graphic interface and enables to simulate the non-linear motion of any mechanical or mechatronic system and therefore wind turbines. It is possible to add controllers to the simulations, as well as to include hydrodynamic and aerodynamic (BEM based) models to the system. Additionally, it is possible to couple own programmes by the use of a predefined environmental interface. For this reason a coupling between FLOWer and SIMPACK was developed in the recent years by [186] and [187]. The flexible bodies can be modeled in SIMPACK as linear or non-linear beam elements, or as modal bodies when the modal properties are provided by a FEM pre-processor. SIMPACK has been often used in the wind turbine field, e.g. [188],

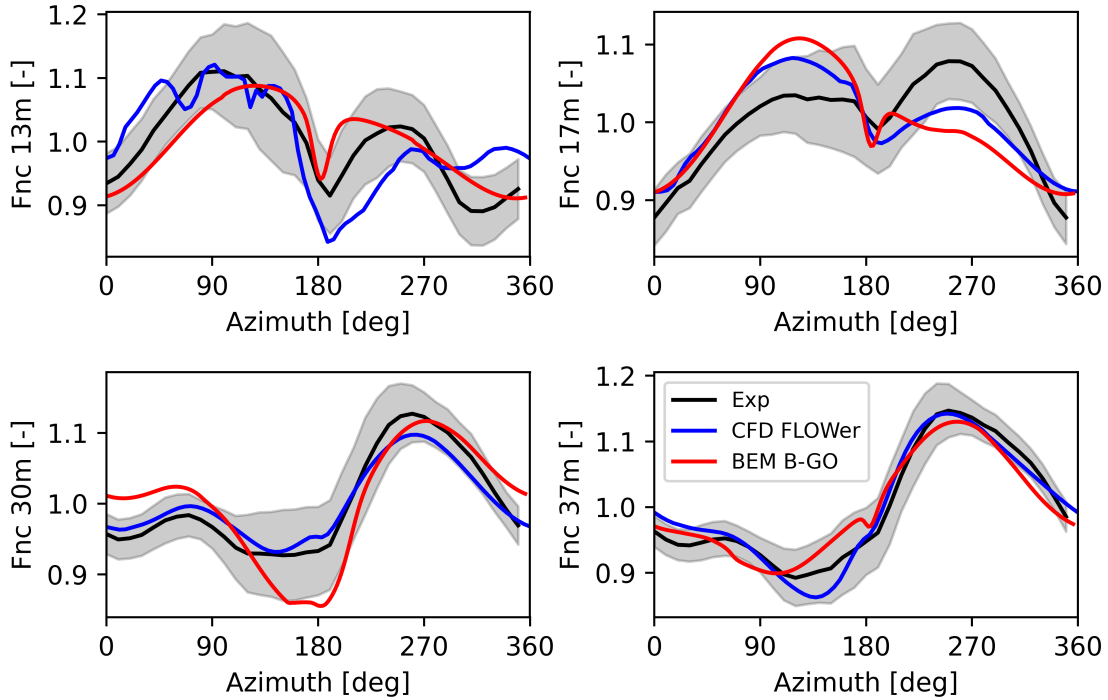


Figure C.14: Comparison between B-GO results and the FLOWer CFD results against measurement data of the DanAero turbine for *Task 2.2: yawed flow*.  $\gamma = -38.34^\circ$ ,  $\alpha_s = 0.262$ ,  $\alpha_p = -4.75^\circ$ .

who investigated a Model Predictive Control on the NREL 5 MW wind turbine with a detailed drive train, and [189] who investigated a flexible hub connection for a 3,4 MW two-bladed wind turbine.

#### C.8.4 AeroDyn

A simplified aerodynamic model based on Blade Element Momentum (BEM) theory has been generated with the NREL code AeroDyn. This has the advantage of being already incorporated in SIMPACK as additional module, and it can be therefore easily coupled to the structural model. In this case, the blade needs to be modeled aerodynamically with as many nodes as structurally, i.e. 21 for each blade. 3D CFD polars generated during the same IEA Task have been used as input for the BEM solver. Axial and tangential induction corrections have been taken into account. The comparison of the subsectional loads per unit length in normal ( $F_N$ ) and tangential ( $F_T$ ) direction between BEM and CFD is depicted in fig. C.15. In this case only one blade, with no tower shadow and rigid conditions has been taken into consideration, averaging the results of the three last revolutions. The curves show a good agreement, and therefore the BEM model of the turbine is validated.

#### C.8.5 Setup for Task 1: Uniform Inflow

The computations were carried out employing the steady Reynolds-Averaged Navier-Stokes (RANS) approach. The closure for the turbulence equations uses the Menter SST model [190] since it is better suited for a wide range of flow cases involving adverse pressure gradient effects. A fully turbulent boundary layer was assumed for the computations. The simulations were carried out assuming a flow periodicity from one blade to the other blades, allowing one to model only one blade. This was realized by utilizing a periodic boundary condition. No hub, nacelle and tower are modeled for this case. The meshes of each structure were generated separately, and they were combined without sacrificing the quality of the meshes by using the Chimera overlapping grid technique [191]. The Jameson-Schmidt-Turkel (JST) [192] scheme

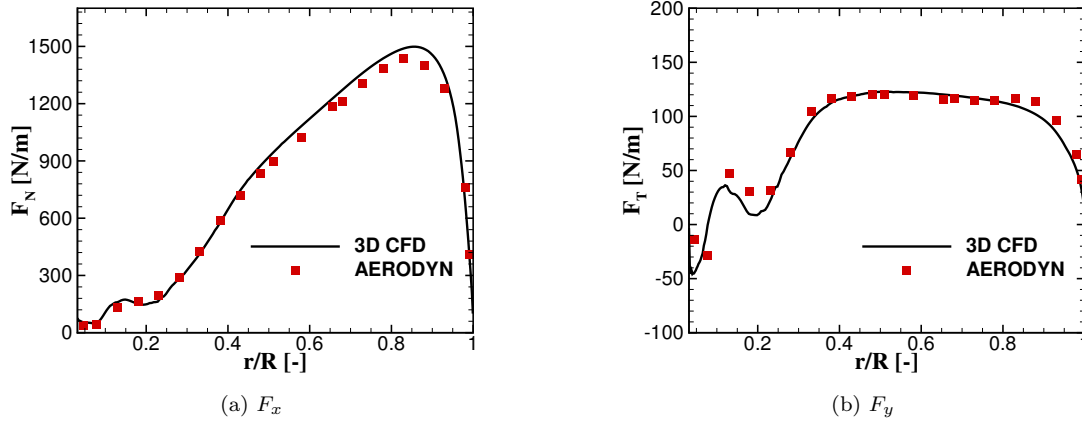


Figure C.15: Normal (on the left) and tangential (on the right) subsectional load in comparison for a single rigid blade 3D CFD vs AeroDyn

was adopted for flux computations.

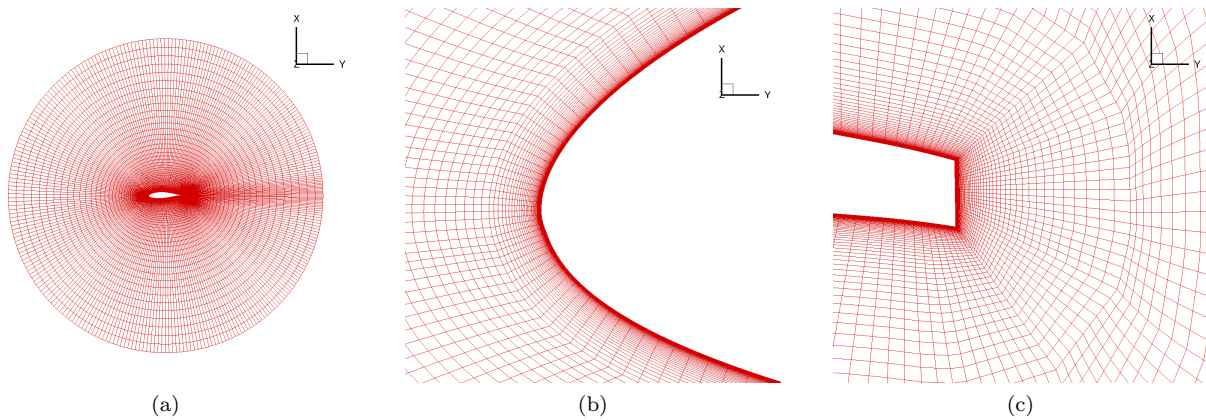


Figure C.16: Overview of the blade mesh (a) blade subsection, (b) enlarged view near the leading edge and (c) near the trailing edge.

A blade mesh convergence test was performed in a previous study [193] for a 10 MW generic AVATAR rotor. Three different resolutions of the blade mesh were examined. The grid convergence index for the fine grid is less than 0.5%. The values of power and thrust for the medium and the fine grids are very close with extrapolated relative errors of less than 0.5%. The outcome of this grid study was used as a basis for generating the mesh in the present work. It was shown [194] that O-mesh saves a lot of number cells with comparable accuracy for CFD simulations. Thus, the O-type mesh topology was applied. The blade mesh has  $[256 \times 128 \times 200]$  grid cells in the chord, wall-normal (including boundary layer block) and radial directions. The blunt trailing edge base is resolved by 32 grid cells. The first wall-off cell size satisfies the condition  $y^+ < 1$ , with an average value of 0.778 on the blade. The boundary layer is resolved with 64 cells with an algebraic growth rate of 1.1. The grid is refined near the leading and trailing edges with a spacing of 0.001 and 0.0005 local chord length, respectively, using a tangent hyperbolic distribution. To avoid a huge change between the cell size on the trailing edge and with the blunt trailing edge base (since the trailing edge base is very thin), the grid on the trailing edge is redistributed locally on the last 32 grid cells starting from both trailing edge points (suction and pressure sides). The grid cells are adjusted according to the local spacing on the blunt trailing edge base, see Figure C.16. The blade mesh amounts  $\sim 8.8$  million cells.

The background grid consists of several mesh components with different refinement levels as shown in

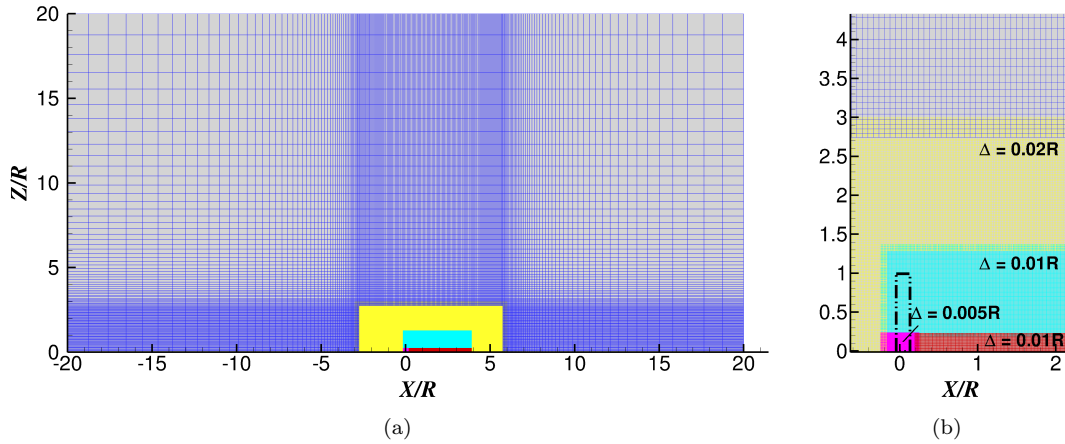


Figure C.17: Overview of the background mesh (a) overall, (b) enlarged view near the rotor area.

Figure C.17. This approach adopts a previous study conducted in [194]. This allows one to use a relatively uniform cell size for each background mesh. The resolution of the background mesh in the wake region is around 0.4 m or  $0.01R$  (Figure C.17). The background grid has a shape of  $1/3$  of cylinder, where the periodic boundary condition was applied on both side planes. For the coarsest background mesh, the steady uniform flow is realized by employing a far field boundary condition. Meanwhile, the communication between different background meshes is facilitated by the Chimera approach. The total number of cells for all mesh components are  $\sim 26$  million. A no-slip condition was used on all wall type boundaries without any wall function.

The blade geometry of the DanAero wind turbine was used. All structures were treated as rigid. The freestream air properties are density  $\rho = 1.22 \text{ kgm}^{-3}$ , temperature  $T = 288.15 \text{ K}$  and dynamic viscosity  $\mu = 1.8375 \times 10^{-5} \text{ kgm}^{-1}\text{s}^{-1}$ . The simulations were carried out until quasi stationary convergence of the rotor thrust and power was achieved over iteration.

### C.8.6 Setup for Tasks 2.1 and 2.2: Shear & Yaw

The computations were carried out employing the Delayed-Detached Eddy Simulation (DDES) approach in combination with the Menter SST model [190] as the Reynolds-Averaged Navier-Stokes (RANS) model near the wall. A fully turbulent boundary layer was assumed for the computations. The simulations were carried out considering all structures including blades, hub, nacelle and tower. Block structured meshes were generated separately, and they were combined without sacrificing the quality of the meshes by using the Chimera overlapping grid technique [191] as shown in Figure C.18.

A blade mesh convergence test was performed in a previous study [193] for a 10 MW generic AVATAR rotor. Three different resolutions of the blade mesh were examined. The grid convergence index for the fine grid is less than 0.5%. The values of power and thrust for the medium and the fine grids are very close with extrapolated relative errors of less than 0.5%. The outcome of this grid study was used as a basis for generating the mesh in the present work. It was shown [194] that O-mesh saves a lot of number cells with comparable accuracy for CFD simulations. Thus, the O-type mesh topology was applied. The blade mesh has  $[256 \times 128 \times 200]$  grid cells in the chord, wall-normal (including boundary layer block) and radial directions. The blunt trailing edge base is resolved by 32 grid cells. The first wall-off cell size satisfies the condition  $y^+ < 1$ , with an average value of 0.778 on the blade. The boundary layer is resolved with 64 cells with an algebraic growth rate of 1.1. The grid is refined near the leading and trailing edges with a spacing of 0.001 and 0.0005 local chord length, respectively, using a tangent hyperbolic distribution. To avoid a huge change between the cell size on the trailing edge and with the blunt trailing edge base (since the trailing edge base is very thin), the grid on the trailing edge is redistributed locally on the last 32 grid cells starting from both trailing edge points (suction and pressure sides). The grid cells are adjusted according to the local spacing on the blunt trailing edge base, see Figure C.19. The blade mesh amounts  $\sim 8.8$  million cells.

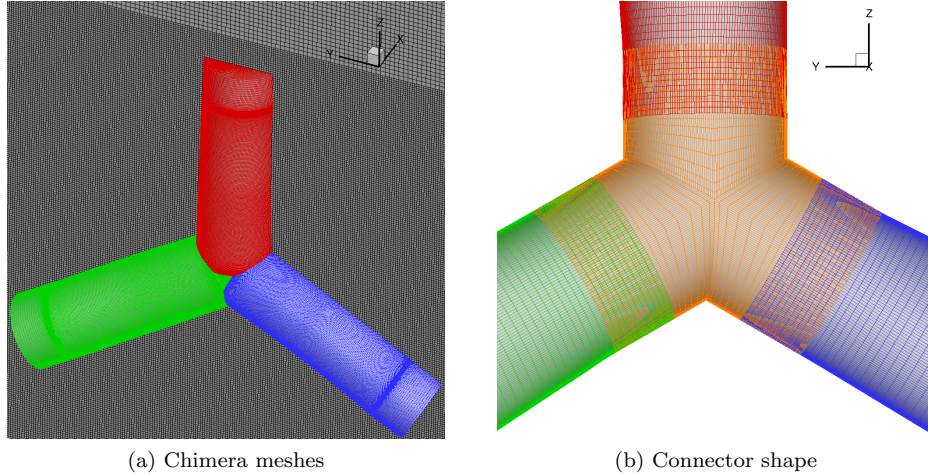


Figure C.18: Mesh topology of a) Chimera meshes of blades and connector and b) shape of connection in blade root region.

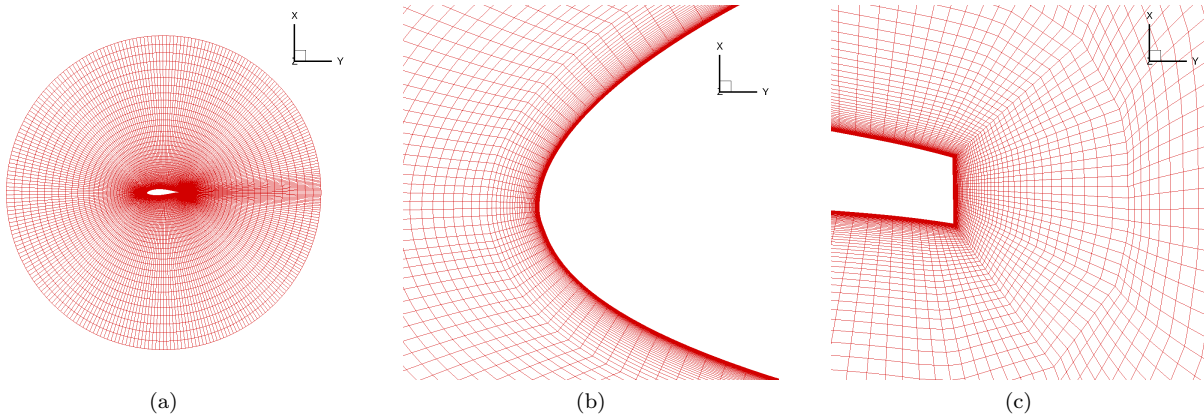


Figure C.19: Overview of the blade mesh (a) blade subsection, (b) enlarged view near the leading edge and (c) near the trailing edge.

The background grid was created applying a non-conformal mesh approach. A uniform grid size was applied with a 1 m resolution [195, 196]. The 1 m resolution extends from  $X = -300$  m up to 400 m downstream from the rotor, see Figure C.20. The mesh is refined twice (0.5 m) starting from -40 m up to 250 m to resolve the turbine wake. Note that the turbine center of rotation is located at  $X = 0$  m and the hub height is 57.19 m. A coarsening of the mesh towards the domain boundaries was applied to reduce the background mesh size ( $\sim 66$  million cells). The domain size was set to  $[1024 \times 2048 \times 1024] \text{m}^3$  in the stream-wise ( $X$ ) and two crossflow ( $Y, Z$ ) directions. The total number of cells for simulations with the rotor, blade connector and local background refinement near the rotor plane are  $\sim 93$  million cells. The Jameson-Schmidt-Turkel (JST) [192] scheme was adopted for the blade, hub, nacelle and tower, while the 5th order weighted essentially non-oscillatory (WENO) scheme [197] scheme was adopted for the background mesh to reduce numerical dissipation and to capture the tip vortices. A no-slip condition was used on all wall type boundaries without any wall function. A velocity profile with a specified shear was set at the inlet background boundary. A far field condition was set at both background boundaries in  $y$  direction, on top of the simulation domain ( $z$  direction) and at the outlet boundary. The wall at  $z = 0$  m assumes a no-slip condition.

The blade geometry of the DanAero wind turbine was used. All structures were treated as rigid. The

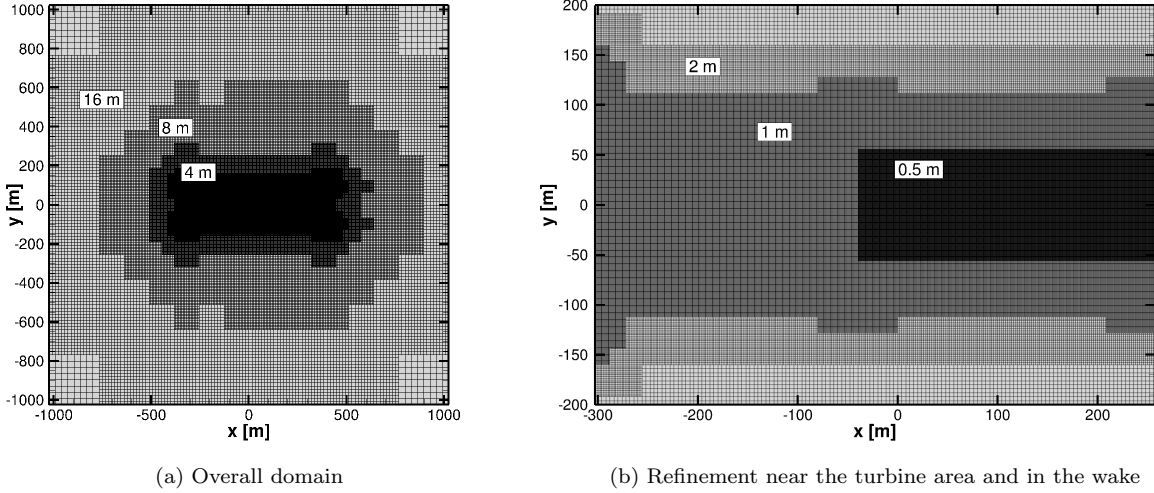


Figure C.20: Mesh topology of a) background mesh for overall view and b) local refinement for turbulence propagation.

freestream air properties are density  $\rho = 1.22 \text{ kgm}^{-3}$ , temperature  $T = 288.15 \text{ K}$  and dynamic viscosity  $\mu = 1.8375 \times 10^{-5} \text{ kgm}^{-1}\text{s}^{-1}$ . The simulations were carried out until quasi stationary convergence of the rotor thrust and power was achieved, and to ensure this aspect a minimum of 20 rotor rotations were simulated. The time step size employed for the sheared inflow case (Task 2.1) is  $5^\circ$  of the blade rotation per physical time step. However, for the yawed inflow case (Task 2.2), the time step has to be reduced to be as small as  $0.1^\circ/\text{step}$ .

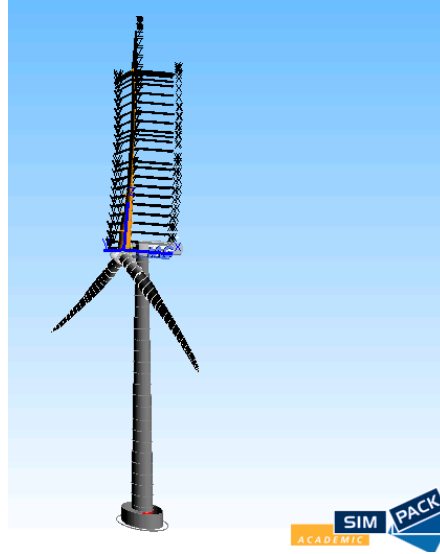
### C.8.7 Setup for Task 3.1: Effects of Inflow Turbulence

The main setup for Task 3.1 is almost the same as Task 2.1 and 2.2 described in Section C.8.6. Some differences are for the following aspects:

- No tower and nacelle for Task 3.1
- Background grid has a smaller domain, but larger area containing the fine wake resolution of 0.5 m
- The boundary condition for the outer domain in two lateral directions ( $-Y$  and  $+Y$ ) assumes periodic flow
- The outflow boundary adopts a constant pressure
- The time step size is  $2^\circ$  of the blade rotation per physical time step.

### C.8.8 Setup for Task 3.5: Aeroelastic Effects

The blades are modeled as non-linear SIMBEAM body types, (three dimensional beam structures in SIMPACK, described by a node-based non-linear finite different approach). These have been discretized into 22 Timoschenko elements in radial direction, taking into consideration gravitational and centrifugal forces. Structural damping is applied using the Rayleigh damping model with  $\alpha = 0.025$  and  $\beta = 0.014$ . The tower, due to its small expected deflections, has been modeled as a linear SIMBEAM discretized into 25 Euler-Bernoulli elements with 0.022 structural damping for the first 10 modes. The hub has been modeled with 2 linear Euler-Bernoulli elements with 0.02 structural damping and the nacelle is modeled with one only rigid node, i.e. it can move but not deform, see Figure C.21. Further info is given in [198].



(a)

Figure C.21: Visualization of the structural MBD model

Table C.6: Comparison natural frequencies between the measured ones and the computed by SIMPACK, for both blade and full turbine.

Single Blade		Full Turbine	
Measured	Computed	Measured	Computed
1.01	0.938	0.437	0.4812
1.91	1.884	0.444	0.4862
2.96	2.687	0.839	0.869
		0.895	0.9201
		0.955	0.9626
		1.838	1.8758
		1.853	1.912
		2.135	2.5477
		2.401	2.7265

Due to the high number of cases required by the task, loads have been provided by the BEM based software AeroDyn, see sec. C.8.4. The choice has been made, additionally, in order to focus on the discrepancies due to the different structural and not aerodynamic modelling approaches, which are already deeply analyzed in other subtasks. AeroDyn is already provided internally into SIMPACK, therefore no additional coupling interfaces are needed. In order to validate the structural model, the natural frequencies of the singles blade and turbine are compared to the measured ones in Table C.6.

The setups and inflow conditions have been chosen according to the provided document "Aeroelastic Comparison Ver2 20200430.pdf". The time series to allow the stability analysis have been created according to the procedure agreed with Polimi and explained in the document "Aeroelastic Stability Analysis Process for NM80".

## C.9 UU Code descriptions

Henrik Asmuth, Gonzalo Navarro Diaz, Karl Nilsson, Stefan Ivanell

### C.9.1 elbe - LBM-LES

Lattice-Boltzmann simulations are performed using the multi-purpose numerical framework elbe [52]. The solver is coupled to an ALM following a similar approach as in classical Navier-Stokes-based solvers. Further details can be found in [199–201]. The collision operator is based on the cumulant LBM with optimised collision rates as proposed by Geier et al. [202]. A standard constant Smagorinsky model is employed as a SGS-model. The Smagorinsky constant is set to  $C_s = 0.1$  and reduced towards the wall using the damping function proposed by Mason and Thomson [203] with a damping exponent of  $n = 1$ .

### C.9.2 OpenFOAM - RANS and LES

One of the most widely used open source CFD software for simulating wind turbine wake interaction problems in atmospheric Boundary layer (ABL) flows is OpenFOAM [58, 204, 205]. This is based on the numerical method of finite volumes and it is coded in C++ and parallelized with MPI [206]. This software has the option of solving the flow using RANS and LES.

In order to ensure compatibility with the flow solution, two different methodologies for wind turbine modeling are chosen. For stationary RANS simulation of wake interaction problems it is appropriate to use the Actuator Disc Model (ADM), due to the stationary force distribution approach [207, 208]. For transient LES solutions it is better to use the Actuator Line Model (ALM) [209], with time dependent rotating blades. Both actuator models have been created in house shearing the same base code, allowing a better comparison between the two of them. Both models calculate the local tangential and normal forces in nodes distributed over lines and use the airfoil data provided in the benchmark. In the case of the ALM, the wind turbine is represented with three rotating lines [98]. In the other hand, the ADM is represented with multiple fixed lines [210, 211] and the number depends on the mesh resolution. The models specifications can be found in Table 7.5.

RANS-type stationary simulation allows to solve wind turbine wake interaction problems with a relative low computational cost compared to LES [208]. Between the solvers included in OpenFOAM, SimpleFOAM has been chosen. One of the key decisions in solving the interaction of wind turbines in RANS is the choice of a turbulence model which diffusion is controlled in the wake region [204]. For this, the Realizable  $k - \varepsilon$  turbulence model with standard coefficients [54] has been chosen, which has shown good agreement with wake velocity measurements in ABL flows [212, 213] and with LES results [207]. The domain size, mesh and boundary conditions configuration can be found in Table 7.3. This configuration follows the recommendations from [207].

In the LES simulation of ALM in ABL flows, the SOWFA OpenFOAM project [214] has been extensively used [215, 216]. Over the SOWFA code, two main modifications have been added; first, the original ALM included in the code has been changed by the ALM developed in house, which shares similar capabilities compared to the original one. Second, the inlet condition has been modified in order to include the Mann inflow. The Schumann-Grotzbach shear stress model [217] has been chosen, using a roughness height ( $z_0$ ) related to the TI at hub height.

Due to the fact that this inflow is already fully turbulent, the domain size has been reduced to the necessary dimensions to analyze the wake interaction and avoid side blockage effect. Despite that, the Mann box size is too small for the inlet face. So, the rest of the free area in the face is filled with extrapolated data from the Mann box.

The problem with the use of Mann turbulent inflow in LES is the fact that it is not in equilibrium with the simulation configuration, obtaining a strong TKE decay in the wake analysis region as result. In order to analyze the influence of this phenomena, an inlet condition using the precursor routine from SOWFA has been also run and provide as alternative inlet condition. The precursor has been set and run up to 20,000 sec. in order to obtain an average velocity and TI at hub height equal to the Mann box at the same height. The mesh for the precursor has an horizontal resolution of 10 m, following the recommendation from [214]. The SOWFA specifications for the Mann and precursor inlet can be found in Table 7.3.



## C.10 NREL `wt_perf` - Code description

A.P. Schaffarczyk (Kiel University of Applied Sciences)

### C.10.1 Code description

`wt_perf` is a former pure aerodynamic [175] BEM-based performance code. From this introduction (from 2003):

`wt_perf` uses blade-element momentum (BEM) theory to predict the performance of wind turbines. It is a descendent of the PROP code originally developed by Oregon State University decades ago. Over the intervening years, many people from many organizations put their marks on the code and it has had several names. More recently, the staff at the NWTC rewrote the program, modernized it, and added new functionality and algorithms.

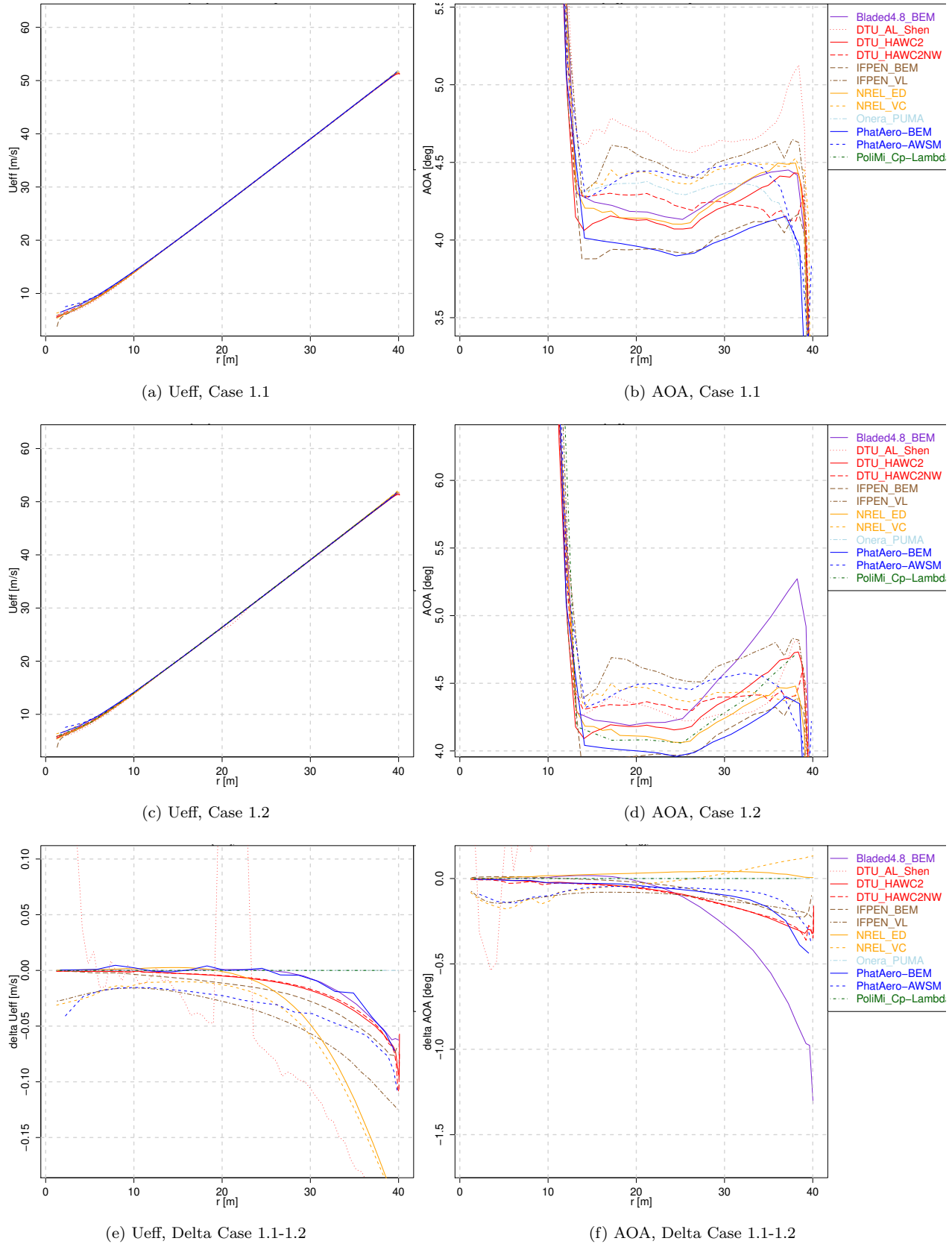
## Appendix D

# WP2 Comparison plots: Axial flow

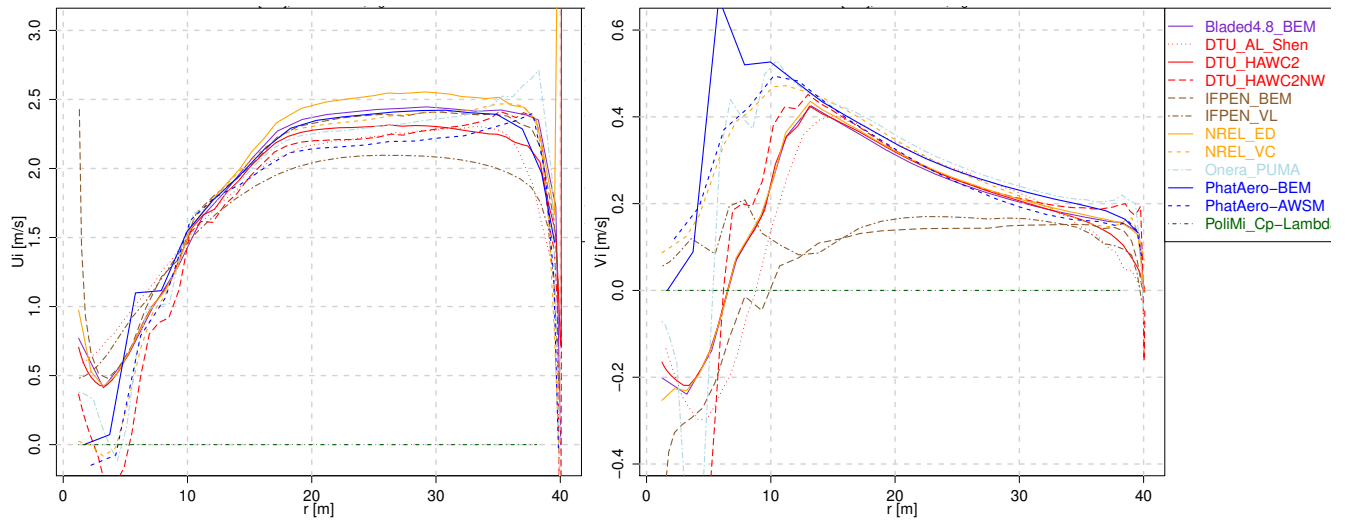
### D.1 Lifting line codes



### D.1.1 Lifting line variables

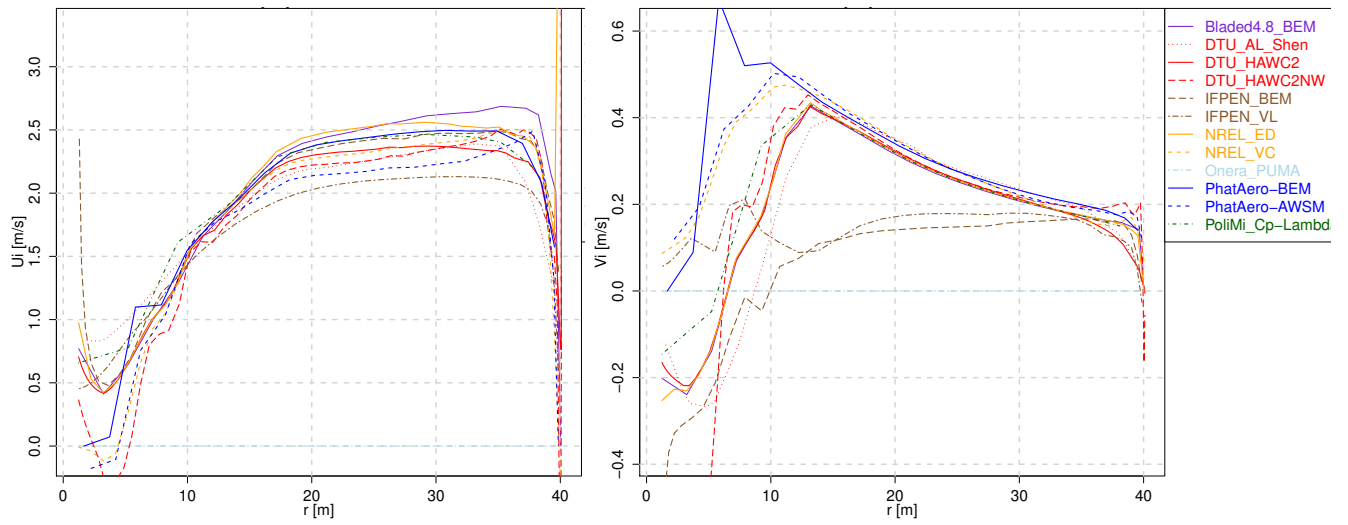


210  
Figure D.1: Lifting line variables (1)



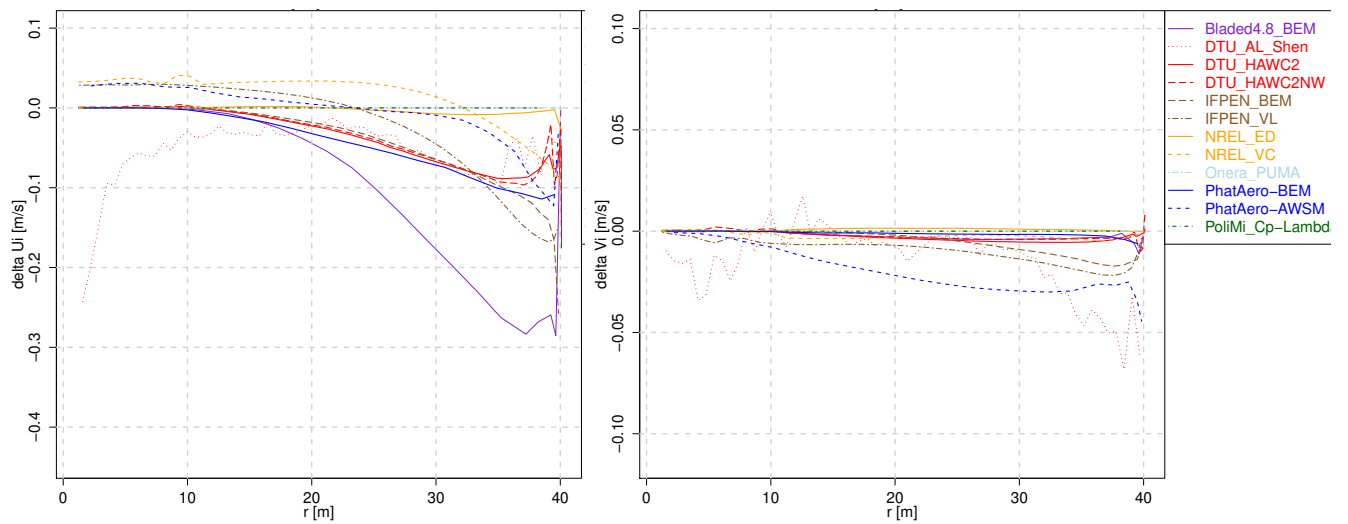
(a)  $U_i$ , Case 1.1

(b)  $V_i$ , Case 1.1



(c)  $U_i$ , Case 1.2

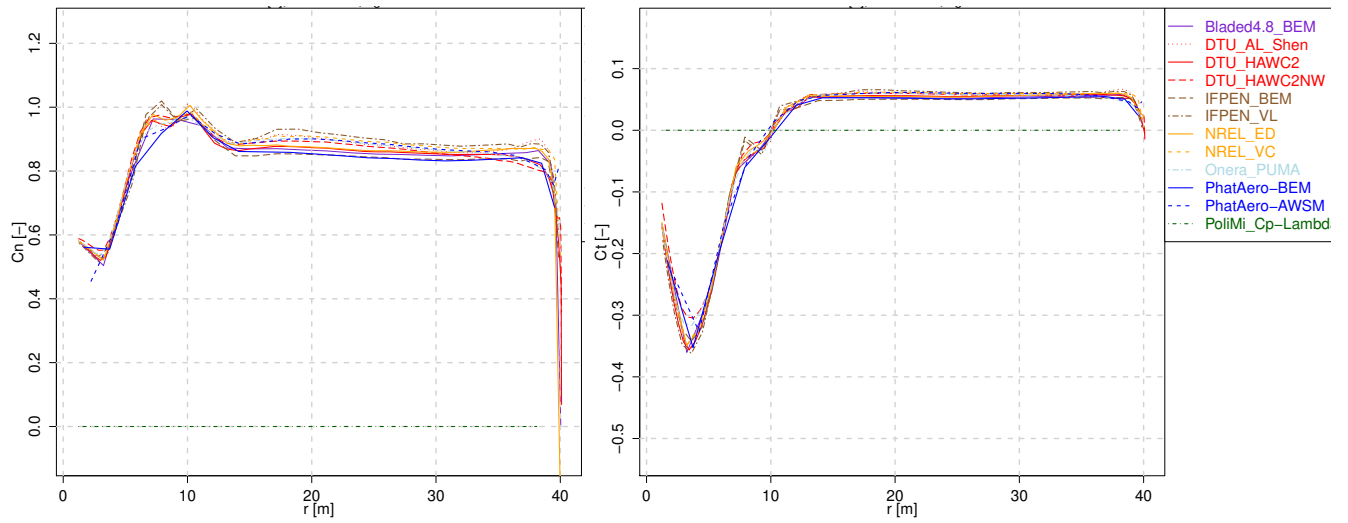
(d)  $V_i$ , Case 1.2



(e)  $\Delta U_i$ , Delta Case 1.1-1.2

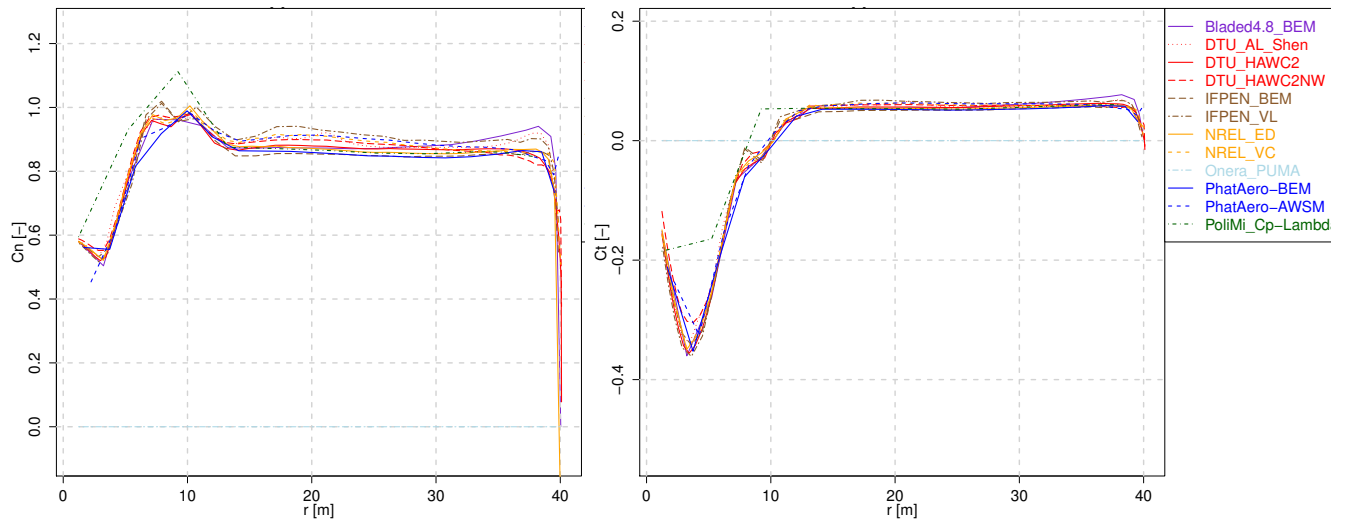
(f)  $\Delta V_i$ , Delta Case 1.1-1.2

Figure D.2: Lifting line variables (2)



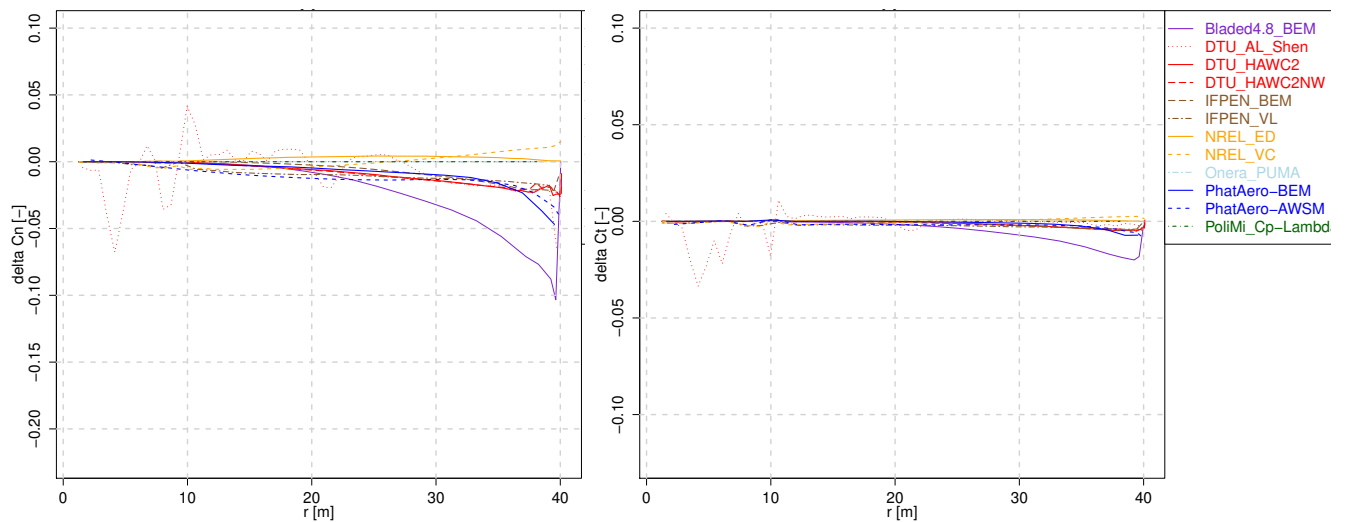
(a)  $C_n$ , Case 1.1

(b)  $C_t$ , Case 1.1



(c)  $C_n$ , Case 1.2

(d)  $C_t$ , Case 1.2



(e)  $\Delta C_n$ , Delta Case 1.1-1.2

(f)  $\Delta C_t$ , Delta Case 1.1-1.2

Figure D.3: Lifting line variables (3)



## D.1.2 Loads and deformations

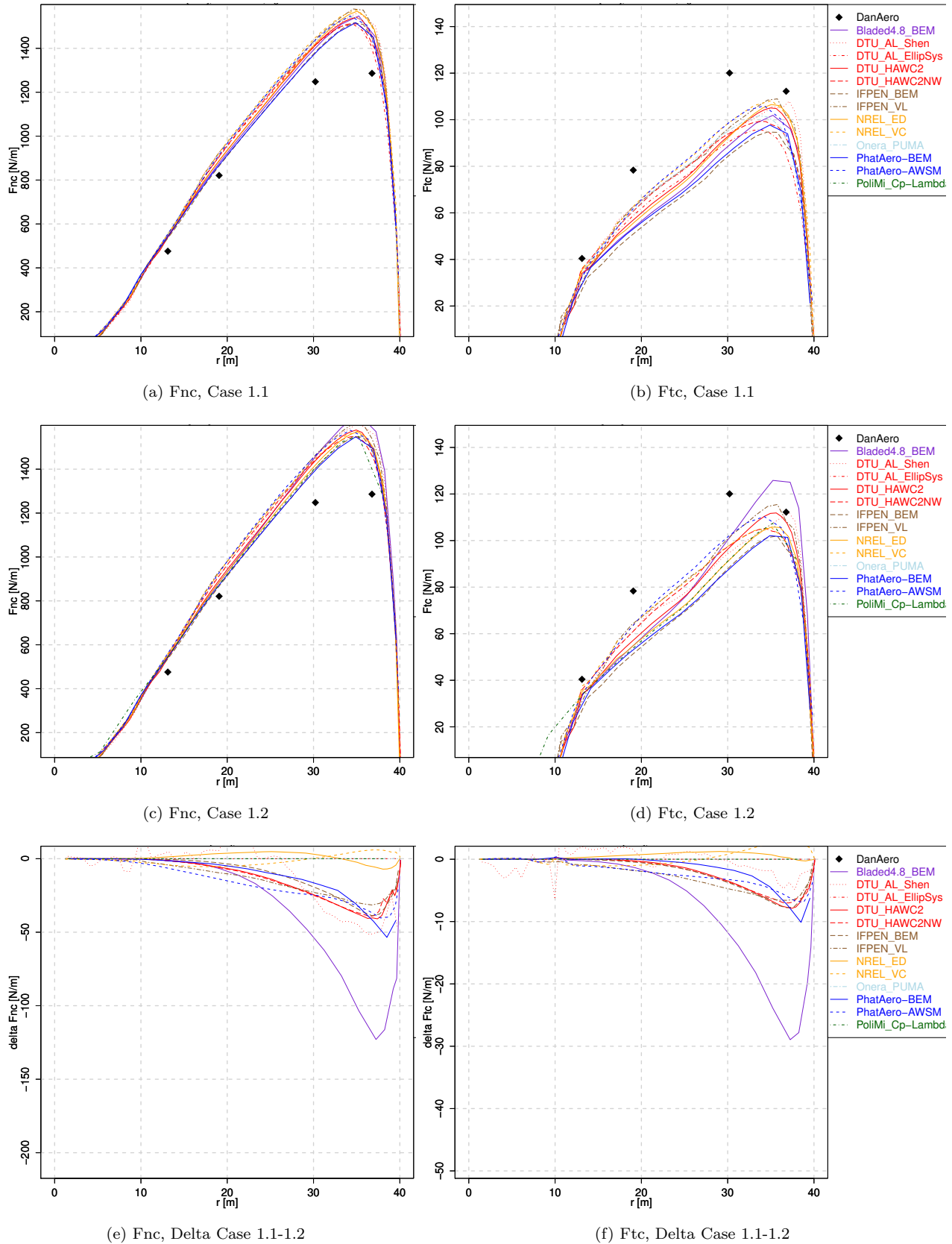
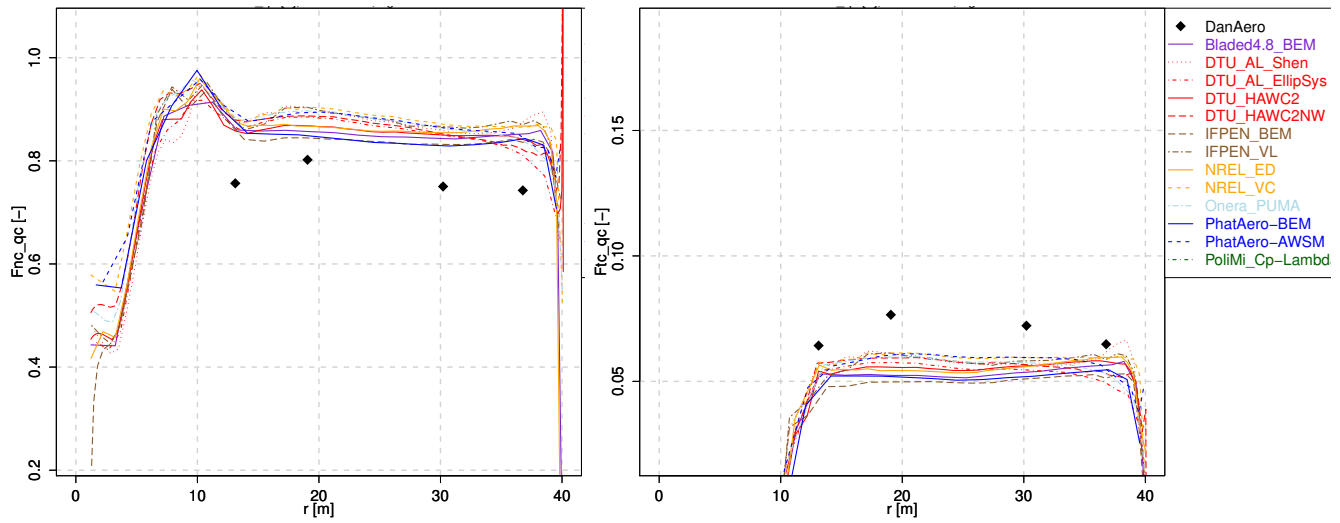


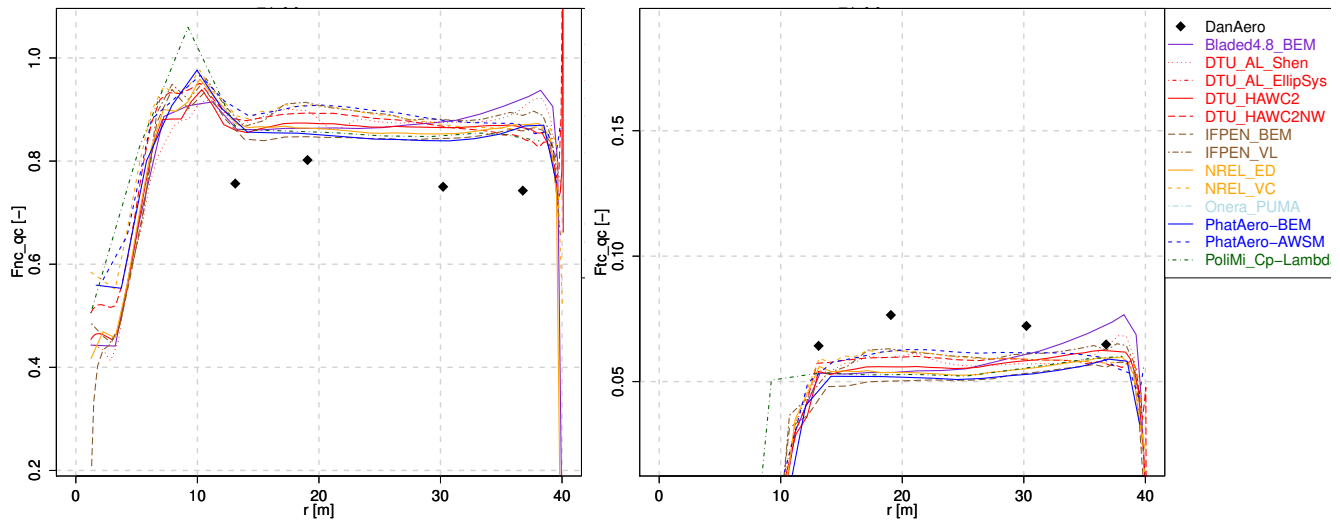
Figure D.4.1: Loads (1)





(a) Fnc<sub>qc</sub>, Case 1.1

(b) Ftc<sub>qc</sub>, Case 1.1



(c) Fnc<sub>qc</sub>, Case 1.2

(d) Ftc<sub>qc</sub>, Case 1.2

Figure D.5: Loads (2)

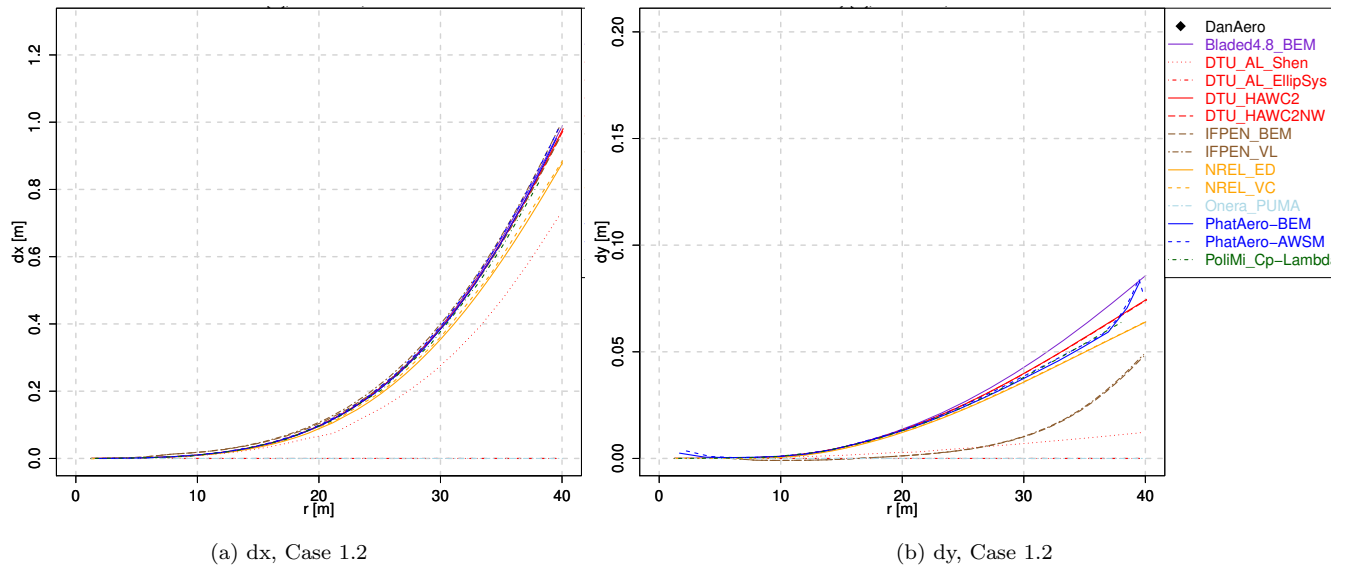


Figure D.6: Deformations

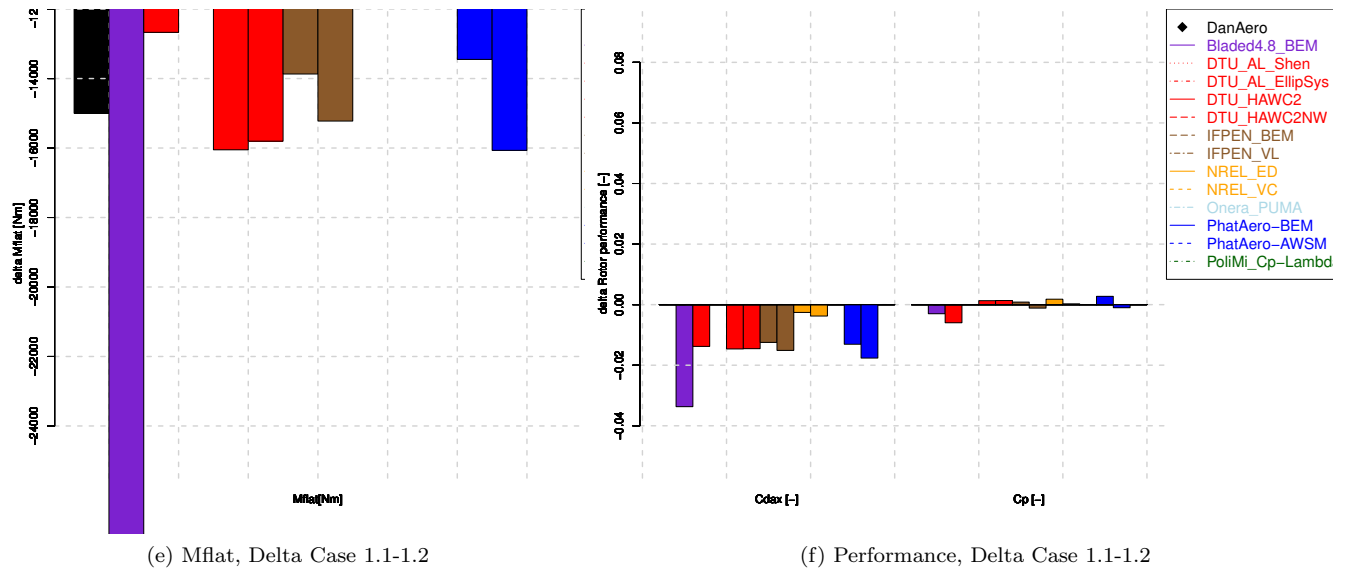
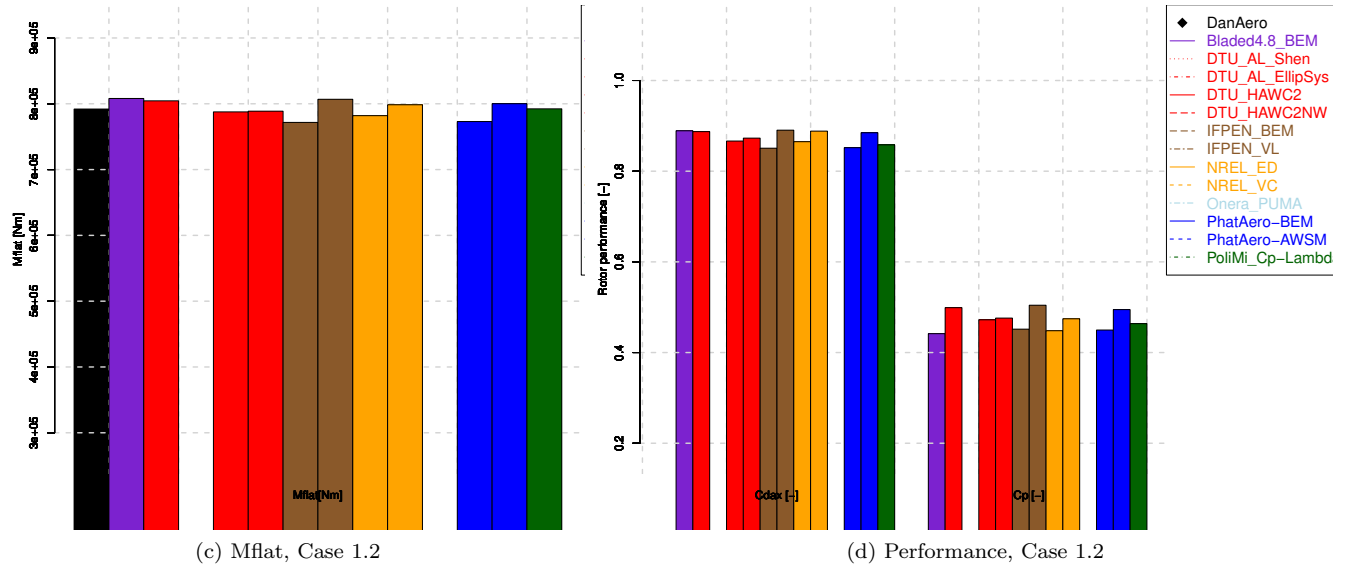
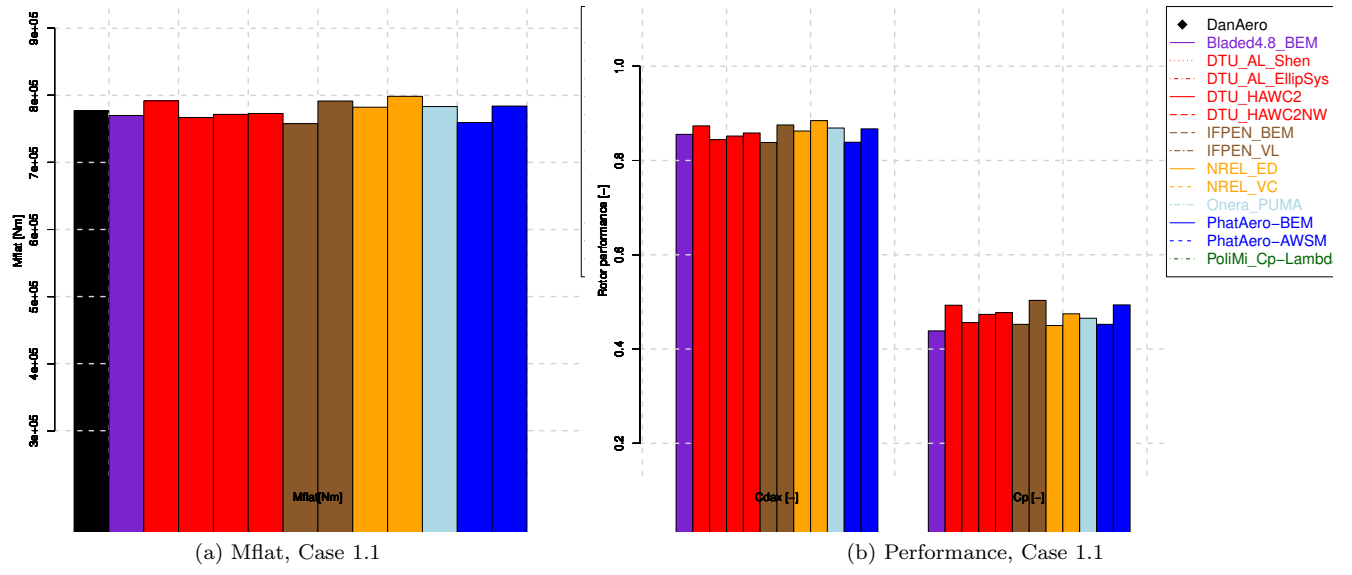


Figure D.7: Integral loads and performance

## D.2 CFD and panel codes

## D.2.1 Pressure distributions

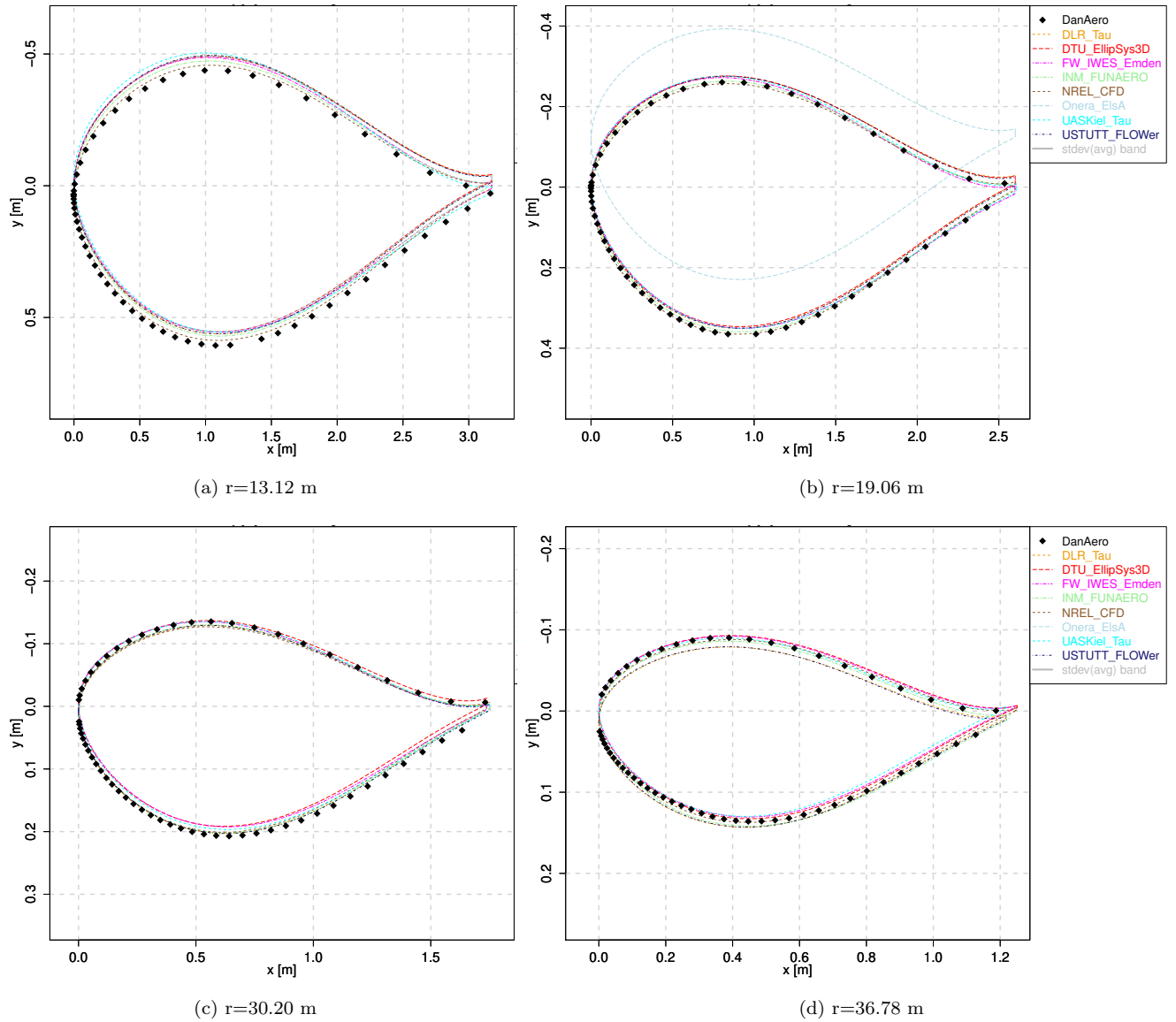


Figure D.8: Sectional geometries

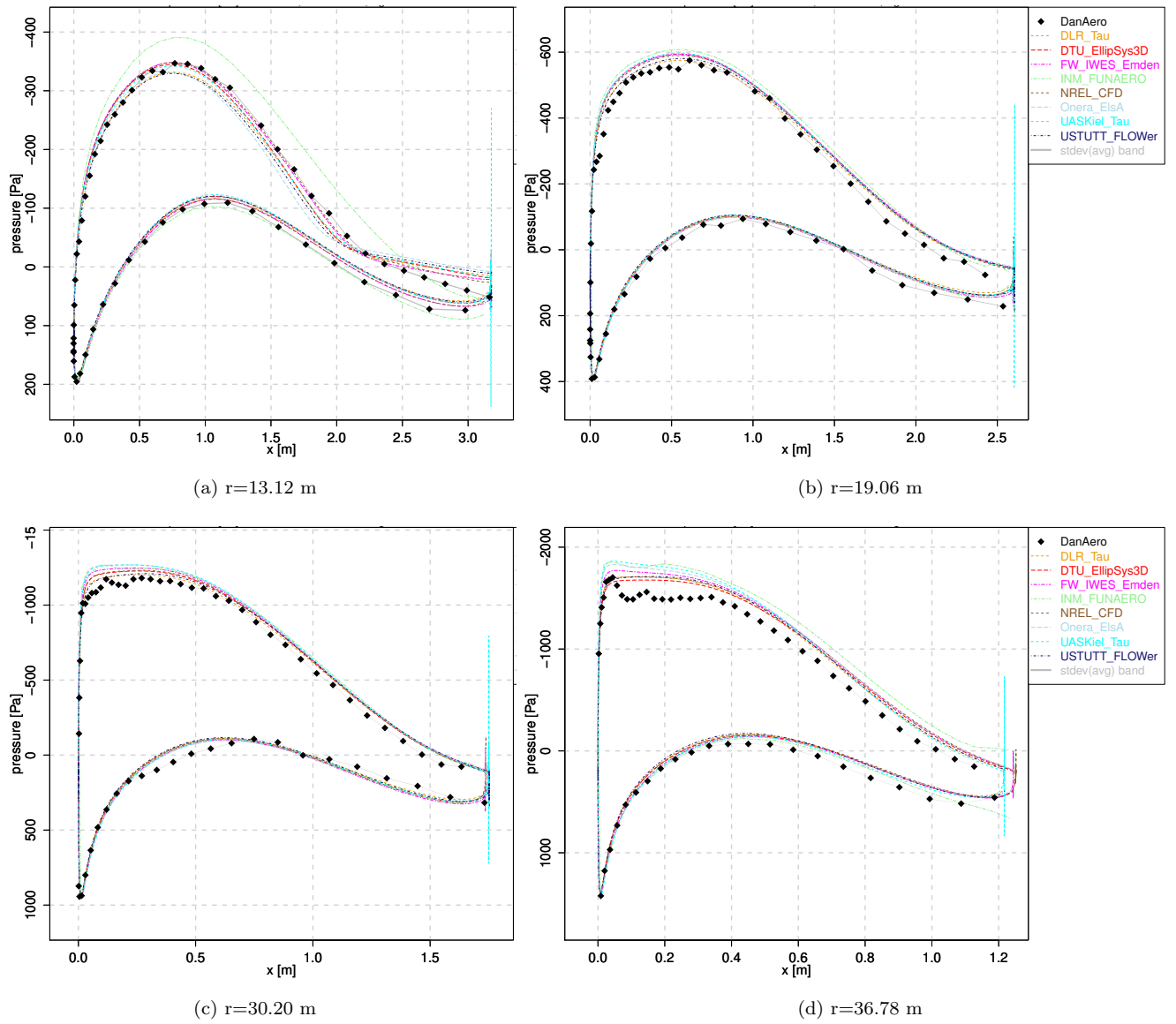


Figure D.9: Pressure distributions (Case 1.1)



## D.2.2 Loads and performance

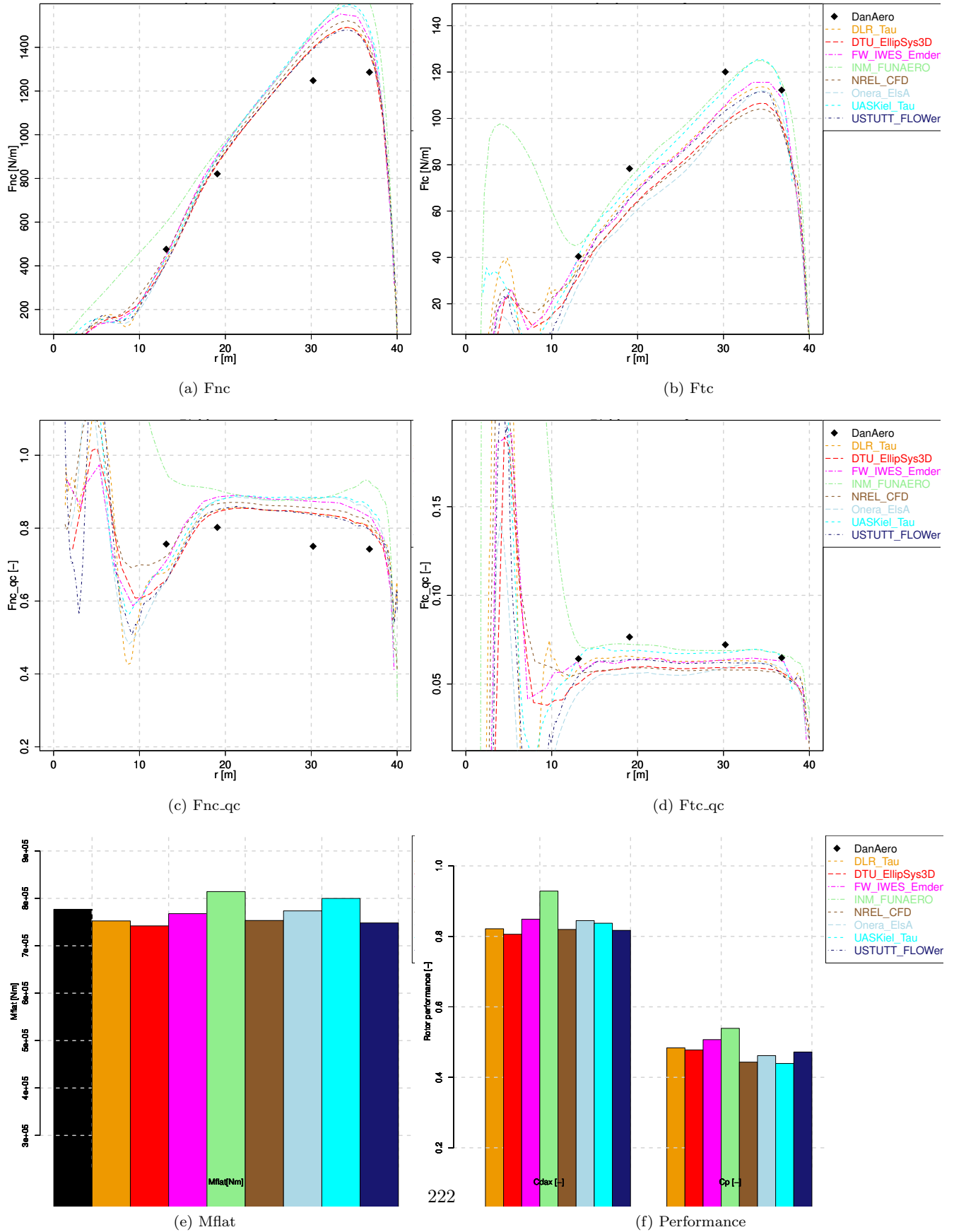


Figure D.10: Loads and performance (Case 1.1)



## Appendix E

# WP2 Comparison plots: Shear and yawed flow

### E.1 Lifting line codes

### E.1.1 Lifting line variables

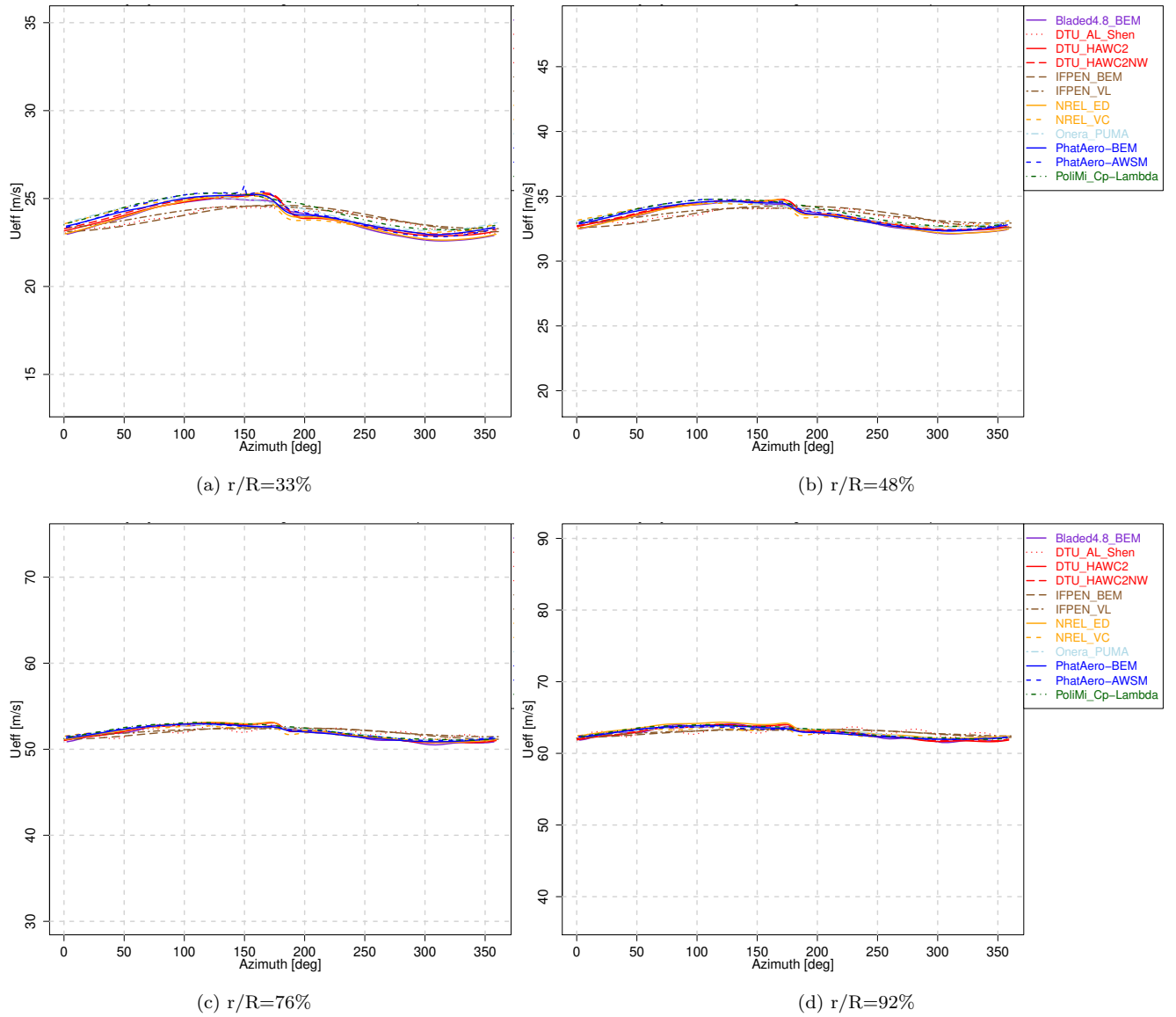


Figure E.1: Effective velocity  $U_{eff}$ , case 2.1

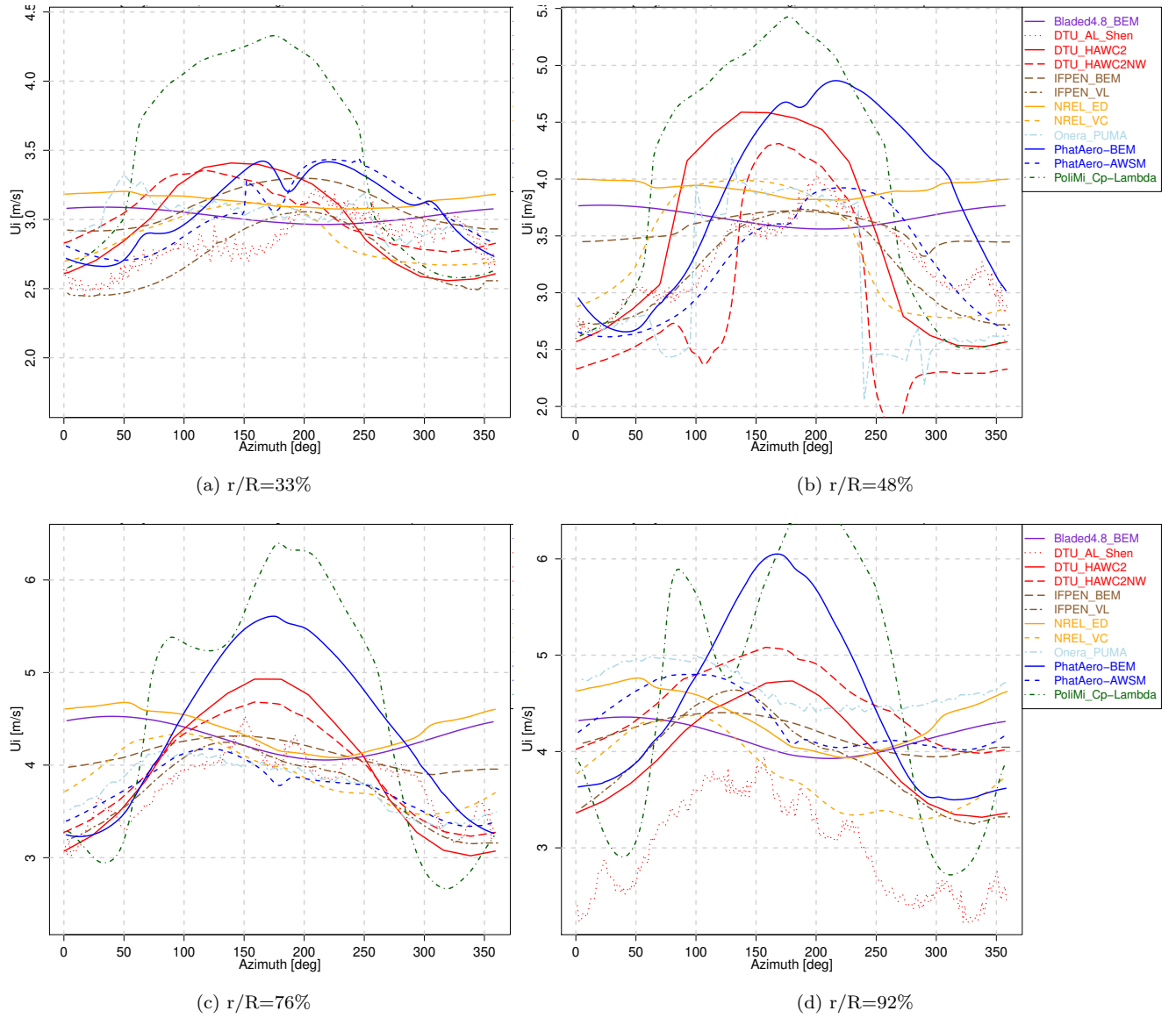


Figure E.2: Axial induced velocity  $U_i$ , case 2.1

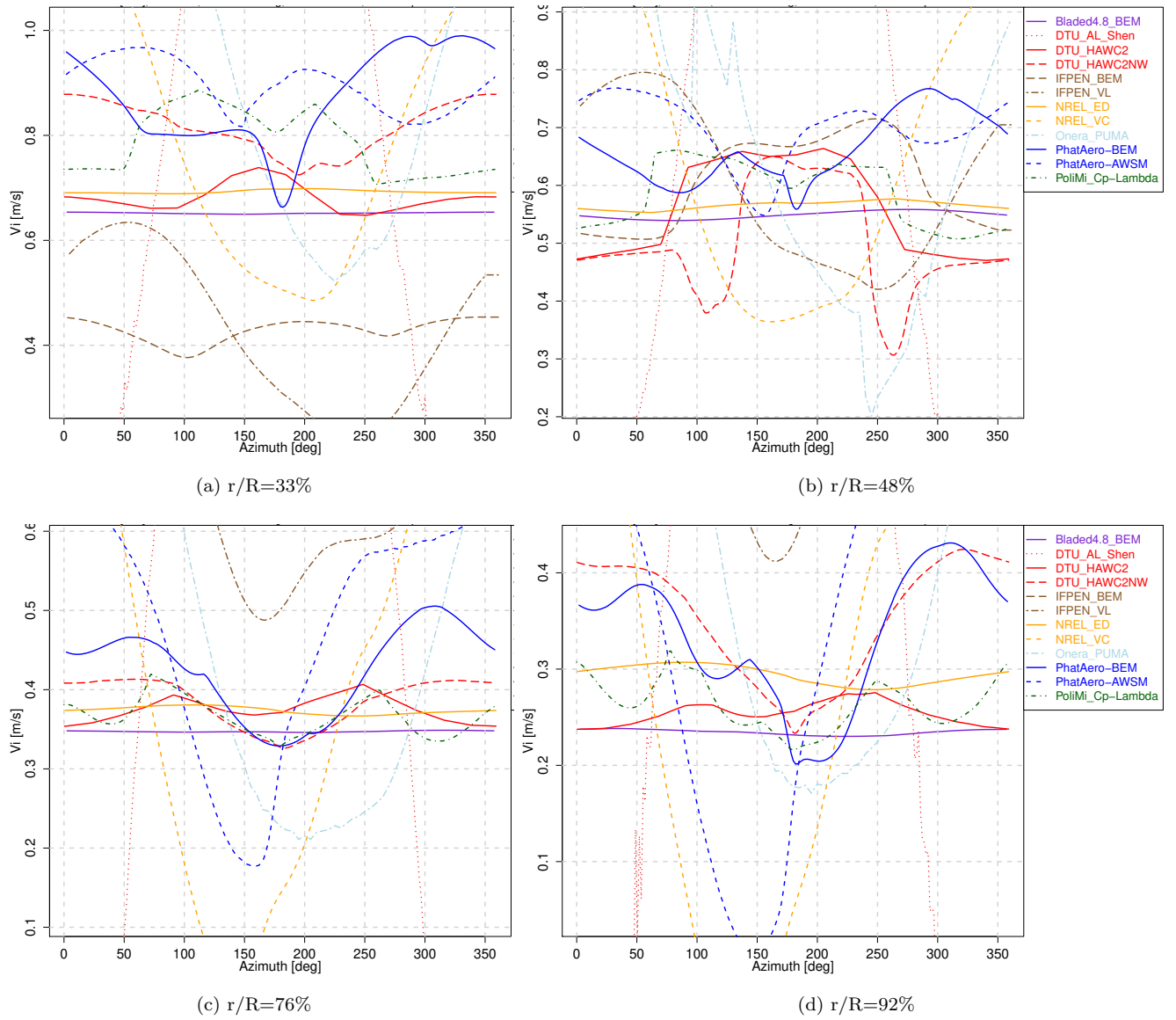


Figure E.3: Tangential induced velocity  $V_i$ , case 2.1

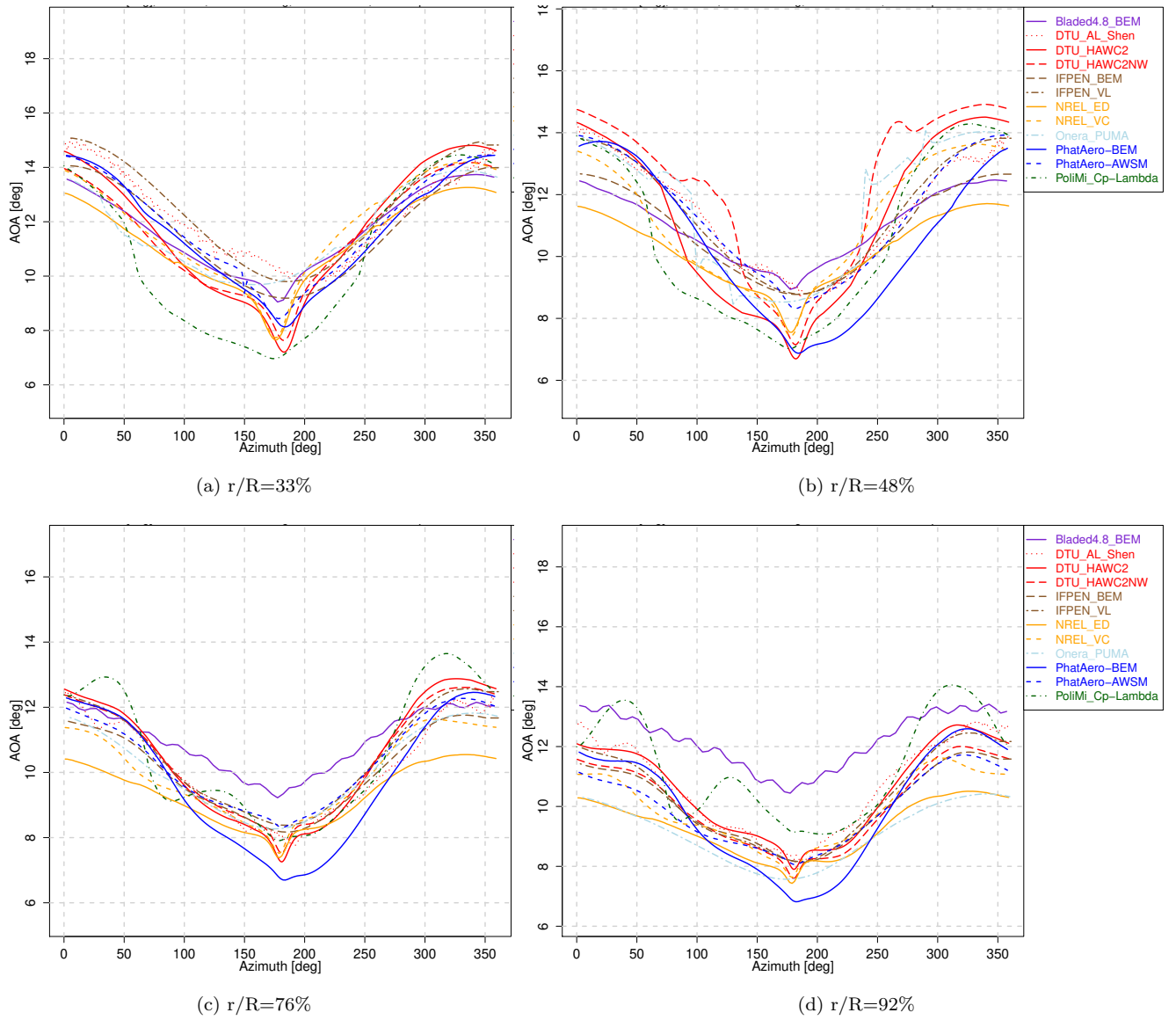


Figure E.4: Angle of attack AOA, case 2.1

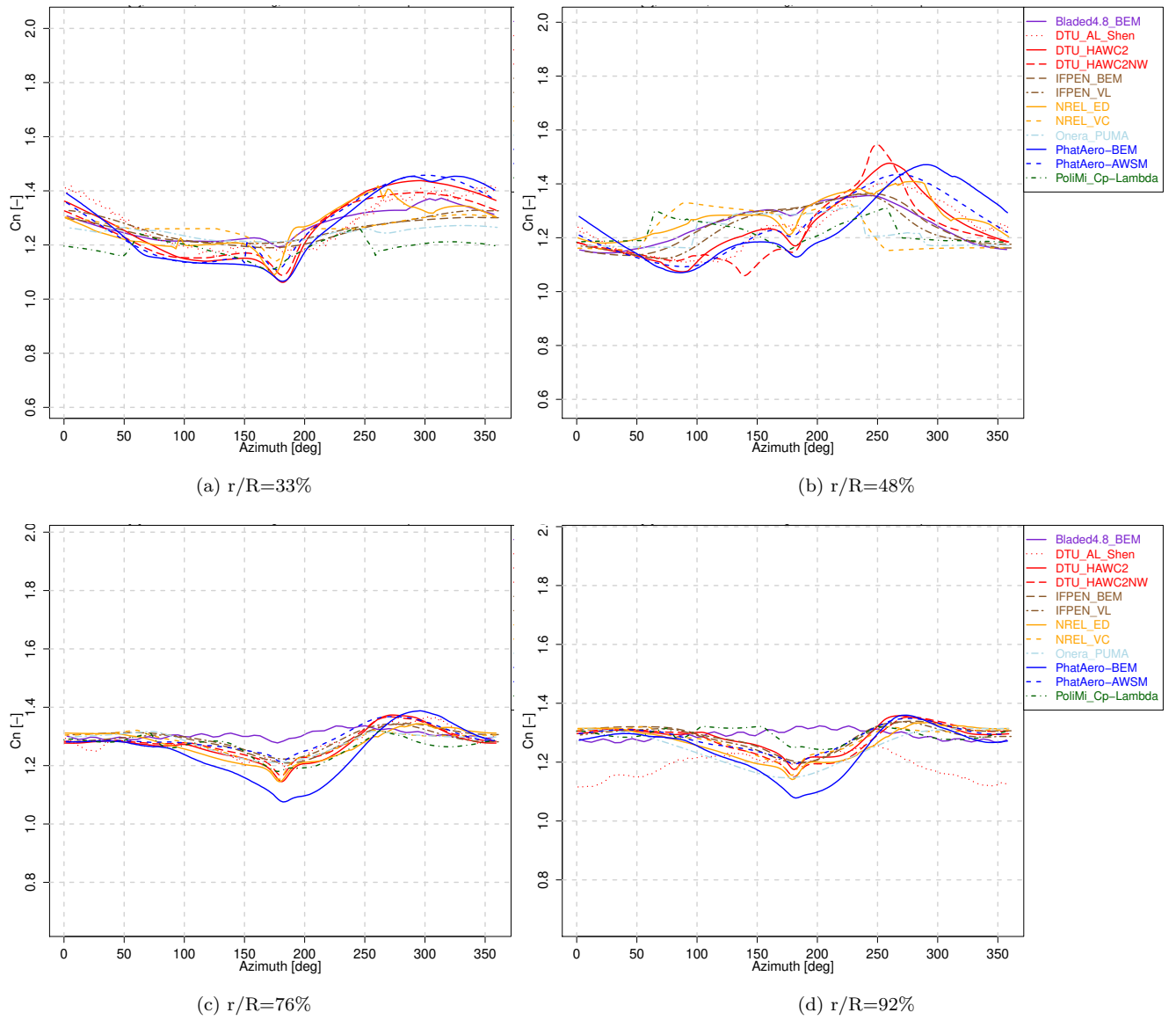


Figure E.5: Normal force coefficient  $C_n$ , case 2.1

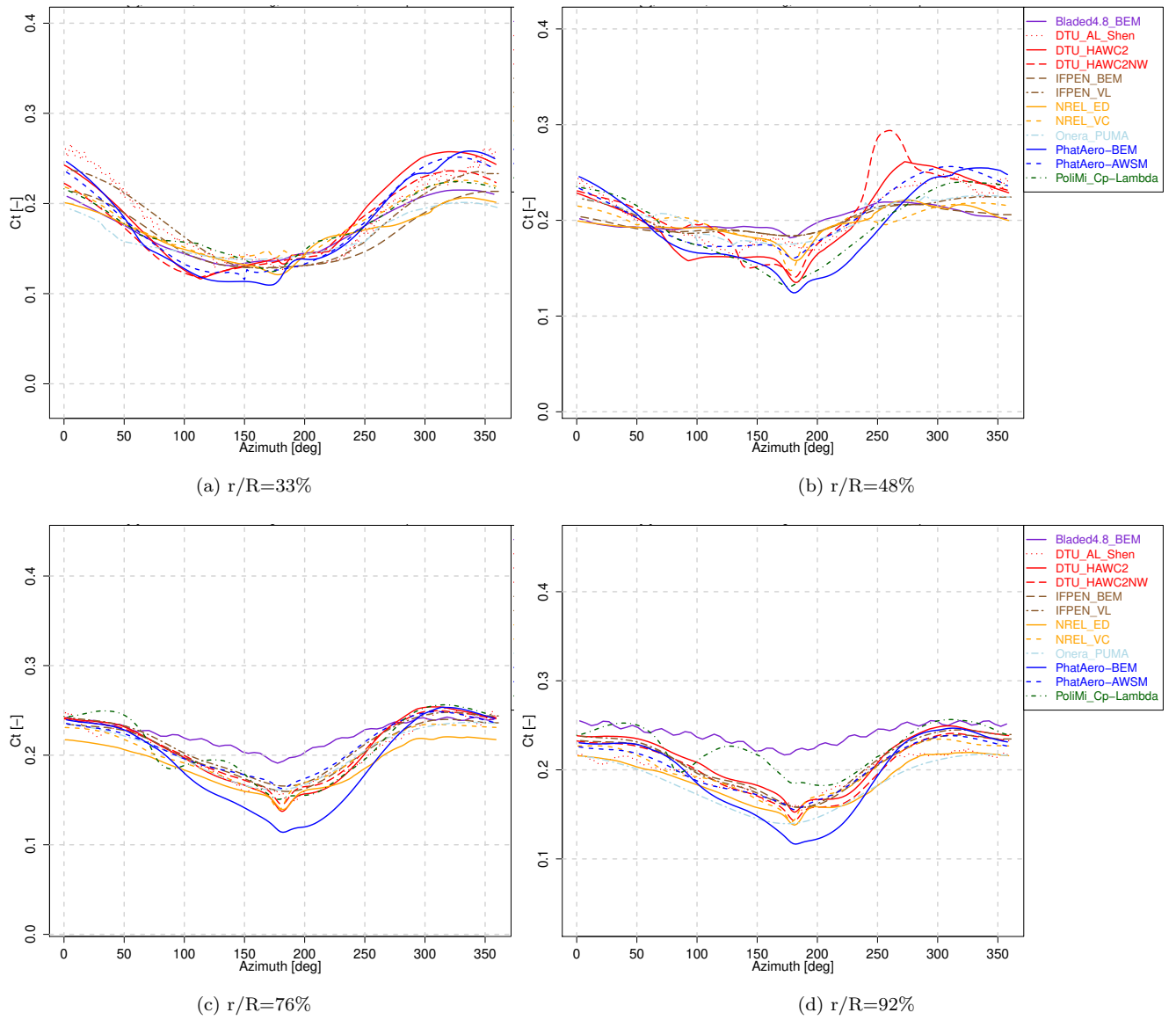
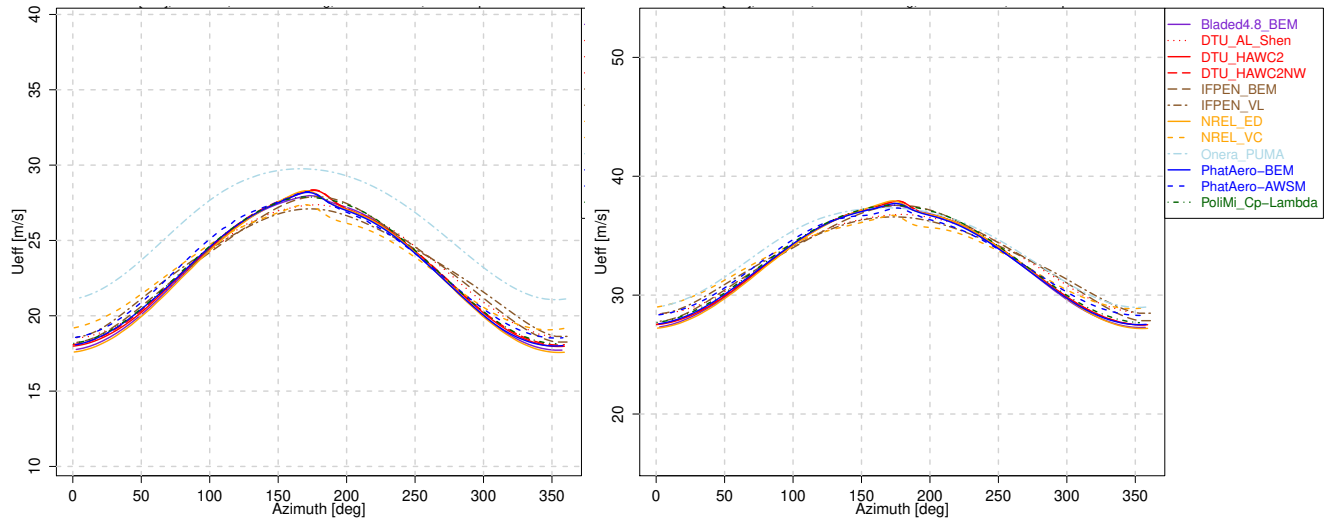
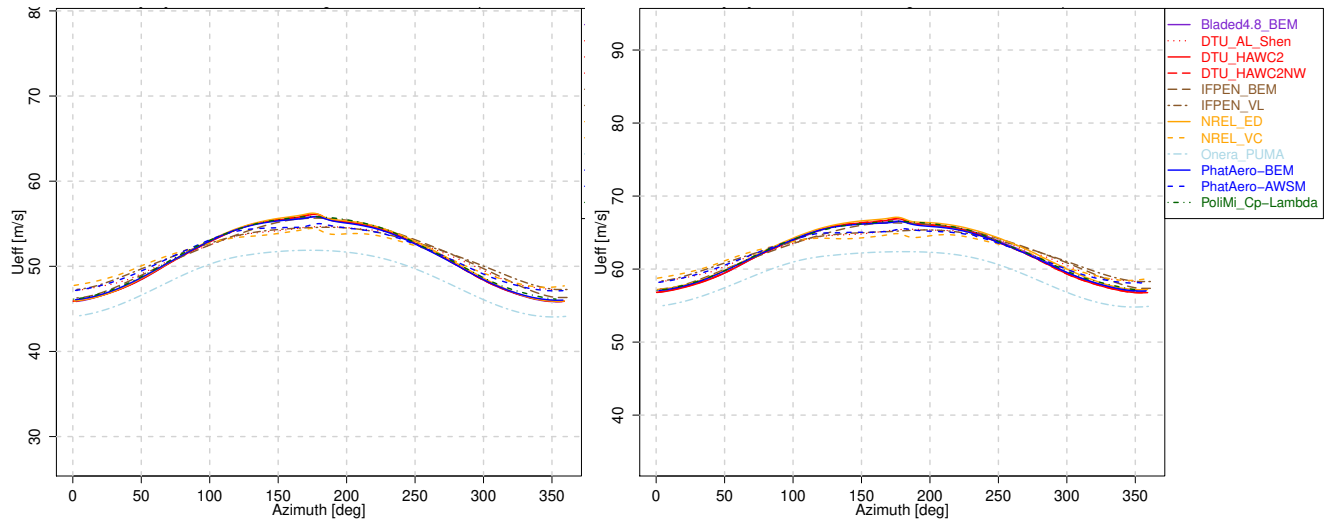


Figure E.6: Tangential force coefficient  $C_t$ , case 2.1



(a)  $r/R=33\%$

(b)  $r/R=48\%$



(c)  $r/R=76\%$

(d)  $r/R=92\%$

Figure E.7: Effective velocity  $U_{eff}$ , case 2.2



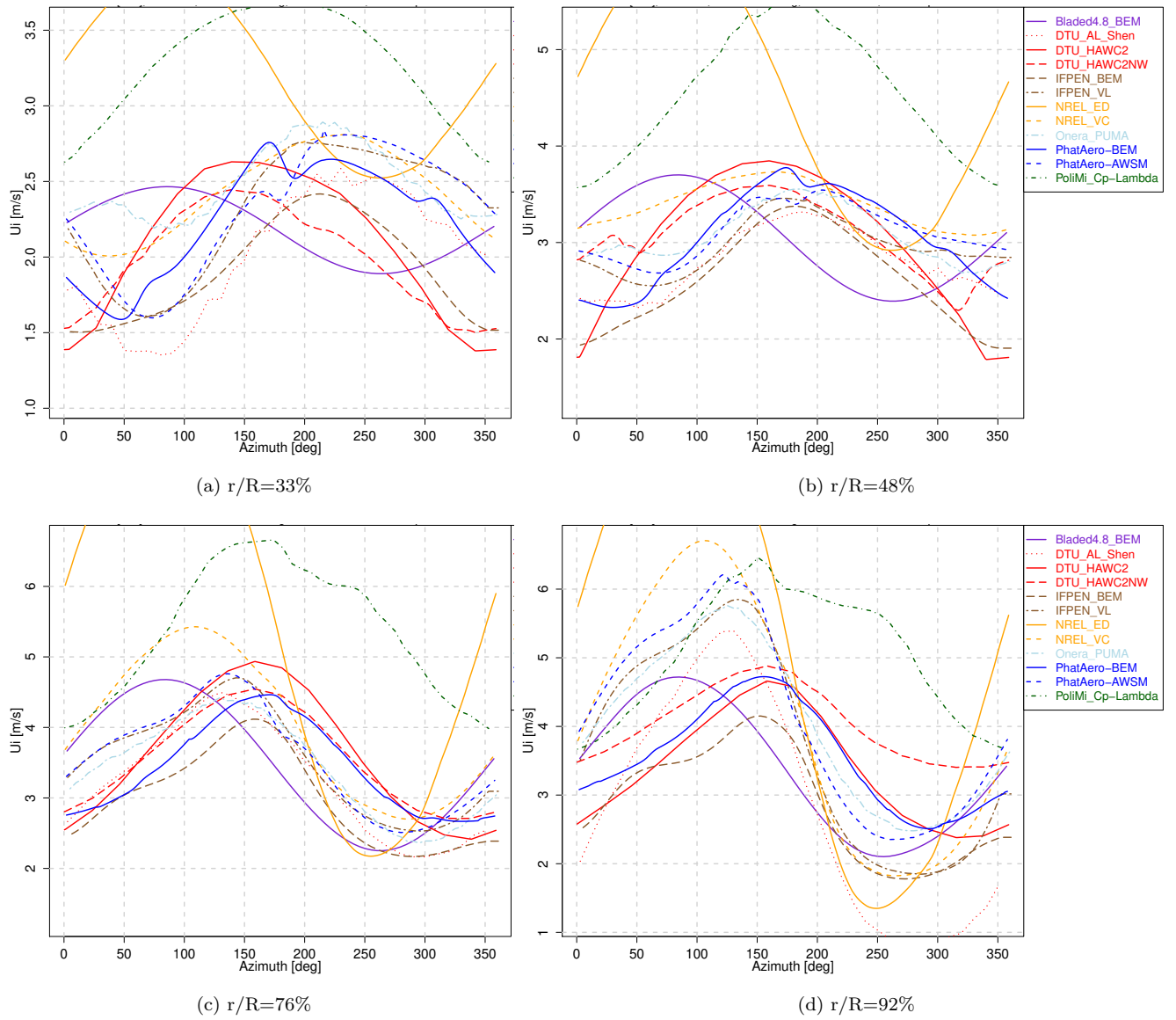


Figure E.8: Axial induced velocity  $U_i$ , case 2.2

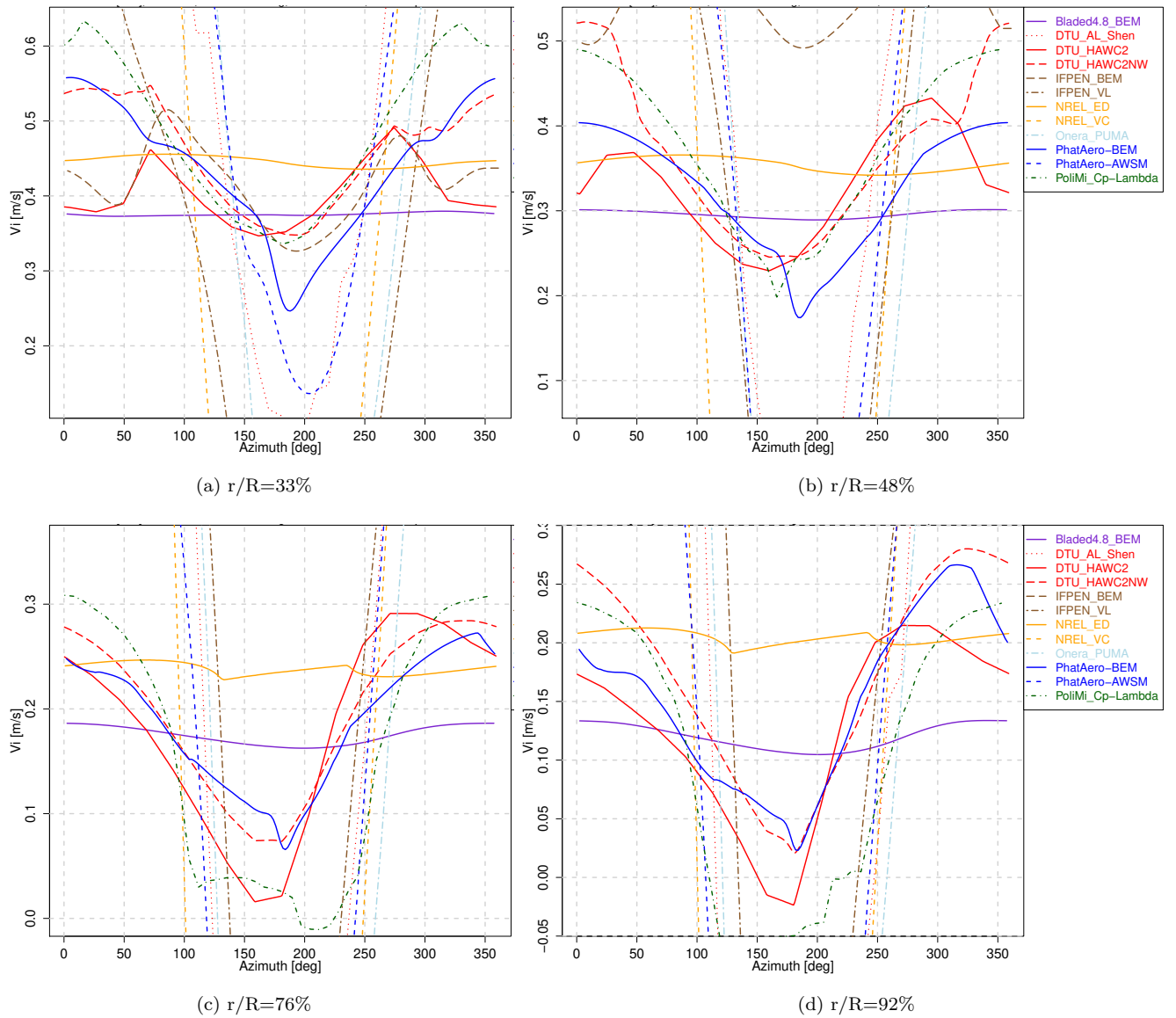


Figure E.9: Tangential induced velocity  $V_i$ , case 2.2

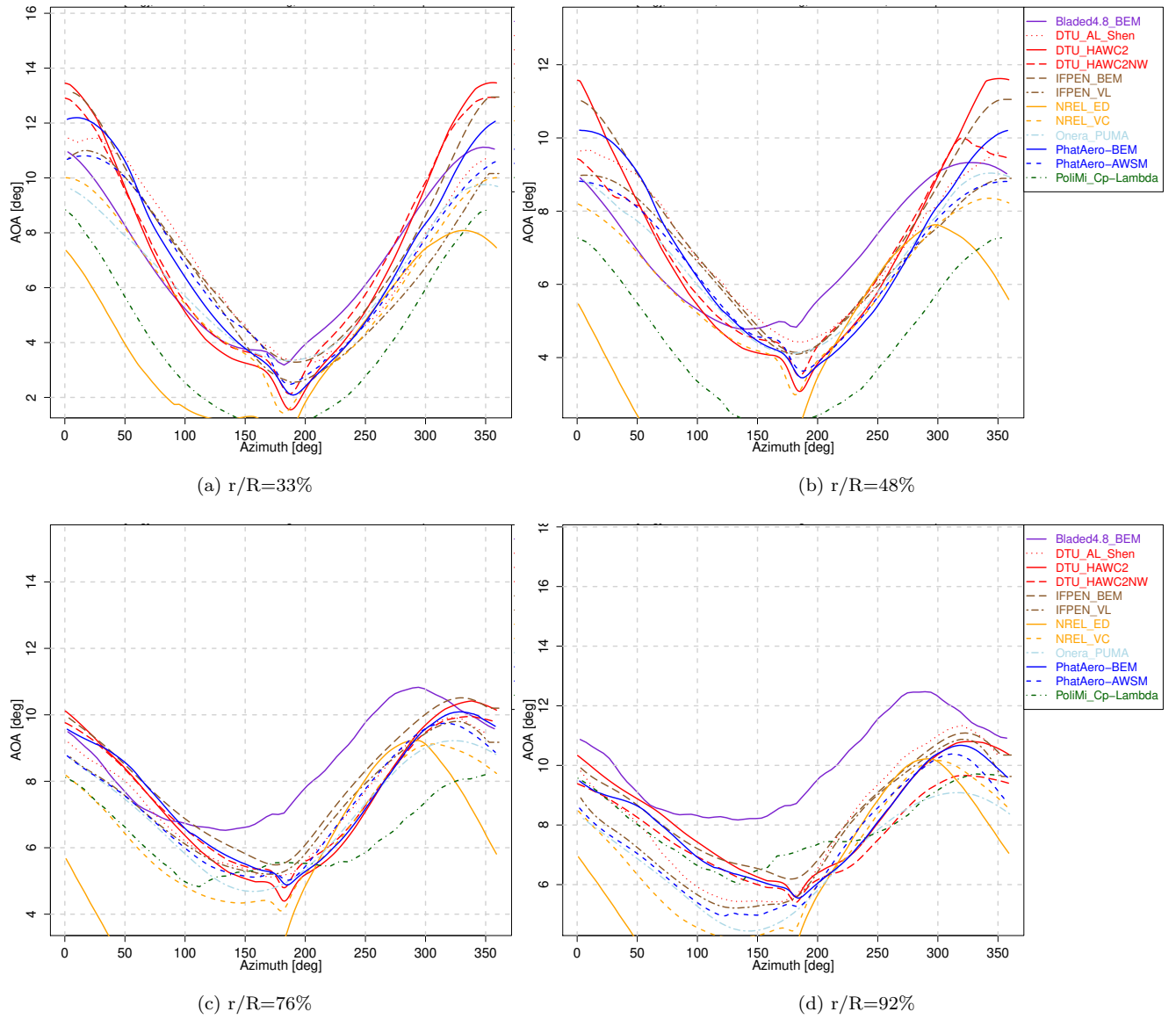


Figure E.10: Angle of attack AOA, case 2.2

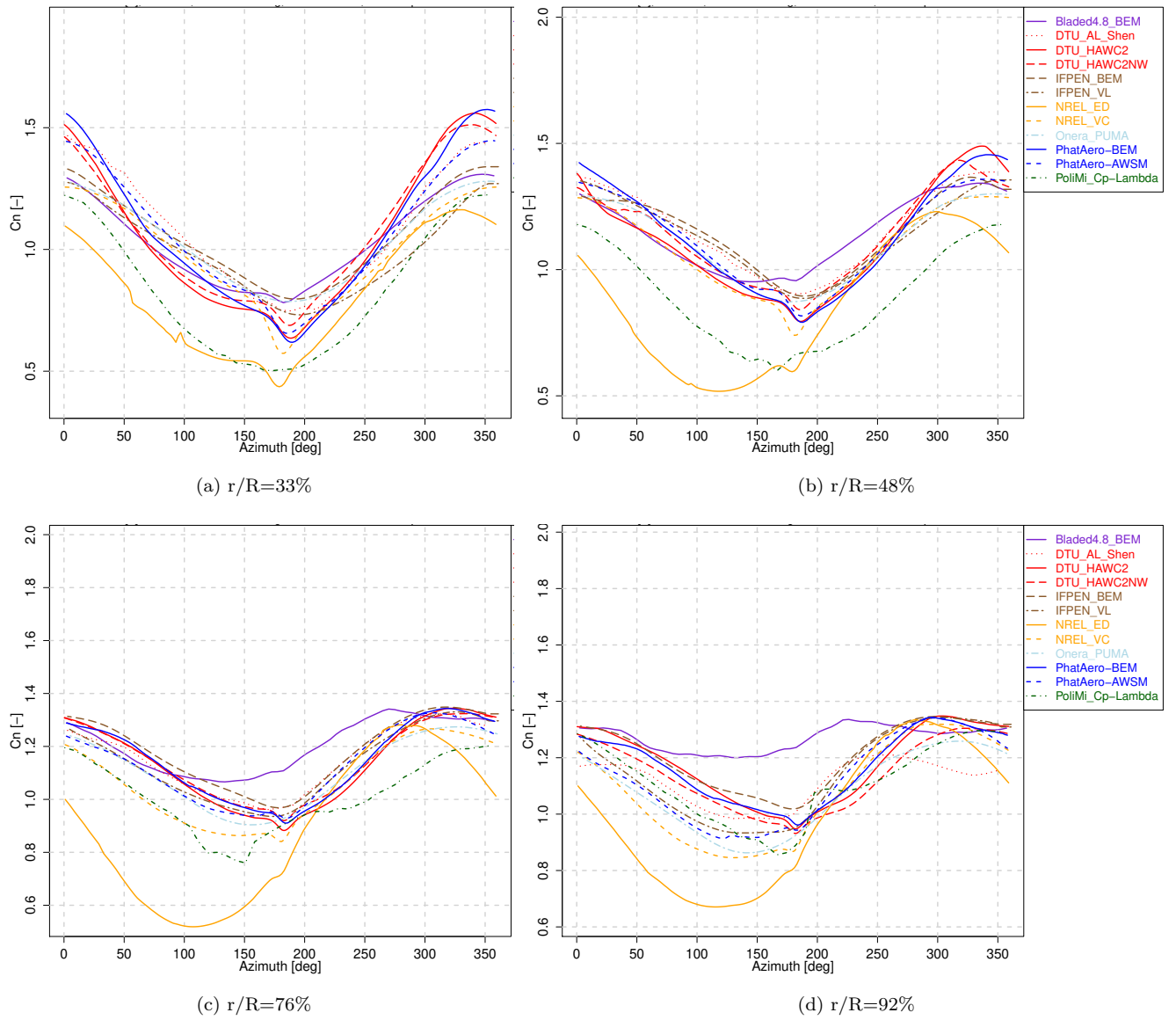


Figure E.11: Normal force coefficient  $C_n$ , case 2.2

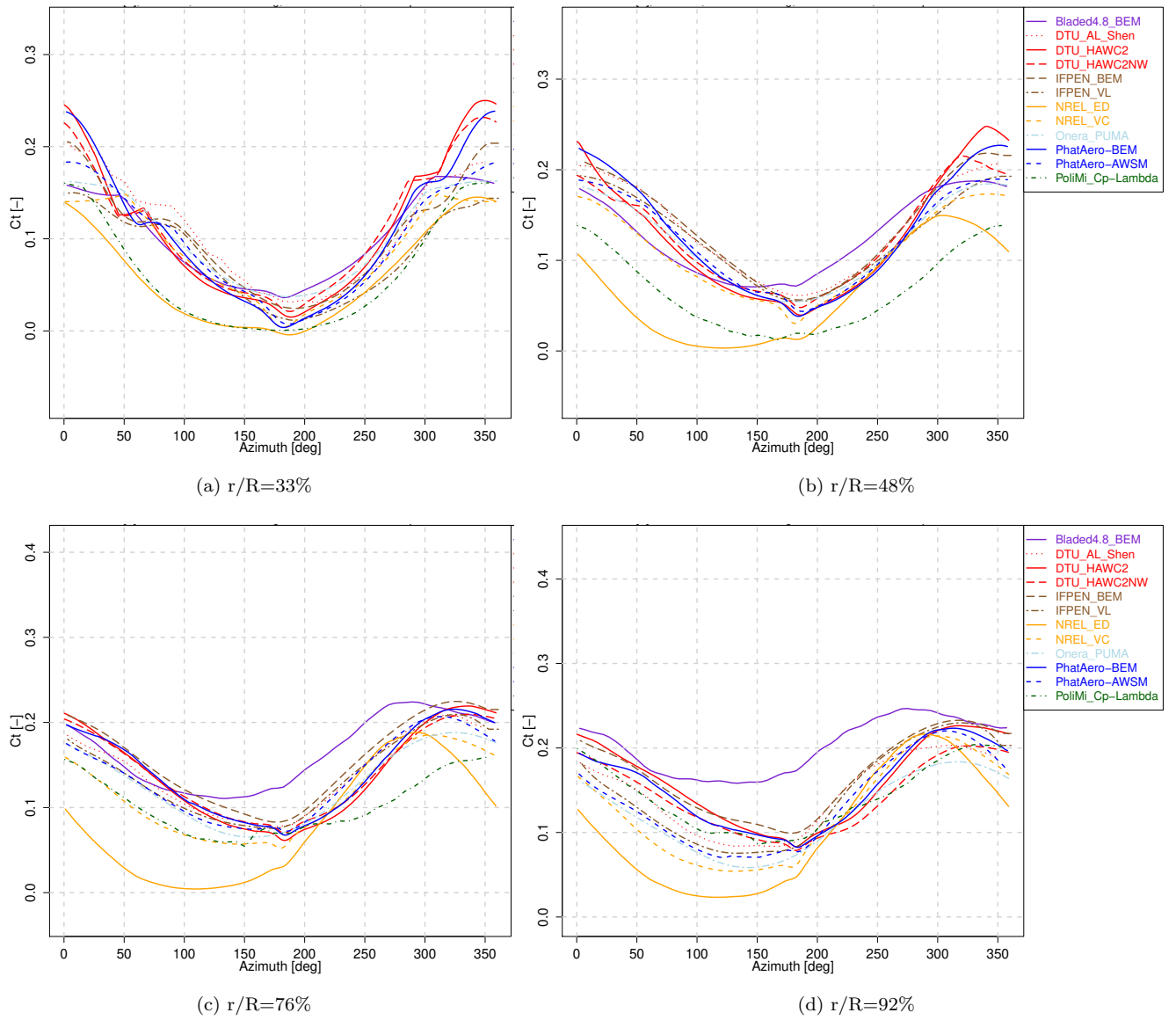


Figure E.12: Tangential force coefficient  $C_t$ , case 2.2



## E.1.2 Loads and performance

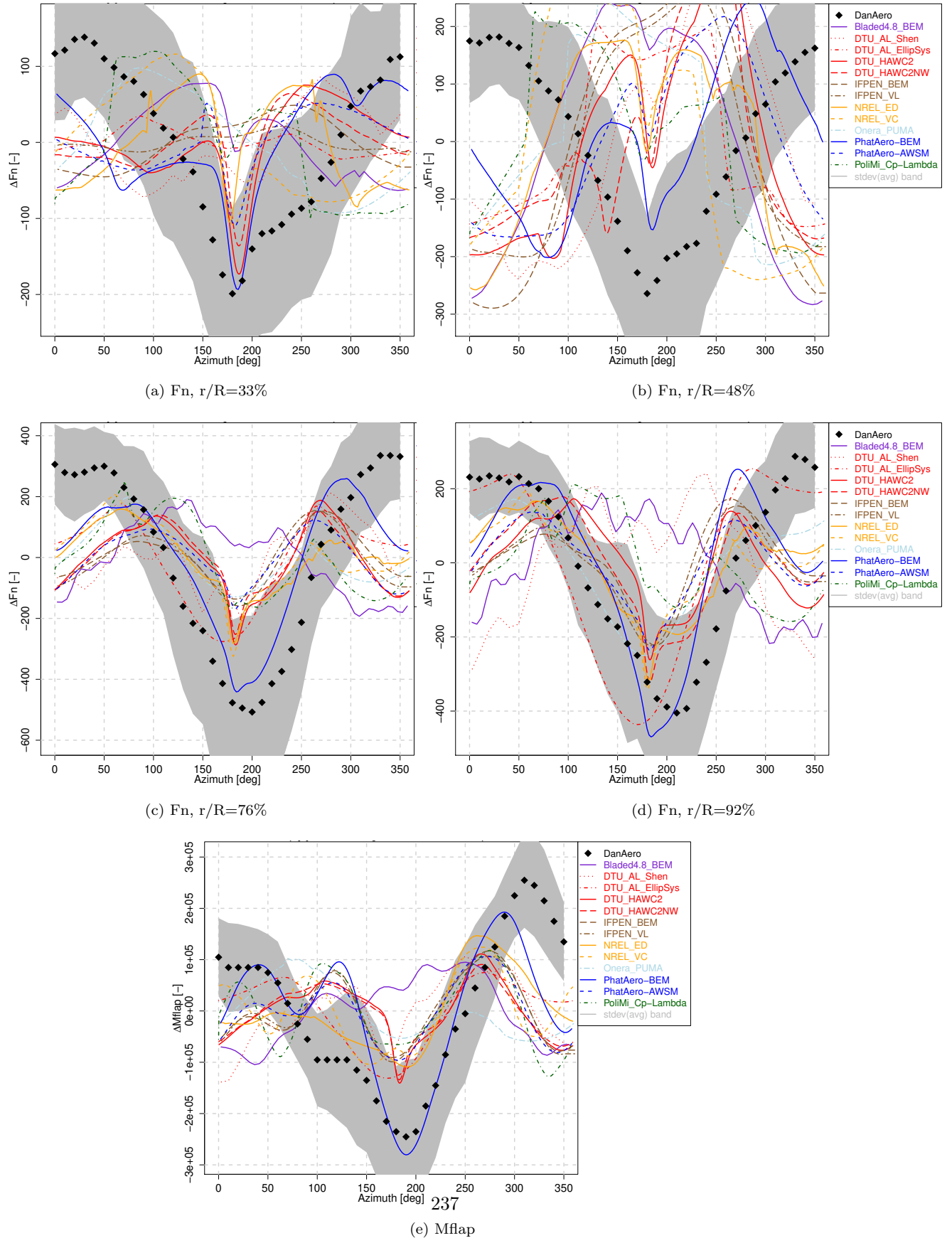


Figure E.13: Normal force  $F_n$  and flapwise moment  $M_{flap}$ , case 2.1

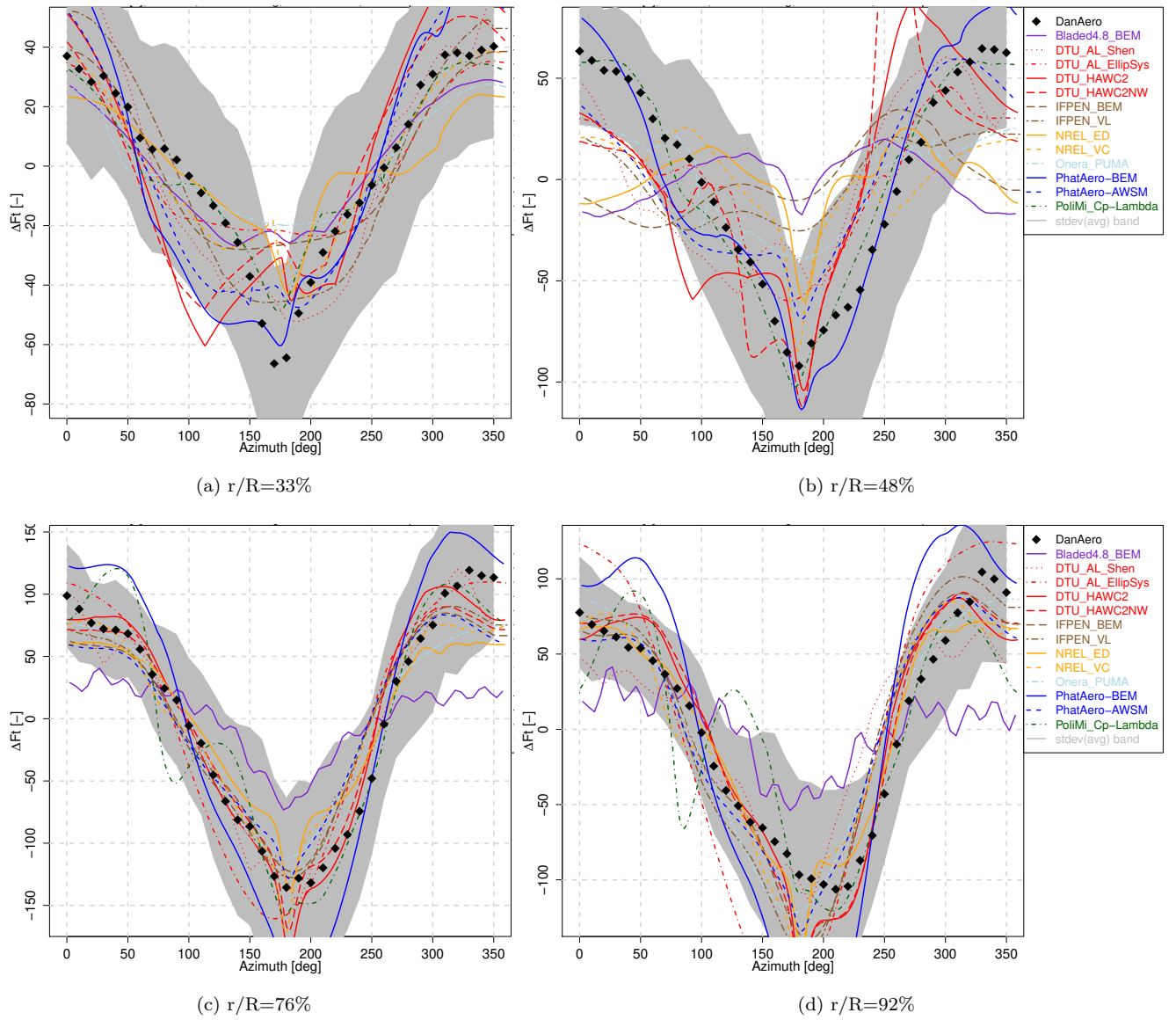
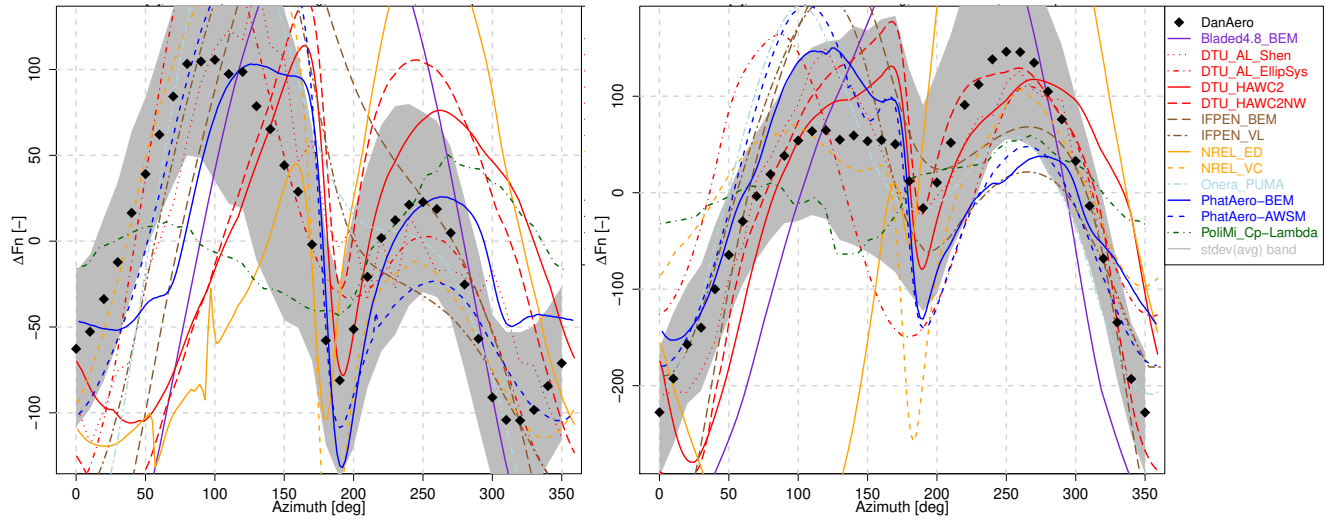


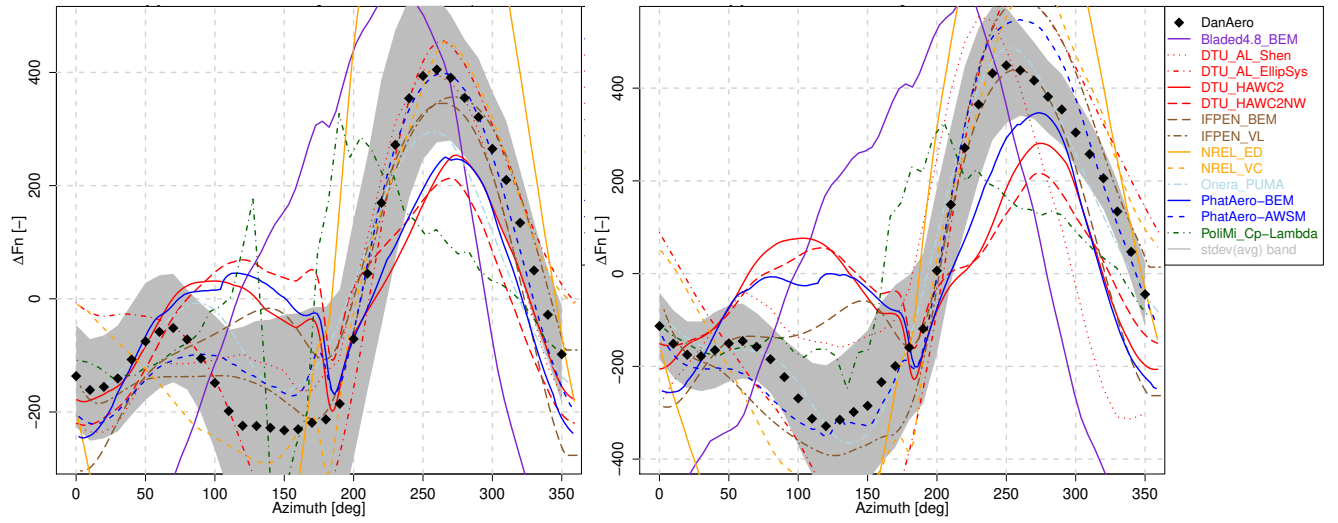
Figure E.14: Tangential force  $F_t$ , case 2.1





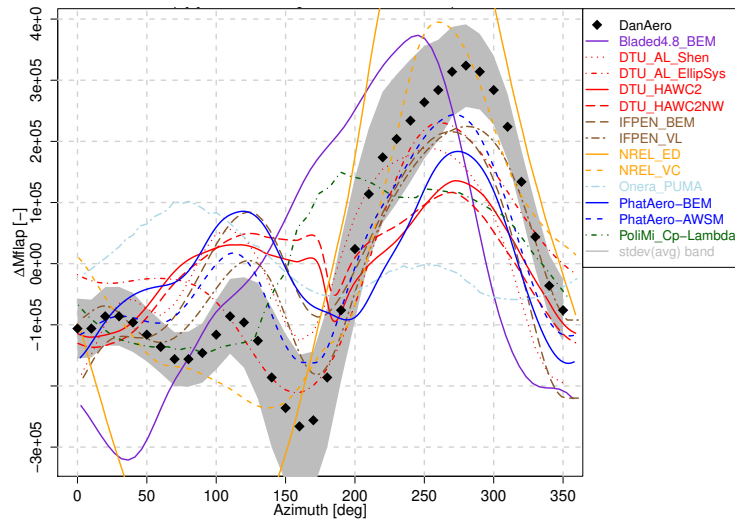
(a)  $F_n$ ,  $r/R=33\%$

(b)  $F_n$ ,  $r/R=48\%$



(c)  $F_n$ ,  $r/R=76\%$

(d)  $F_n$ ,  $r/R=92\%$



(e)  $M_{flap}$

Figure E.15: Normal force  $F_n$  and flapwise moment  $M_{flap}$ , case 2.2

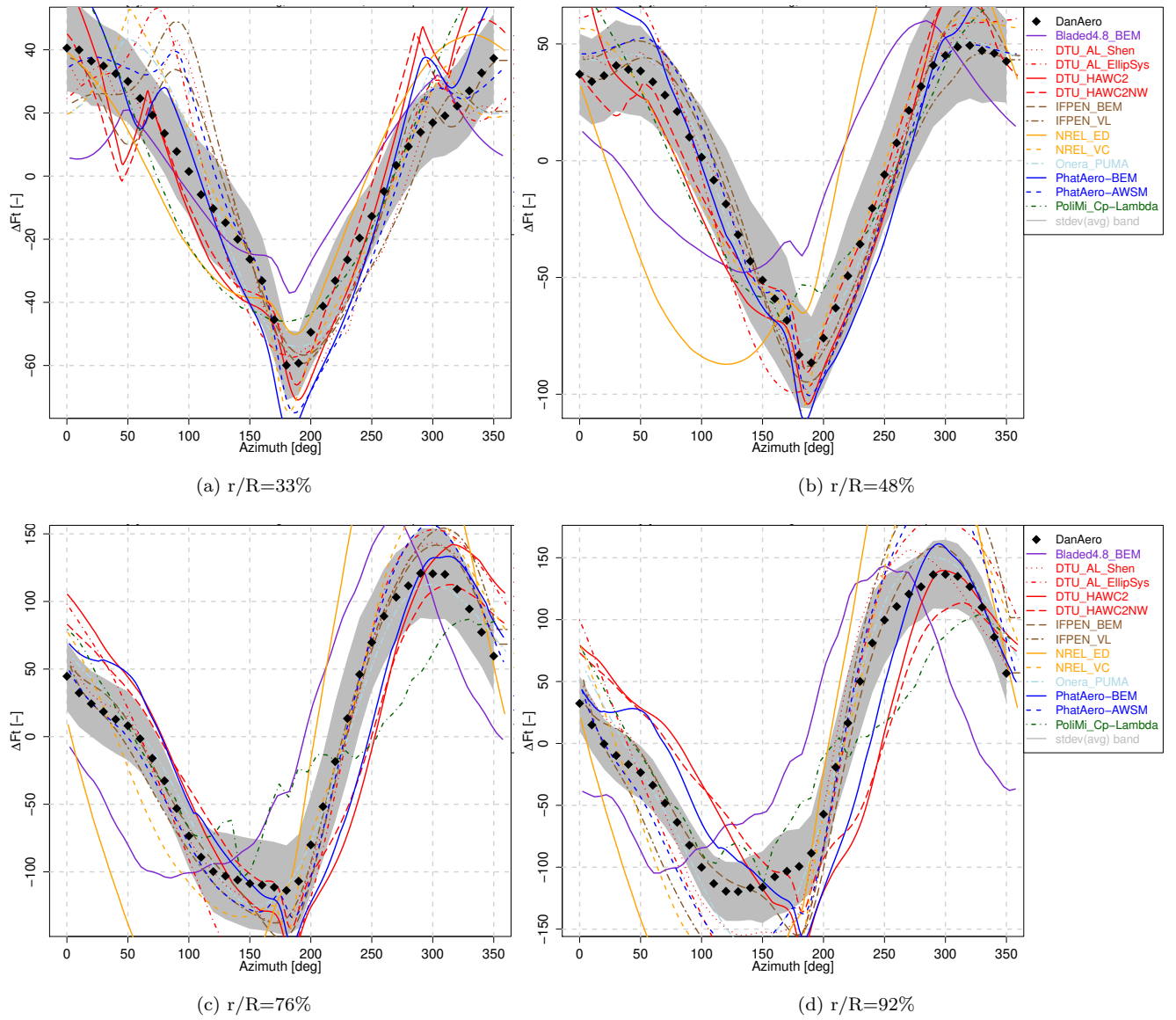


Figure E.16: Tangential force  $F_t$ , case 2.2

## E.2 CFD and panel codes

## E.2.1 Pressure distributions

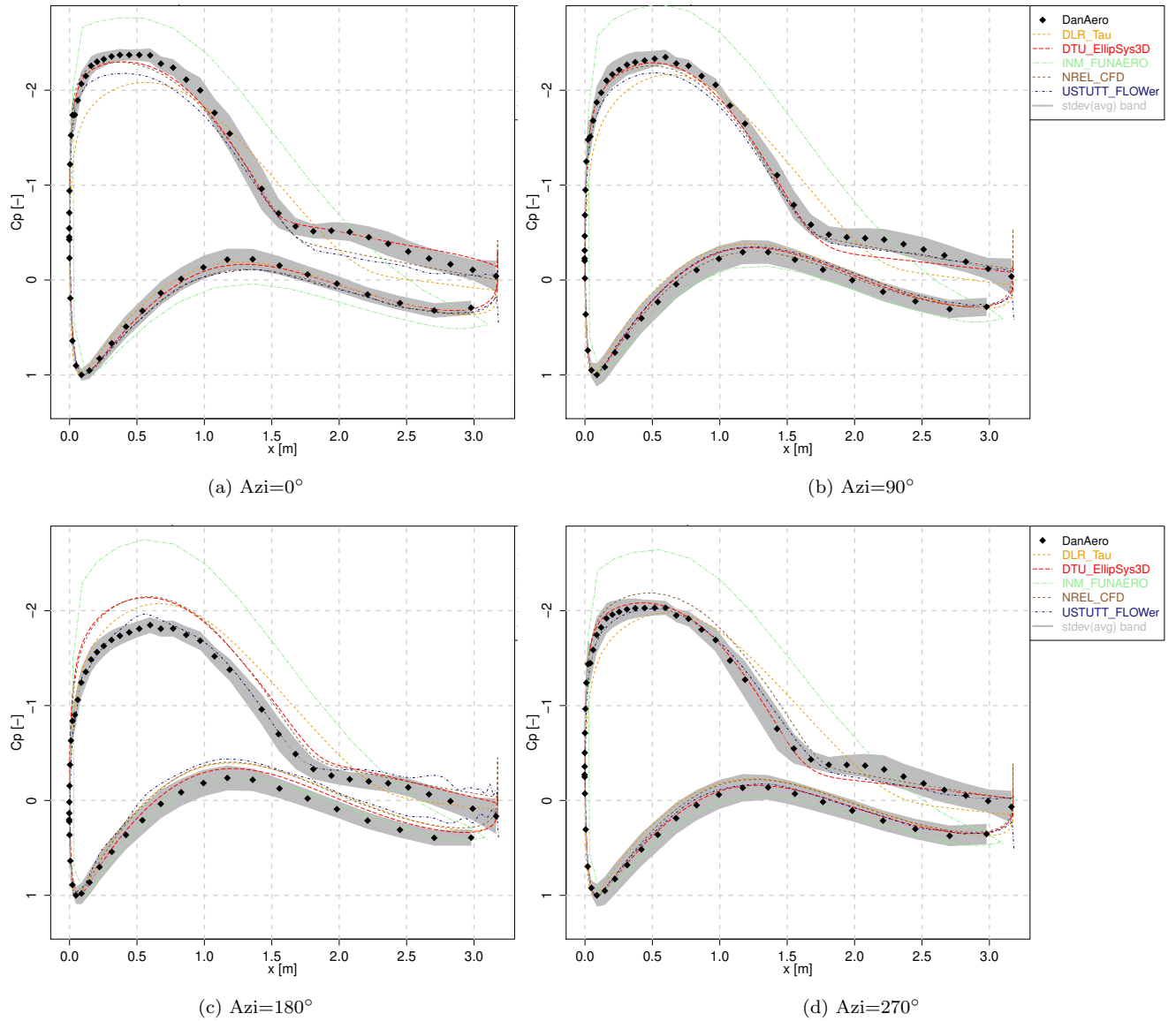
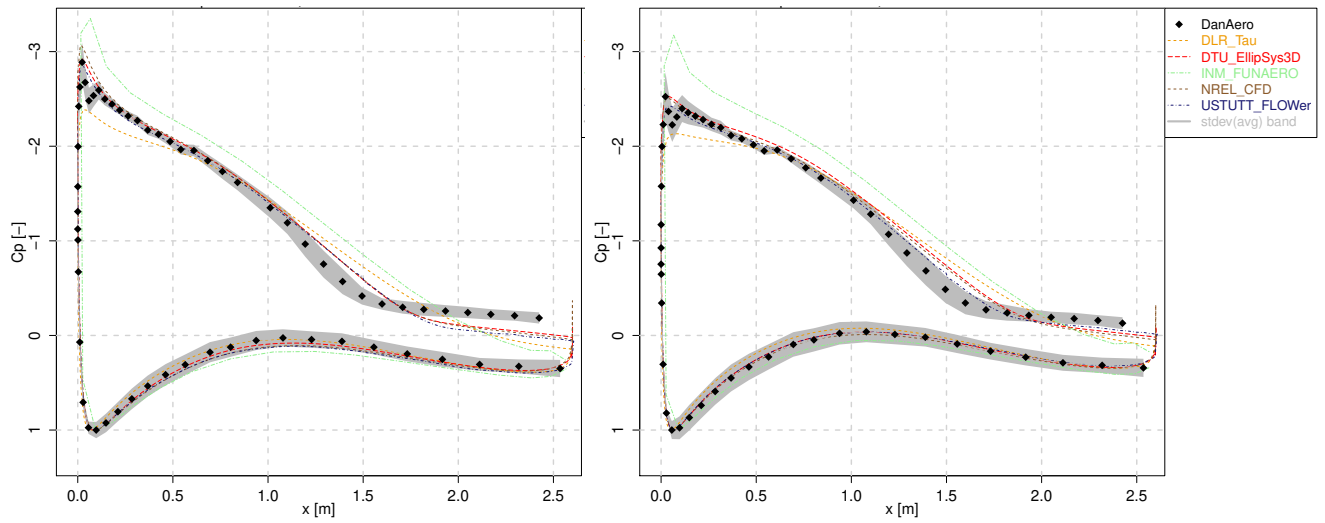
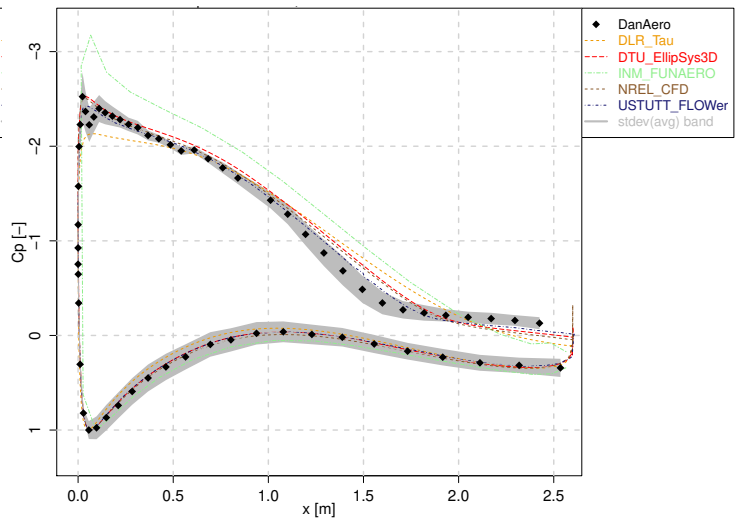


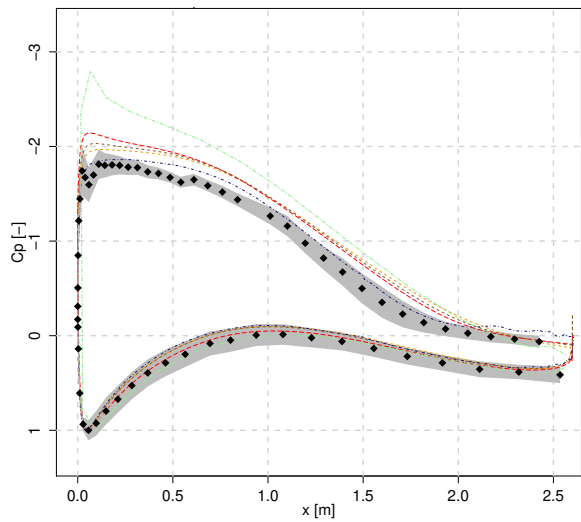
Figure E.17: Pressure distribution variation at  $r/R=33\%$ , case 2.1



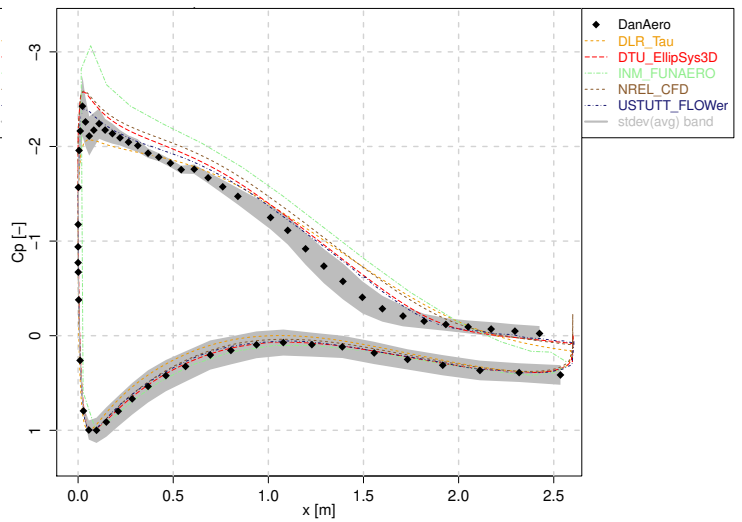
(a)  $Azi=0^\circ$



(b)  $Azi=90^\circ$



(c)  $Azi=180^\circ$



(d)  $Azi=270^\circ$

Figure E.18: Pressure distribution variation at  $r/R=48\%$ , case 2.1

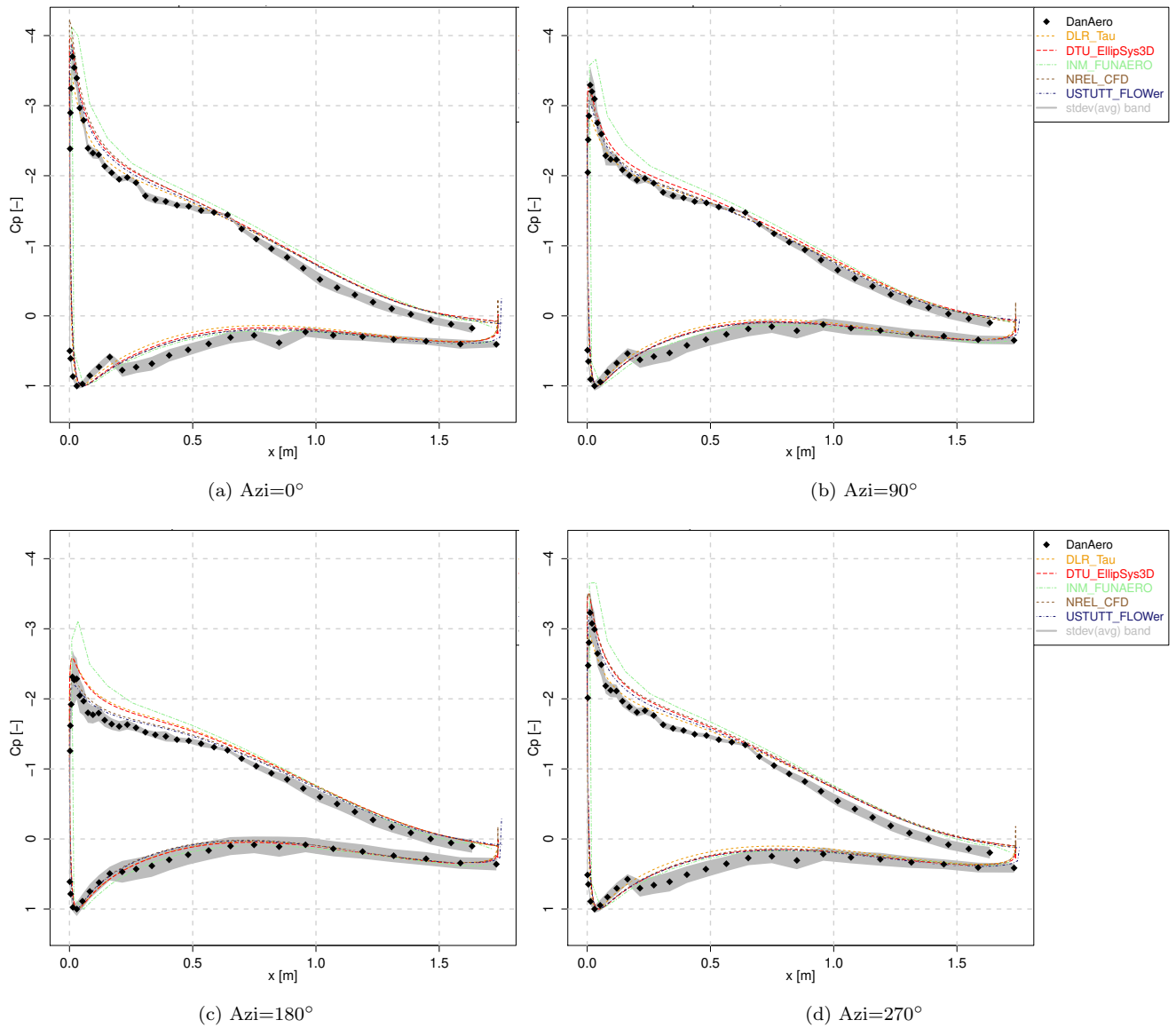
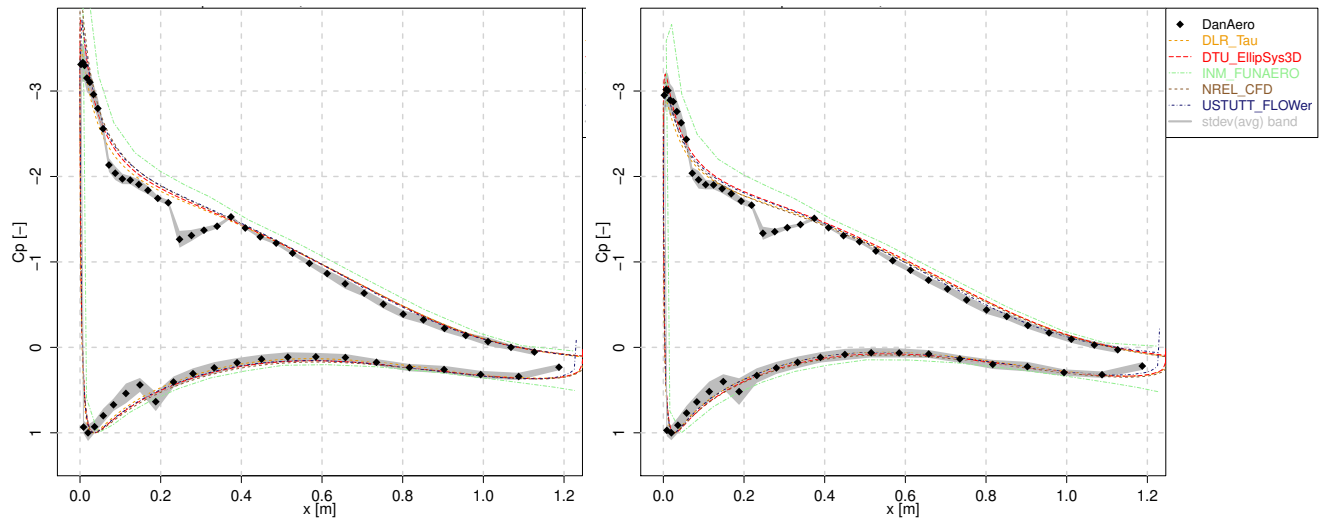
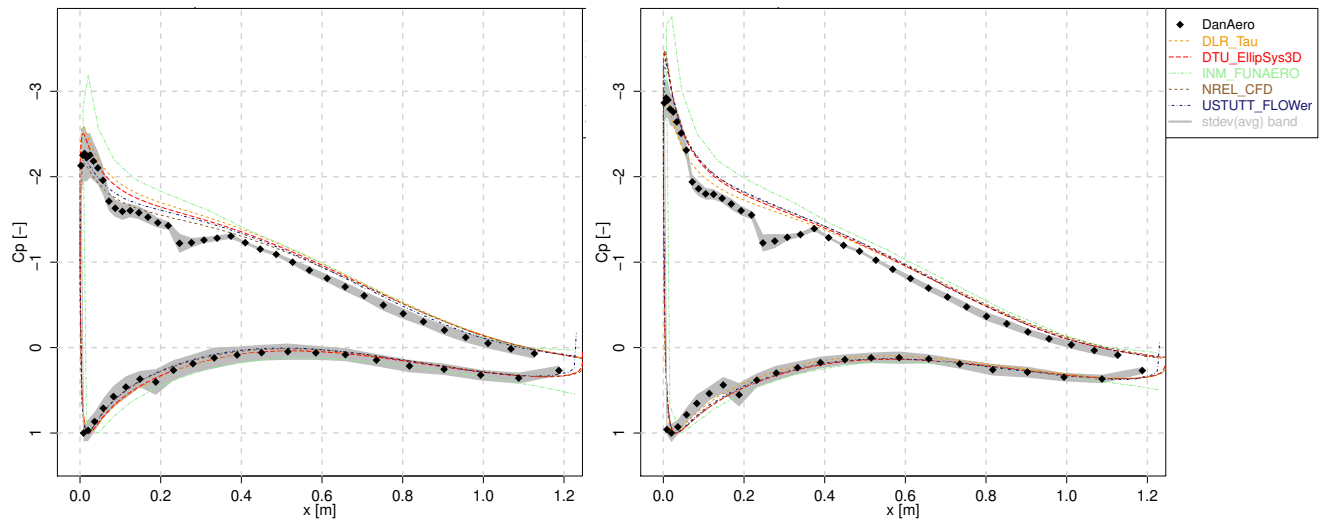


Figure E.19: Pressure distribution variation at  $r/R=76\%$ , case 2.1



(a)  $Azi=0^\circ$

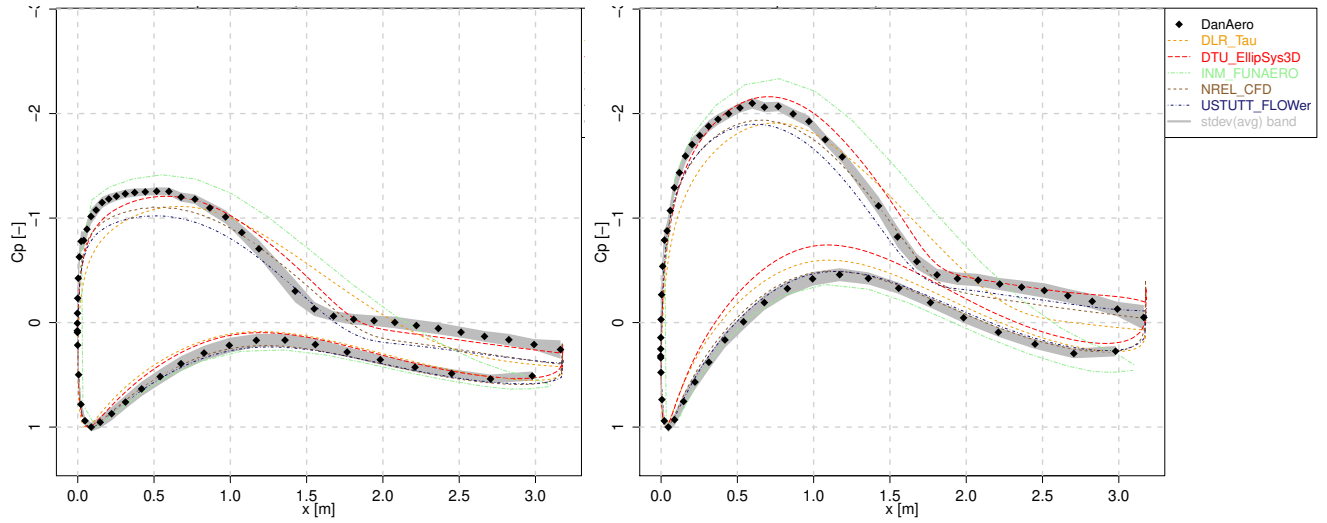
(b)  $Azi=90^\circ$



(c)  $Azi=180^\circ$

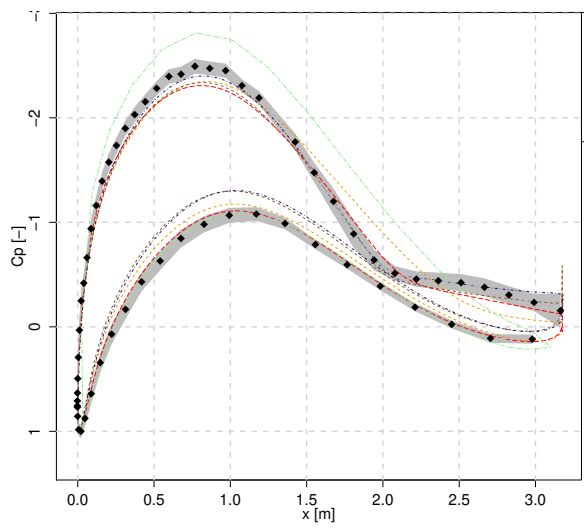
(d)  $Azi=270^\circ$

Figure E.20: Pressure distribution variation at  $r/R=92\%$ , case 2.1

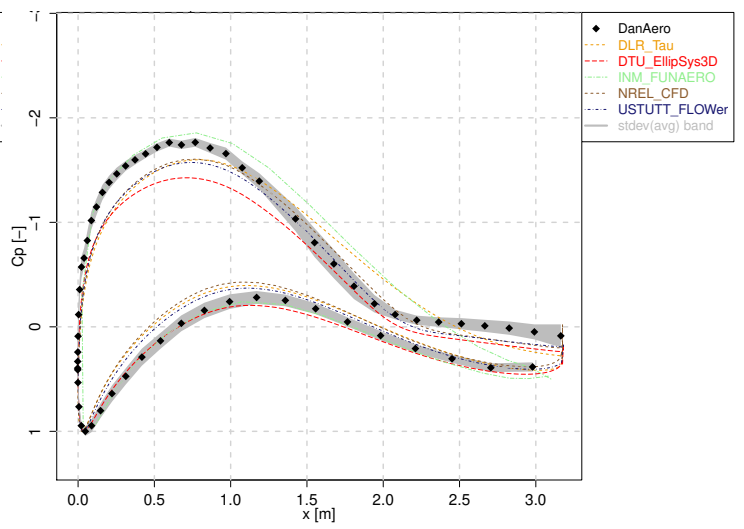


(a)  $Azi=0^\circ$

(b)  $Azi=90^\circ$



(c)  $Azi=180^\circ$



(d)  $Azi=270^\circ$

Figure E.21: Pressure distribution variation at  $r/R=33\%$ , case 2.2



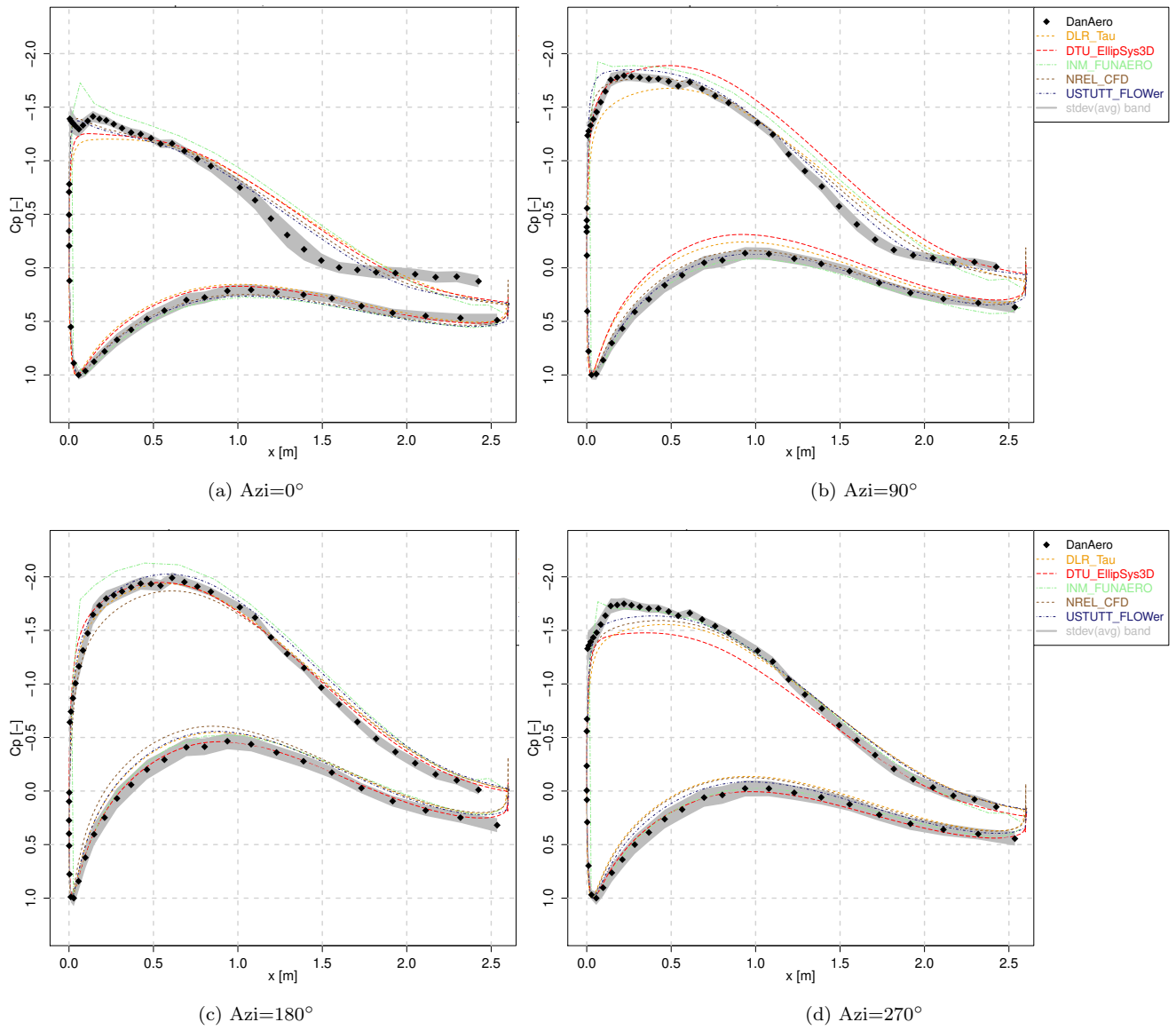


Figure E.22: Pressure distribution variation at  $r/R=48\%$ , case 2.2

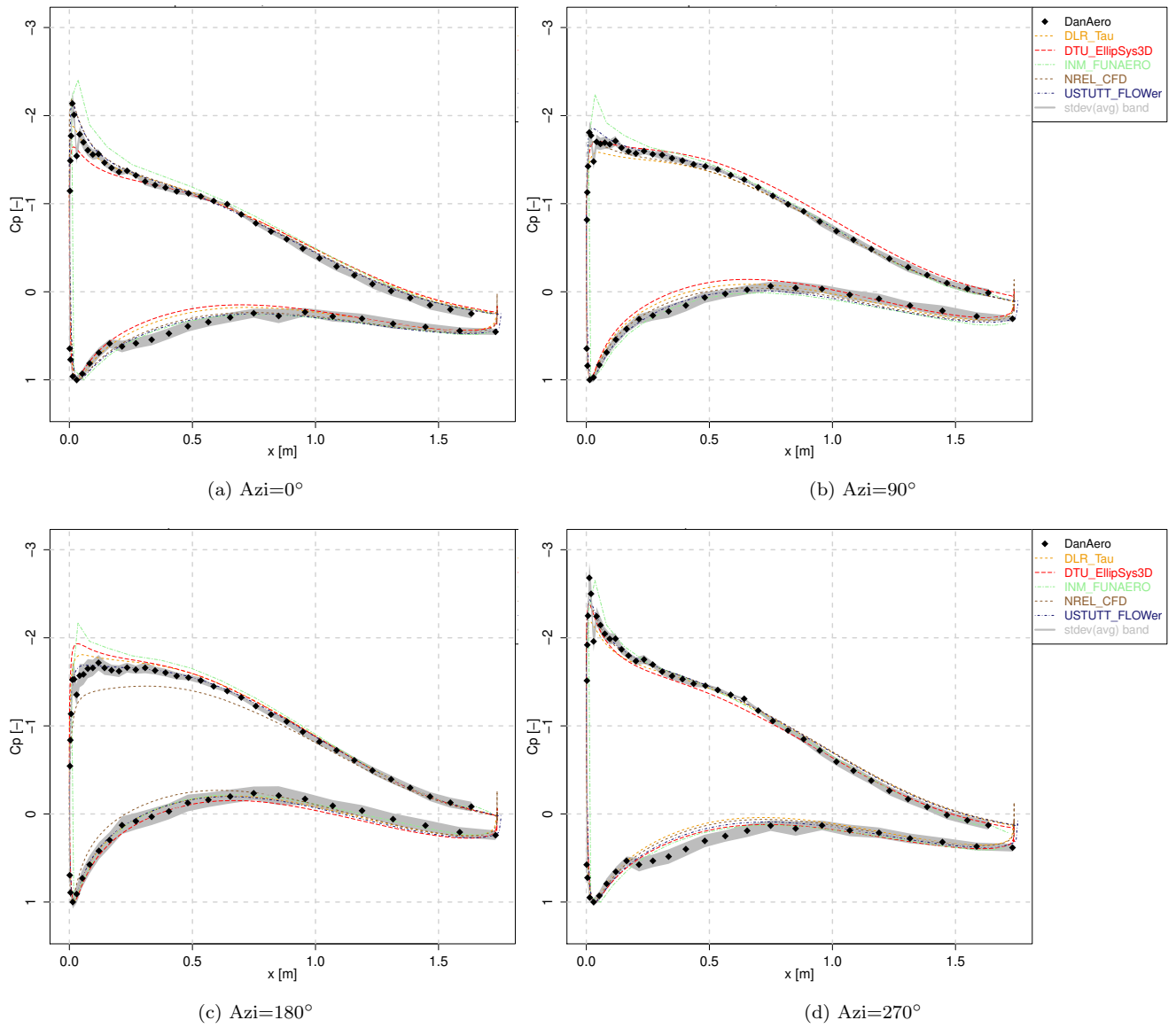
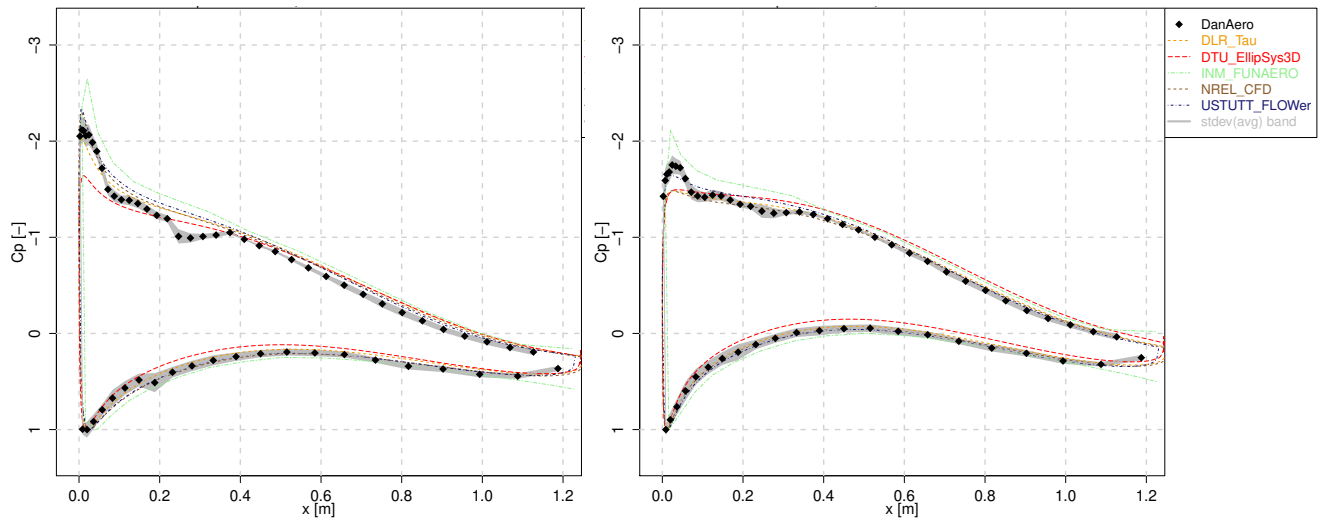
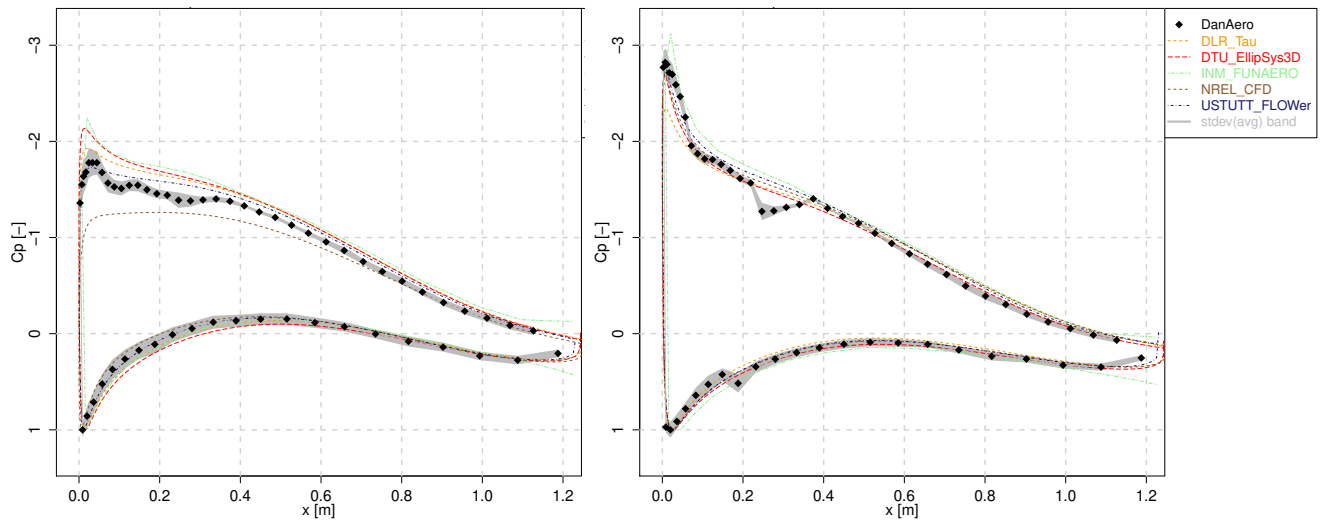


Figure E.23: Pressure distribution variation at  $r/R=76\%$ , case 2.2



(a)  $Azi=0^\circ$

(b)  $Azi=90^\circ$



(c)  $Azi=180^\circ$

(d)  $Azi=270^\circ$

Figure E.24: Pressure distribution variation at  $r/R=92\%$ , case 2.2



## E.2.2 Loads and performance

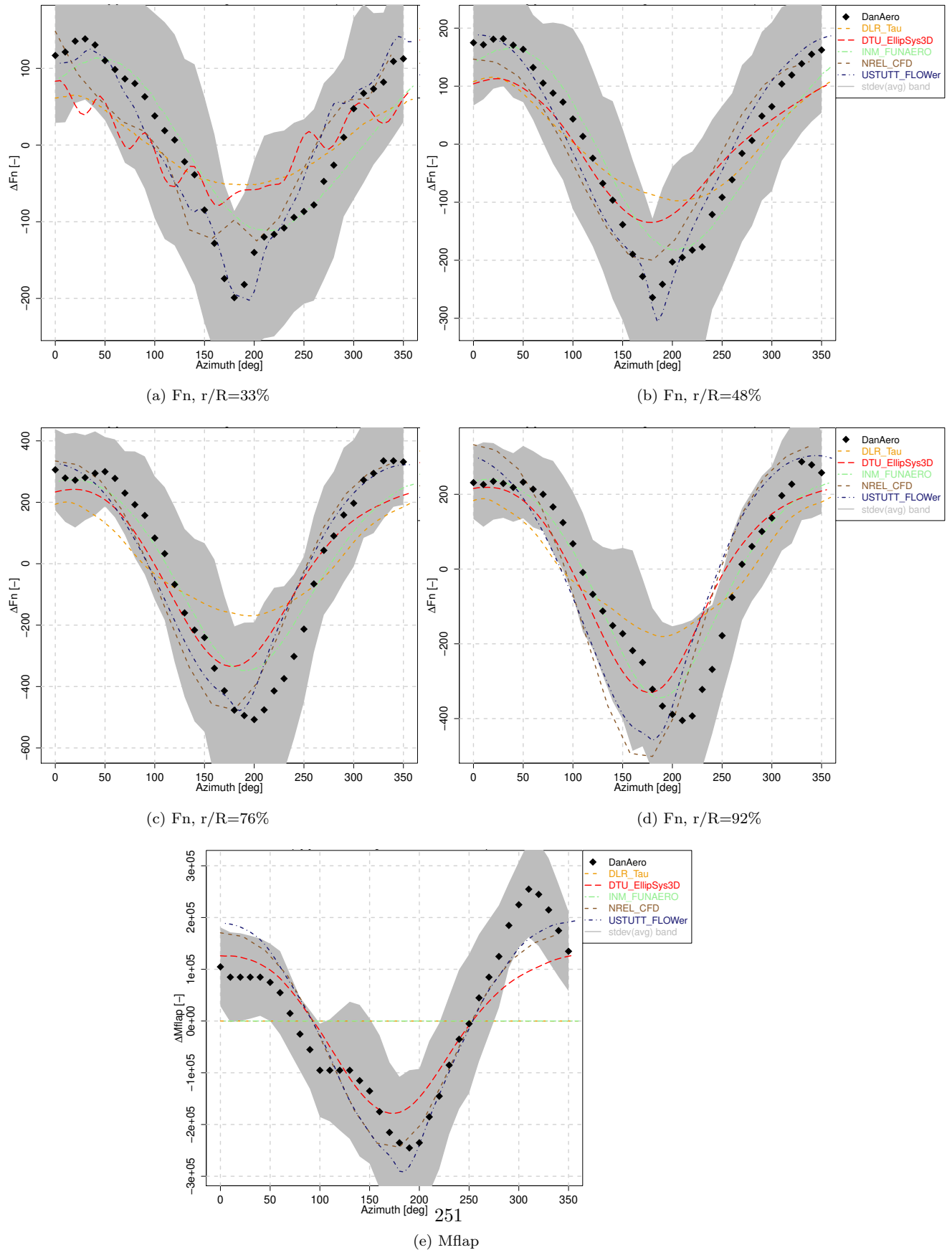


Figure E.25: Normal force  $F_n$  and flapwise moment  $M_{flap}$ , case 2.1

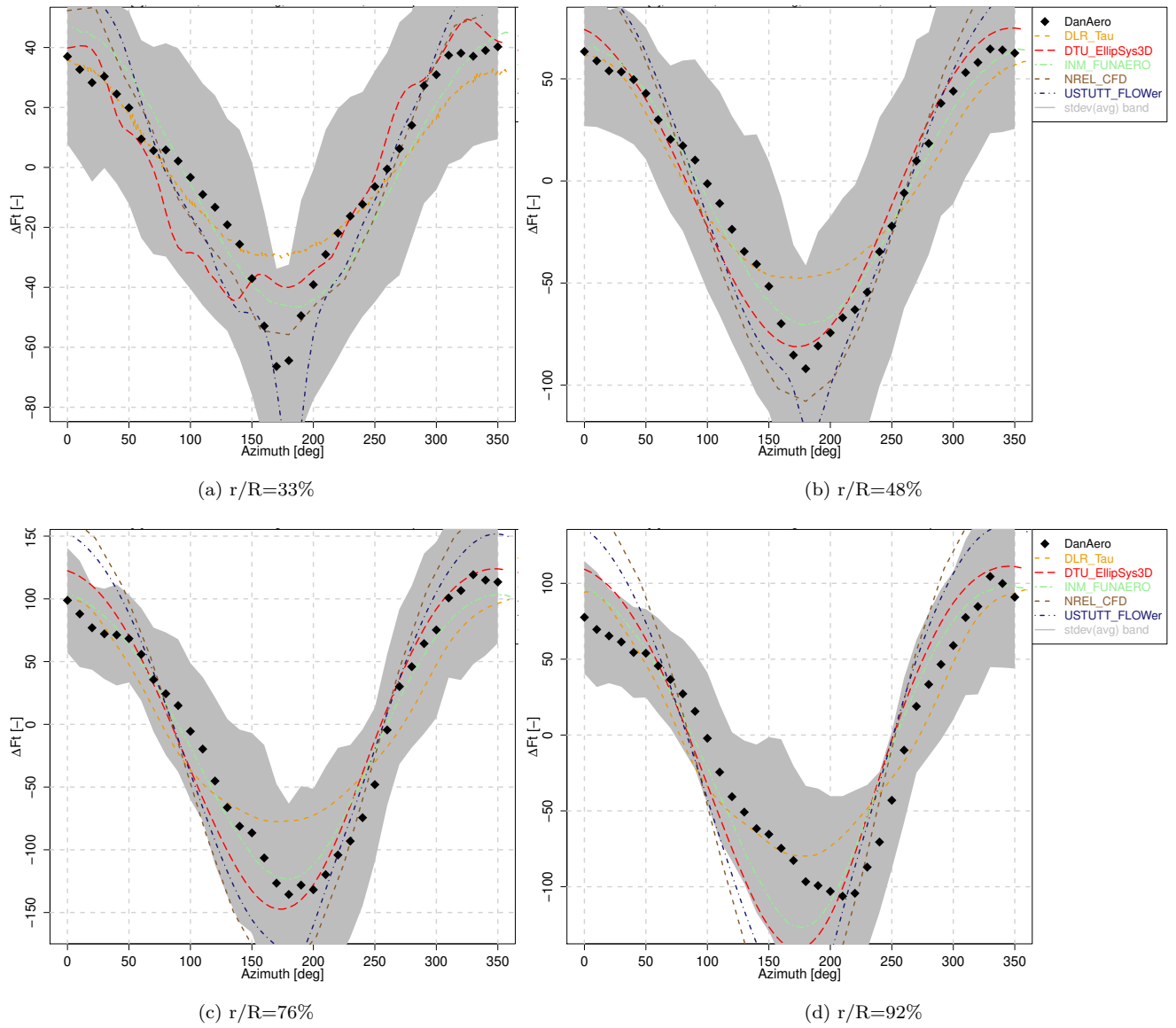
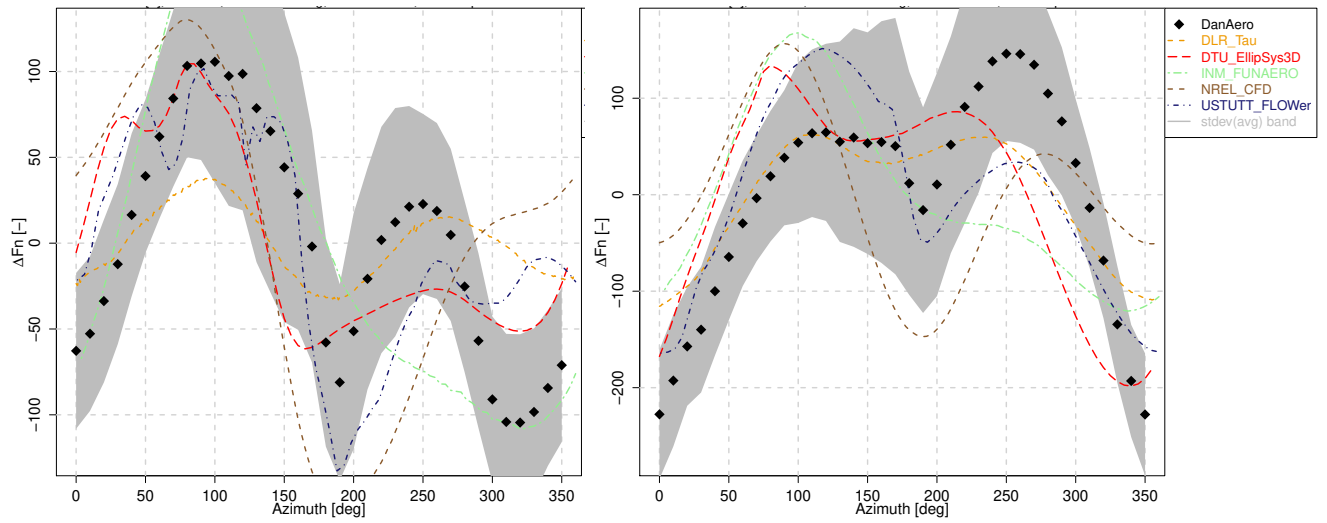
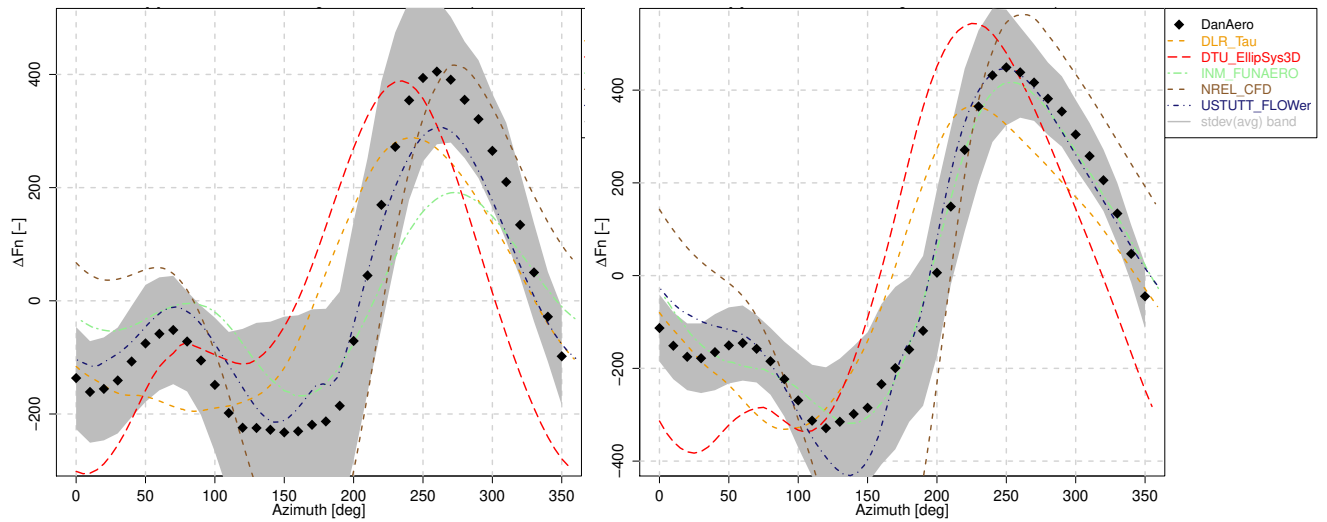


Figure E.26: Tangential force  $F_t$ , case 2.1



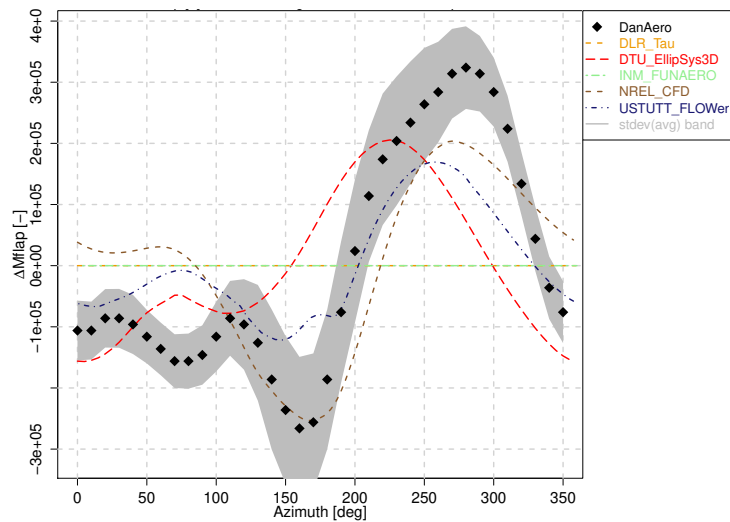
(a)  $F_n$ ,  $r/R=33\%$

(b)  $F_n$ ,  $r/R=48\%$



(c)  $F_n$ ,  $r/R=76\%$

(d)  $F_n$ ,  $r/R=92\%$



(e)  $M_{flap}$

Figure E.27: Normal force  $F_n$  and flapwise moment  $M_{flap}$ , case 2.2

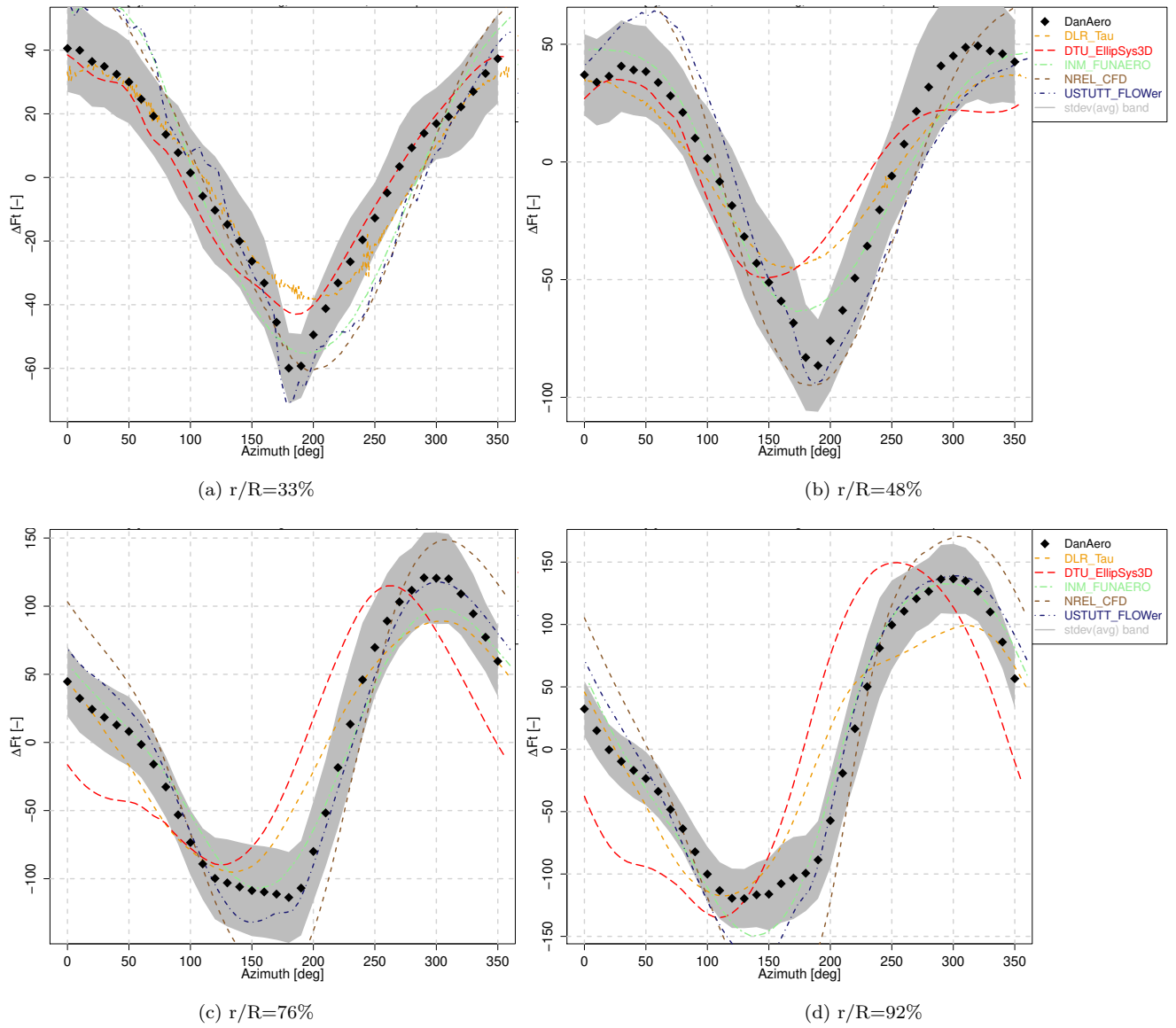


Figure E.28: Tangential force  $F_t$ , case 2.2



## Appendix F

# WP1: The database - Figures for shear and yaw cases

### F.1 File and graphs for second round of benchmark - sheared flow IV.2.1

In the figures below from Figure F.1 to F.9 the experimental data for the shear case are presented.

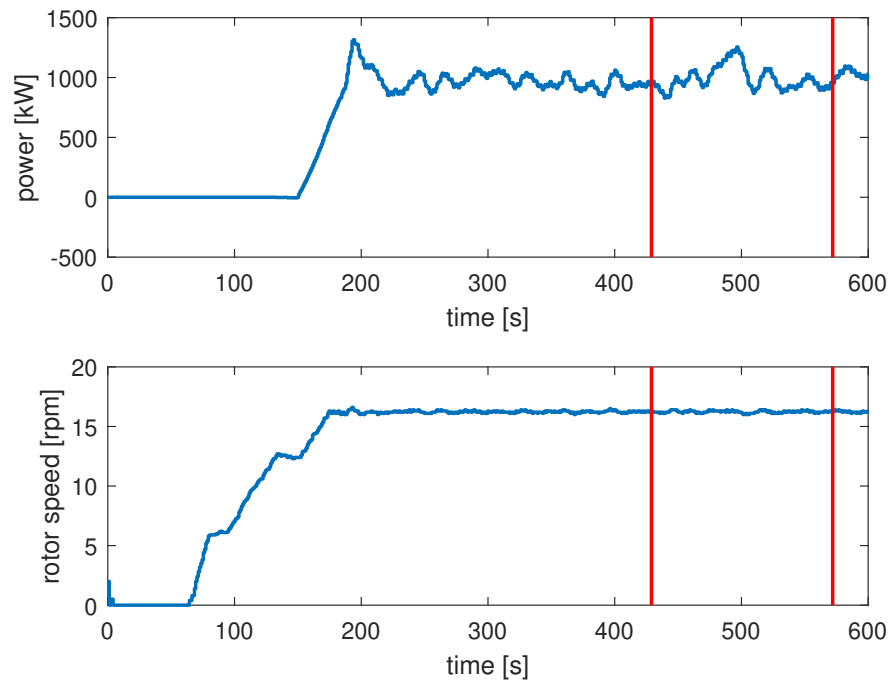


Figure F.1: Rotor power and rotor speed for the whole 10min. data file.

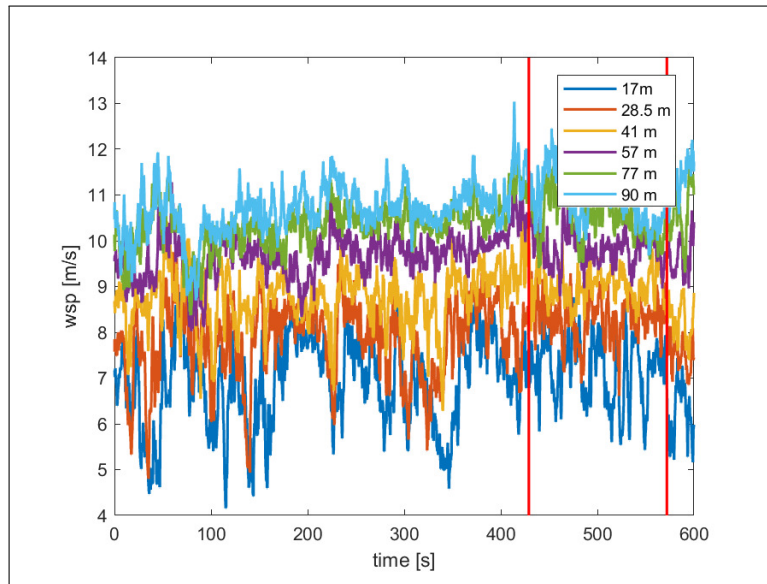


Figure F.2: Wind speed at the meteorological mast at the different heights.

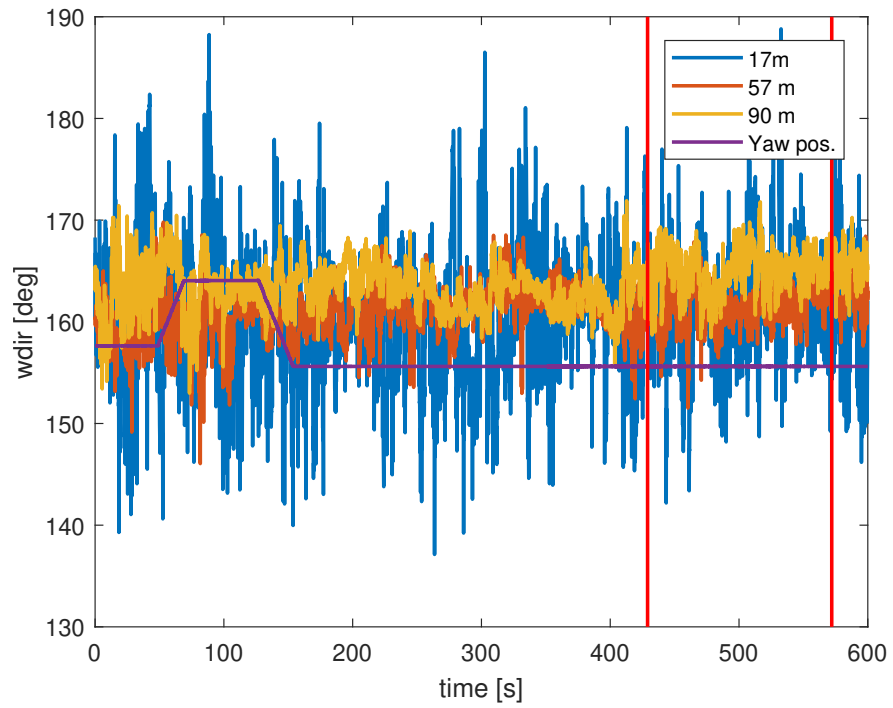


Figure F.3: Rotor power and rotor speed for the whole 10min. data file.

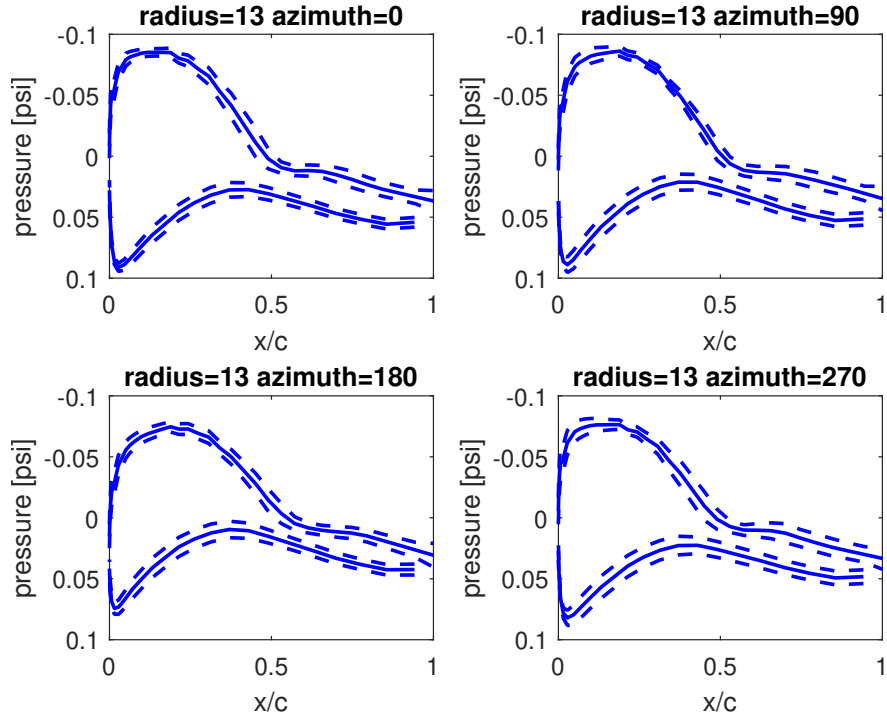


Figure F.4: Pressure distributions at radius 13m at four azimuth positions. Dashed lines show mean  $p$  plus/minus one standard deviation, respectively.

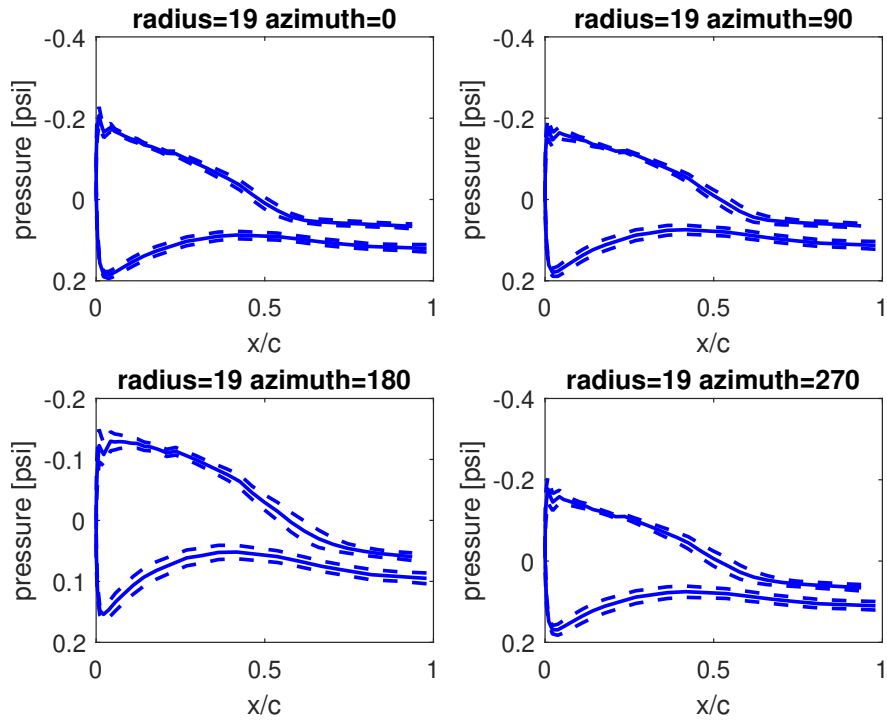


Figure F.5: Pressure distributions at radius 19m at four azimuth positions. Dashed lines show mean  $p$  plus/minus one standard deviation, respectively.

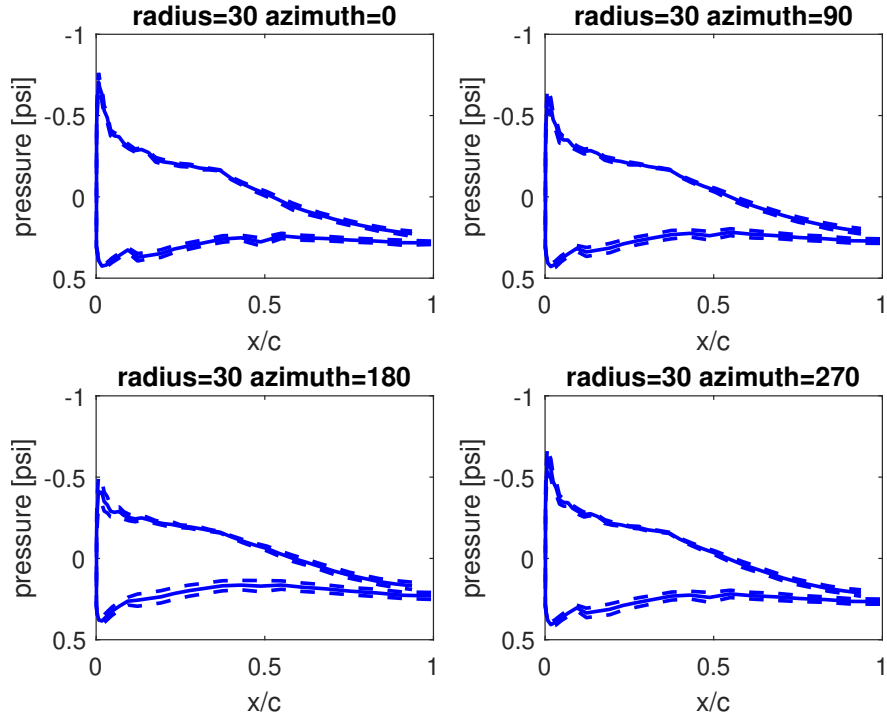


Figure F.6: Pressure distributions at radius 30m at four azimuth positions. Dashed lines show mean p plus/minus one standard deviation, respectively.

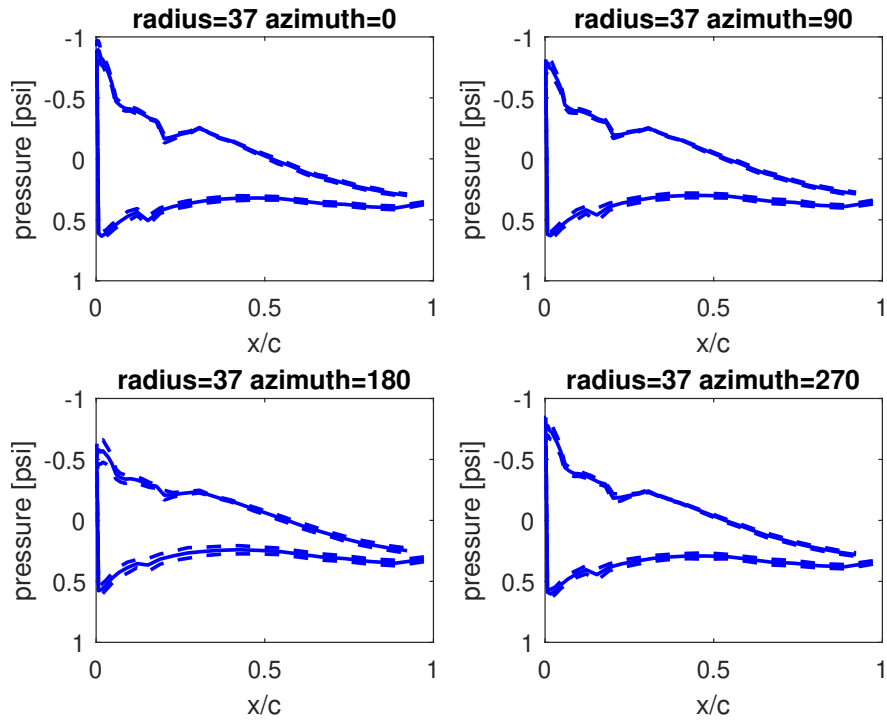


Figure F.7: Pressure distributions at radius 37m at four azimuth positions. Dashed lines show mean p plus/minus one standard deviation, respectively.

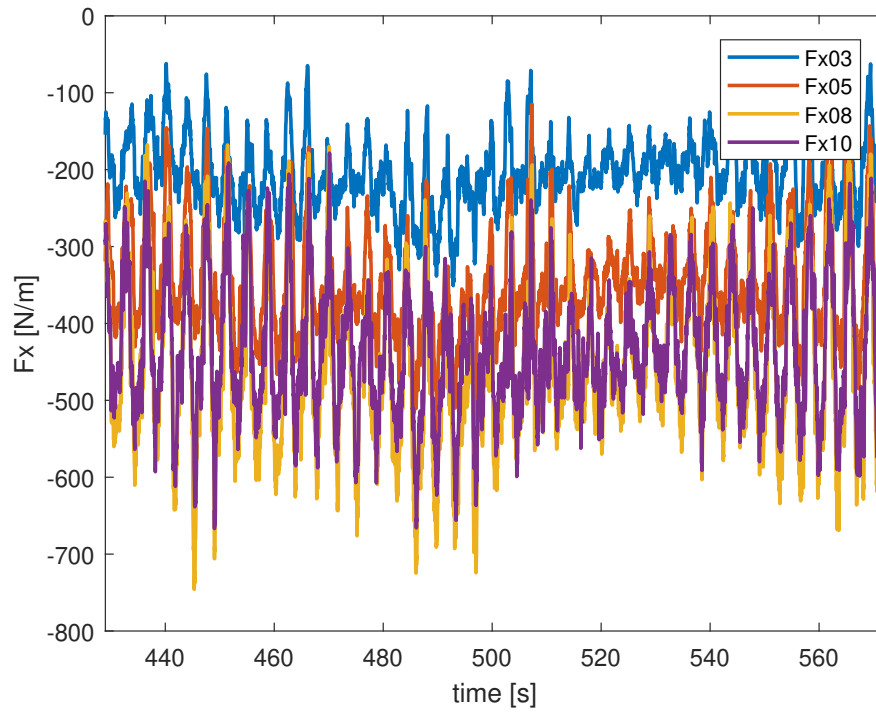


Figure F.8: Time traces of tangential force at four radial positions.

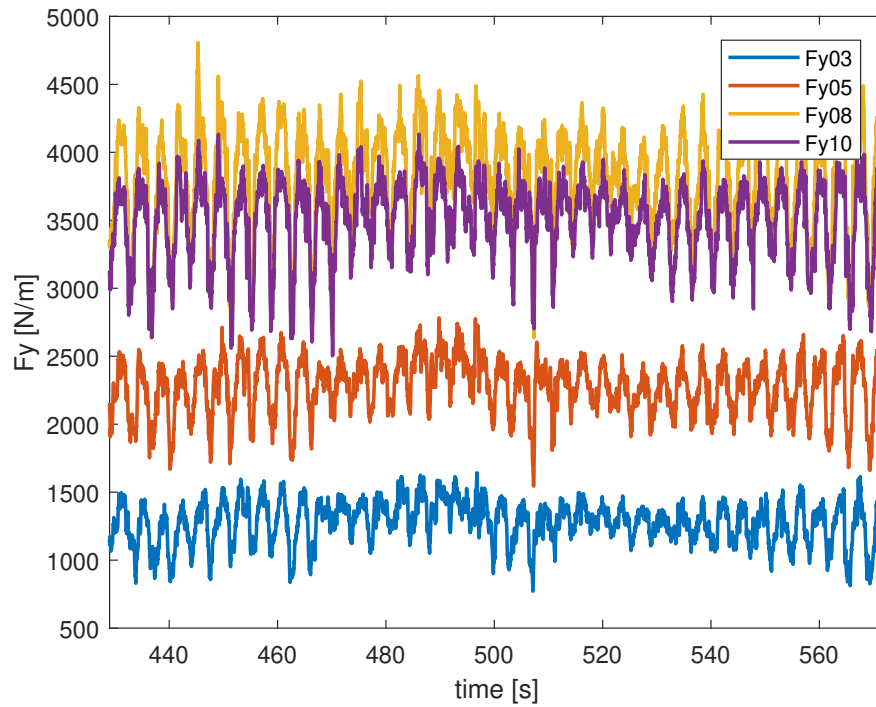


Figure F.9: Time traces of normal force four radial positions.

## F.2 File and graphs for second round of benchmark - yawed flow IV.2.2

In the figures below from Figure F.10 to F.18 the experimental data for the yaw case are presented.

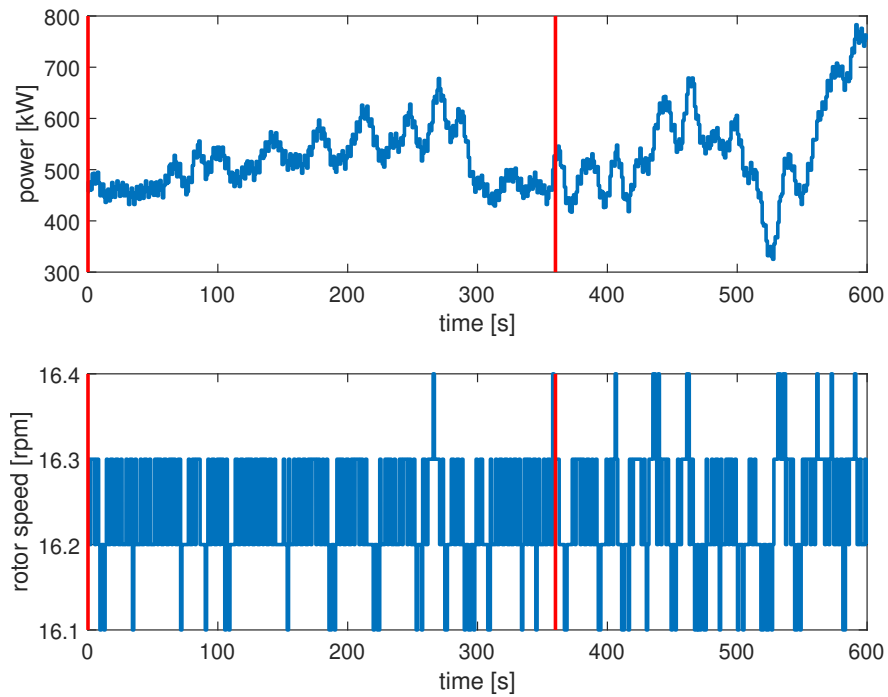


Figure F.10: Rotor power and rotor speed for the whole 10min. data file.

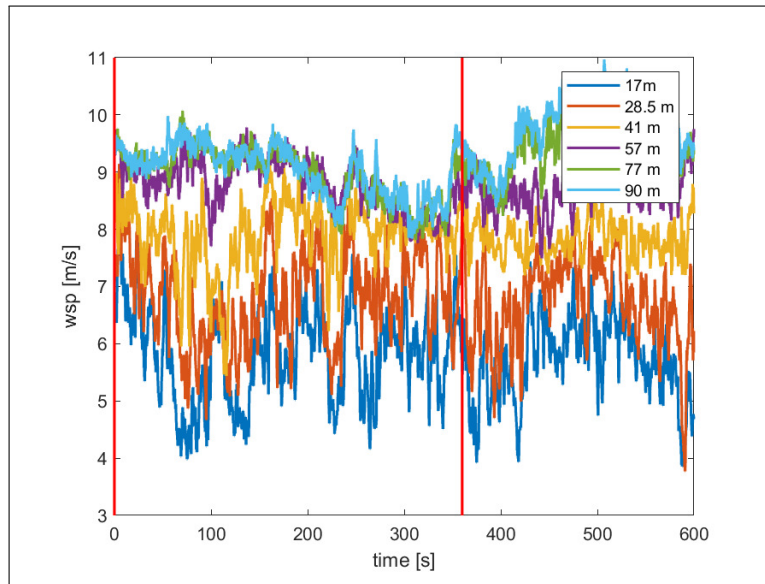


Figure F.11: Wind speed at the meteorological mast at the different heights.

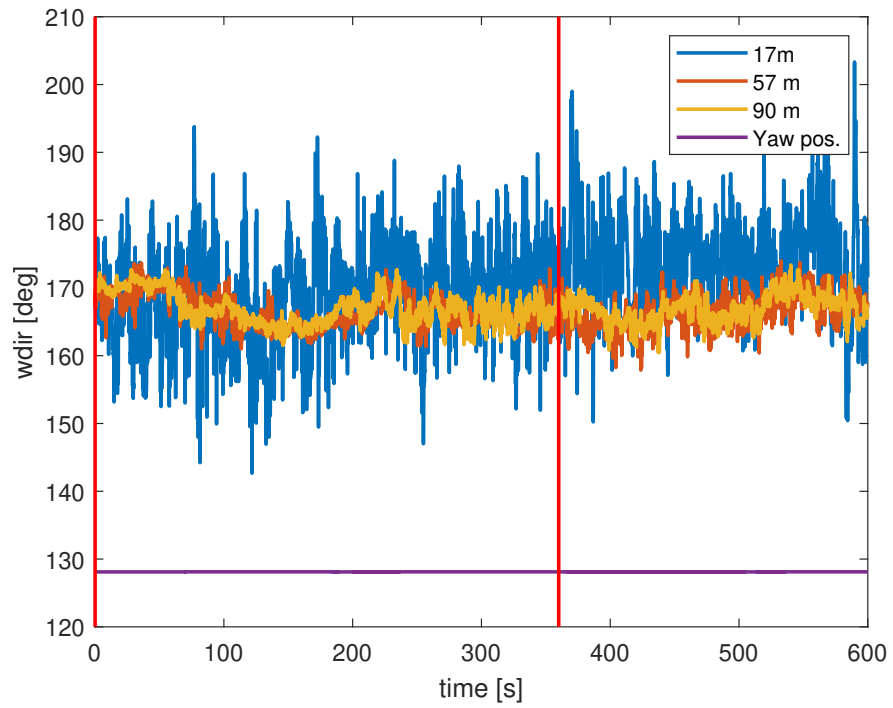


Figure F.12: Rotor power and rotor speed for the whole 10min. data file.

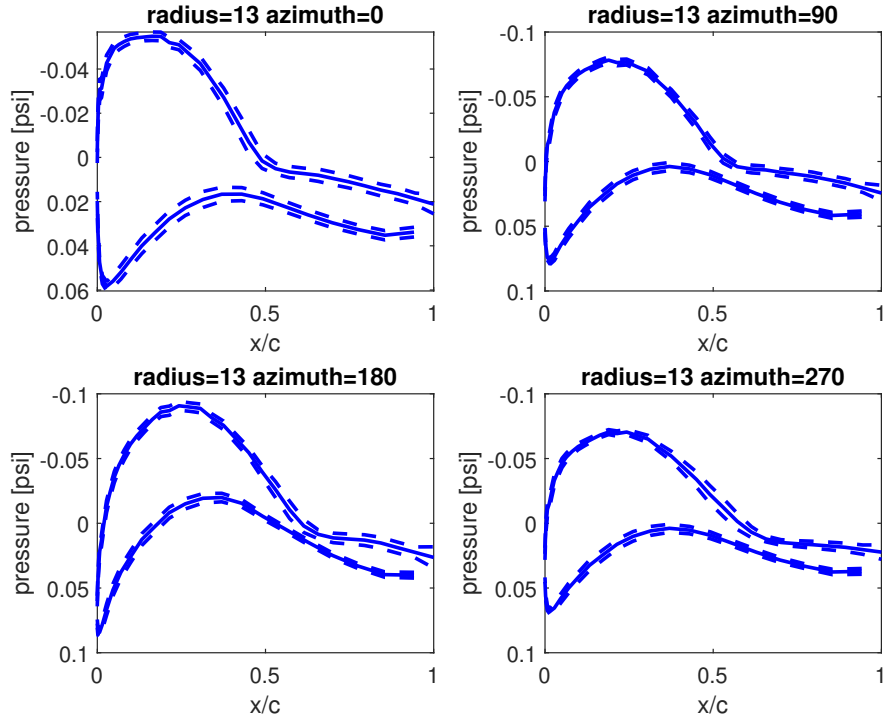


Figure F.13: Pressure distributions at radius 13m at four azimuth positions. Dashed lines show mean  $p$  plus/minus one standard deviation, respectively.

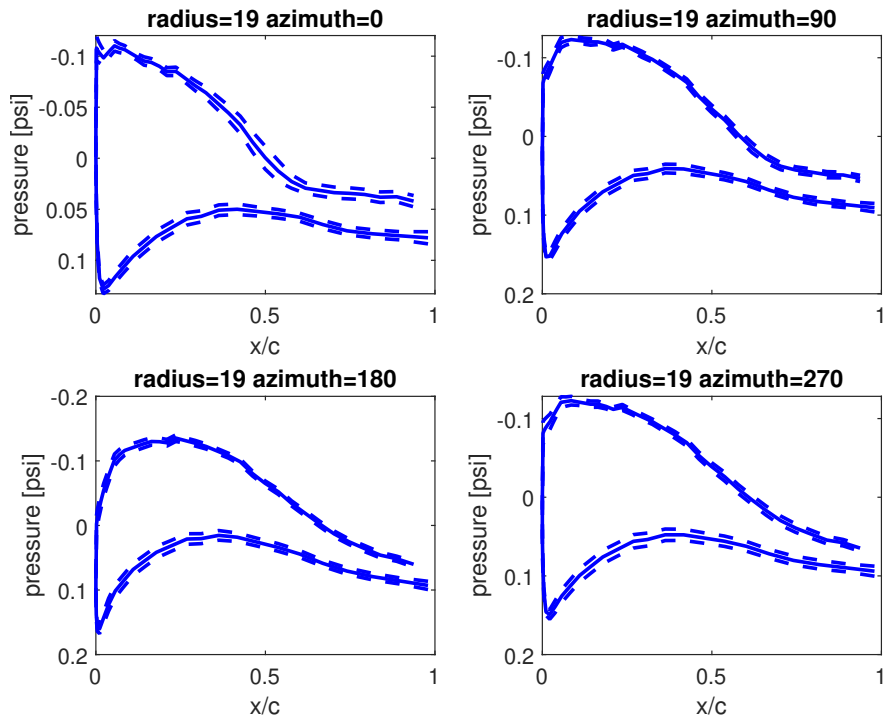


Figure F.14: Pressure distributions at radius 19m at four azimuth positions. Dashed lines show mean  $p$  plus/minus one standard deviation, respectively.



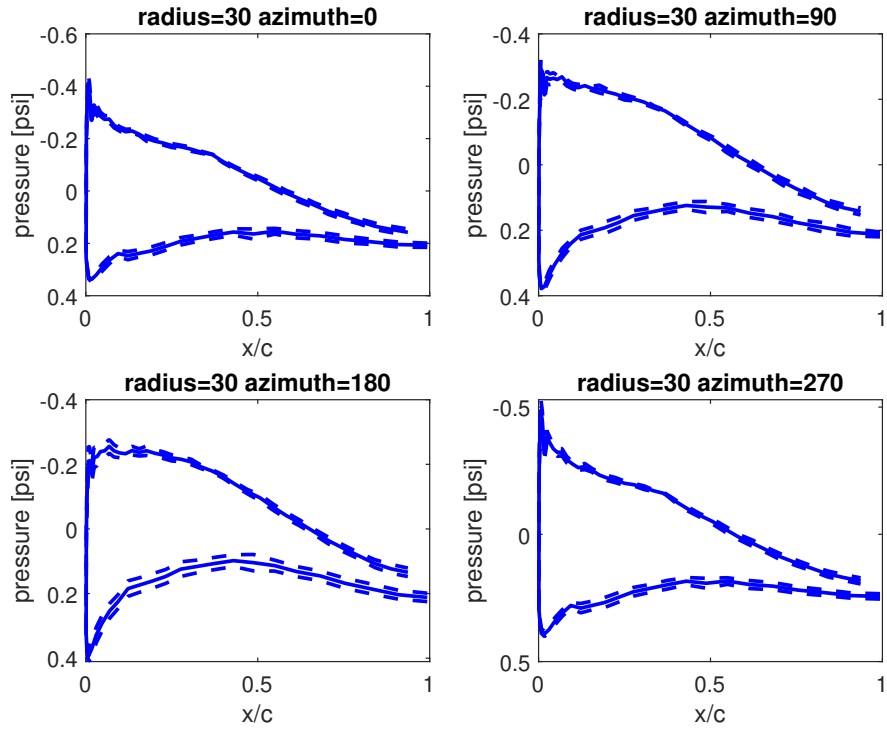


Figure F.15: Pressure distributions at radius 30m at four azimuth positions. Dashed lines show mean  $p$  plus/minus one standard deviation, respectively.

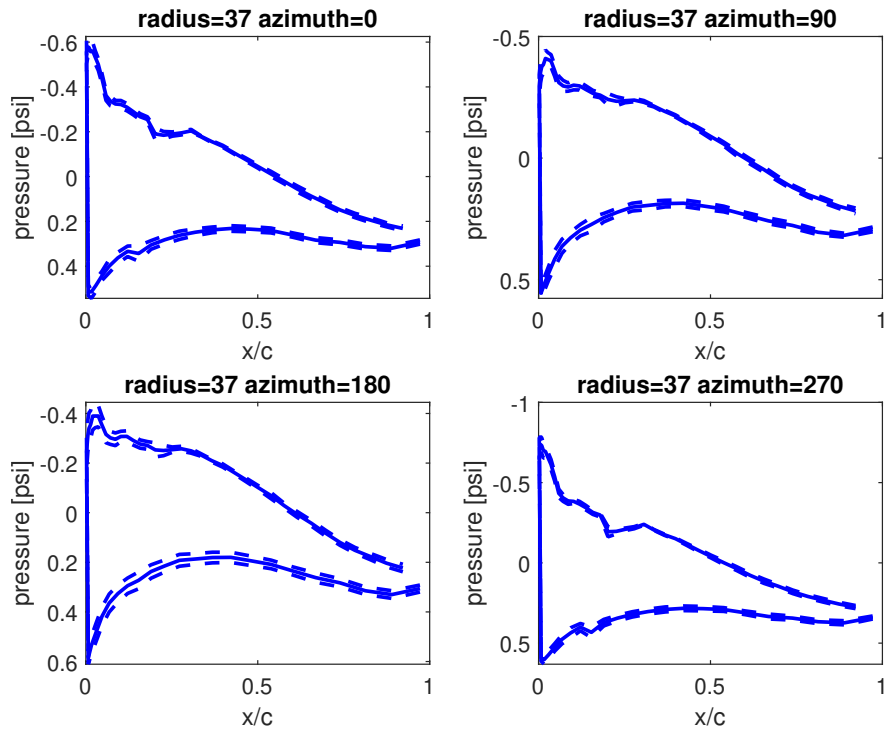


Figure F.16: Pressure distributions at radius 37m at four azimuth positions. Dashed lines show mean  $p$  plus/minus one standard deviation, respectively.

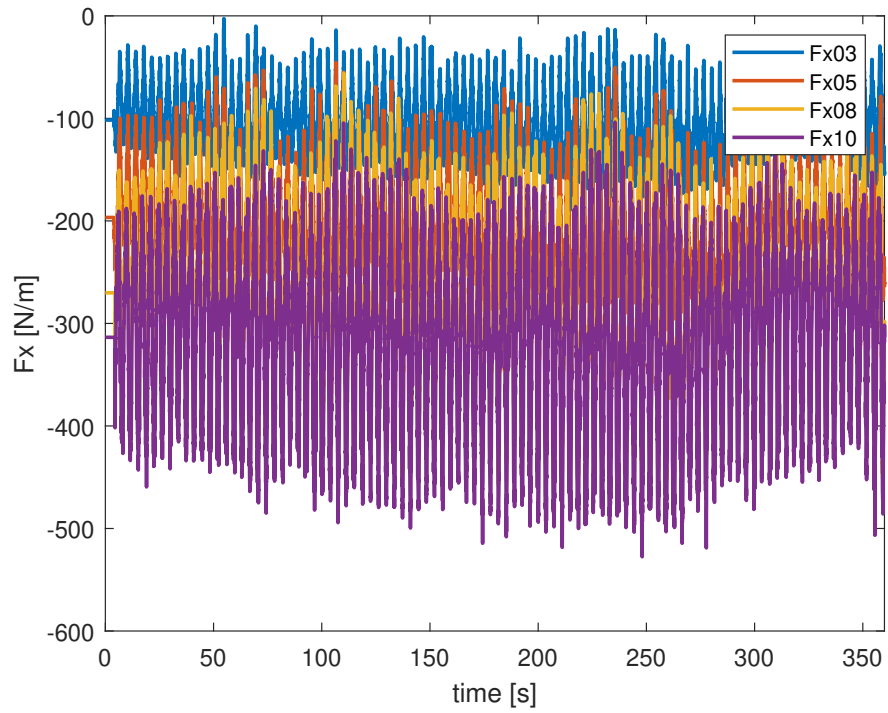


Figure F.17: Time traces of tangential force at four radial positions.

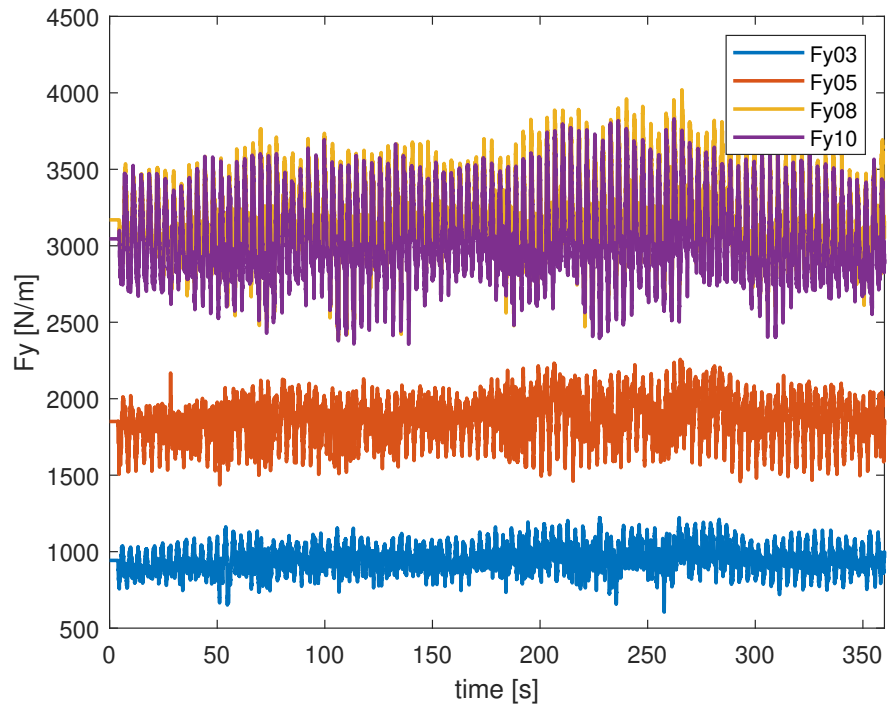


Figure F.18: Time traces of normal force four radial positions.